Analytical and Numerical Study of Percussive Riveting Process

Sai C Krovvidi

A dissertation

submitted in partial fulfillment of the

requirements for the degree of

Doctor of Philosophy

University of Washington

2021

Reading Committee:

Mamidala Ramulu, Co-Chair

Per Reinhall, Co-Chair

Joseph Garbini

Program Authorized to Offer Degree:

Mechanical Engineering

University of Washington

Abstract

Analytical and Numerical Study of Percussive Riveting Process

Sai C Krovvidi

Co-Chair of the Supervisory Committee: Prof. Mamidala Ramulu
Co-Chair of the Supervisory Committee: Prof. Per Reinhall

Mechanical Engineering

Percussive riveting is a dependable assembly method that produces high-quality joints in the aerospace industry. Its successful application is derived from its ease to implement in an assembly floor environment. The rivets are formed on the shank end of the rivet using a forming tool like a bucking bar and the head is constrained and impacted with a rapid succession of hits using a pneumatic gun with a special purpose die head. Research studies focused on the dynamics modeling of the percussive riveting process for robotic automation have not delivered an understanding of the temporal evolution of stress and strain fields in the vicinity of the rivet and the rivet hole. No modeling efforts have been published up to this point in time. This understanding is important to produce joints of predictable strength. In this work, squeeze riveting and percussive riveting numerical analysis was performed using finite element method. Inner skin region adjacent to the rivet button was observed to be most critical location for crack

nucleation by compression-induced shearing. For a good quality percussive rivet joint, friction coefficient and rivet hammer impact energy need to be maintained high, and skin thickness ratio needs to be comparatively low. In three-dimensional percussive riveting numerical analysis performed in this work using finite element method, bucking bar (under asymmetric motion) dwell time was observed to impact magnitude of rivet deformation.

TABLE OF CONTENTS

LIST OF FIGURES

LIST OF TABLES

ACKNOWLEDGEMENTS

I would like to thank Prof. Ramulu and Prof. Reinhall for their enduring encouragement, support and guidance. I would also like to thank Prof. Garbini, Prof. Kramlich and Prof. Salviato for serving on my graduate committee. I am grateful for the support provided by Mechanical Engineering department and Aeronautics and Astronautics department. This effort would not have been possible without the support of friends and family I cherish. Curtis, Jeremy and Rishi—Thank you.

DEDICATION

To my parents, sister and grandparents. O.S.R.

Chapter 1. INTRODUCTION

1.1 RIVETING PROCESS PHENOMENON

Percussive riveting is implemented ubiquitously in the aerospace industry. At any given time two persons or a person and a machine are required to perform the riveting process. Historically, the rivets have been formed on the shank end of the rivet using a forming tool like a bucking bar and the head has been constrained and impacted using a pneumatic gun with a special purpose die head. Refer to the schematics in figures 1.1 and 1.2. The rivet forms an interference fit joint. This happens because of the residual compressive stresses that are set up in the radial (r) and hoop (θ) direction due to plastic flow of rivet material [Szolwinski, 1]. These compressive stresses are balanced by tensile stresses in the skin and stiffener bulk material. Compressive stresses in the longitudinal (z) direction help keep the skins pressed together.

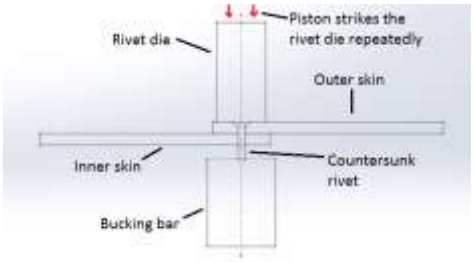

Figure 1.1. Schematic of the percussive riveting process implemented in an unstiffened stack-up.

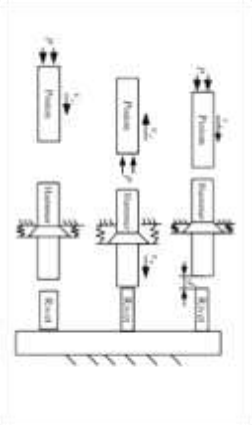

Figure 1.2. Schematic of the percussive riveting process. Bucking bar side is shown fixed in this figure [Li, Xi, Behdinan, 2].

With increase in squeeze force, the region of beneficial compressive residual stresses expands beyond the rivet hole into the surrounding skin material. Thereby the probability that fatigue cracks will initiate from the rivet hole reduces [Szolwinski, 1; Briles, 3].

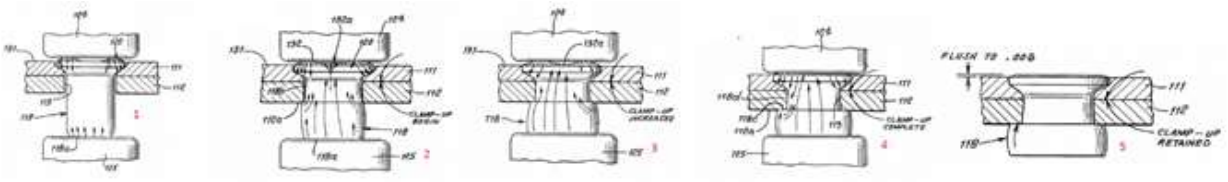

Figure 1.3. Schematic of the countersunk Briles rivet installation process [Briles, 3]. 1: Contact established. 2: Material yielding and increase in squeeze force causes rivet button to form. This leads to onset of clamp-up. 3: Squeeze force increases, thereby compressing rivet further. Rivet shank deforms and contacts rivet hole 4: Desired rivet button diameter and rivet shank deformation attained. 5: Residual stress state established after springback.

By driving rivets into the drilled and reamed holes, joint is formed. However, holes need to have smooth surfaces and need to be free from machining defects. Any hole eccentricity or misalignment of hole in the stack up causes improper fill. The counterbore tool is used to create

the countersink. Deburring is performed as the last step of the hole preparation process [Ahn, 4]. Rivets are preferred over threaded fasteners because compared of its economic advantages (tapping operation is avoided, lower unit cost for the fastener, and faster assembly). Also, it is a permanent fastener unlike a threaded fastener [Szolwinski, 1].

1.2 Framework of the Percussive Riveting Modeling Effort

It is essential to establish the required resources to tackle this research problem. The issues that will be studied and used to aid this effort are:

- Percussive riveting process parameters,
- Prior experiments and observations relating to squeeze riveting,
- Rivet and sheet geometry,
- Rivet and sheet material thermal and mechanical behavior,
- Dynamic thermal and mechanical effects,
- Literature on the alloy microstructures,
- Finite Element (FE) analysis literature relating to explicit dynamics simulations, adiabatic analysis, adaptive meshing, metal plasticity, structural element selection and capabilities, hourglass phenomenon, establishing boundary conditions, contact algorithms and friction modeling.

These questions were considered over the course of the modeling effort:

- What set of boundary conditions best help describe the percussive riveting assembly process adopted on the work floor?
- What process parameters and geometric parameters help describe the joint formation process?
- What is the resulting residual stress/ strain distribution and their trends? How do these trends compare with squeeze riveting process trends?

It is surprising to find that not much pertinent literature exists tackling this process. The need to understand the process is evident, and it appears to the author that there is scope for contributing to the current knowledge base.

Let us consider a relevant, dynamic study by Szymczyk, Jachimowicz, and Puchala [5]. It observes certain parameters relating to the sheets and the mushroom head rivet over the duration of the simulation comprising of 4 hits. The actual riveting process lasts for about 0.6 seconds which corresponds to around 15 hits. The authors of the study simulated first few hits because large proportion of plastic deformation is thought to happen initially. The subsequent hits are thought not to produce much deformation because the rivet material undergoes strain hardening.

In this study, the bucking bar is held against the mushroom head rivet and not the shank; contradicting what is implemented on the workfloor where bucking bar is held against the rivet shank. The bucking bar is held fixed in space. This is a simplification. Evolution of the stress and strain fields are affected by these boundary condition assumptions and simplifications.

The authors indicate that the initial impact energy of the gun die has an influence on the extent of the plastic region surrounding the rivet and the rivet hole and that the residual stress and strain fields are indistinguishable between both squeeze and dynamic riveting processes. This work did not include thermal effects during the forming process. The thermal softening is thought to affect the deformation and the stress/strain distributions.

1.3 Research Objectives and Tasks

Residual stress and strain distributions of percussive riveted joint have yet to be studied and characterized. Finite Element Analysis (FEA) of percussive riveting has not been performed till date. It is necessary to perform FEA because the percussive riveting process is dynamic and nature of rivet deformation is different in the percussive process compared to the squeeze riveting process. In squeeze riveting, the deformation is continuous and completed in single loading step. In percussive riveting, the deformation is discontinuous and based on stress wave propagation.

There are multiple loading steps in the percussive process. Hence, the process of characterizing the stress/strain fields in a percussive riveted joint forming was undertaken as with following specific objectives:

- Compare the analytical method deformation, stress and strain results with unstiffened stackup squeeze riveting numerical modeling and analysis FE simulation results. (Chapters 3 and 5)
- Build a numerical thermomechanical two-dimensional FE model of the percussive riveting process for an unstiffened stackup. (Chapters 6 and 7)
- Compare the squeeze riveting simulation results with in-house percussive riveting results. (Chapters 6 and 7)
- Study the effects of rivet shank diameter, sheet thickness, friction coefficient, piston impact energy, rivet die constraint force and bucking bar constraint force on the deformations, residual stresses and strains in the percussive riveting process. This is a numerical thermomechanical two-dimensional percussive FE design of experiments (DOE) effort. (Chapter 8)
- Build a numerical thermomechanical three-dimensional FE model of the unstiffened percussive riveting simulation with asymmetric bucking bar motion. Study the effect of asymmetric bucking bar motion on the deformations, residual stresses and strains. Compare the results with the squeeze riveting FE model and two-dimensional percussive riveting FE model. (Chapter 9)

1.4 DISSERTATION LAYOUT

- The second chapter of the dissertation presents and discusses literature relevant to percussive riveting analysis.
- Analytical study of squeeze riveting process using plasticity theory is presented in the third chapter of the dissertation.

- The fourth chapter of the dissertation presents the finite element modeling methodology (mesh layout, riveting stackup assembly layout, stackup materials, stackup boundary conditions and other important information) of the two-dimensional quasistatic squeeze riveting process, two-dimensional fixed rivet hammer -- movable bucking bar (partial dynamic) riveting process, two-dimensional movable rivet hammer -- movable bucking bar (full dynamic) riveting process and three-dimensional full dynamic riveting process.
- Residual stress and strain distributions of the two-dimensional quasistatic squeeze riveting process are presented and discussed in the fifth chapter.
- Residual stress and strain distributions of the two-dimensional partial dynamic riveting process are presented and discussed in the sixth chapter. Comparison of partial dynamic distributions with two-dimensional quasistatic squeeze riveting process is presented.
- Residual stress and strain distributions of the two-dimensional full dynamic riveting process are presented and discussed in the seventh chapter. Comparison of full dynamic distributions with two-dimensional quasistatic squeeze riveting process is presented.
- The eighth chapter of the dissertation contains a discussion of a two-dimensional, full dynamic FEA DOE study in which the effects of skin-thickness ratio, rivet-hole clearance, friction coefficient, rivet piston impact energy, bucking bar constraint force and rivet hammer constraint force on the stackup deformation and stresses are studied.
- The development of FE model and analysis of three-dimensional full dynamic riveting process is discussed in the ninth chapter of the dissertation. Comparison of the FEA results with results from chapters 5 and 7 is presented in this chapter.
- Conclusions and recommendations for future work are presented in the tenth chapter of the dissertation.

Chapter 2. LITERATURE SURVEY

2.1 TYPES OF RIVETING PROCESSES

Different variations of the riveting process exist in the aviation and automotive industry [5-13]. **Squeeze riveting** (figures 2.1 and 2.2) is performed by dies mounted on large C-frames and it is a quasi-static process that employs squeeze loads in the order of magnitude of thousands of pound force [Zieve, 7]. Consider a rivet of shank radius 2.5 mm and yield strength of 400 MPa, the force required to initiate plastic deformation is $(400*10^6*\pi*(0.0025)^2)$ which is 7854 N (1767 lbf). And if the material of the rivet exhibits hardening, the force required for further deformation increases beyond 7854 N. Slug or universal head rivets can be used in this sort of process. In the aviation industry, aerodynamic requirements necessitate use of a rivet head geometry that sits flush with the skin. So, countersunk rivets are employed. They also provide the added benefit of improved material fill in the outer (or upper skin) because of improved material flow in the radial direction. With the countersunk geometry, frictional slip occurs between the countersunk sheet and rivet head. The head expands through a wedging action (wedge expansion) [Rans, 14].

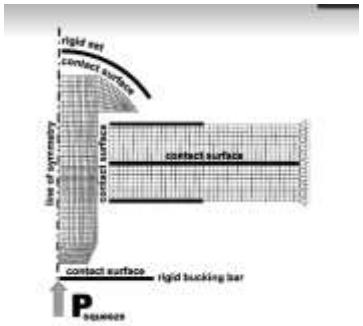

Figure 2.1. Schematic of the squeeze riveting process [Szolwinski, 1].

Much of the existing literature pertaining to the riveting process [1, 5, 14-21] mostly focus on universal head or slug rivets in either stiffened or unstiffened joints (figure 2.3). Studies that have

analyzed the behavior of countersunk rivet joints [1, 5,14-17] have not presented findings on how the percussive riveting process impacts the joint performance.

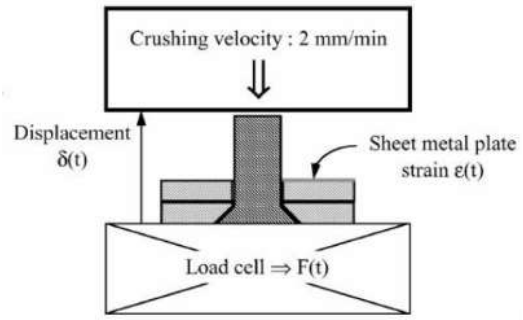

Figure 2.2. Schematic of the squeeze riveting process [Langrand, 18].

Either the riveting process is described differently [Szymczyk, 5] or conventional squeeze riveting has been implemented [1, 14-17, 19-20] which is not the case in the workfloor setting. This dissertation work addresses that analytical need. The percussive riveting process is a strain rate and temperature dependent boundary value problem. A dynamic thermal-structural simulation framework is required to study various issues. Purpose of this dissertation work is to better explain the local effects during the percussive riveting process by analysis. Most assembled percussive joints are imperfect but found to be entirely adequate when tested in a practical setting. This work will aim to address the origin of the adequate joint strength.

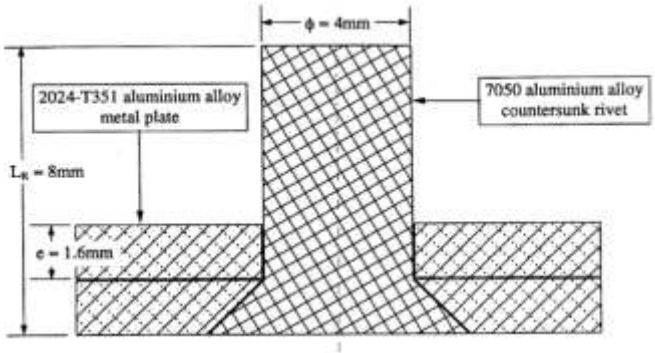

Figure 2.3. Schematic of an unstiffened stack-up [Langrand, 18].

Other studies [Li, 2; Abdelal, 21] focused on the dynamics modeling of the percussive riveting process for robotic automation. These studies did not aim to deliver an understanding of the

temporal evolution of stress and strain fields in the vicinity of the rivet and the rivet hole. Their aim was to achieve cost reduction by replicating the riveting process to produce joints of equivalent quality.

The main problem tackled by these automation studies was to accommodate the rapidly changing boundary conditions and structural stiffness during the riveting process. These automation studies did this by focusing on the change in the length of the rivet after each hit and used it as a parameter to improve their dynamic model.

The publication by Szymczyk, Jachimowicz and Puchala [5] comes closest to studying repeated impact. But this study *does not adequately address dynamic FE modeling*. By incorporating some simplifying assumptions (like a spatially fixed bucking bar), phenomena like the free motion of the rivet during the forming process and the evolution of contact were not captured. Figure 2.4 shows the representation of a single-impact dynamic riveting study where the rivet die is held fixed in space.

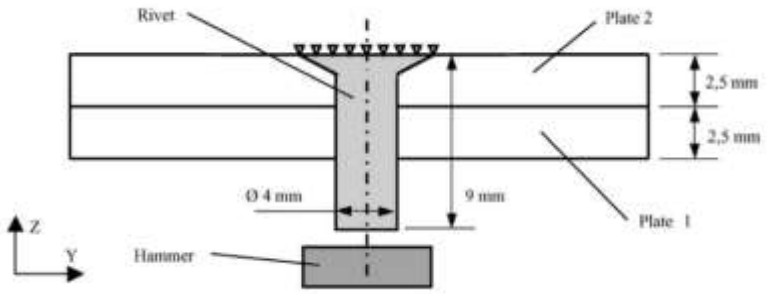

Figure 2.4. Schematic of a dynamic riveting process [Blanchot, 22].

Force controlled squeeze riveting was first proposed by Muller [15] in his dissertation as he found that the joint fatigue life increased significantly with an increase in squeeze force. The region and magnitude of the compressive residual hoop stresses were found to increase with rivet squeeze force. Larger driven rivet head dimensions associated with larger squeeze forces have been observed to shift the crack nucleation location away from the fastener hole region [Rans, 14].

This results in a higher chance of initiation of cracks due to fretting fatigue because the sheets faying surface carries the bulk of the joint load [Szolwinski, 1].

Electromagnetic riveting [Deng, 6; Zieve, 7] is a contemporary riveting process (refer to figures 2.5 and 2.6). It essentially deforms a slug rivet by synchronizing impacts of electromagnetically accelerated dies on both sides of the rivet. The riveting force is produced by the interaction between electric field and magnetic field. In EMR process, the magnetic force is responsible for the motion of the driver plate made from copper. It is generated due to a strong electromagnetic field created by feeding a short duration, high intensity current pulse through the coil. The driver plate accelerates due to the axial component of the magnetic which has a main effect on rivet deformation. When the punch impacts the rivet, the rivet shaft is first deformed. Subsequently, the formed rivet shaft is pushed further into the hole. After the rivet shaft contacts with the plate stack, the rivet head begins to deform. It is amenable for low to moderate strength aluminum alloy rivets, but it has been found to be lacking capability when it was used to form rivets made from high strength aluminum alloys.

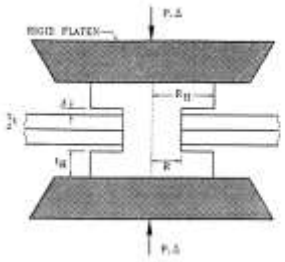

Figure 2.5. Schematic of the electromagnetic riveting process.

In the **percussive riveting process**, the rivets are driven manually by technical workers who handle bucking bars and pneumatic rivet hammers (or guns). Occasionally, automated equipment is also utilized in the percussive riveting process. The die is impacted repeatedly by a guided mass (piston) that oscillates inside the hammer. The kinetic energy imparted by the piston upon the die causes the bucking bar and the joint assembly to rebound from the surface of the die.

Because of the reflection of the stress waves at the rivet tail-bucking bar interface the rivet deforms inelastically and the bucking bar rebounds and returns to contact the deformed rivet tail before the next hit of the piston.

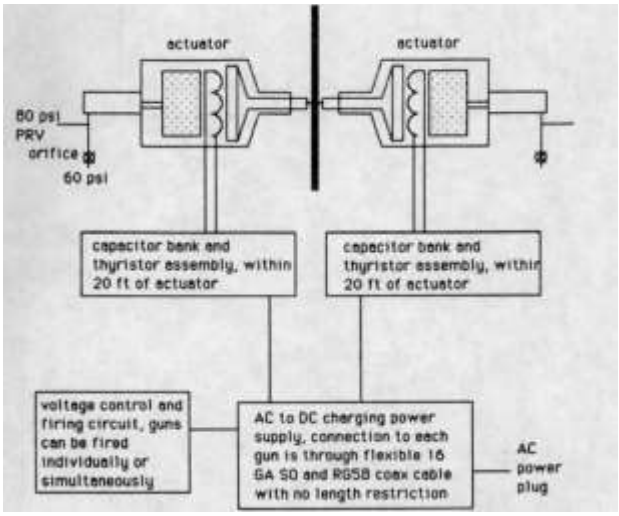

Figure 2.6. Schematic of the low-voltage electromagnetic riveting process [Zieve, 7].

Successive hits deform the rivet shank until the button size is deemed adequate by the workers. This judgment is made from prior experience gained through training and day-to-day work of driving hundreds of rivets. As a result, the displacement and traction boundary conditions vary dynamically.

Self-pierce riveting process [8-12] is mostly used in the automotive industry (refer to figures 2.7-2.9). It is used in conjunction with aluminum and magnesium sheets. This process also involves large-scale deformation within the rivet material to form the joint. **Orbital riveting** [Di Bella, 13] is also used in the automotive industry, but it involves smaller material deformations compared with the self-pierce process (refer to figure 2.10).

Riveting FE analysis (predominantly squeeze and electromagnetic riveting) has been performed until now using coarse rivet mesh geometries to produce fast solutions. These solutions sacrifice accuracy and do not necessarily capture gradients effectively because they are masked by aliasing effects.

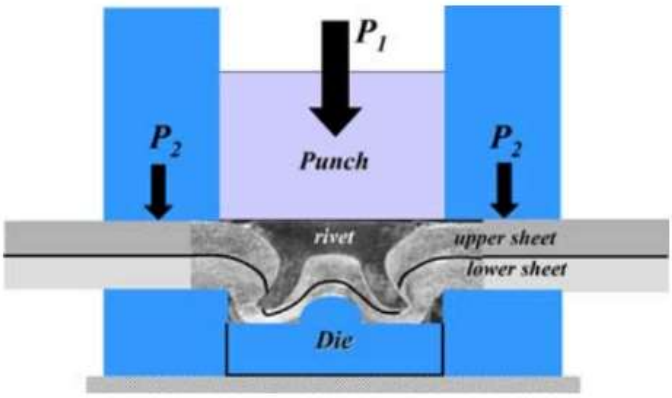

Figure 2.7. Schematic of the self-pierced riveting process [Iyer, 11].

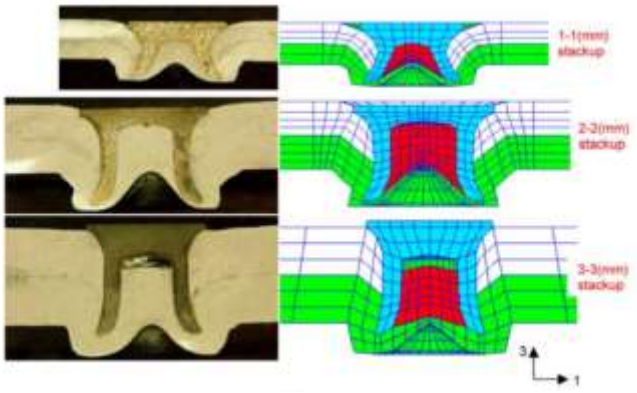

Figure 2.8. Representative images of the self-pierced riveting process [Iyer, 11].

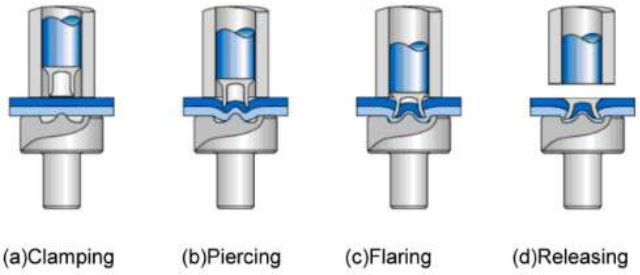

Figure 2.9. Schematic of the self-piercing riveting process [Huang, 8].

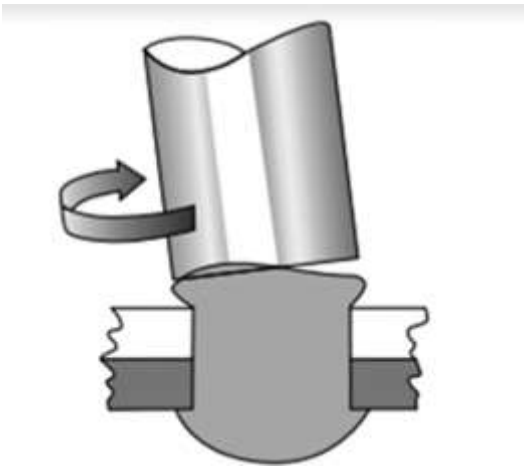

Figure 2.10. Schematic of the orbital riveting process [Di Bella, 13].

According to the author of this dissertation, a fine rivet mesh is required to study the variation of stresses and strains both in the longitudinal and the lateral directions, especially at the rivet-sheet interface inside the percussive riveting stackup. Too fine a mesh will result in an inability to tackle microstructure-level anisotropy. A balanced mesh element density is sought with mesh element characteristic size greater than alloy grains.

These variations help us in establishing how these quantities (stresses and strains) are affected by various riveting process parameters (which will be established) and because of change in geometric parameters like physical dimensions of the skins and the rivet. The **percussive riveting** technique is a challenging problem to model. Any FE modeling effort requires *decisions regarding the level of detail. What effects must be captured and what effects can be neglected to obtain accurate and usable results*.

Replicating existing FE analysis studies to establish a benchmark for this dissertation work was a challenging task. The issue that impeded faithful replication was incomplete information pertaining to traction and displacement boundary conditions and contact and material properties. If similar stress and strain trends were obtained, we assumed the replication was a success. The constraints that exist to limit this FE analysis effort are acknowledged. For instance, the rivet geometry is already established. The choice of boundary conditions is varied. Making the problem

manageable is a big priority. By researching empirical evidence and creating pertinent Design of Experiment (DOE) studies, the author of this dissertation aims to promote a deeper understanding of the local and global phenomena that occur during the implementation of this (percussive) riveting technique.

This manufacturing technique is a discontinuous and rapid process. Compared to the squeeze riveting process, percussive riveting is a dynamic, high strain-rate process. Sustained efforts from engineers and researchers in production settings have resulted in overcoming issues plaguing joint production like crack development, skin damage and inferior material fill (which results in poor joint fatigue life).

The joint assembly model consists of a stiff bucking bar and a stiff gun die. These segments of the model are used in workfloor setting and the geometries of these parts is known. The other model elements include the upper sheet with the countersunk hole, lower sheet with a through hole; and the countersunk rivet which is set in place into the hole.

To produce a tractable percussive riveting DOE for this dissertation work, the squeeze riveting process will be first studied. The simulations will be axisymmetric. This is covered in chapters 4 and 5. The riveting process in this case is monotonic loading followed by monotonic unloading. Stress wave propagation within the rivet and the sheets is not a significant aspect that affects the result because the process is quasistatic.

The simulation issues can be categorized into four distinct types. These will be discussed throughout this work. Also, since development of an in-house simulation code is not in the scope of this work, pre-packaged code of Dassault Systemes' ABAQUS suite is utilized to perform the simulations. The suitability and robustness of the contact algorithms, material plasticity models and mesh adaptivity algorithms will also be established. The four distinct types of simulation issues are: Boundary conditions, material modeling, contact algorithms and mesh distortion.

This will be followed up with a DOE for percussive riveting. The DOE study is covered in chapter 8. Building and analyzing percussive riveting model is discussed in chapter 7. Judgment

will be exercised to decide the suitable boundary conditions because here stress wave propagation within the sheets and the rivet is a pertinent issue. For instance, three frame bays and three stringer bays can be selected to perform riveting simulations at a global level. But for a local simulation, a set of boundary conditions (traction and displacement sets) will be tested. The domain of interest will be restricted to few inches from the rivet axis.

Eventually, recommendations will be made for production of joints with consistent predictable strength and performance. There is a dearth in research pertaining to percussive riveting joint analysis. As it has already been mentioned, dynamics modeling research has been carried out by few research groups [2,5,21,22]. Focus has been on automating the currently existing process as presented in [Yuwen, 2]. When research into stress analysis has been carried out, it discusses the riveting problem with inadequate boundary conditions, unrealistic riveting technique and rivet geometries that are not ubiquitous in the domestic aerospace industry or simply unrealistic [Szymczyk, 5; Blanchot, 22].

Also, not much research pertaining to the thermal (adiabatic) effects in percussive riveting exists. The fuselage structure gradually stiffens as more rivets get bucked, the boundary conditions keep evolving. Structural embrittlement is a potential issue. Also, in the literature there is motivation for quantifying and testing riveting sequence effect on the strength of the joint.

2.2 RIVETING PROCESSES IMPLEMENTATION

Riveted joints of aluminum-alloy sheet material are extensively adopted in designing aircraft structures. For instance, many lap joints are used in pressurized fuselages of transport aircraft. The number of flight cycles in the economic life of these aircraft is now well in the range of 50,000–100,000 flights. As a result, durability and damage tolerance of riveted joints in a fuselage are now recognized as a serious design and airworthiness topic [de Rijck, 24].

Typical riveted aircraft structure is manufactured by layering either two (single-lap joint) or three (double-lap joint) sheets of material and then joining the assembly together with a fastener. Common fastening techniques rely on either bolts or other threaded fasteners and rivets. When compared to threaded fasteners, the use of rivets is more attractive because of both its economic advantages (no threading of bulk material required, lower unit cost for the fastener, and faster cycle time for installation) and its permanence after installation (no ability to back out after installation) [Szolwinski, 1].

The rivet installation does not impart a large amount of residual stress, such as the split-sleeve cold working process, or a large amount of clamp-up, as with steel threaded fasteners with torque-off collars.

After the riveting process is completed, the rivet naturally grips the plates with a clamping force in the shank and a frictional force between all contacting surfaces (refer to figure 1.3). It has been noted that the drifting of holes during assembly can produce initial cracks or nicks that can subsequently lead to fatigue failures in riveted joints [Fung, 19].

The importance of the degree of rivet flushness before rivet installation on fatigue performance is alluded to by a standard riveting practice regarding the range of acceptable heights the countersunk rivet head is permitted to protrude above the countersunk sheet [Rans, 14].

This practice ensures that the countersunk depth of the sheet does not exceed the height of the countersunk rivet head, which would result in poor hole filling within the countersunk sheet during riveting. Additionally, too deep a countersink would minimize the rivet-sheet contact during riveting, reducing the benefit of through-thickness compressive stresses. Comparison of results for the two flushness cases from this study showed that the degree of rivet flushness influences the amount of hole expansion and formation of residual stresses at high squeeze forces [Rans, 14].

In addition to the wedge-expansion mechanism seen in a countersunk rivet, a protruding rivet head localizes the through-thickness compressive stress resulting from the squeeze force. For the

perfectly flush case, the rivet die contacts both the rivet and the surrounding outer sheet, distributing the riveting tool squeeze force over a larger area. A small degree of rivet protrusion eliminates contact between the rivet set and the outer sheet, localizing the transfer of force into the sheets at the countersunk conical contact region between the rivet and outer sheet. This contributes to the formation of residual stresses beneath the rivet head [Rans, 14].

The most common upsetting tool (refer to figure 2.11) used in an aircraft is the pneumatic hammer (so called rivet gun). The shank's end is bucked with a bucking bar and the manufactured head is hammered with the rivet hammer. The rivet driving requires a few hammer strokes [Szymczyk, 5].

Upsetting should be performed with strong blows of hammers or press. To obtain uniform height reduction in the forming process, with decreasing height to radius (h/r) ratio of the rivet, higher load is necessary [Kajtoch, 23].

Figure 2.11. Pneumatic Rivet Gun. (Image: Atlas Copco Company)

In percussive riveting, each hammer hit only causes the rivet to deform a small amount. However, after a series of impulses, the accumulated deformation of the rivet will be substantial [Yuwen, 2]. Strains of magnitude 1.2-1.6 are obtained from rivets formed using percussive riveting process.

Manufacturers use empirical rules to design the riveted joint dimensions under cyclic loading. Tolerances, pitches, edge margins, rivet numbers and schemes are determined as a function of the sheet metal plate thickness and the load [Langrand, 26]. In ref. [28], spliced joints were

fastened with eight 4.76-mm-diameter 7050-T73 protruding head rivets with a 2D edge distance and a 4D spacing. D is the rivet shank diameter.

Percussive riveting has two significant characteristics: the repetitive impacts acting on the rivet under the hammer hits from the gun, and the elastoplastic deformation that the rivet experiences in the process. In literature, apart from Szymczyk, E. Jachimowicz, J. Puchala [5], no significant work has been published on the modeling of this riveting process. FE models were applied to analyze the deformation and stress of rivets. However, these studies are for high-pressure riveting processes, in which the rivet is deformed by a large squeezing force. Thus, these models are not applicable for percussive riveting. Modeling of pneumatic percussive hammers was investigated by Bloxsom [27], but these hammers are not used for riveting, thus, these cannot be used to analyze the elastoplastic deformation of the rivet [Yuwen, 2].

Another riveting technique used is the electromagnetic riveting (EMR) (refer to figures 2.5 and 2.6). According to the principle of EMR, the riveting force is produced by the interaction between electric field and magnetic field. In EMR process, the magnetic force responsible for the motion of the driver plate is due to a strong electromagnetic field created by feeding a short duration, high intensity current pulse through the coil. The driver plate is a copper plate. The magnetic force is the loading for rivet deformation analysis during EMR process. According to the distribution of magnetic force vector, the driver plate is mainly subjected to the axial component which has a main effect on rivet deformation [Deng, 6].

Due to the low voltage, the Low Voltage Electromagnetic Riveter (LVER) provides a force risetime much slower than the high-voltage system. This is beneficial for strain rate sensitive alloys. A narrow force pulse is generated, thereby minimizing the recoil transmitted to positioning equipment [Zieve, 7].

Another riveting technique is the squeeze riveting process (refer to figures 2.11 and 2.12). A hydraulic squeeze press reaches around the structure and squeezes the rivet from opposing sides. The bending moment that must be resisted is proportional therefore to the distance from the

center to the edge of the plate. Thus, hydraulic machines become large for fasteners located far from the edge of the structure. Because of their massive size, hydraulic squeezing machines often are unable to function in difficult-to-reach areas [Zieve, 7]. The squeeze riveting technique implies that a squeeze force is applied on the rivets to obtain the closing head. The countersink rivet shape is mainly used for rivets at the outside skin of the fuselage. Rivets with a protruding head are preferred if aerodynamic requirements are not applicable [de Rijck, 24].

In the squeeze riveting approach used in [Szolwinski, 1], the rivet/joint assembly was compressed quasistatically between a set of hydraulic platens forming the rivet head. A compressive residual hoop stress is often induced around rivet holes prior to riveting by cold working the hole with an expanding mandrel, with the goal of retarding the growth of fatigue damage that may nucleate in the material at and around the hole [Szolwinski, 1].

Specimens having untreated and cold expanded holes were fatigue tested. Unexpectedly, the fatigue resistance of specimens having cold expanded holes was lower than that of untreated specimens. The assembly of the specimens was performed by Hi-Lok rivets, after having treated the surface wtih Alodine and epoxy primer [Boni, 25].

In the automotive industry, self-piercing riveting (SPR) technique is implemented [8-12]. In self-piercing riveting, a tubular rivet made from a high-strength steel alloy is forced through a pair of partially overlapping sheets that are supported by a rigid circular die with an axisymmetric cavity (refer to figure 2.7). The diameter of the die and rivet are similar. The sheet material is typically an automotive aluminum alloy such as 5754-O or 6111-T4. The entire process, completed in approximately 1000 ms, involves high strain rates. A clamping force is applied to prevent lateral sheet movements while a displacement-controlled punch forces the rivet through the sheets. As is the case with other types of riveted and bolted joints, the local movements at contacting surfaces, contact pressures and bulk stresses ostensibly determine the monotonic and cyclic strength of SPR joints. These parameters are related to the amount of fretting damage also [Iyer, 11].

Orbital riveting is comparable to impact and compression forming, where a compressive axial load is applied with a tool to deform the piece. When compared to other riveting processes, in orbital forming, the tool rotates at a fixed angle (i.e. typically 3° to 6°) and applies axial and radial forces to progressively deform material until the specific shape is reached (refer to figure 2.10). Moreover, the process requires more tool revolutions and typically takes 1.5–3.0 s to complete. During the process, the deformation work influences only the tool/ rivet line of contact, not the whole tool surface [Di Bella, 13].

This fact reduces axial loads of about 80% by inducing several advantages; i.e.: lower level of stress on the parts that have to be fastened or mated; smooth surface finish; elimination of cracks caused by impact riveting; cold-head forming by avoiding bending or swelling of the fastener shank; use of smaller presses in terms of sizes and costs; less rigid fixturing and longer lasting tools. However, the industrial applicability of this joining technology is strongly limited by highly aggressive environmental conditions that can induce localized corrosion mechanisms like the conditions encountered in the aerospace industry [Di Bella, 13].

This phenomenon can be intensified by crevices (i.e., crevice corrosion attack) or irregularities. For this fact, in joining design, the metal sheets are chosen by evaluating electrochemical and corrosion properties. In particular, the goal of this research was to study the performance of a hybrid joint between an aluminum sheet and a steel one, realized with an orbital forming process by focusing the attention not only on the mechanical resistance but mainly on the durability in salt spray fog [Di Bella, 13].

The advantages and disadvantages of the various riveting processes discussed in this chapter are presented in table 2.1. Careful selection of riveting process must be made based on the working environment and operational loads encountered by the assembled joint.

Table 2.1. Comparison of Riveting Processes

Riveting Method	Advantages	Disadvantages
Squeeze (Primarily used in the aerospace industry)	▪ Force-controlled squeeze riveting process is beneficial for obtaining joints with consistent fatigue strength. ▪ Force magnitude can be varied depending on process requirements.	▪ Gantry mechanism is required in aircraft assembly. It is not portable. ▪ Low accessibility for hard-to-reach areas of the structure ▪ Lower throughput compared with percussive riveting. ▪ High upset forces around 20-40 kN required to obtain joints with good fatigue strength. ▪ Meticulous hole preparation required.
EMR (Primarily used in the aerospace industry)	▪ Impact force can be controlled. ▪ Lightweight equipment makes it possible for this process to become portable for the operators. ▪ Throughput is high. ▪ Provides good accessibility for operators.	▪ Rivets made from materials with high static shear strength develop cracks during the EMR process. Al 7050-T73 has exceptionally high shear strength. ▪ Its implementation is not feasible with Briles rivet because of the flush geometry. ▪ Meticulous hole preparation required. .
SPR (Primarily used in the automotive industry)	▪ No hole-drilling is required. ▪ No surface pre-treatment needed. ▪ Dissimilar materials can be joined.	▪ Since no hole is drilled, the sheet material is pierced during assembly process creating spots with high stress concentration.

		▪ Current equipment does not accommodate the massive size of aircraft panels. ▪ High processing temperature required for joints that include titanium and magnesium alloy sheets. ▪ Cycle time varies between 1-4 seconds. ▪ High upset force between 20-100 kN
Orbital (Primarily used in the automotive industry)	▪ Low power consumption. ▪ Preferred for joints that require low residual stresses. ▪ Dissimilar materials can be joined.	▪ Current equipment does not accommodate the massive size of aircraft panels. ▪ With less downforce on the rivet, there is minimal rivet shank swell. But shank swelling is required in aircraft joints to attain high residual stresses. ▪ Meticulous hole preparation required.
Percussive (Primarily used in the aerospace industry)	▪ Joints with fatigue strength greater than or equal to EMR and Squeeze riveting are obtained. ▪ Preferred joining technique for aerospace alloys with high static shear strength. ▪ High throughput. ▪ Ideal process for forming countersunk rivets. ▪ Highly portable equipment.	▪ Meticulous hole preparation required. ▪ Consistent air pressure required. ▪ Providing adequate clamping force requires intensive assembly worker training. ▪ Moderate to high vibration exposure to the assembly worker.

2.3 DEFORMATION BEHAVIOR

The global strain rate changes from 1500/s to 2000/s for one hammer stroke in the percussive riveting process. The local strain rate is about two times greater than the global one [Szymczyk, 5]. After upsetting, the side surface becomes distorted. Its profile and character of deformation depends on frictional conditions and initial dimensions ratio of rivet shank height (h) and rivet shank radius (r) given by h/r. Interaction of stress zones in the bulk is associated with simultaneous effect of friction forces in the head surfaces and distribution of deformation resistance within the specimen. The height of the specimen plays a big role in this interaction. While upsetting low aspect ratio specimens (h/r ~ 2). There is triaxial state of stress in the entire volume, causing deformation of the entire specimen. In the deformed region, zones can be distinguished based on the extent of deformation. In the zone adjacent to flat surfaces of the tools, the least deformation occurs due to the friction of the tools [Kajtoch, 23]. Mechanics of the rivet clamping force is fairly subtle, requiring an understanding of the multi-axial stress history in the rivet during the riveting process [Deng, 29].

The largest deformations, both in axial and radial directions, are found in the interior (denoted by 'B' in figure 2.12). There are no distinct borders between these zones, with smooth transition from to one zone to another. The zone C is the volume adjacent to the free surface which undergoes intermediate deformation [Kajtoch, 23].

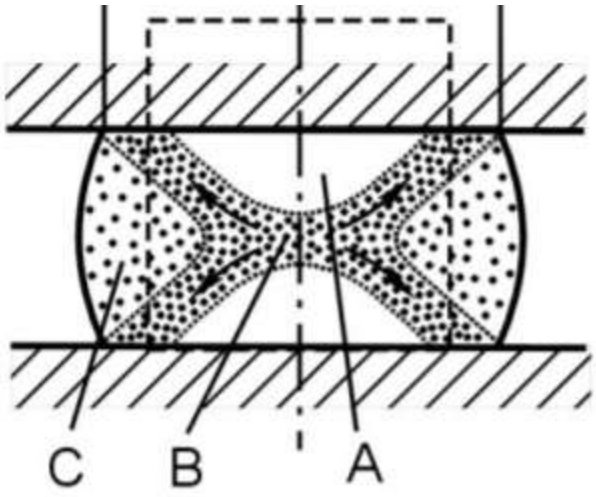

Figure 2.12. Deformation zones in a specimen undergoing compression. Zone A: Material which undergoes least deformation. Zone B: Material undergoing maximum deformation. Zone C: Intermediate deformation is observed in the material within this zone [Kajtoch, 23].

The EMR process consists of the whole free upsetting and the local free upsetting. When the punch impacts the rivet, the rivet shaft firstly produces the whole free upsetting. As the EMR process continues, the already formed rivet shaft is further pushed into the hole of the plate stack.

After the rivet shaft contacts with the plate stack, the rivet deformation region changes to the rivet head which is the free deformation region and the deformation belongs to the local free upsetting [Deng, 6].

Typically, aerospace standards dictate that a rivet must interfere with the hole by at least 25 μm. Rivet interference is measured by cutting the rivet from a test plate and subtracting the initial hole diameter from the rivet body diameter. A properly installed rivet flows into, fills and stretches from the hole. Good interference enhances mechanical properties and ensures that the joint is sealed against air and fuel leakage [Zieve, 7].

A larger squeeze force implies more flattening and a reduced height of the driven rivet head. Large plastic strains occur in the rivet material during the squeezing process. Comparison of the initial shape of the rivet as manufactured with the shape after riveting indicates that large plastic deformations are involved, larger than few percent [de Rijck, 24].

Characteristic dimensions of the driven rivet head during application of the squeeze force are the diameter and the height of the driven rivet head. In addition, the rivet hole will slightly expand because some material of the rivet is driven into the hole. The percentage of the hole expansion is just few percent. A calculation of the volume of the rivet after squeezing confirmed that the volume remained constant if the small volume contribution due to the small hole expansion was considered. The rivet material apparently behaves as an incompressible material as should be expected. At the same time, the only visible indication of the squeeze force after riveting appears to be reflected by the shape of the driven rivet head, given by final rivet button diameter-initial rivet shank diameter ratio (D/D_o) and final rivet shank length- initial rivet shank length ratio (H/H_o). This emphasizes the significance of assessing a correlation between the squeeze force and the dimensions of the driven rivet head [de Rijck, 24].

Considering the three-dimensional nature of the stresses in the center of the sheet versus two-dimensional nature near the surface, the rivet develops a barrel-like shape, "fattest" in the middle of the sheet's thickness. This results in lateral flow in the near-surface regions when the yield strength is exceeded there and not yet in the center. The interior then acts to impede this flow, leading to compressive residual stresses in the near-surface regions [Fitzgerald, 30].

In ref. [21], the time to carry out the forming procedure was around 3 ms, during which time large plastic deformations of the slug rivet are experienced that create significant localized heating of the rivet material and high strain rates of around 1000/s. The large diametrical expansion of the slug rivet creates a residual compressive stress field in the adjacent material around the hole, improving the fatigue life and the fluid retention of the joint.

2.4 MANUFACTURED JOINT OBSERVATIONS

The riveted joints are critical areas of the aircraft structure due to phenomena like severe stress concentrations, plastic strain and secondary bending as well as micro-local effects such as surface damage (fretting wear). These phenomena cause fatigue crack initiation at the rivet holes

or between the sheets, which propagate and decrease fatigue resistance of the riveted joint. The total stress experienced by the material at a given location within a component depends on the residual stress and applied load. Residual post-riveting stress fields are widely accepted to have a significant influence on the fatigue life of aircraft structures. Especially, a compressive uniform residual stress state can be beneficial because it tends to decrease probability of stress corrosion and fatigue cracking [Szymczyk, 5].

State of stresses and strains in a specimen during upsetting depends mainly on friction conditions in the contact surface of the die. In the riveting process due to action of normal stresses, produced by external loading, tangential friction stresses arise at the contact surface, which are directed towards the center of the specimen. The stresses, dependent on friction coefficient, restrict lateral flow of the metal. Thus, the shape of a free surface of the specimen and the curvature of the barrel depend a great deal on friction coefficient in the contact surface.

When the friction coefficient has values reaching zero, it can be assumed that the process is frictionless, and a uniaxial stress state is present within the specimen. Normal stress equals flow stress, which allows uniform deformation in the bulk at every stage of compression. If friction coefficient is non-zero, triaxial state of stress is produced in the material, differing in various areas of the specimen, dependent on h/r ratio, which causes nonuniform deformation.

When the ratio is high, in the middle of the height, linear state of stress is observed. This region does not undergo deformation in the beginning. In the end zones of the specimen, a triaxial state of stress prevails, where the bucked end barrels under the tool [Kajtoch, 23].

Most studies in the past have avoided a detailed analysis of contact conditions that arise during riveting process by either introducing an artificial interference condition between a rigid pin and the rivet hole [Fitzgerald, 30] or simply calculating the resulting radial residual stresses due to uniform expansion of the rivet hole [Figueira, 35]. Even for models that have attempted to resolve the contact in more detail, uniform interference between rivet and hole is assumed and relatively unsubstantiated estimates of through-thickness clamping constraint provided by the

installed rivets are used in their analyses [Fung, Smart, 19]. In comparing the radial residual stresses, an indicator of the residual interference between the rivet and plate, two features stand out. First, as expected, the magnitude of the compressive residual stresses increases with squeeze force, with greater expansion of the rivet against the hole interface. Second, and more important, is the variation of the magnitude of the radial stresses (and hole expansion, as reflected in the results) through the thickness of the plates. *Hoop stress can have a marked impact on the propagation of fatigue cracks that nucleate at either the edge of the rivet hole or the faying surfaces of the plates*. As with the radial residual stresses, the contours of residual hoop stress exhibited both a variation in the thickness direction and a dependence on maximum squeeze force [Szolwinski, 1].

Of particular interest is the zone of compressive residual stress at the edge of the hole near the driven head. At first, the compressive nature of this residual hoop stress might seem to conflict with the notion of hole expansion. The presence of this area of compressive hoop stress can be explained qualitatively, though, by looking at the yielding behavior of the material in the absence of stress in the thickness direction. As the rivet expands against the hole and the interfacial contact pressure exceeds the yield point of the material, the material deforms in such a manner as to force hoop stress < 0, according to Tresca criterion. Such a compressive residual hoop stress is often induced around rivet holes prior to riveting by cold working the hole with an expanding mandrel, with the goal of retarding the growth of fatigue damage that may nucleate in the material at and around the hole [Szolwinski, 1].

In the contours of the residual hoop stress, the size and magnitude of the compressive zone increases with increasing maximum squeeze force. To maintain the compatibility of the material in the hoop direction, however, this compressive zone is balanced by an area of tensile stress away from the hole periphery. A region of tensile hoop stress is present beyond the compressive region in the lower sheet. The location of this tensile zone becomes critical when considering the nucleation and subsequent propagation of fatigue cracks that nucleate not at the rivet/hole

interface, but at the faying surface, away from the hole periphery. An increasing maximum squeeze force not only pushes the zone of tensile stress away from the hole periphery, but also results in a larger driven head size [Szolwinski, 1].

Although most experimental measurement techniques cannot provide adequate results for verification of the FE model, methods such as neutron diffraction can determine the residual strain state beneath the rivet head. Experience has shown that a small protrusion of the rivet head above the sheet surface during rivet installation has a beneficial effect on fatigue performance of riveted splices, likely due to improved hole filling of the conical recess of the countersunk sheet [Rans, 14].

The regions of compressive hoop stress near the rivet hole are of primary interest due to their positive influence on prolonging crack nucleation and reducing crack growth rates. Knowledge of residual stress distributions along the faying joint surfaces is important as they are most adversely affected by fretting and tensile secondary bending stresses under joint loading conditions, making them a likely location for crack initiation. Large radial stresses plastically deform the sheet material surrounding a fastener hole. Elastic springback of the bulk material then compresses the plastically deformed material producing the residual stress state. *The importance of through-thickness stress on the formation of residual stresses is often overlooked in discussions on riveting* [Figueira, 35]. It contributes to the plastic deformation of the sheet beneath the rivet head and resulting residual stress state. The region and magnitude of the compressive residual hoop stresses was found to increase with rivet squeeze force. Under the footprint of the larger driven rivet head dimensions, peak secondary bending stresses resulting from rivet rotation flow around the fastener hole, driving the shift in crack nucleation location. At higher squeeze forces, frictional slip occurs causing the countersunk sheet to slide up the countersunk rivet head and expand through a wedging action (wedge expansion). *The addition of this expansion mechanism increases the radial pressure between the rivet and the countersunk sheet, resulting in the radial stress dominated region of plasticity*. The higher magnitude and larger region of residual

compressive stress associated with wedge expansion of the countersunk rivet head would be beneficial to the fatigue performance of the countersunk sheet [Rans, 14]. However, the residual stresses can intensify the strength of the riveted joint, but they may also embrittle the joint [Langrand, 26].

2.5 Finite Element Riveting Literature Observations

Process modeling and analysis using FEA has not been done before for the percussive riveting process. Dynamics modeling has been done by several research groups but they did not discuss the residual stress and strain trends [Ahn, 4; Johnson, 31]. Ref. [2] models rivet deformation as a cylinder striking a rigid surface. This is a simplification because both rivet hammer's die and bucking bar are both deformable members. All prior riveting stress modeling have utilized fixed rivet hammer [1, 14, 17, 20, 22, 26, 32-40]. This may be appropriate for squeeze riveting process, but it is a simplification of the percussive process boundary conditions. Rivet hammer and bucking bar are kept in contact with the stackup with a continuous applied force [Ahn, 4; Johnson, 31]. Knife edges at the rivet-outer skin contact surface are present in most studies [14, 17, 20, 22, 26, 33, 34, 37-40]. The countersunk rivet used in this dissertation work does not have a knife edge. Knife edges act as stress raisers.

2.6 Summary

In this chapter, the various types of riveting processes implemented in aerospace and automotive industries were disussed. The means of implementation of these processes were discussed. The deformation and stress distribution characteristics within the riveted joint were discussed. The limitations of FEA studies performed by researchers in the past was also discussed.

Chapter 3. ANALYTICAL STUDY OF SQUEEZE RIVETING AND COMPARISON WITH SIMULATION RESULTS

3.1 ANALYTICAL DEVELOPMENT

Squeeze rivet analysis can be thought of consisting of three steps: elastic deformation during loading, plastic deformation during loading and elastic springback after unloading. The analysis that follows is based on the work presented in [Figueira, 35]. In this analytical work, following assumptions were made: Axisymmetry is considered around the axis of the rivet length (z-axis). Countersunk portion of the rivet and counterbore region of the outer sheet are neglected in this analysis. Initially, rivet shank diameter (D_0) and sheet hole diameter (d_1) remain constant across sheet thickness. At the end of the forming process, D_0 and d_1 increase to d_2 in the rivet hole region. Final rivet button diameter (D) is constant along the final rivet button height (H). The rivet button and rivet shank region are both assumed to be right cylinders throughout the forming process. Elastic strains are neglected. Elastic springback is neglected. Formed rivet dimensions are assumed to be constant during the unloading step and of same magnitude at the end of the loading step. No friction is present between sheets, rivet and tools.

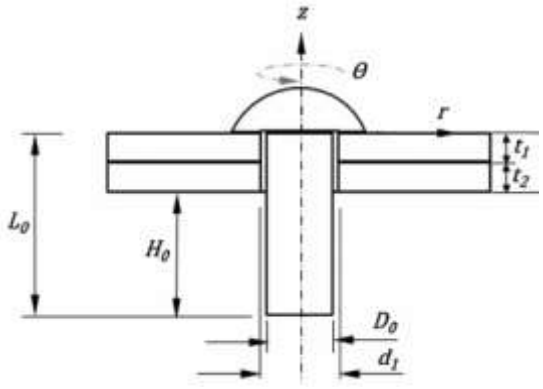

Figure 3.1. Dimensions of the squeeze riveting stackup [Figueira, 35].

Referring to figure 3.1, values of parameters assumed in this analysis: $t_1 = t_2 = 0.1$” (2.54 mm), $H_0 = 0.179$” (4.55 mm), $L_0 = 0.379$” (9.63 mm), $d_1 = 0.226$” (5.74 mm), $D_0 = 0.225$” (5.72 mm),

D=0.285” (7.24 mm), H= 0.108” (2.74 mm). Rivet material effective flow stress is given by $(\bar{\sigma})$ = 467 + 380 $(\bar{\varepsilon})^{0.1}$ (MPa), where $\bar{\varepsilon}$ is the effective strain. Sheet material effective flow stress is given by $(\bar{\sigma})$ = 369 + 684 $(\bar{\varepsilon})^{0.73}$ (MPa). These parameters are taken from a quasistatic finite element simulation performed with friction coefficient of 0.2 between tool surfaces and stackup surfaces and a friction coefficient of 0.25 between stackup surfaces. Details of this quasistatic finite element simulation are discussed in chapters 4 and 5. Results from this simulation will be compared with the analytical results in this chapter.

From experimental observations, the rivet button does not have a constant diameter, D, across the height of the rivet button because presence of friction between contact surfaces of the stackup and tools causes a barreling effect as shown in figure. 2.12. Also rivet shank diameter, d_2, is higher near the rivet button than near the countersunk head. Figure 3.2 shows the dimensions of the squeeze riveting stackup at the end of the forming process.

Initial volume of the shank portion of the rivet is given by,

$$V_0 = \frac{\pi}{4} D_0^2 L_0 = \frac{\pi}{4}(0.225^2)(0.379) = 0.01507 in^3 \ (2.47\ X\ 10^{-7}\ m^3) \tag{3.1}$$

Volume of the rivet shank when the shank contacts the hole surface is given by,

$$V_1 = \frac{\pi}{4} d_1^2 L_1 = \frac{\pi}{4} 0.226^2 L_1 \tag{3.2}$$

And because volume is conserved in plastic deformation of the rivet,

$$V_0 = V_1 \rightarrow L_1 = \frac{0.01507}{\frac{\pi}{4} 0.226^2} = 0.3757\ in\ (9.541\ mm) \tag{3.3}$$

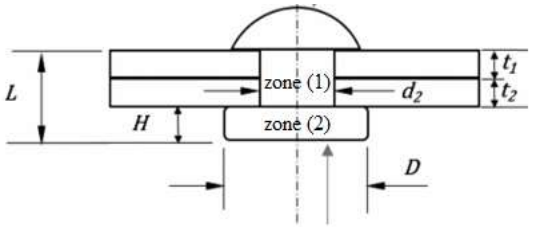

Figure 3.2. Dimensions of the squeeze riveting stackup at end of forming process [Figueira, 35].

Shank region of the rivet is indicated as zone (1) and button region of the rivet is indicated as zone (2) in figure 3.2.

Using incompressibility of rivet shank material, final rivet shank diameter d_2 is calculated as,

$$V_f = \frac{\pi}{4} d_2^2 (t_1 + t_2) + \frac{\pi}{4} D^2 H = \frac{\pi}{4} d_2^2 (0.2) + \frac{\pi}{4} 0.285^2 (0.108) \tag{3.4}$$

$$V_0 = V_1 = V_f \rightarrow \frac{\pi}{4} D_0^2 L_0 = \frac{\pi}{4} d_1^2 L_1 = \frac{\pi}{4} d_2^2 (t_1 + t_2) + \frac{\pi}{4} D^2 H \tag{3.5}$$

$$d_2 = \sqrt{\frac{0.01507 - \frac{\pi}{4} 0.285^2 (0.108)}{\frac{\pi}{4} (0.2)}} = 0.2282\ in\ (5.796\ mm)$$

The squeeze force (F_{sq}) applied to the shank end of the rivet by the forming tool at the end of the loading step is calculated using the highest axial stress (σ_{sq}) reached in the rivet buttton during forming, σ_{sq} is assumed to be follow the form of $(A+B(\varepsilon_{sq})^n)$.

$$F_{sq} = \frac{\pi}{4} D^2 \sigma_{sq} \tag{3.6}$$

$$\sigma_{sq} = A_{rv} + B_{rv} \varepsilon_{sq}^{n_{rv}} = 467 + 380\ \varepsilon_{sq}^{0.1}\ \text{(MPa)} \tag{3.7}$$

Axial strain (ε_{sq}) in the zone (2) of the rivet is calculated as,

$$\varepsilon_{sq} = 2\ ln\left(\frac{D_0}{D}\right) = 2 \ln\left(\frac{0.225}{0.285}\right) = -0.4728 \tag{3.8}$$

This value of axial strain can be inserted in eq. (3.7) to calculate F_{sq} in eq. (3.6),

$$F_{sq} = \frac{\pi}{4} D^2 (A_{rv} + B_{rv} \left[2\ ln\left(\frac{D}{D_0}\right)\right]^{n_{rv}})$$

$$F_{sq} = \left(\frac{\pi}{4}(0.285\ X\ 0.0254)^2\right)\left(467\ \text{X}\ 10^6 +\ 380\ \text{X}\ 10^6\ (0.4728^{0.1})\right)\ =\ 33707.8\ N$$

Axial strain (ε_{sq}) in the zone (1) of the rivet is calculated as,

$$\varepsilon_{sq} = 2\ ln\left(\frac{D_0}{d_2}\right) = 2\ln\left(\frac{0.225}{0.2282}\right) = -0.02824 \tag{3.9}$$

Sheet radial strain at the hole can be calculated as,

$$\varepsilon_{rr} = -ln\left(\frac{d_2}{d_1}\right) = -\ln\left(\frac{0.2282}{0.226}\right) = -0.0097 \tag{3.10}$$

Volume conservation law (incompressibility condition) in the sheet material is given by,

$$\varepsilon_{zz} + \varepsilon_{\theta\theta} + \varepsilon_{rr} = 0 \tag{3.11}$$

Sheet material effective stress ($\bar{\sigma}$) is calculated using the relation shown in eq. (3.12),

$$\bar{\sigma} = \sqrt{\frac{(\sigma_{rr} - \sigma_{\theta\theta})^2 + (\sigma_{\theta\theta} - \sigma_{zz})^2 + (\sigma_{zz} - \sigma_{rr})^2}{2}} \tag{3.12}$$

In the sheet material, axial stress (σ_{zz}) is negligible compared to the radial and hoop stress components. The effective stress expression in eq. (3.12) reduces to,

$$\bar{\sigma} = \sqrt{(\sigma_{\theta\theta})^2 + (\sigma_{rr})^2 - \sigma_{\theta\theta}\sigma_{rr}} \tag{3.13}$$

Volume conservation law (incompressibility condition) in zone (1) of rivet can also be described by eq. (3.11).

Zone (1) rivet radial strain (ε_{rr}), axial strain (ε_{zz}) and hoop strain ($\varepsilon_{\theta\theta}$) are given by,

$$\varepsilon_{rr} = ln\left(\frac{d_2}{D_0}\right) = \ln(\frac{0.2282}{0.225}) = 0.01412 \tag{3.14}$$

$$\varepsilon_{zz} = \varepsilon_{sq} = -2\ ln\left(\frac{d_2}{D_0}\right) = -0.02824 \tag{3.15}$$

$$\varepsilon_{\theta\theta} = ln\left(\frac{d_2}{D_0}\right) = 0.01412 \tag{3.16}$$

$$\varepsilon_{rr} = \varepsilon_{\theta\theta} = 0.01412 \rightarrow d\varepsilon_{rr} = d\varepsilon_{\theta\theta} \tag{3.17}$$

Zone (1) rivet effective strain ($\bar{\varepsilon}$) is given by,

$$\bar{\varepsilon} = \sqrt{\frac{2((\varepsilon_{rr})^2 + (\varepsilon_{\theta\theta})^2 + (\varepsilon_{zz})^2)}{3}} = 2\ ln\left(\frac{d_2}{D_0}\right) = 0.02824 \tag{3.18}$$

Zone (1) rivet effective stress ($\bar{\sigma}$) is given by,

$$\bar{\sigma} = (A_{rv} + B_{rv}[\bar{\varepsilon}]^{n_{rv}}) = (A_{rv} + B_{rv}\left[2\ ln\left(\frac{d_2}{D_0}\right)\right]^{n_{rv}}) \tag{3.19}$$

$$\bar{\sigma} = \left(467\ \text{X}\ 10^6 + 380\ \text{X}\ 10^6\ (0.02824^{0.1})\right) = 732.99\ MPa$$

Also, zone (1) rivet effective stress ($\bar{\sigma}$) can be written using the same relation as eq. (3.12).

Axial stress (σ_{zz}) in zone (1), using eq.(3.6) is given by,

$$\sigma_{zz} = -\frac{F_{sq}}{\frac{\pi}{4}D^2} = -(A_{rv} + B_{rv}\left[2\ ln\left(\frac{D}{D_0}\right)\right]^{n_{rv}})$$

$$\sigma_{zz} = -\left(467\ \text{X}\ 10^6 + 380\ \text{X}\ 10^6\ (0.4728^{0.1})\right) = -819.57\ MPa$$

Using Levy-Mises relations in zone (1) of the rivet, we have,

$$d\varepsilon_{rr} = \frac{d\bar{\varepsilon}}{\bar{\sigma}}(\sigma_{rr} - \frac{1}{2}[\sigma_{\theta\theta} + \sigma_{zz}]) \tag{3.20}$$

$$d\varepsilon_{\theta\theta} = \frac{d\bar{\varepsilon}}{\bar{\sigma}}(\sigma_{\theta\theta} - \frac{1}{2}[\sigma_{rr} + \sigma_{zz}])$$

$$d\varepsilon_{zz} = \frac{d\bar{\varepsilon}}{\bar{\sigma}}(\sigma_{zz} - \frac{1}{2}[\sigma_{\theta\theta} + \sigma_{rr}])$$

Using eq. (3.17), in zone (1) of the rivet we get,

$$\left(\sigma_{rr} - \frac{1}{2}[\sigma_{\theta\theta} + \sigma_{zz}]\right) = \left(\sigma_{\theta\theta} - \frac{1}{2}[\sigma_{rr} + \sigma_{zz}]\right) \rightarrow \sigma_{rr} = \sigma_{\theta\theta} \quad (3.21)$$

Effective stress relation ($\bar{\sigma}$) for zone (1) of the rivet from eq. (3.12) reduces to,

$$\bar{\sigma}^2 = (\sigma_{zz} - \sigma_{rr})^2 \rightarrow \bar{\sigma} = |\sigma_{zz} - \sigma_{rr}| \quad (3.22)$$

Using eq. (3.19), eq. (3.21) and eq. (3.22), the radial stress (σ_{rr}) and hoop stress ($\sigma_{\theta\theta}$) in the zone (1) are calculated as,

$$\sigma_{rr} = \sigma_{\theta\theta} = -86.58\ MPa$$

In the sheets, $\sigma_{zz} \approx 0$ is assumed. Also, in the sheets' region near the hole, $\varepsilon_{zz} \approx 0$ is assumed. Equilibrium equation for the sheets can be written as,

$$\frac{d\sigma_{rr}}{dr} + \frac{1}{r}(\sigma_{rr} - \sigma_{\theta\theta}) = 0 \quad (3.23)$$

Applying Levy-Mises relations of eq. (3.20) to the sheet material,

$$d\varepsilon_{rr} = \frac{d\bar{\varepsilon}}{\bar{\sigma}}(\sigma_{rr} - \frac{1}{2}[\sigma_{\theta\theta}]) \quad (3.24)$$

$$d\varepsilon_{\theta\theta} = \frac{d\bar{\varepsilon}}{\bar{\sigma}}\left(\sigma_{\theta\theta} - \frac{1}{2}[\sigma_{rr}]\right)$$

$$d\varepsilon_{zz} = \frac{d\bar{\varepsilon}}{\bar{\sigma}}(-\frac{1}{2}[\sigma_{\theta\theta} + \sigma_{rr}])$$

Using $\varepsilon_{zz} \approx 0$ assumption and the relations of eq. (3.24),

$$\varepsilon_{zz} = 0 \rightarrow d\varepsilon_{zz} = 0 \rightarrow \sigma_{\theta\theta} = -\sigma_{rr} \rightarrow d\varepsilon_{rr} = -d\varepsilon_{\theta\theta} \tag{3.25}$$

Using eq. (3.12) and eq. (3.25), the effective stress of the sheets can be obtained as,

$$\bar{\sigma} = \sqrt{3}|\sigma_{rr}| \tag{3.26}$$

Eq. (3.23) can be simplified as,

$$\frac{d\sigma_{rr}}{dr} + \frac{2}{r}(\sigma_{rr}) = 0 \tag{3.27}$$

Solution of eq. (3.27) is given by,

$$\sigma_{rr} = \frac{C_1}{r^2} \tag{3.28}$$

$$d\varepsilon_{rr} = \frac{3}{2}\frac{d\bar{\varepsilon}}{\bar{\sigma}}\sigma_{rr}, \quad d\varepsilon_{\theta\theta} = -\frac{3}{2}\frac{d\bar{\varepsilon}}{\bar{\sigma}}\sigma_{rr} \tag{3.29}$$

Now we need to evaluate C_1 by obtaining value of σ_{rr} at r = $d_2/2$. Using eq. (3.25) and eq. (3.26), we get

$$d\bar{\varepsilon} = \sqrt{\frac{2((d\varepsilon_{rr})^2 + (d\varepsilon_{\theta\theta})^2 + (d\varepsilon_{zz})^2)}{3}} \tag{3.30}$$

$$d\bar{\varepsilon} = \frac{2}{\sqrt{3}}|d\varepsilon_{rr}| \rightarrow \bar{\varepsilon} = \frac{2}{\sqrt{3}}|\varepsilon_{rr}| \tag{3.31}$$

$$at\ r = \frac{d_2}{2}, \qquad \varepsilon_{rr} = -\varepsilon_{\theta\theta} = -ln\left(\frac{d_2}{d_1}\right) = -0.0097 \tag{3.32}$$

Effective stress of the sheets at the hole wall (r = $d_2/2$) can also be expressed as,

$$\bar{\sigma} = (A_{sk} + B_{sk}[\bar{\varepsilon}]^{n_{sk}}) = (A_{sk} + B_{sk}\left[\frac{2}{\sqrt{3}}|\varepsilon_{rr}|\right]^{n_{sk}}) = (A_{sk} + B_{sk}\left[\frac{2}{\sqrt{3}}\ln\left(\frac{d_2}{d_1}\right)\right]^{n_{sk}}) \quad (3.33)$$

$$\bar{\sigma} = \left(369\ \mathrm{X}\ 10^6 + 684\ \mathrm{X}\ 10^6\ (0.0112^{0.73})\right) = 394.76\ MPa$$

Using eq. (3.26) and eq. (3.33) and remembering that sheet radial stress at the hole is compressive,

$$at\ r = \frac{d_2}{2}, \qquad \sigma_{rr} = -\frac{1}{\sqrt{3}}(A_{sk} + B_{sk}\left[\frac{2}{\sqrt{3}}\ln\left(\frac{d_2}{d_1}\right)\right]^{n_{sk}} \quad (3.34)$$

$$\sigma_{rr} = -\frac{1}{\sqrt{3}}(394.76) = -227.91\ MPa$$

Using eq. (3.28) and eq. (3.34),

$$At\ r = \frac{d_2}{2}, \qquad \sigma_{rr} = -227.91\ MPa \rightarrow C_1 = -227.91\ X\ 10^6\ X\ (\frac{0.2282\ X\ 0.0254}{2})^2$$

$$C_1 = -1914.27\ MPa - m^2 \rightarrow \sigma_{rr} = \frac{-1914.27}{r^2}\ MPa$$

3.2 Simulation Results Comparison

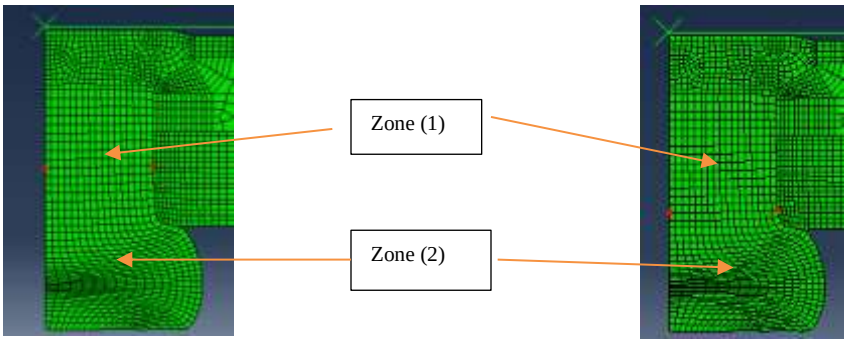

$d_2 = 0.2293$” $d_2 = 0.2323$”

Figure 3.3. d_2 measurement locations in simulation.

Squeeze simulation modeling procedure is described in section 4.1. All simulation result comparisons are made with analytical results at the end of the unloading step in the finite element squeeze riveting simulation (i.e., elastic springback is completed). Simulation observation of d_2 indicates that d_2 is not constant across the length of the rivet shank as can be seen in figure 3.3. Analysis d_2 is 0.2282". Distances for d_2 are measured between the red dots as shown in figure 3.3.

Simulation observations of ε_{sq} of rivet's zone (2) (rivet button) indicate that ε_{sq} is not constant across the rivet button as can be seen in figure 3.4. Analysis ε_{sq} of zone (2) is constant in the rivet button, -0.4728. Values of -1.45, -1.27, -0.84 and -0.32 can be seen in figure 3.4.

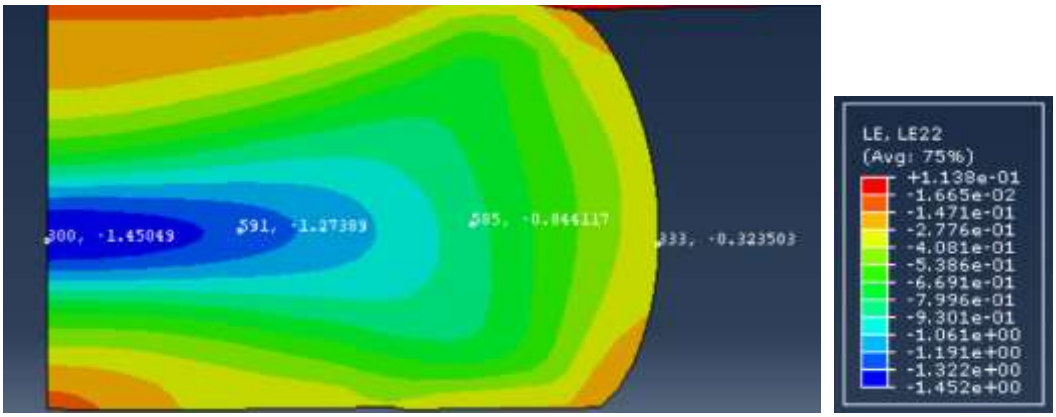

Figure 3.4. Rivet zone (2) axial strain (ε_{sq}) measurement locations in simulation.

Simulation observations of F_{sq} indicate that F_{sq} of simulation is higher than that predicted by analysis. Analysis gave a value of maximum squeeze force of 33707.8 N. Simulation results show a maximum squeeze force value of 42145 N in figure 3.5. This discrepancy can be attributed to absence of friction in analysis.

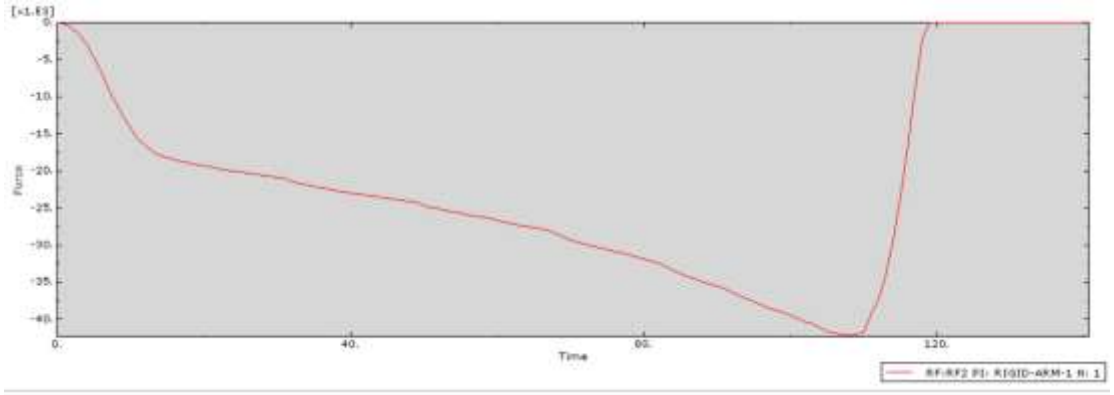

Figure 3.5. Squeeze force (F_{sq}) plot. X-axis: time (seconds), Y-axis: Force (N)

Simulation observations of ε_{sq} in zone (1) of rivet indicate that the axial strain is not constant in the rivet zone (1) as shown in figure 3.6. Analytical result is -0.02824. Magnitude can be found to be higher closer to zone (2) in figure 3.6.

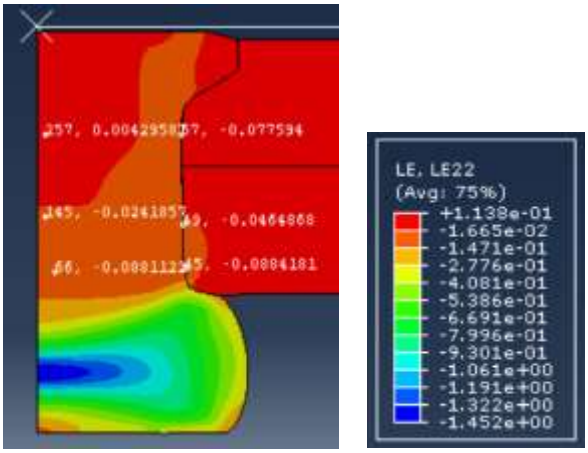

Figure 3.6. Rivet zone (1) axial strain (ε_{sq}) measurement locations in simulation.

Simulation observations of ε_{rr} in zone (1) of rivet indicate that the radial strain is not constant in the rivet zone (1) as shown in figure 3.7. Analytical result is 0.01412. Magnitude can be found to be higher closer to zone (2) and closer to the rivet hole in figure 3.7.

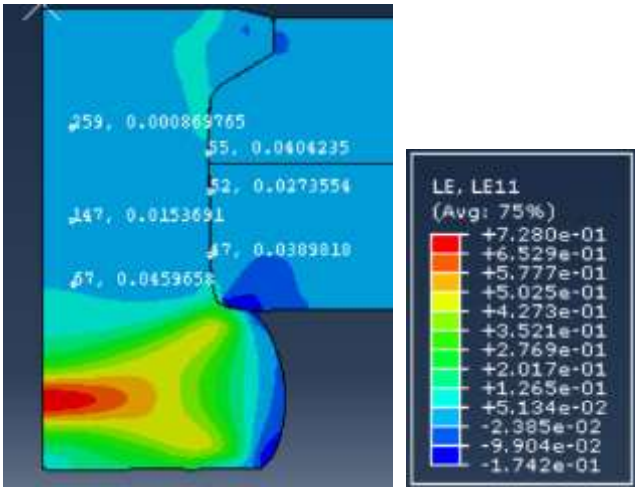

Figure 3.7. Rivet zone (1) radial strain (ε_{rr}) measurement locations in simulation.

Simulation observations of $\varepsilon_{\theta\theta}$ in zone (1) of rivet indicate that the hoop strain is not constant in the rivet zone (1) as shown in figure 3.8. Analytical result is 0.01412. Magnitude can be found to be higher closer to zone (2) and closer to the rivet hole in figure 3.8.

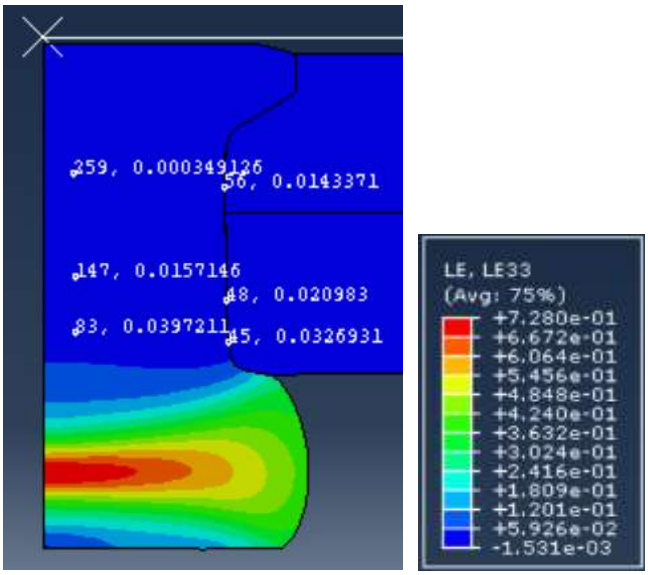

Figure 3.8. Rivet zone (1) hoop strain ($\varepsilon_{\theta\theta}$) measurement locations in simulation.

Simulation observations of effective strain ($\bar{\varepsilon}$) in zone (1) of rivet indicate that the effective strain is not constant in the rivet zone (1) as shown in figure 3.9. Analytical result is 0.02824. Magnitude can be found to be higher closer to zone (2) and closer to the rivet hole in figure 3.9.

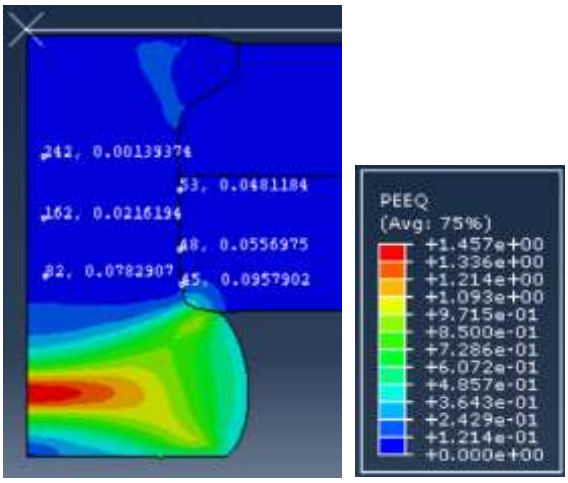

Figure 3.9. Rivet zone (1) effective strain ($\bar{\varepsilon}$) measurement locations in simulation.

Simulation observations of effective stress ($\bar{\sigma}$) in zone (1) of rivet indicate that the effective stress is not constant in the rivet zone (1) as shown in figure 3.10. Analytical result is 732.99 MPa. This analytical result neglects the effect of unloading and springback. Magnitudes of 228.58 MPa, 189.89 MPa and 192.78 MPa can be found closer to the rivet hole in figure 3.10.

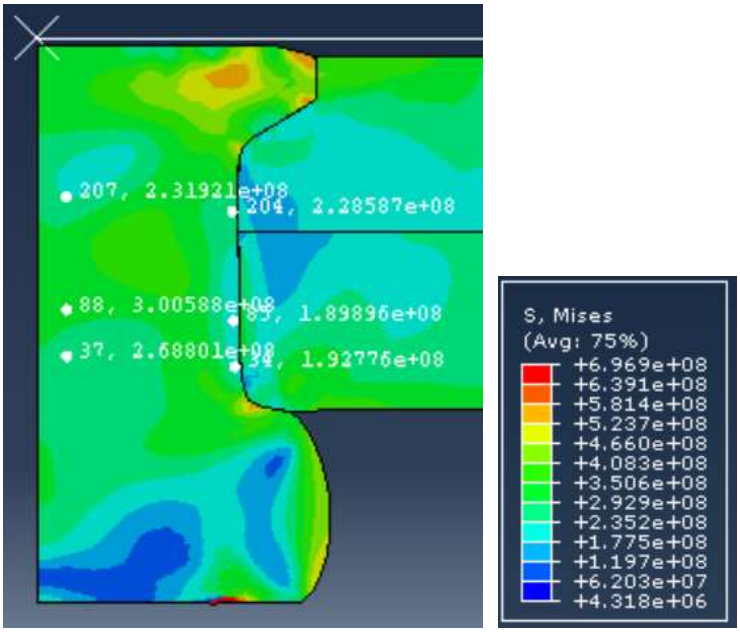

Figure 3.10. Rivet zone (1) effective stress ($\bar{\sigma}$) measurement locations in simulation.

Simulation observations of axial stress (σ_{zz}) in zone (1) and zone (2) of rivet indicate that the axial stress is not constant in both zones and axial stress of zone (1) is not the same as axial stress of zone (2) as shown in figure 3.11. Analytical result of zone (1) σ_{zz} and zone (2) σ_{zz} is -819.57 MPa. This analytical result neglects the effect of springback. Magnitudes of -24.96 MPa, -13.91 MPa, 222.90 MPa and -168.11 MPa are found in zone (1) and magnitudes of 7.75 MPa, 47.67 MPa, -67.42 MPa and 55.75 MPa are found in zone (2) in figure 3.11.

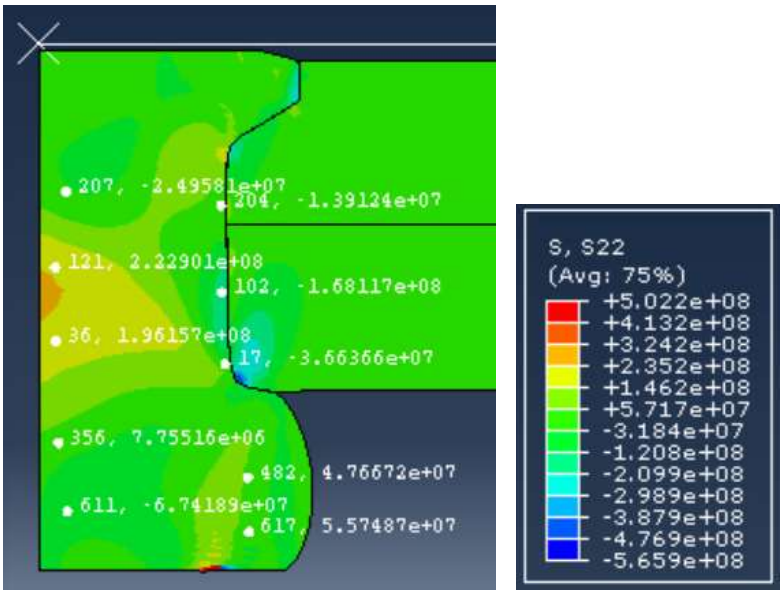

Figure 3.11. Rivet zones (1) and (2) axial stress (σ_{zz}) measurement locations in simulation.

Simulation observations of radial stress (σ_{rr}) in zone (1) of rivet indicate that the radial stress is not constant in zone (1) as shown in figure 3.12. Analytical result of zone (1) σ_{rr} is -86.58 MPa. This analytical result neglects the effect of springback. Magnitudes of -257 MPa, -169.81 MPa, -329.87 MPa are found in zone (1) in figure 3.12.

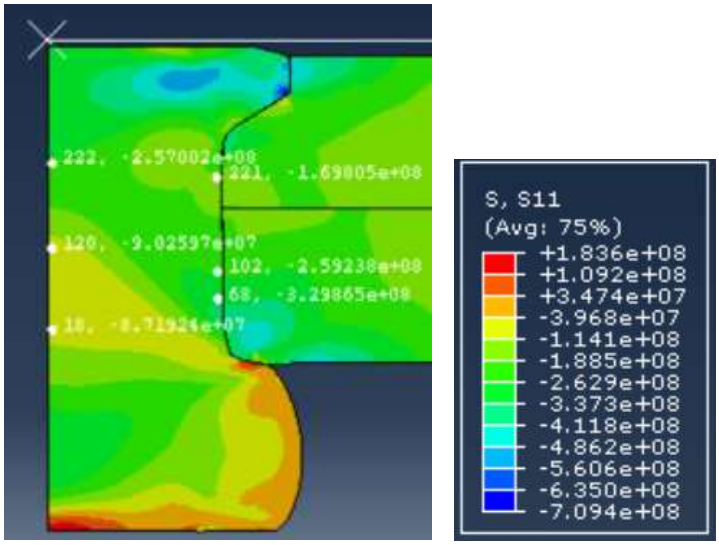

Figure 3.12. Rivet zone (1) radial stress (σ_{rr}) measurement locations in simulation.

Simulation observations of hoop stress ($\sigma_{\theta\theta}$) in zone (1) of rivet indicate that the hoop stress is not constant in zone (1) as shown in figure 3.13. Analytical result of zone (1) $\sigma_{\theta\theta}$ is -86.58 MPa. This analytical result neglects the effect of springback. Magnitudes of -257 MPa, -346.04 MPa, -104.65 MPa are found in zone (1) in figure 3.13.

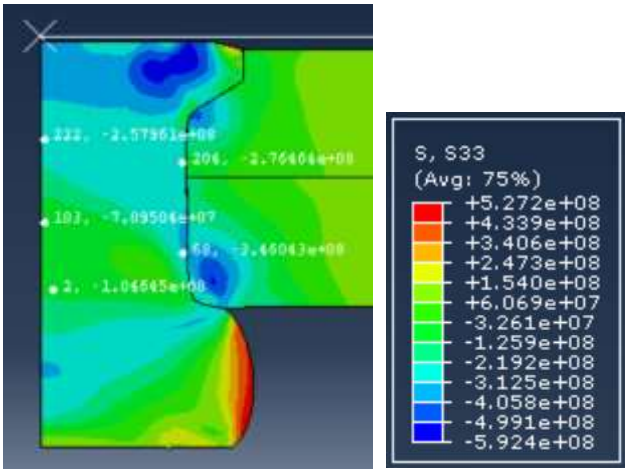

Figure 3.13. Rivet zone (1) hoop stress ($\sigma_{\theta\theta}$) measurement locations in simulation.

Simulation observations of axial stress (σ_{zz}) in sheet material of stackup at the hole wall indicate that the axial stress is not zero as shown in figure 3.14. Analytical assumption is plane stress state (σ_{zz} is 0 MPa) across both sheets. Magnitudes of -3.04 MPa, 104.41 MPa and -224.02 MPa are found in figure 3.14. Stress magnitudes are found to decrease away from the rivet hole.

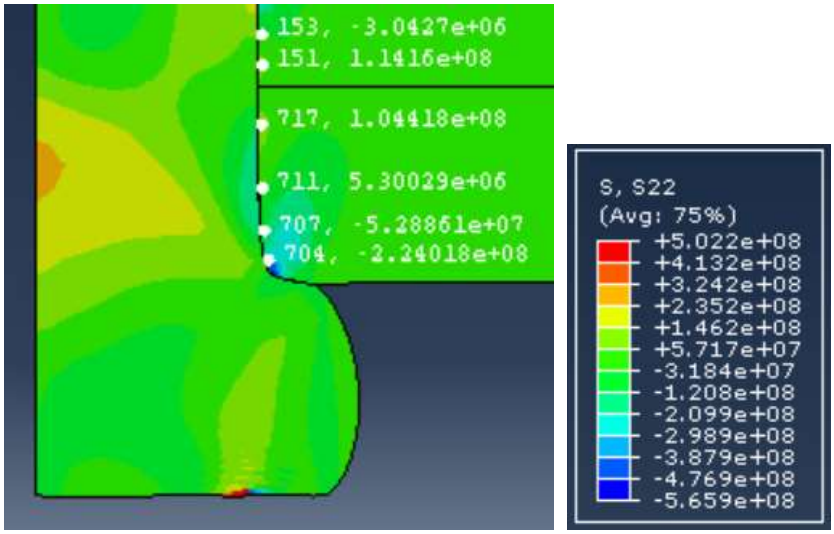

Figure 3.14. Sheet material hole wall axial stress (σ_{zz}) measurement locations in simulation.

Simulation observations of axial strain (ε_{zz}) in sheet material of rivet indicate that the axial strain is not zero as shown in figure 3.15. Analytical assumption is plane strain state (ε_{zz} is 0) across both sheets. It is interesting to note that both plane stress and plane strain have been imposed in the analysis of the sheets in the squeeze riveting process. Magnitudes of -0.0082, -0.025 and -0.073 are found in figure 3.15. Strain magnitudes are found to decrease away from the rivet hole.

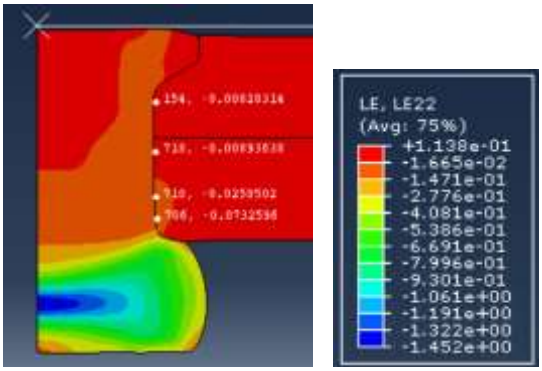

Figure 3.15. Sheet material hole wall axial strain (ε_{zz}) measurement locations in simulation.

In the sheet material of the stackup, analysis showed hoop stress ($\sigma_{\theta\theta}$) and radial stress (σ_{rr}) at the hole wall are equal in magnitude and opposite in sign. This can be seen in eq. (3.25). Radial stress at the hole wall in the sheet material is shown analytically to be -227.91 MPa. Hoop stress at the hole wall in the sheet material is shown analytically to be 227.91 MPa. This analysis neglects springback. Simulation observations in figure 3.16 show radial stress and hoop stress are not constant at the hole wall along the length of the hole. Also hoop stresses are compressive in the simulation results. This contradicts the analytical finding.

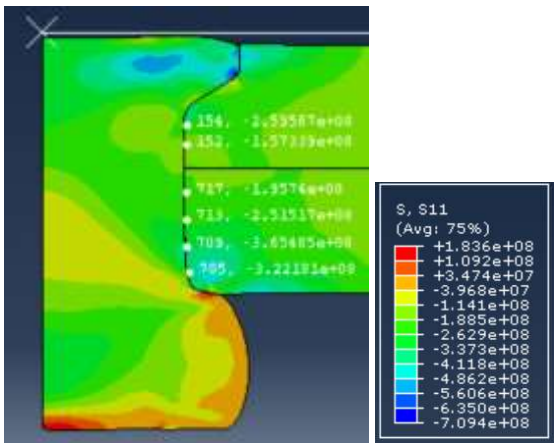

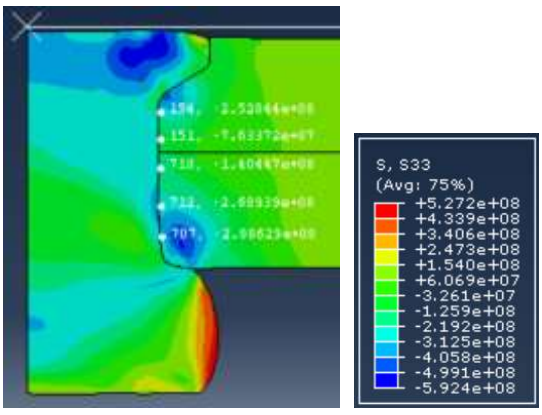

Figure 3.16. Sheet material hole wall radial stress (σ_{rr}) measurement locations in simulation shown on left. Sheet material hole wall hoop stress ($\sigma_{\theta\theta}$) measurement locations in simulation shown on right.

In the sheet material of the stackup, analysis showed hoop strain ($\varepsilon_{\theta\theta}$) and radial strain ($\varepsilon_{rr}$) at the hole wall are equal in magnitude and opposite in sign. This can be seen in eq. (3.32). Radial strain at the hole wall in the sheet material is shown analytically to be -0.0097. Hoop strain at the hole wall in the sheet material is shown analytically to be 0.0097. Simulation observations in figure 3.17 show radial stress and hoop stress are not constant at the hole wall along the length of the hole. Strain magnitudes are higher than the analytical result closer to the rivet button.

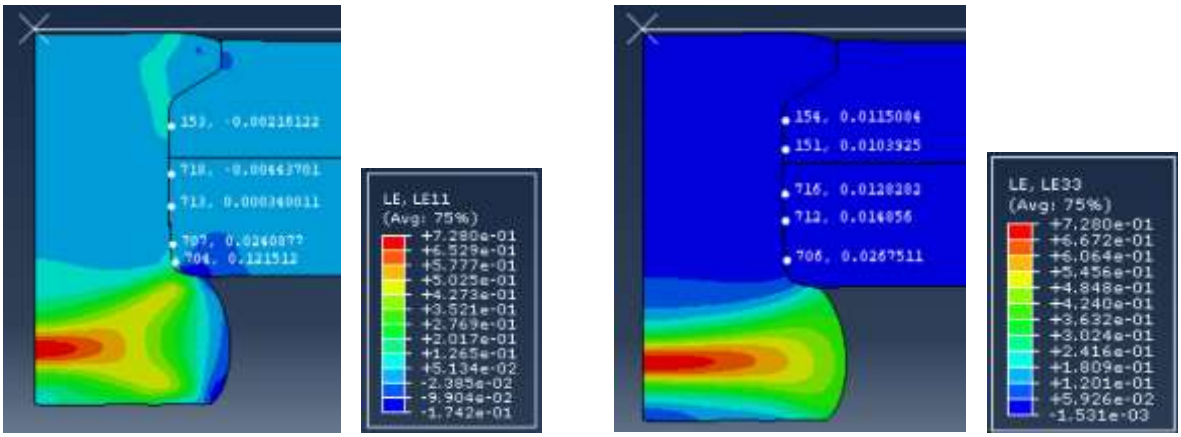

Figure 3.17. Sheet material hole wall radial strain (ε_{rr}) measurement locations in simulation shown on left. Sheet material hole wall hoop strain ($\varepsilon_{\theta\theta}$) measurement locations in simulation shown on right.

Simulation observations of effective strain ($\bar{\varepsilon}$) at hole wall of sheet material indicate that the effective strain is not constant as shown in figure 3.18. Analytical result is 0.0112. Magnitude increases toward direction of the rivet button.

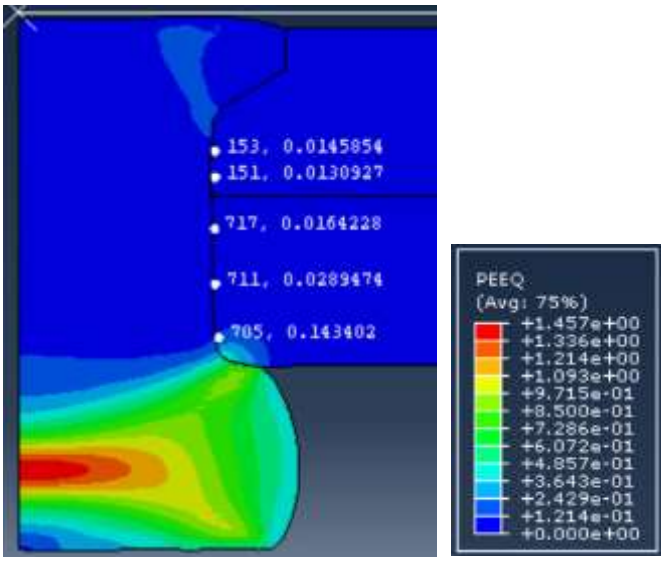

Figure 3.18. Sheet material effective strain ($\bar{\varepsilon}$) at hole wall measurement locations in simulation.

Simulation observations of effective stress ($\bar{\sigma}$) at hole wall of sheet material indicate that the effective stress is not constant as shown in figure 3.19. Analytical result is 394.76 MPa.

Based on the comparison of results obtained from classical analysis and finite element simulation, there are several discrepancies because of the underlying assumptions of the analysis. Friction and springback affect the deformation behavior of the stackup and the residual stresses and strains that are set up as a result of the forming process. Neglecting the important roles these phenomena play can lead to wrong estimation of stress/strain magnitudes, joint strength and force requirements. Owing to the complex, nonlinear nature of the riveting process, a thorough numerical study is required to study the nature of the residual stress and strain distributions within the riveting stackup.

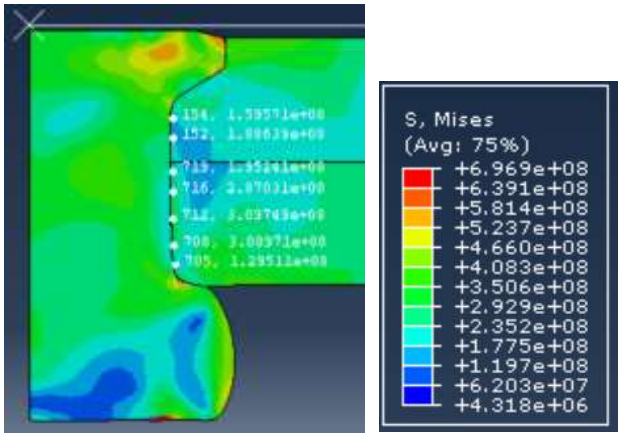

Figure 3.19. Sheet material effective stress ($\bar{\sigma}$) at hole wall measurement locations in simulation.

3.3 SUMMARY

In the squeeze riveting axisymmetric analytical work presented in this chapter, countersunk portion of the rivet and counterbore region of the outer sheet were neglected. Springback and friction and elastic strains were neglected. The residual strains were underpredicted by the analysis and the stackup stress distribution of the analysis was different from the simulation distributions because springback and friction were neglected and because simplifying assumptions were made during the analysis of the stackup skins.

Chapter 4. MODELING PROCEDURE

In this chapter, the modeling procedure of the FE simulations will be discussed. Four types of simulations were developed and performed as part of this dissertation work: Two-dimensional quasistatic squeeze riveting model, two-dimensional thermomechanical partial dynamic percussive riveting model, two-dimensional thermomechanical full dynamic percussive riveting model and three-dimensional thermomechanical full dynamic percussive riveting model.

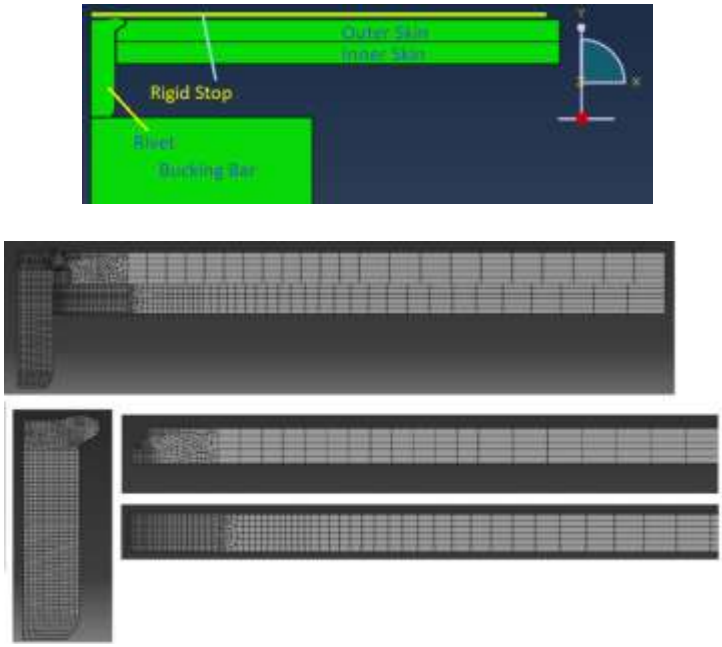

Figure 4.1. Rivet Stackup Assembly and Stackup Mesh.

4.1 TWO-DIMENSIONAL SQUEEZE RIVETING MODELING PROCEDURE

The assembly layout and mesh layout are described in figure 4.1. For the squeeze simulation described in chapter 5, the FE model has 2666 nodes and 2425 mesh elements. Typically, a squeeze riveting simulation was completed in 4 hours.

There is a bucking bar that forms the rivet button from one end while moving at a low velocity. At the other end there is a rigid stop that prevents axial motion of the stackup [Szolwinski, 1]. The outer skin and the inner skin are both hinged at the outer end as shown in figure 4.2.

Figure 4.2. Hinge Boundary Conditions of the Skins.

The skins are not free to translate in any direction. After the button is formed per requirements, the bucking bar moves in the opposite direction unloading the rivet. Velocity profile of the bucking bar is shown in figure 4.3. Loading rate of around 2 mm/min similar to ref. [18] was used. The bucking bar in the quasistatic squeeze simulation was prescribed to travel axially at an average velocity of 30-40 μm/s for 110 seconds in the loading step. Care was taken to ensure that the kinetic energy of the model was near zero.

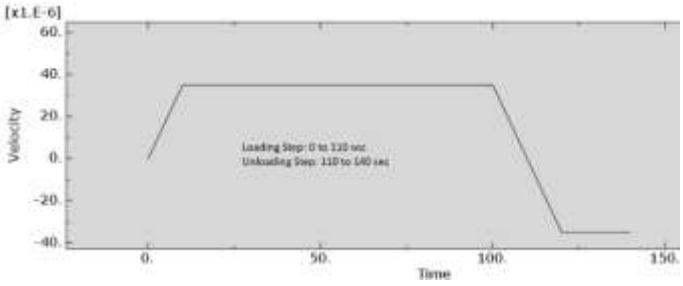

Figure 4.3. Quasistatic Squeeze Simulation Bucking Bar Velocity-Time Profile.

Geometric attributes of the squeeze simulation model are shown in table 4.1 normalized with rivet shank diameter. Shank diameter of the rivet ranges between 0.223” and 0.225”. The dimensions are also labeled in table 4.1.

Table 4.1. Quasistatic Stackup Dimensions normalized using D_{shank}=0.225”

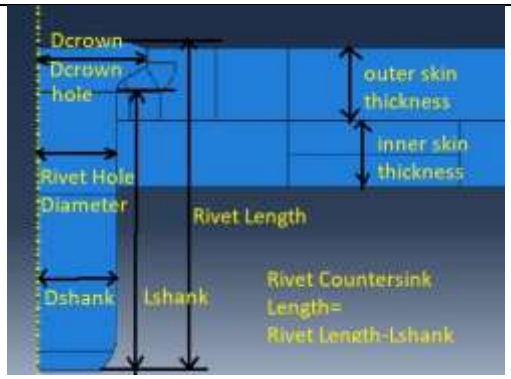

Dimension	Model 2 QS
D_{shank}	1
Rivet hole diameter	1.004
Inner skin diameter	18.782
Inner skin thickness	0.444
Outer skin diameter	18.782
Outer skin thickness	0.444
Rivet length	1.96
L_{shank}	1.685
Rivet countersink length	0.275
D_{crown}	1.396
Countersunk hole diameter	1.396
Bucking bar diameter	8.87
Bucking bar length	31.1
Rigid stop diameter	17.15

Rivet part was assigned AA 7050-T7451 properties [Yi, 41], skins were assigned AA 2024-T3 properties [Lesuer, 42] and bucking bar was assigned generic tungsten tool steel properties like the one found in ref. [43]. Rigid stop does not have any material properties. The Johnson-Cook (JC) material model was implemented. Refer to table 4.2 for material properties. The JC model has been shown to be reliably used to model aluminum alloys and steels constitutive behavior by capturing thermal softening effect, strain hardening effect and strain-rate hardening effect [Johnson, 44]. In the squeeze simulation, there is no thermal or strain-rate hardening effect, so it is effectively only the strain hardening effect that is observed [Szolwinski, 1]. JC model is an isotropic hardening model.

The JC model effective flow stress is given by eq. (4.1)

$$\sigma_{eff} = [A + B(\varepsilon)^n] [1 + C \log_e (\frac{\dot{\varepsilon}}{\dot{\varepsilon}ref})] [1-(\frac{T-Tref}{Tmelting-Tref})^m] \quad (4.1)$$

Table 4.2. Material Properties of Stackup Parts

	AA 7050-T7451	**AA 2024-T3**	**Tool Steel**		**AA 7050-T7451**	**AA 2024-T3**	**Tool Steel**
Density [kg]/[m^3]	2830	2712.63	7800	$\dot{\varepsilon}_{ref}$ [1/s]	0.0001	1	1
Young's Modulus [GPa]	71.7	74	210	$T_{melting}$ [K]	901	901	1645
Poisson ratio	0.33	0.33	0.3	T_{ref} [K]	298	298	298
A [MPa]	467	369	674.8	c [W/m/K]	157	121	42.6
B [MPa]	380	684	239.2	k [J/kg/K]	860	875	675
C	0.0077	0.0083	0.027	α [1/K]	23 X 10^{-6}	24 X 10^{-6}	12 X 10^{-6}
n	0.1	0.73	0.28	f [Inelastic Heat Fraction]			
m	1.06	1.7	1.3		0.9	0.9	0.9

Here $[A + B(\varepsilon)^n]$ captures the strain hardening effect, $[1 + C \log_e(\frac{\dot{\varepsilon}}{\dot{\varepsilon}ref})]$ captures the strain-rate hardening effects and $[1-(\frac{T-Tref}{Tmelting-Tref})^m]$ captures thermal softening effect. The quasistatic squeeze simulation is completed in two load steps. As shown in figure 4.3, there is loading step where the bucking bar forms the rivet and the unloading step where there is elastic springback that occurs after the bucking bar disengages from the stackup. The loading step is 110 seconds long and the unloading step is 30 seconds long. Disengagement of the bucking bar with the stackup happens around 15 seconds after the unloading step begins.

The squeeze simulation is performed using ABAQUS coupled structural-thermal, explicit dynamic solver. This solver also handles nonlinear geometric effects that are present because of the high levels of strain present within the formed rivet button.

This solver utilizes direct solution of the structural dynamics equation (eq. 4.2) where the mass matrix is a diagonal matrix and matrix inversion is a trivial process [Dassault, 45]. [M] is the FE model mass matrix, [C] is the FE model damping matrix, [K] is the FE model stiffness matrix. $\{\ddot{x}\}$, $\{\dot{x}\}$, $\{x\}$ are the acceleration, velocity and displacement vectors of the FE model degrees of freedom respectively. {F(t)} is the external load vector.

$$[M]\{\ddot{x}\} + [C]\{\dot{x}\} + [K]\{x\} = \{F(t)\} \tag{5.2}$$

The Explicit dynamics scheme is coupled with thermal computations. The scheme is restrictive because to maintain stability and accuracy, the stress waves cannot propagate more than the minimum characteristic length (~50 μm) of the finite element mesh in a single time increment. Time-increments of the order of 10^{-6} seconds are taken in the squeeze riveting simulation. As the elastic wave speeds of Al and steel alloys are of the order of 1000 ms^{-1}, this severely limits the acceptable time increment for each step. Allowable time increment is of the order of: 50 μm/ 5000 ms^{-1}= 10^{-8} seconds. Mass scaling is a procedure used for quasistatic simulations where the density of the material is artificially increased to increase the allowable time-increment, thereby reducing computation time. Mass scaling can be done without loss of accuracy only in cases where dynamic effects are absent like in the case of squeeze riveting. For a time increment to increase from 10^{-8} seconds to 10^{-6} seconds, material wave velocity must be reduced to 50 ms^{-1}. Density is inversely proportional to square of wave velocity. This means that density of stackup must be increased by 10000 times for an increase in allowable time-increment from 10^{-8} seconds to 10^{-6} seconds.

An element-by-element stable time-increment scheme is used and mass scaling is used for the entire model after every time step. No adaptive remeshing is needed for the quasistatic squeeze simulation because of low strain-rate of rivet deformation. Because no matrix inversion operations are required (the explicit scheme is not an iterative scheme like the Newton-Raphson

based implicit dynamics procedure), several thousands of time increments can be performed by a reasonable computing source in few seconds.

Penalty constraint enforcement method was used for all mating surfaces of the stackup. Finite sliding formulation was used. A shear stress limit was used to initiate slipping between mating surfaces. An infinite slip stiffness was used. Hard pressure-overclosure was utilized for normal direction penetration of master surface nodes. The fraction of energy dissipated by friction that is converted into heat is 100 percent. This is the default setting in ABAQUS. And the fraction of this dissipated energy that is distributed to each surface of a contact surface pair is 50 percent.

The rigid stop, the rivet and the bucking bar are prescribed axisymmetric constraint about the axial direction (Y-axis) [Szolwinski, 1]. The rigid stop is a rigid body that does not have any material properties. It is prescribed displacement constraint in the axial direction and it is held fixed in the axial direction. It is also prescribed constant nodal temperature of 298 K. The rivet, bucking bar and the two skins are also prescribed initial temperature of 298 K. The two skins are prescribed hinge constraints, as mentioned earlier. The bucking bar, the rigid stop and the skins act as thermal sinks for the heat that is generated within the plastically deforming rivet.

CAX4RT (coupled thermal-structural continuum solid quad element with reduced integration) type element is used in rivet, bucking bar and the two skins. The rigid stop is a rigid element with an assigned inertia. CAX4RT elements are used with stiffness hourglass control to attenuate spurious energy modes that are generated due to use of reduced integration [Dassault, 45]. Typical element mesh dimensions in the outer skin were 120 μm, in the inner skin were 112 μm and in the rivet were 62 μm. The mesh element size of the bucking bar was several dozen mm^2. These are larger than the grain sizes found in their respective materials. These element sizes play the critical role in determining the stable time increment for the explicit dynamics solution. The entire model is scanned after every time increment to estimate the stable time increment.

The assembly was divided into four topological domains for parallelization of the simulation. Each domain was assigned to one processor. The four processors access the same memory. Double numerical precision was used to ensure that the nodal force errors were minimized.

4.2 Two-Dimensional Thermomechanical Partial Dynamic Percussive Riveting Modeling Procedure

The partial dynamic percussive FE model comprises of a rigid stop that emulates the rivet hammer, the countersunk rivet, the inner skin and the outer skin, and the bucking bar. The rivet is bucked at the shank end and compresses both axially and radially. The rigid stop is fixed in the axial direction (shown in figure 4.4). For the partial dynamic model discussed in chapter 6, the FE model has 2770 nodes and 2524 mesh elements.

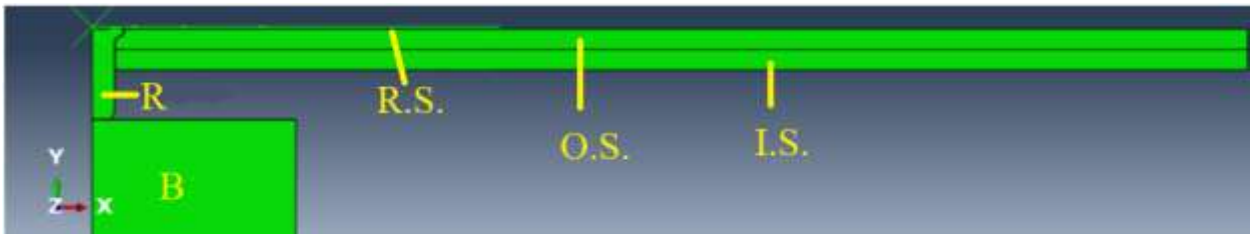

Figure 4.4. Partial Dynamic Percussive Model Layout. Full Length of Bucking Bar not shown. R: Briles Rivet, R.S.: Rigid Stop Emulating Rivet Die, O.S.: Outer Skin, I.S.: Inner Skin, B: Bucking Bar.

It was decided that the rivet would be subjected to hits only from the bucking bar in this type of simulation. Subsequently, in the next iteration of the full dynamic percussive FE model described in section 4.3, the rivet hammer will be subjected to hits from the oscillating piston mass inside the pneumatic hammer. This would then completely model the percussive riveting kinematics. Stack-up component relative dimensions are given in Table 4.3 where ‘d’ is the rivet shank diameter. In table 4.3, d is 0.223”.

Table 4.3. Stackup component relative dimensions. ‘d’ is Rivet Shank Diameter

Part	Relative Dimension
Inner skin radius	25.375 d
Inner skin thickness	0.4485 d
Outer skin radius	25.375 d
Outer skin thickness	0.4485 d
Rivet length	2.018 d
Rivet shank length	1.7 d
Rivet countersink length	0.318 d
Rivet crown diameter (d_C)	1.4 d
Bucking bar diameter	8.95 d
Bucking bar length	31.39 d
Rigid stop diameter	8.97 d

CAX3T (coupled thermal-structural continuum solid tri element) and CAX4RT (coupled thermal-structural continuum solid quad element with reduced integration) type elements are used in rivet, bucking bar and the two skins. The rigid stop is a rigid element with an assigned inertia. CAX4RT elements are used with enhanced hourglass control in the mesh of the rivet because adaptive meshing is used in the rivet [Dassault, 45]. Typical element mesh dimensions were same as the squeeze riveting simulation (typical mesh element dimensions were 120 μm in the outer skin, were 112 μm in inner skin and 62 μm in the rivet).

The Johnson-Cook material model was selected for performing the partial dynamic percussive simulation as this has been adopted with a high degree of confidence by many previous researchers for other dynamic forming simulations [Blanchot, 22]. JC model and material physical properties have been described in section 4.1. Rivet part was assigned AA 7050-T7451 properties, skins were assigned AA 2024-T3 properties, bucking bar was assigned generic tungsten tool steel properties. Rigid stop does not have any material properties.

The simulations were performed in an explicit dynamics framework [Dassault, 45]. The time step in the partial dynamic percussive simulation, is small and of the order of 10^{-8} seconds. Because this is a rapid forming process, adaptive meshing was implemented along with enhanced hourglass scheme [45]. Adaptive meshing is performed for the rivet mesh after every time

increment to improve the stable time increment. Mesh smoothing is performed 3 times for every mesh adaptation. Since, the mesh nodes do not correspond to the same material point for the whole duration of the simulation, care needs to be taken when gathering the stress/strain data. With adaptive meshing, only reduced integration elements can be used because of solver restrictions. These elements have only one integration (or Gauss) point per element. In the reduced integration elements, because of certain approximations pertaining to linearization of the FE model's displacement field, zero strain energy modes appear called hourglass modes which are attenuated by introducing artificial forces. Otherwise, these mode artifacts grow unbounded and eventually lead to singularities. The work done by these artificial forces has to be almost zero for a solution to be acceptable.

As the simulation progresses, the element with the smallest dimension changes. This necessitates the use of a small amount of mass scaling that has an effect of damping higher frequencies present in the model. Based on the data output of the conditionally-stable explicit dynamics solver, the mass of the entire model was increased by 0.003%. This ensures that the dynamic response is not affected adversely.

Penalty constraint enforcement method was used for all mating surfaces of the stackup. Finite sliding formulation was used. A shear stress limit was used to initiate slipping between mating surfaces. An infinite slip stiffness was used. Hard pressure-overclosure was utilized for normal direction penetration of master surface nodes. The fraction of energy dissipated by friction that is converted into heat is 100 percent. And the fraction of this dissipated energy that is distributed to each surface of a contact surface pair is 50 percent.

All parts of the model are axisymmetric. The Explicit dynamics scheme is coupled with thermal computations like the squeeze simulation described in previously. The boundary conditions constitute an important part in this modeling effort. The dimensions of the skins and the bucking bar are obviously important as that affects the stress wave propagation characteristics and the associated rebounding mechanism that is vital to the process. The mechanical and

thermal boundary conditions are described in the next paragraph. There is not enough time in the process for thermal energy to diffuse from the rivet to the surrounding environment. This results in rapid heating of the rivet material. Flow behavior of the rivet material is thus affected.

The rigid stop, rivet and bucking bar are prescribed axisymmetric boundary conditions in the radial direction. The inner skin and outer skin have their radial and axial displacements constrained at the far end with hinge constraints. The skins, rivet and bucking bar are initially at 298 K (room temperature). The rigid stop is prescribed an isothermal boundary condition at 298 K. The bucking bar is imparted the kinetic energy over a duration of 0.001 seconds.

For constraining the motion of the skins in the axial direction, a tie constraint was implemented. The displacements and nodal temperatures of the inner surface of the outer skin are forced to be same as those of the outer surface of the inner skin. This prevents formation of gaps between the skins. Any gaps are potential stress raisers and serve as crack nucleation sites. In actual practice, temporary spring-loaded fasteners are used in adjacent reamed holes to restrict the relative axial motion of the skins during assembly.

4.3 Two-Dimensional Thermomechanical Percussive Riveting Modeling Procedure

The two-dimensional full dynamic percussive riveting FE model assembly is described in figure 4.5. There is a bucking bar that forms the rivet button from one end while constrained under a push force (bucking bar push force: b_Y) in positive Y-direction. At the other end there is a deformable rivet die that is constrained under a push force (rivet hammer push force: h_Y) of in negative Y-direction. The forces used were approximations of load cell measurements of a comparable stackup from ref. [4]. For the full dynamic simulation described in chapter 7, the FE model has 4058 nodes and 3405 mesh elements. This simulation was completed in 22 hours.

From the schematic in figure 4.5, the piston strikes the die once every 40 ms and because of the constraint force applied, the bucking bar rebounds from the rivet after the stress waves propagate back and forth inside the rivet thereby deforming it (the rivet) [Krovvidi, 46]. Figure 4.6 shows the stackup region from figure 4.5 circled in red. Geometric attributes of the percussive rivet model stackup is shown in table 4.4 normalized with rivet shank diameter of 0.225". Typical element mesh dimensions were same as the squeeze riveting simulation (typical mesh element dimensions were 120 μm in the outer skin, were 112 μm in inner skin and 62 μm in the rivet).

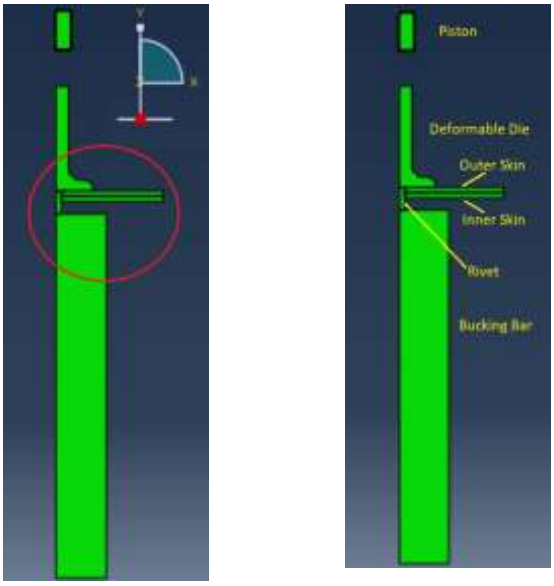

Figure 4.5. Percussive Riveting Model Stackup.

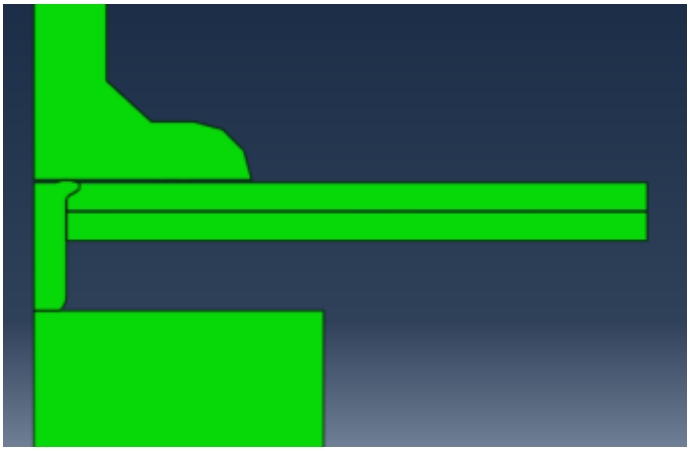

Figure 4.6. Figure 4.5's Percussive Stackup Region Circled in Red.

Rivet part was assigned AA 7050-T7451 properties, skins were assigned AA 2024-T3 properties, bucking bar, deformable die and piston were assigned generic tungsten tool steel properties. The Johnson-Cook (JC) material model was implemented. In the percussive riveting simulation, there are thermal and strain-rate hardening effects along with strain hardening effects. Material properties are described in section 4.1.

Table 4.4. Percussive Model 2 Dyn Stackup dimensions normalized using D_{shank}=0.225”

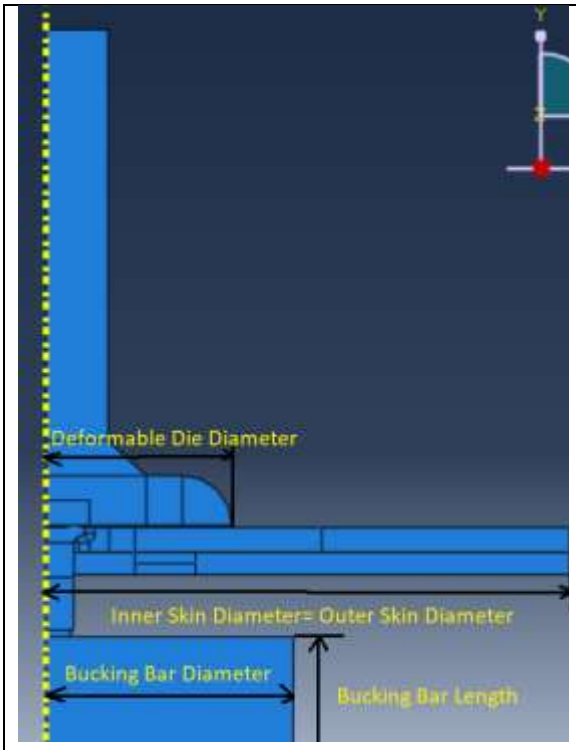

Dimension	Model 2 Dyn
D_{shank}	1
Rivet hole diameter	1.004
Inner skin diameter	18.782
Inner skin thickness	0.444
Outer skin diameter	18.782
Outer skin thickness	0.444
Rivet length	1.96
L_{shank}	1.685
Rivet countersink length	0.275
D_{crown}	1.396
Countersunk hole diameter	1.396
Bucking bar diameter	8.87
Bucking bar length	31.1
Deformable die diameter	6.67

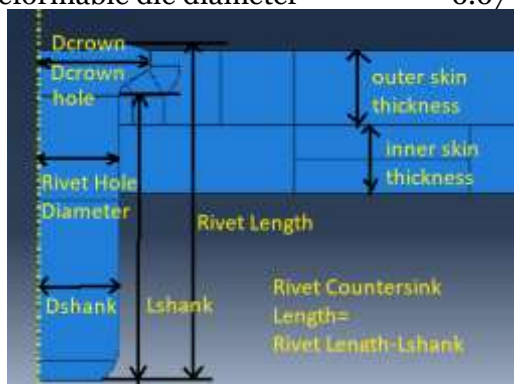

The simulation is performed using coupled structural-thermal, explicit dynamic solver. Short time-steps of the order of 10^{-8} seconds are taken to ensure system stability. Element-by-element stable time increment scheme is used and mass scaling is used for the entire model after every time step. Penalty constraint enforcement method, finite sliding formulation, stick-slip shear

stress limit, slip stiffness, pressure-overclosure, friction energy dissipation fraction and distribution fraction of dissipated energy of quasistatic squeeze simulation are used in the percussive riveting simulation.

The piston, the deformable die, the rivet and the bucking bar are prescribed axisymmetric constraint about the axial direction (Y-axis). The rivet, bucking bar, two skins, piston and deformable die were prescribed initial temperature of 298 K. The two skins are prescribed hinge constraints just like the quasistatic simulation. In the full dynamic percussive simulation, the two skins are prescribed tie constraint like the partial dynamic percussive model to minimize Y-direction motion. The displacements and nodal temperatures of the inner surface of the outer skin are forced to be same as those of the outer surface of the inner skin. This prevents formation of gaps between the skins.

Adaptive meshing is performed for the rivet mesh after every time increment to improve the stable time increment. Mesh smoothing is performed 3 times for every mesh adaptation. CAX4RT type elements are used in rivet, bucking bar and the two skins. CAX4RT elements are used with enhanced hourglass control in the rivet mesh because when using adaptive remeshing, only this type can be used to attenuate spurious energy modes.

4.4 Three-Dimensional Thermomechanical Percussive Riveting Modeling Procedure

The three-dimensional full dynamic percussive riveting FE model is described in figure 4.7. This assembly is a three-dimensional, 180-degree sector. There is a bucking bar that constrains and forms the rivet button from one end under a push force in positive Y-direction. At the other end of the rivet, there is a deformable rivet die that is constrained under a push force in negative Y-direction. The three-dimensional full dynamic percussive riveting simulation was completed in

around 215 hours (~9 days). For the three-dimensional full dynamic simulation described in chapter 9, the FE model has 15627 nodes and 13415 mesh elements.

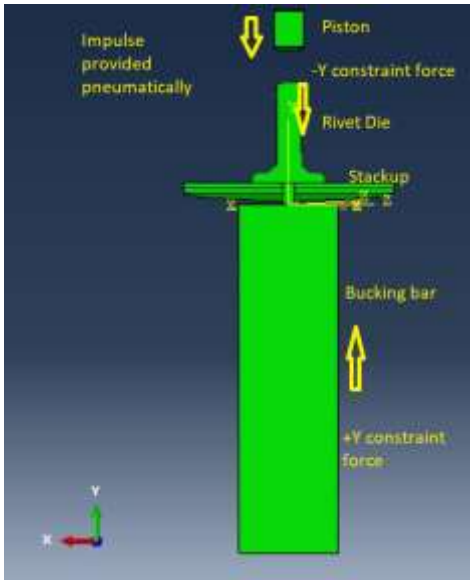

Figure 4.7. Three-Dimensional Percussive Riveting Model Stackup.

In figure 4.7, the piston strikes the die once every 40 ms with a kinetic energy and because of the constraint force applied, the bucking bar rebounds from the rivet. Stress waves propagate back and forth inside the rivet and deform it [Krovvidi, 46].

Geometric attributes and dimensions of this FE model are shown in table 4.5 normalized with rivet shank diameter of 0.225". Rivet was assigned AA 7050-T7451 properties and skins were assigned AA 2024-T3 properties [Yi, 41; Lesuer, 42]. The bucking bar, deformable die and piston were assigned generic tungsten tool steel properties in this simulation.

The Johnson-Cook (JC) material model described in section 4.1 was implemented in this FE model. Each load-unload cycle takes 40 ms to complete. This simulation was performed using coupled structural-thermal, explicit dynamic ABAQUS solver. Time-steps of the order of 10^{-9} seconds, were taken to ensure system stability by avoiding stress-wave-propagation-induced element collapse.

Table 4.5. Three-dimensional Percussive Simulation Stackup Dimensions Normalized Using D_{shank}=0.225”

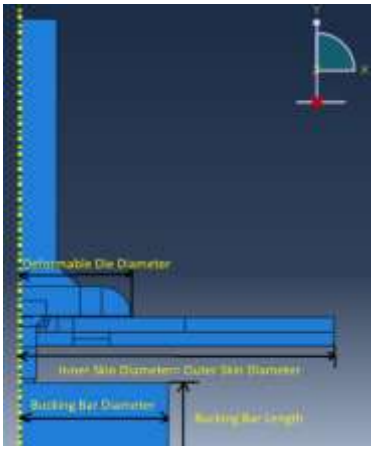

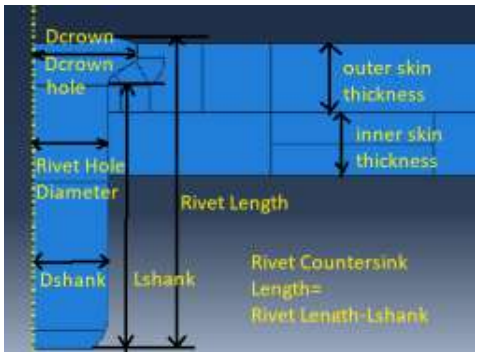

Dimension	
D_{shank}	1
Rivet hole diameter	1.004
Inner skin diameter	18.782
Inner skin thickness	0.444
Outer skin diameter	18.782
Outer skin thickness	0.444
Rivet length	1.96
L_{shank}	1.685
Rivet countersink length	0.275
D_{crown}	1.396
Countersunk hole diameter	1.396
Bucking bar diameter	8.87
Bucking bar length	31.1
Deformable die diameter	6.67

Note: Two-dimensional stackup is shown in place of three-dimensional stackup.

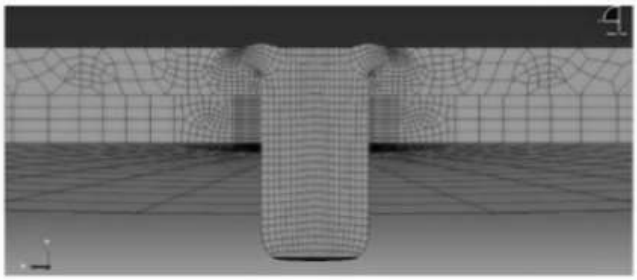

Figure 4.8. Three-Dimensional Percussive Riveting Model Stackup Mesh.

Stackup mesh of this simulation is shown in figure 4.8. Rivet mesh, inner skin mesh and outer skin of this simulation are shown in figures 4.9, 4.10 and 4.11, respectively. An element-by-element stable time increment scheme was used, and mass scaling was used for the entire model

after every time step. Adaptive remeshing is needed for this simulation because of high strain-rate of rivet deformation. Adaptive remeshing with enhanced hourglass method is utilized only for the rivet mesh because the rivet experiences the highest strain concentration in the stackup.

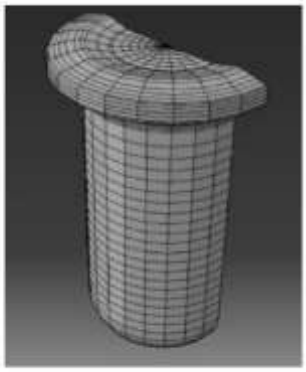

Figure 4.9. Rivet Mesh.

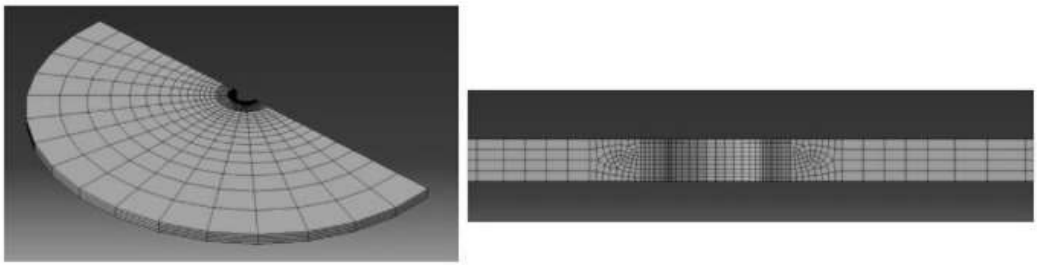

Figure 4.10. Inner Skin Mesh.

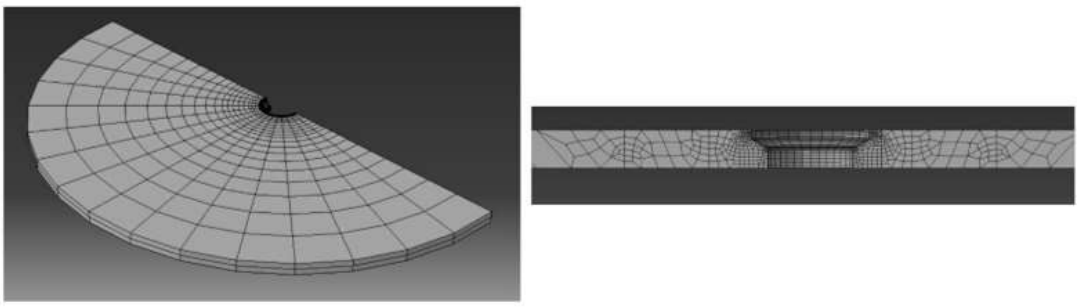

Figure 4.11. Outer Skin Mesh.

Penalty constraint enforcement method was used for all mating surfaces and finite sliding formulation was used. An infinite slip stiffness was used. A stick-slip shear stress limit was used. Hard pressure-overclosure was utilized for normal direction penetration of master surface nodes. The fraction of energy dissipated by friction that is converted into heat was set at 100 percent. And the fraction of this dissipated energy that is distributed to each surface of a contact surface pair was set at 50 percent.

The rivet, bucking bar, two skins, piston and deformable die were prescribed initial temperature of 298 K. The two skins were prescribed hinge constraints in this simulation. Also, the two skins were prescribed tie-constraint to minimize Y-direction motion. X-direction and Z-direction displacement of rivet die were constrained in this simulation.

C3D8RT brick element, C3D6RT wedge element and C3D4T tetrahedral element were used in constructing the mesh of this assembly. Characteristic mesh element size of this simulation model is 0.3 mm. A coarse mesh was used for this simulation because of computational time constraints. In this simulation, the assembly was divided into three topological domains for parallel processing. Again, double numerical precision was used to ensure that the nodal force errors were minimized.

Chapter 5. QUASISTATIC SQUEEZE RIVETING ANALYSIS

5.1 INTRODUCTION

In squeeze riveting, there are no thermal or strain-rate effects, only strain hardening is encountered. An axisymmetric unstiffened rivet stackup with an initial positive rivet-hole clearance is considered. Its FE analysis will be performed in this chapter. Comparable analysis of squeeze formed rivet [Szolwinski, 1; Atre, 17] is offered and residual stress and strain fields will be discussed. The distribution and magnitude of residual stress in a riveted joint have an effect on the fatigue strength of the riveted joint.

Squeeze riveting simulation is the first step taken toward creating a model for the percussive riveting process. The process mechanics and boundary conditions of percussive riveting are very different compared to the squeeze riveting process. Nonetheless, squeeze riveting also features nonlinearities because of large deformations and contact friction.

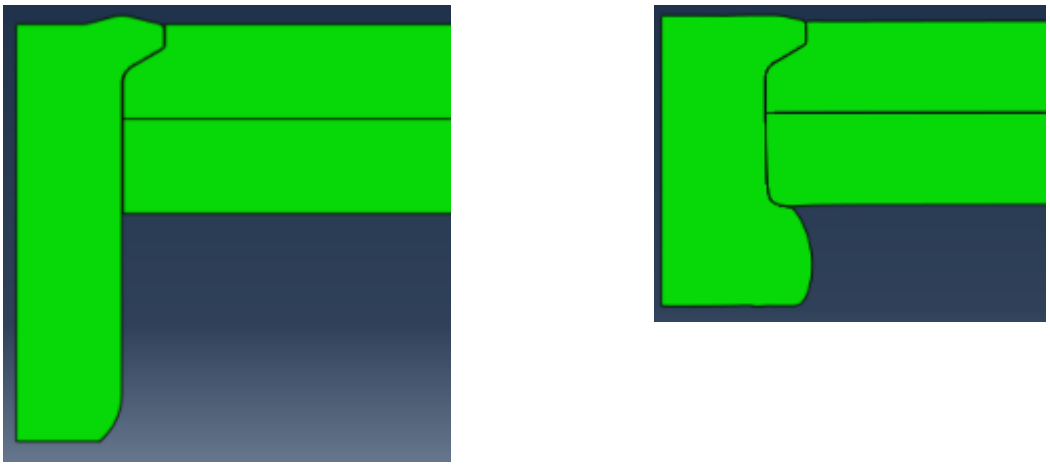

Figure 5.1. Axisymmetric stackup layout on the left and Deformed stackup on the right.

Figure 5.1 shows the layout of the axisymmetric squeeze riveting stackup on the left and shows the deformed stackup after the squeeze riveting is performed on the right. Measurements of

residual stresses and strains were made at seven different locations inside the deformed stackup. These locations are shown in figure 5.2. Location 'A' is the rivet crown region or the rivet countersink region. 'B' is the rivet shank region. 'C' is the rivet button region. Location 'D' is the region adjacent to the outer skin counterbore. This is also referred to as the outer skin crown region. 'd' is the rivet shank diameter. 'E' is the area of the outer skin starting at a distance of 1.14d away from rivet axis. Location 'F' is the area of the inner skin that is adjacent to the rivet shank. 'G' is located with the inner skin starting at a distance of 1.14d away from rivet axis.

Figure 5.2. Residual Stresses/Strains measurement stackup locations.

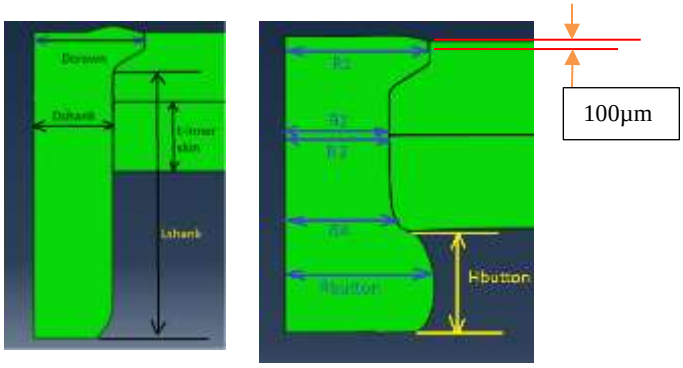

Figure 5.3. Stackup Geometric Attributes and Measured Geometric Features.

Figure 5.3 shows the important geometric features of the stackup and the standard geometric measurements that are used to evaluate the quality of a riveted joint. Namely R_1, R_2, R_3, R_4, height of rivet button (H_b) and radius of the rivet button (R_b). R_1 (rivet-outer skin interface metric) is measured roughly 100 µm below the outer surface of the outer skin, R_2 (rivet-outer skin interface

metric) is measured 100 μm above the inner-skin-outer-skin interface, R_3 (rivet-inner skin interface metric) is measured 100 μm below the inner-skin-outer-skin interface and R_4 (rivet-inner skin interface metric) is measured 100 μm above the top of the rivet button.

5.2 ADDITIONAL MODELING INFORMATION

Squeeze riveting modeling discussion was presented in section 4.1. All traction and displacement boundary conditions are described in detail in section 4.1 along with the geometric dimensions, model mesh layout and material properties. In this chapter, an axisymmetric quasistatic simulation was performed for establishing a modeling baseline, this is referred to as "Model 2 QS". Clearance Ratio (CL) is the ratio of rivet shank diameter to hole diameter. Thickness Ratio (TR) is the ratio of inner skin thickness to outer skin thickness. Refer to table 5.1 for the values of CL, TR and other important parameters of the "model 2 QS" simulation.

Table 5.1. Clearance and Thickness Ratio Values of the Simulation Stackup

Simulation	Clearance Ratio (CL)	Thickness Ratio (TR)	Friction Coeff. (μ)	Shear Stress Limit (MPa)	D_{shank} (in.)	D_{hole} (in.)
Model 2 QS	0.9956	1	0.25	269.62	0.225	0.226

5.3 RESULTS AND DISCUSSION

Data was collected for the geometric features described in the previous section. Normalized values are shown in table 5.2. Residual stress distributions are shown for radial, axial and hoop components. Residual logarithmic strain distributions are shown for radial, axial and hoop components. Distinctions have also been made to show regions that have compressive and tensile stresses. Data was collected for the residual stress and strain distributions at the mesh element

integration points that are located at the seven areas within the deformed stackup as shown in figure 5.2.

Table 5.2. Normalized geometric attribute measurements. R1 is normalized with R_{crown}; R2, R3, R4 and R_b are normalized with R_{shank}; H_b is normalized with L_{rivet}

R_1/R_{crown}	R_2/R_{shank}	R_3/R_{shank}	R_4/R_{shank}	R_b/R_{shank}	H_b/L_{rivet}
1.01	1.016	1.017	1.044	1.48	0.286

Data from table 5.2 tells us that there is radial expansion of the rivet at all measured locations. Maximum expansion in the shank region of the rivet of 4.4 percent is seen at R_4. R_b/R_{shank} value of 1.4-1.6 is usually considered satisfactory in the literature. That target is achieved in this squeeze riveting simulation.

Referring to figure 5.4a, radial stress distribution in region ‘A’ model 2 QS is shown. Radial stress is compressive across region ‘A’. Radial stress is compressive adjacent to the crown of the upper skin. It is compressive adjacent to the wedge region. At the head of the crown near the rivet axis, stress is compressive. At the base of the crown near the rivet axis, stress is compressive. Within the interior of the region 'A', stress is compressive.

Referring to figure 5.4b, axial stress distribution in region ‘A’ of model 2 QS is shown. Axial stress is compressive adjacent to the crown of the upper skin. It is tensile adjacent to the wedge region. At the head of the crown near the rivet axis, compressive stress of small magnitude exists. At the base of the crown near the rivet axis, stress is compressive. At the base of the crown below the wedge, the stress is observed to be tensile. Within the interior of the region 'A', there are areas of both tensile and compressive stresses.

Referring to figure 5.4c, hoop stress distribution in region ‘A’ of model 2 QS is shown. Hoop stress is both tensile and compressive adjacent to the crown of the upper skin. It is compressive adjacent to the wedge region. At the head of the crown near the rivet axis, stress is compressive.

At the base of the crown near the rivet axis, stress is compressive. Within the interior of the region 'A', stress is mostly compressive.

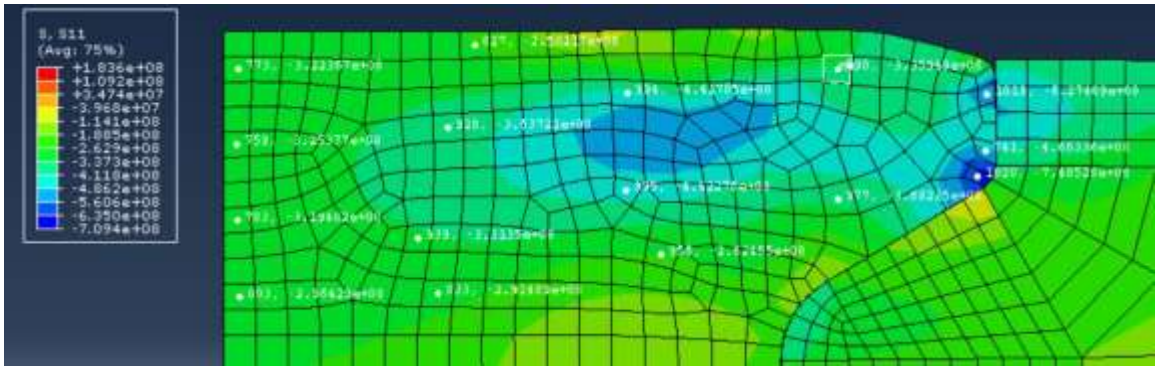

a: Radial

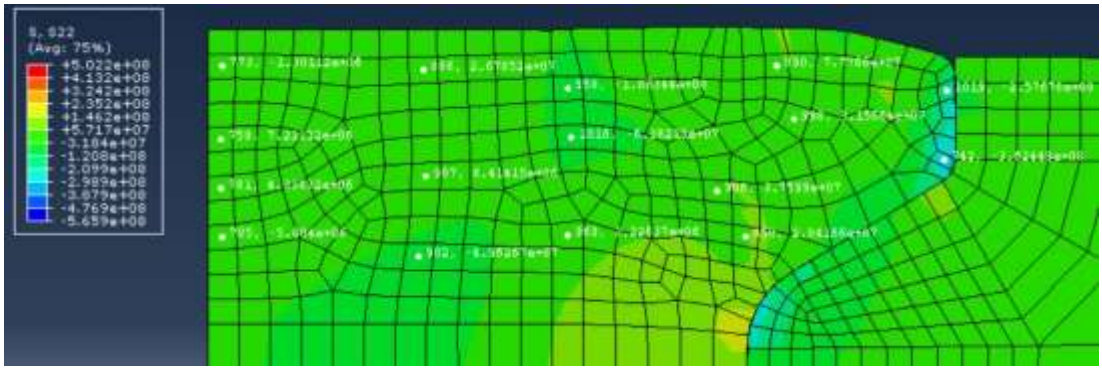

b: Axial

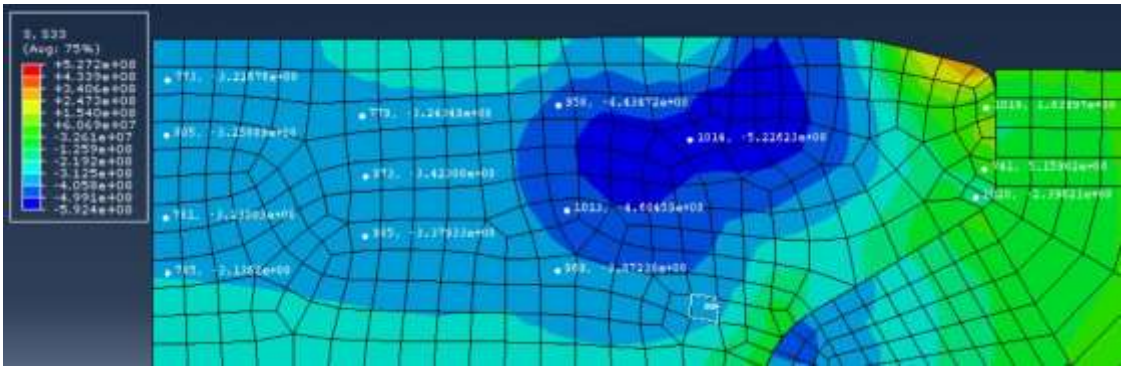

c: Hoop

Figure 5.4. Stress distributions within region 'A' of the 'Model 2 QS' stackup. a: Radial Stress, b: Axial Stress, c: Hoop Stress

Referring to figure 5.5a, logarithmic radial strain distribution in region ‘A’ of model 2 QS is shown. Radial strain is compressive adjacent to the crown of the upper skin. It is compressive adjacent to the wedge region. At the head of the crown near the rivet axis, strain is compressive. At the base of the crown near the rivet axis, strain is compressive. At the base of the crown below the wedge, the strain is observed to be tensile. Within the different areas of interior of the region 'A', the strain is observed to be tensile and compressive.

Referring to figure 5.5b, logarithmic axial strain distribution in region ‘A’ of model 2 QS is shown. Axial strain is tensile adjacent to the crown of the upper skin. It is tensile adjacent to the wedge region. At the head of the crown near the rivet axis, strain is tensile. At the base of the crown near the rivet axis, strain is tensile. At the base of the crown below the wedge, the strain is observed to be compressive. Within different areas of the interior of the region 'A', the strain is observed to be tensile and compressive.

Referring to figure 5.5c, logarithmic hoop strain distribution in region ‘A’ of model 2 QS is shown. The hoop strain is tensile in the areas adjacent to the outer skin crown and the wedge. The strain is observed to be compressive in the areas adjacent to the rivet axis. Strain magnitude is small across region 'A'.

a: Radial

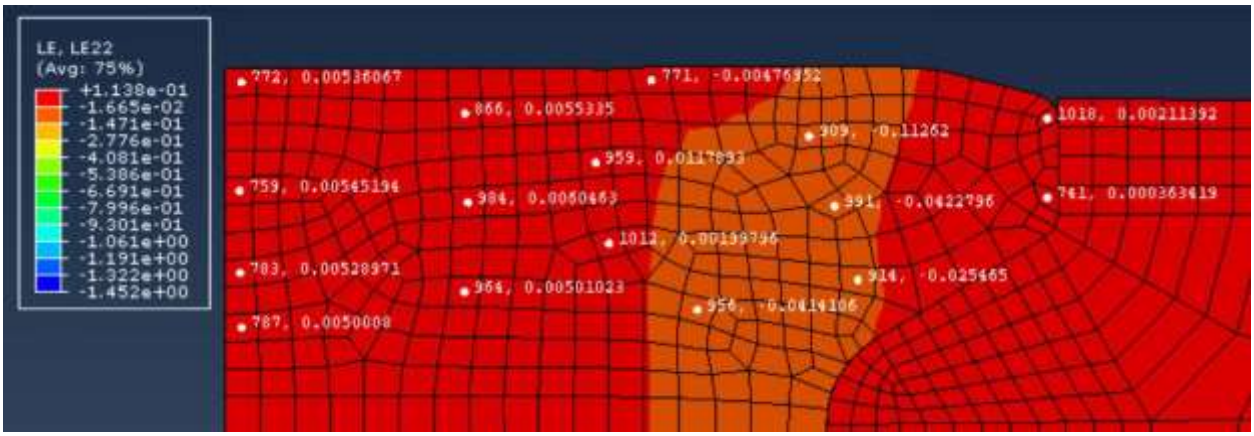

b: Axial

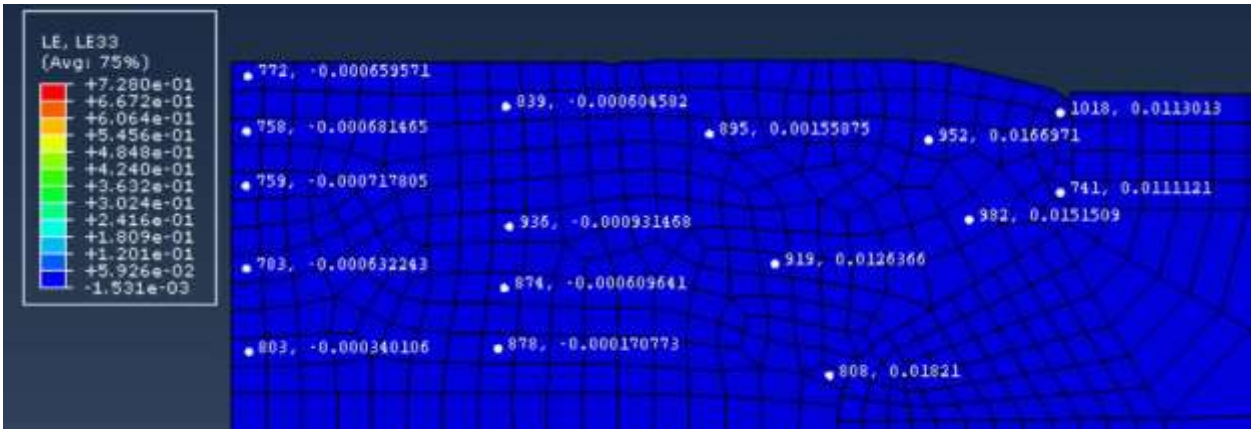

c: Hoop

Figure 5.5. Strain distributions within region 'A' of the 'Model 2 QS' stackup. a: Radial Strain, b: Axial Strain, c: Hoop Strain

Referring to figure 5.6a, radial stress distribution in region ‘B’ of model 2 QS is shown. Radial stress is compressive adjacent to skins. It is compressive in the interior of region 'B'. It is also compressive near the rivet axis.

Referring to figure 5.6b, axial stress distribution in region ‘B’ of model 2 QS is shown. Axial stress is compressive adjacent to inner skin and it is tensile adjacent to the outer skin. It is tensile in the interior of region 'B' except adjacent to the base of the rivet crown. It is tensile near the rivet axis.

Referring to figure 5.6c, hoop stress distribution in region ‘B’ of model 2 QS is shown. Hoop stress is compressive across region ‘B’. The magnitude of the stress is high adjacent to the two skins. It is also high in the upper half of region 'B' compared to the lower half.

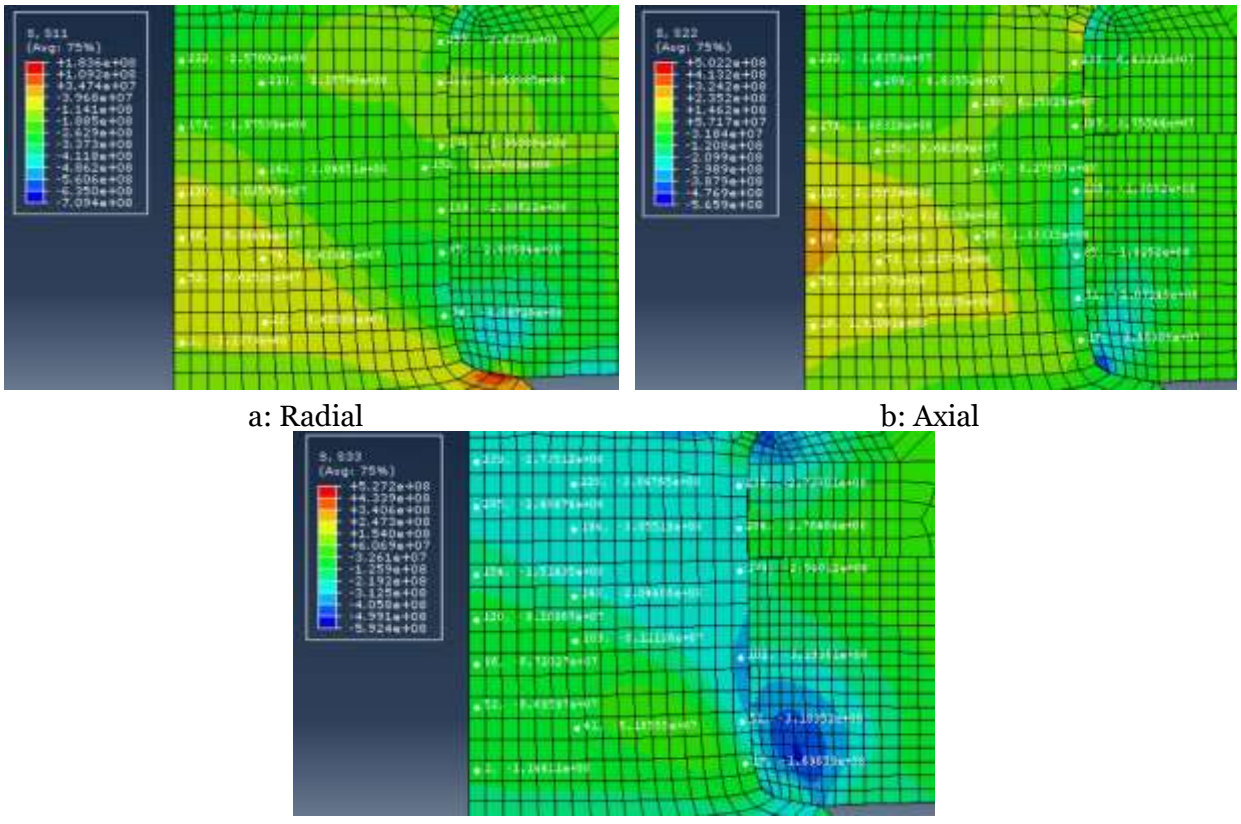

a: Radial b: Axial

c: Hoop

Figure 5.6. Stress distributions within region ‘B’ of the ‘Model 2 QS’ stackup. a: Radial Stress, b: Axial Stress, c: Hoop Stress

Referring to figure 5.7a, logarithmic radial strain distribution in region ‘B’ of model 2 QS is shown. Strain is tensile across region ‘B’. Magnitude is higher near the head of the rivet button compared to the interior of region ‘B’ and compared to area near base of the region ‘A’.

Referring to figure 5.7b, logarithmic axial strain distribution in region ‘B’ of model 2 QS is shown. Strain is compressive across region ‘B’ except near the rivet axis at the base of region ‘A’. Magnitude of compressive strain is higher near the head of the rivet button compared to the interior of region ‘B’.

Referring to figure 5.7c, logarithmic hoop strain distribution in region ‘B’ of model 2 QS is shown. Strain is tensile across region ‘B’. Magnitude is higher in the lower half of region 'B' compared to the upper half.

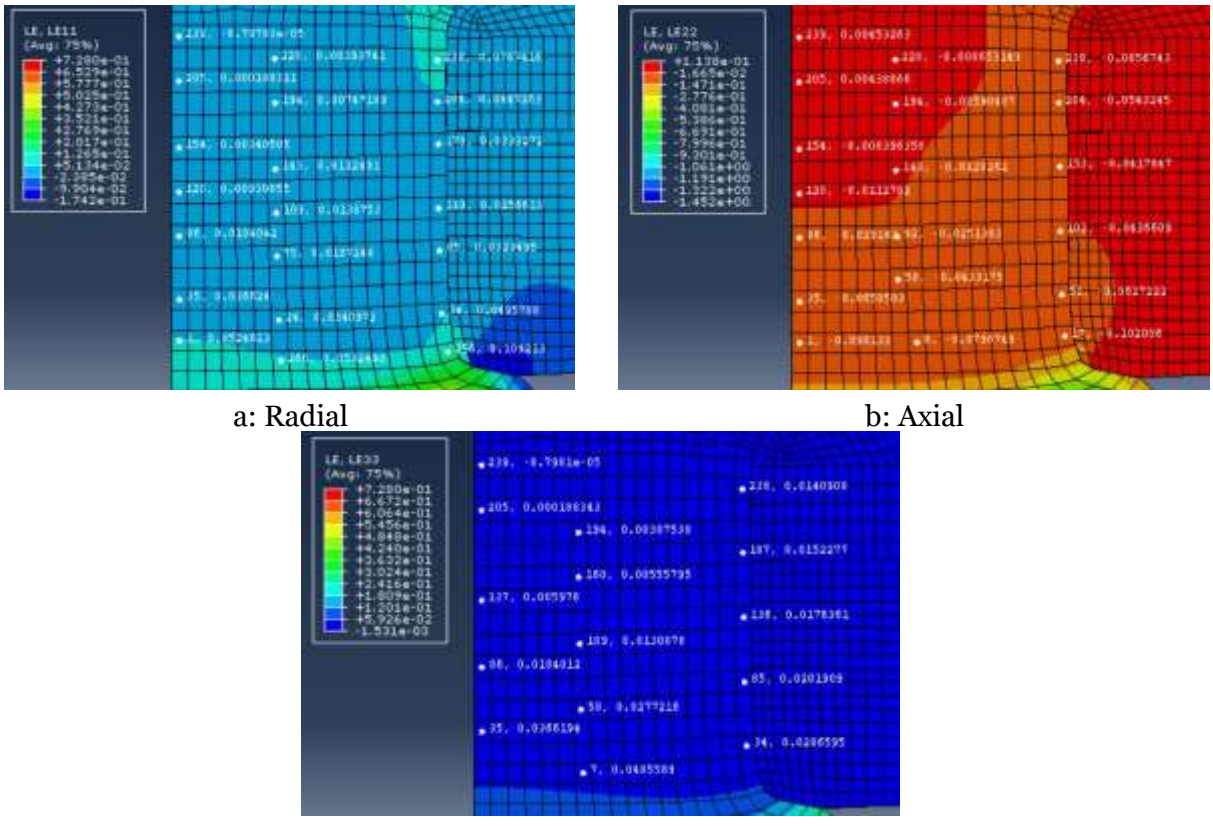

a: Radial b: Axial

c: Hoop

Figure 5.7. Strain distributions within region ‘B’ of the ‘Model 2 QS’ stackup. a: Radial Strain, b: Axial Strain, c: Hoop Strain

Referring to figure 5.8a, radial stress distribution in region ‘C’ of model 2 QS is shown. Radial stress is compressive across region 'C', except near head of the rivet button and base of the rivet button where it is tensile. Stress is also tensile in some areas of the free surface of the rivet button.

Referring to figure 5.8b, axial stress distribution in region ‘C’ of model 2 QS is shown. Axial stress is compressive near the head of the rivet button. It is compressive near the rivet axis close to the base of the rivet button. Stress is tensile at and adjacent to the free surface of the rivet button. It is tensile near the rivet axis at the top of region 'C'.

Referring to figure 5.8c, hoop stress distribution in region ‘C’ of model 2 QS is shown. Stress is compressive near the rivet axis, across a large area in the interior of region ‘C’, and near the head of the rivet button. But there is an area in the interior of region ‘C’ adjacent to the rivet button free surface and at the free surface of the rivet button where the hoop stress is tensile.

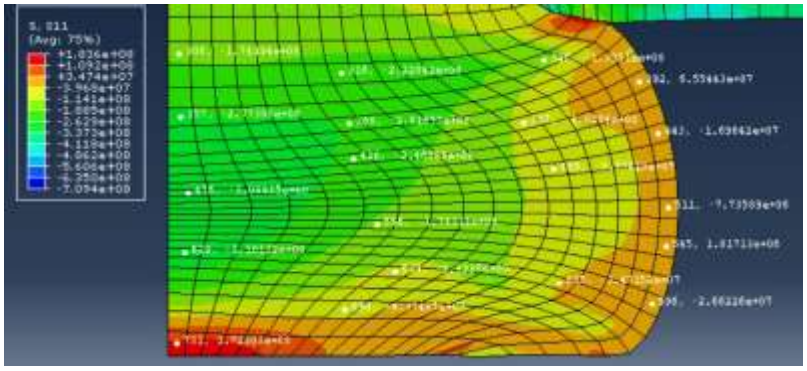

a: Radial

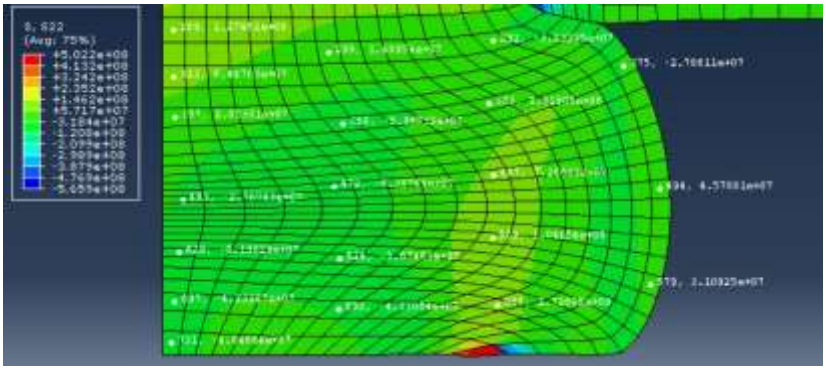

b: Axial

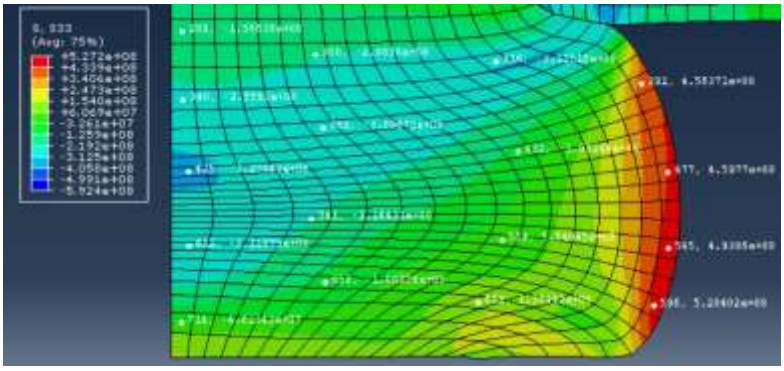

c: Hoop

Figure 5.8. Stress distributions within region ‘C’ of the ‘Model 2 QS’ stackup. a: Radial Stress, b: Axial Stress, c: Hoop Stress

Referring to figure 5.9a, logarithmic radial strain distribution in region ‘C’ of model 2 QS is shown. Strain is tensile across region ‘C’. It is compressive at the free surface of the rivet surface. Referring to figure 5.9b, logarithmic axial strain distribution in region ‘C’ of model 2 QS is shown. Axial strain is compressive across region ‘C’. There is region that stretches from the rivet axis to the head of the rivet button and base of the rivet button where high magnitude of strain is observed. Areas outside this band in region ‘C’ have a lower axial strain magnitude.

Referring to figure 5.9c, logarithmic hoop strain distribution in region ‘C’ of model 2 QS is shown. Hoop strain is tensile across region ‘C’. Strain is found to have a higher magnitude in the central area of region ‘C’.

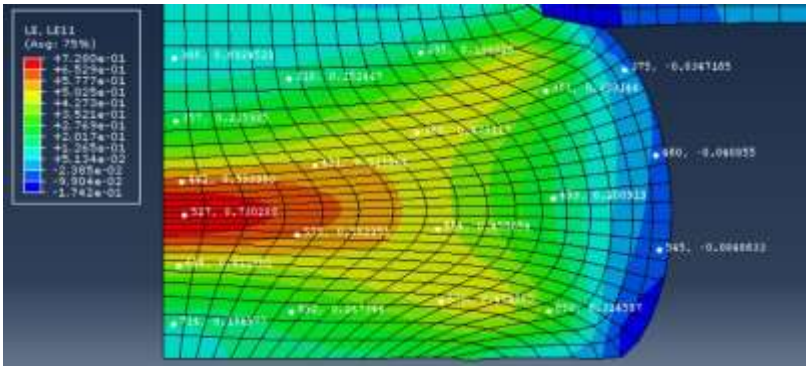

a: Radial

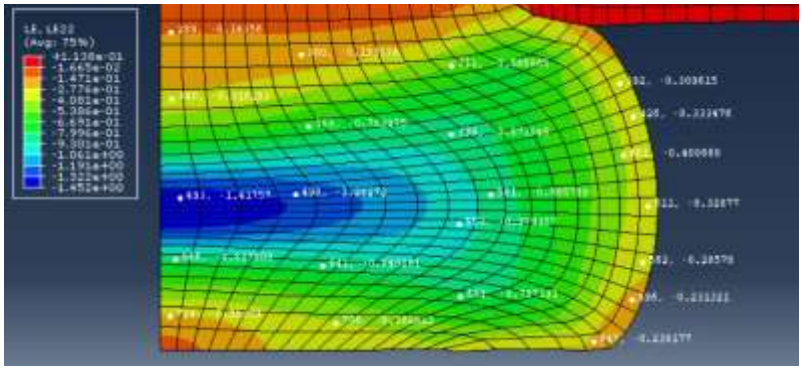

b: Axial

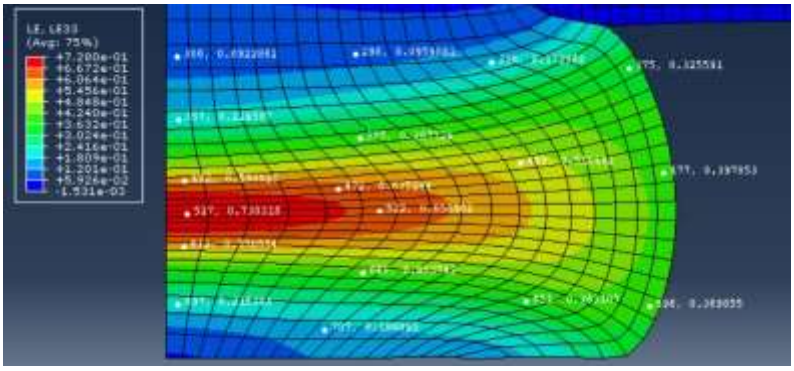

c: Hoop

Figure 5.9. Strain distributions within region ‘C’ of the ‘Model 2 QS’ stackup. a: Radial Strain, b: Axial Strain, c: Hoop Strain

Referring to figure 5.10a, radial stress distribution in region ‘D’ of model 2 QS is shown. Radial stress is compressive accross region 'D'. Radial stress is compressive in the area adjacent to the rivet crown. Stress is compressive in the wedge area and below the wedge area. Stress is compressive adjacent to the rivet shank. The radial stress is compressive in the interior of region 'D'.

Referring to figure 5.10b, axial stress distribution in region ‘D’ of model 2 QS is shown. Axial stress is compressive in the area adjacent to the rivet crown. Stress is tensile and compressive in the wedge area. Stress is compressive below the wedge area. Stress is tensile adjacent to the rivet shank. The axial stress has small magnitude in interior of region 'D'. It is compressive in some interior areas and tensile in others.

Referring to figure 5.10c, hoop stress distribution in region ‘D’ of model 2 QS is shown. Hoop stress is compressive in the area adjacent to the rivet crown. Stress is compressive in the wedge area and below the wedge area. Stress is compressive adjacent to the rivet shank. The hoop stress is compressive in some interior areas of region 'D' and it is tensile in other interior areas.

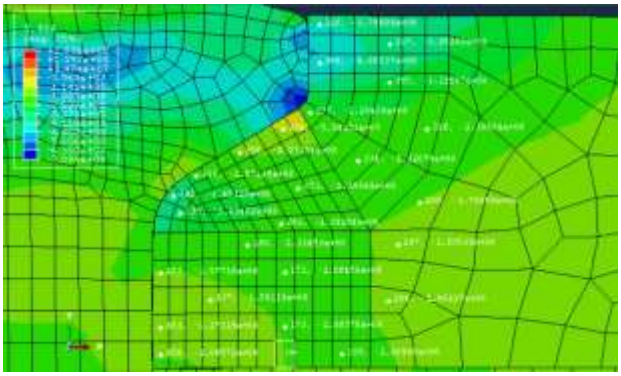

a: Radial

b: Axial

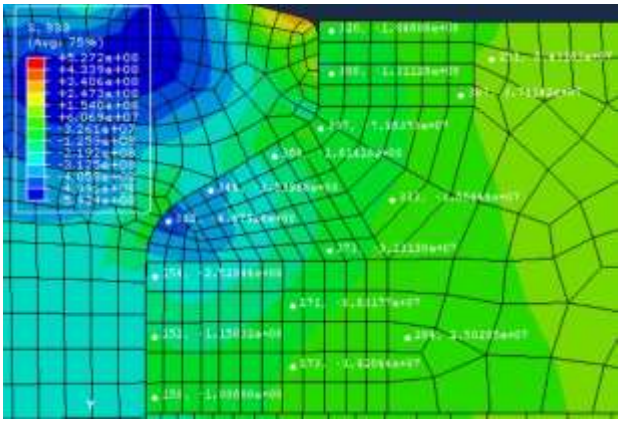

c: Hoop

Figure 5.10. Stress distributions within region ‘D’ of the ‘Model 2 QS’ stackup. a: Radial Stress, b: Axial Stress, c: Hoop Stress

Referring to figure 5.11a, logarithmic radial strain distribution in region ‘D’ of model 2 QS is shown. Radial strain is compressive in the area adjacent to the rivet crown. Strain is compressive in the wedge area. It is tensile below the wedge area. Strain is compressive adjacent to the rivet shank. The radial strain is compressive in the interior area of region 'D' adjacent to rivet crown, wedge and rivet shank.

Referring to figure 5.11b, logarithmic axial strain distribution in region ‘D’ of model 2 QS is shown. Axial strain is tensile in the area adjacent to the rivet crown. Strain is compressive in the wedge area and below the wedge area. Strain is compressive adjacent to the rivet shank. The axial strain is tensile in the interior area of region 'D' adjacent to rivet crown and wedge. The axial strain is compressive in the interior area of region 'D' adjacent to the rivet shank.

Referring to figure 5.11c, logarithmic hoop strain distribution in region ‘D’ of model 2 QS is shown. Hoop strain is tensile across region 'D'. The magnitude is higher near the rivet-skin interface compared to the magnitude away from the rivet-skin interface.

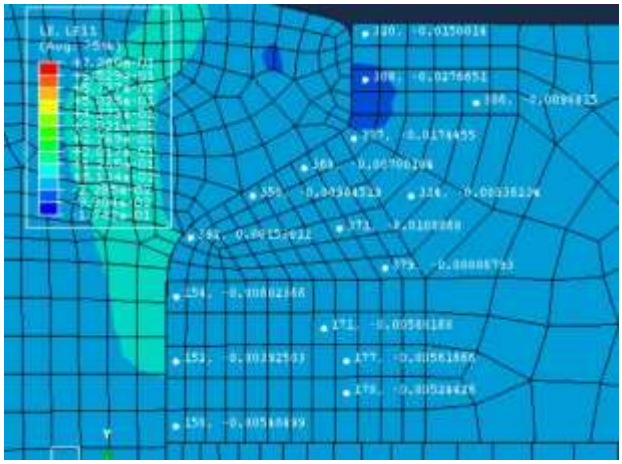

a: Radial

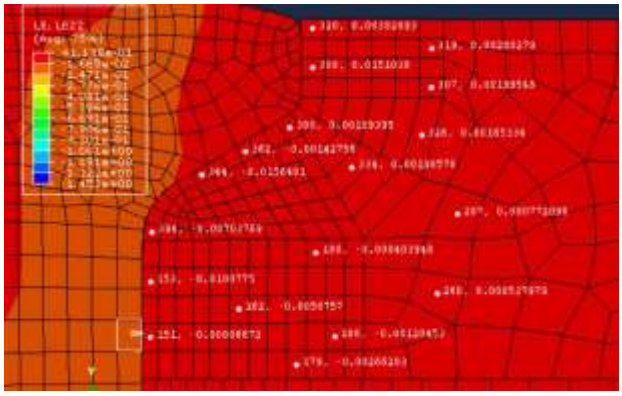

b: Axial

c: Hoop

Figure 5.11. Strain distributions within region 'D' of the 'Model 2 QS' stackup. a: Radial Strain, b: Axial Strain, c: Hoop Strain

Referring to figure 5.12a, radial stress distribution within regions ‘E’ and ‘G’ of Model-2 QS simulation is shown. Radial stress is compressive across regions 'E' and 'G'. The magnitude is higher in the areas adjacent to regions 'D' and 'F' compared to the magnitude in the areas away from these regions.

Referring to figure 5.12b, axial stress distribution within regions ‘E’ and ‘G’ of Model-2 QS is simulation is shown. The magnitude of compressive and tensile axial stresses in regions ‘E’ and ‘G’ is small.

Referring to figure 5.12c, hoop stress distribution within regions ‘E’ and ‘G’ of Model-2 QS simulation is shown. Hoop stress is tensile across regions 'E' and 'G'. The magnitude is higher in the areas adjacent to regions 'D' and 'F' compared to the magnitude in the areas away from these regions.

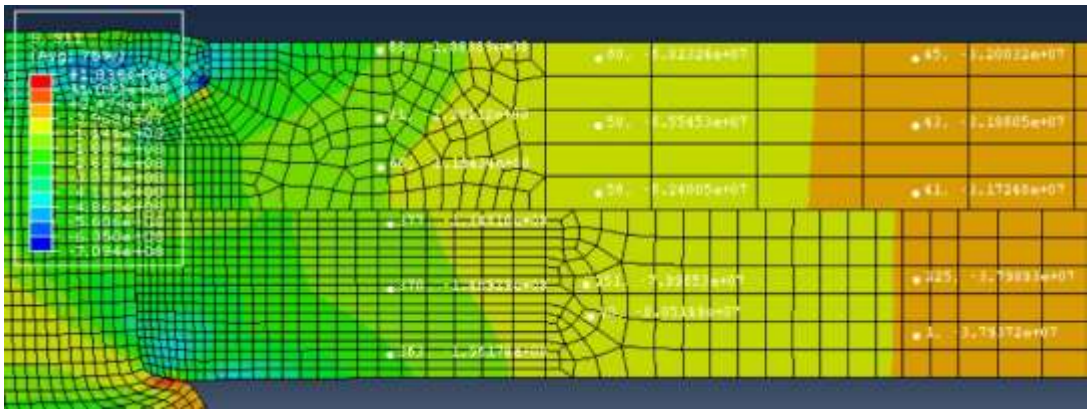

a: Radial

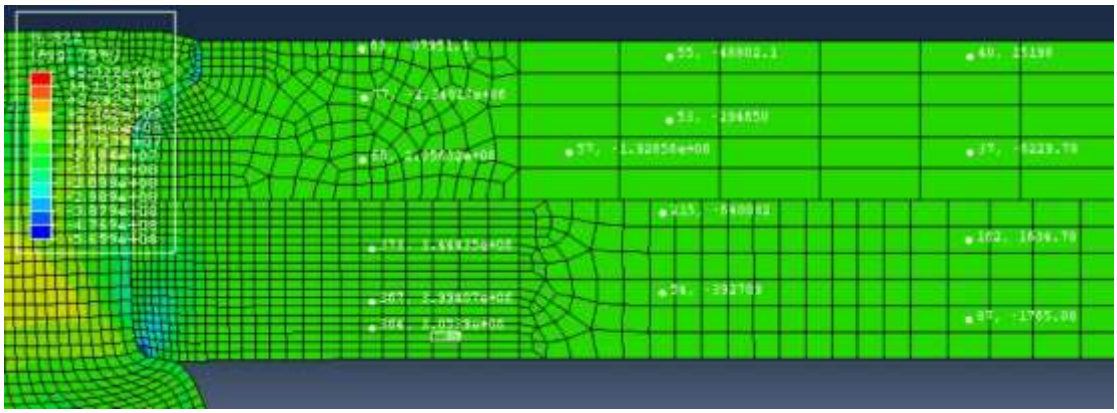

b: Axial

c: Hoop

Figure 5.12. Stress distributions within regions ‘E’ and ‘G’ of the ‘Model 2 QS’ stackup. a: Radial Stress, b: Axial Stress, c: Hoop Stress

Referring to figure 5.13a, logarithmic radial strain distribution within regions ‘E’ and ‘G’ of Model-2 QS simulation is shown. The radial strain is compressive and has small magnitude across regions ‘E’ and ‘G’. The magnitude decreases with increasing distance from the rivet axis.

Referring to figure 5.13b, logarithmic axial strain distribution within regions ‘E’ and ‘G’ of Model-2 QS simulation is shown. The axial strain is tensile in some areas and compressive in other areas. But it has small magnitude across regions ‘E’ and ‘G’.

Referring to figure 5.13c, logarithmic hoop strain distribution within regions ‘E’ and ‘G’ of Model-2 QS simulation is shown. The hoop strain is tensile and has small magnitude across regions ‘E’ and ‘G’. The magnitude decreases with increasing distance from rivet axis.

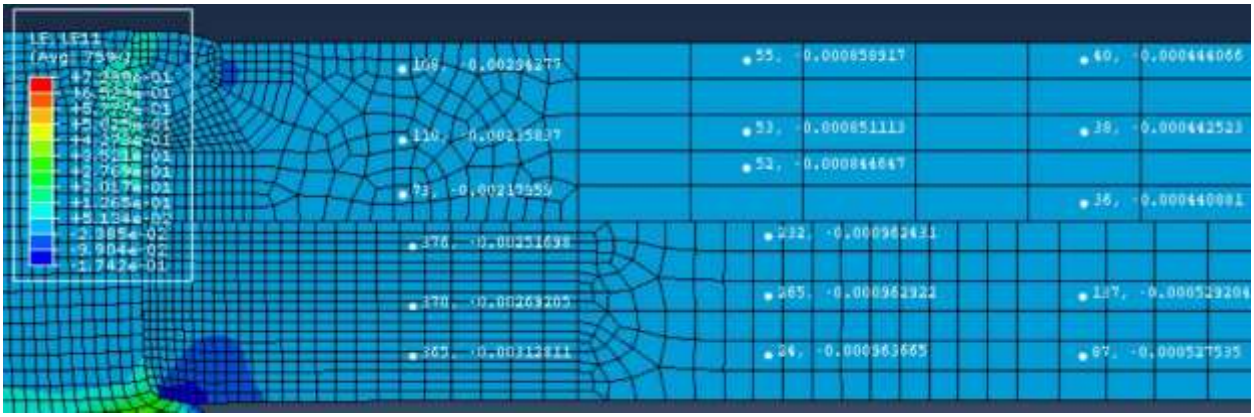

a: Radial

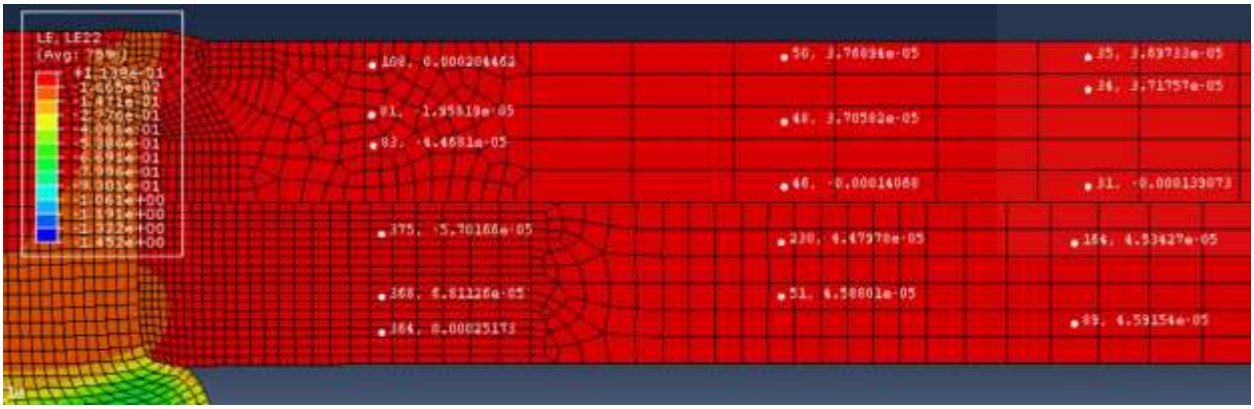

b: Axial

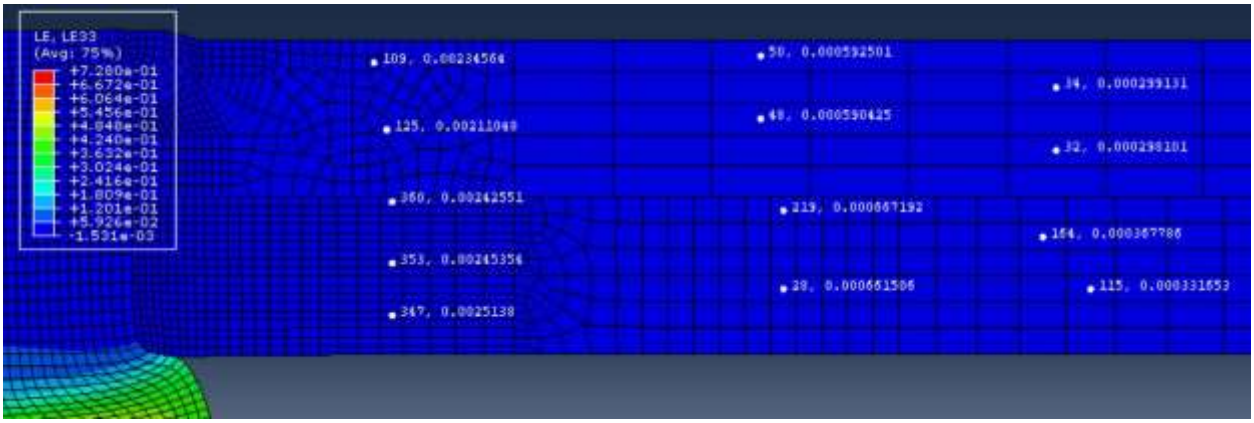

c: Hoop

Figure 5.13. Strain distributions within regions ‘E’ and ‘G’ of the ‘Model 2 QS’ stackup. a: Radial Strain, b: Axial Strain, c: Hoop Strain

Referring to figure 5.14a, radial stress distribution within region ‘F’ of Model-2 QS simulation is shown. Radial stress is compressive across region ‘F’. Magnitude is higher in the area of region ‘F’ adjacent to head of the rivet button.

Referring to figure 5.14b, axial stress distribution within region ‘F’ of Model-2 QS simulation is shown. Axial stress is compressive in area of region ‘F’ adjacent to the rivet shank near the head of the rivet button. Stress is also compressive in some interior areas of region 'F'. Tensile stresses are found adjacent to the rivet shank near the top of region 'F' and in some interior areas of region ‘F’.

Referring to figure 5.14c, hoop stress distribution within region ‘F’ of Model-2 QS simulation is shown. Hoop stress is compressive across region ‘F’. There is small area of tensile hoop stress at the top of region 'F' adjacent to region 'D'.

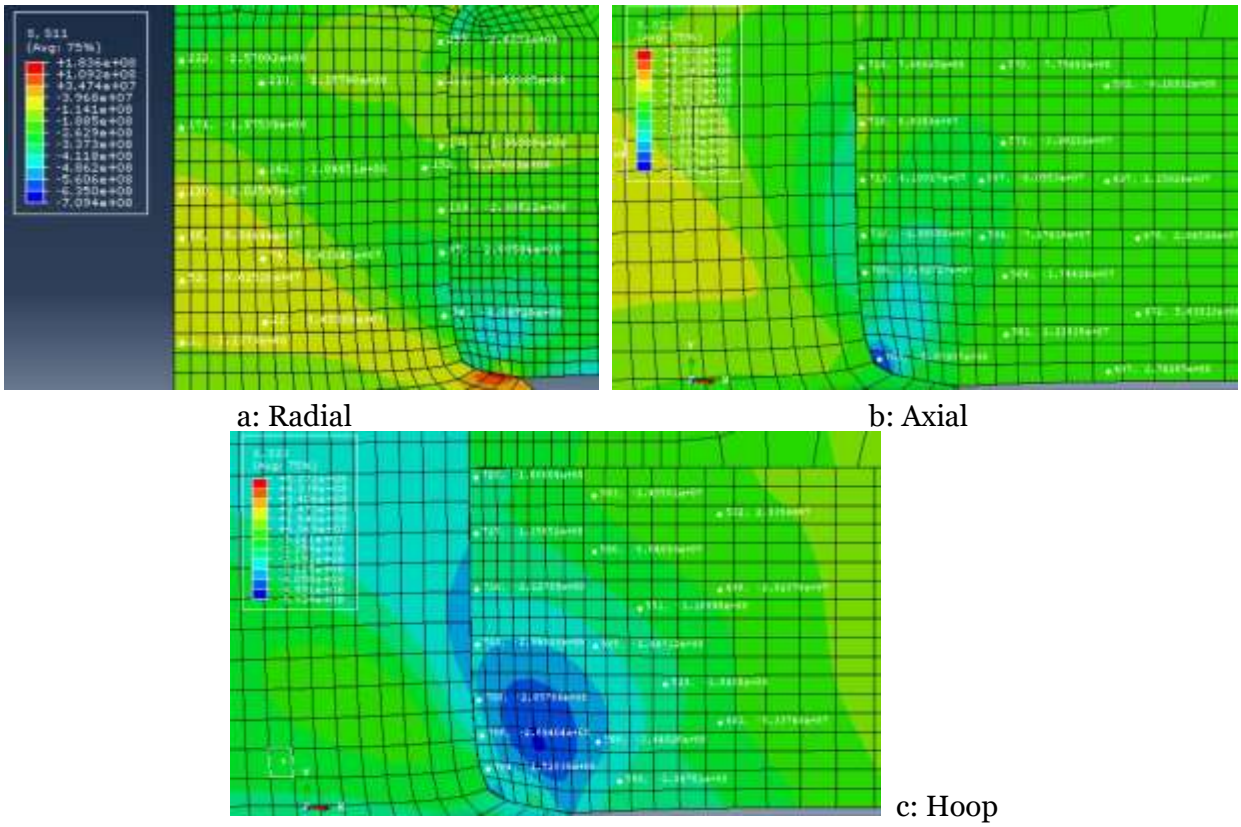

a: Radial b: Axial

c: Hoop

Figure 5.14. Stress distributions within region ‘F’ of the ‘Model 2 QS’ stackup. a: Radial Stress, b: Axial Stress, c: Hoop Stress

Referring to figure 5.15a, logarithmic radial strain distribution within region ‘F’ of Model-2 QS simulation is shown. Radial strain is compressive across region ‘F’ except near the rivet shank. The magnitude is higher near the head of the rivet button compared to other areas in region ‘F’.

Referring to figure 5.15b, logarithmic axial strain distribution within region ‘F’ of Model-2 QS simulation is shown. Axial strain is compressive near the rivet shank. It is tensile in the interior of region 'F'. The magnitude is higher near the head of the rivet button compared to other areas in region ‘F’.

Referring to figure 5.15c, logarithmic hoop strain distribution within region ‘F’ of Model-2 QS simulation is shown. Hoop strain is tensile across region ‘F’. The magnitude is higher near the head of the rivet button compared to other areas in region ‘F’.

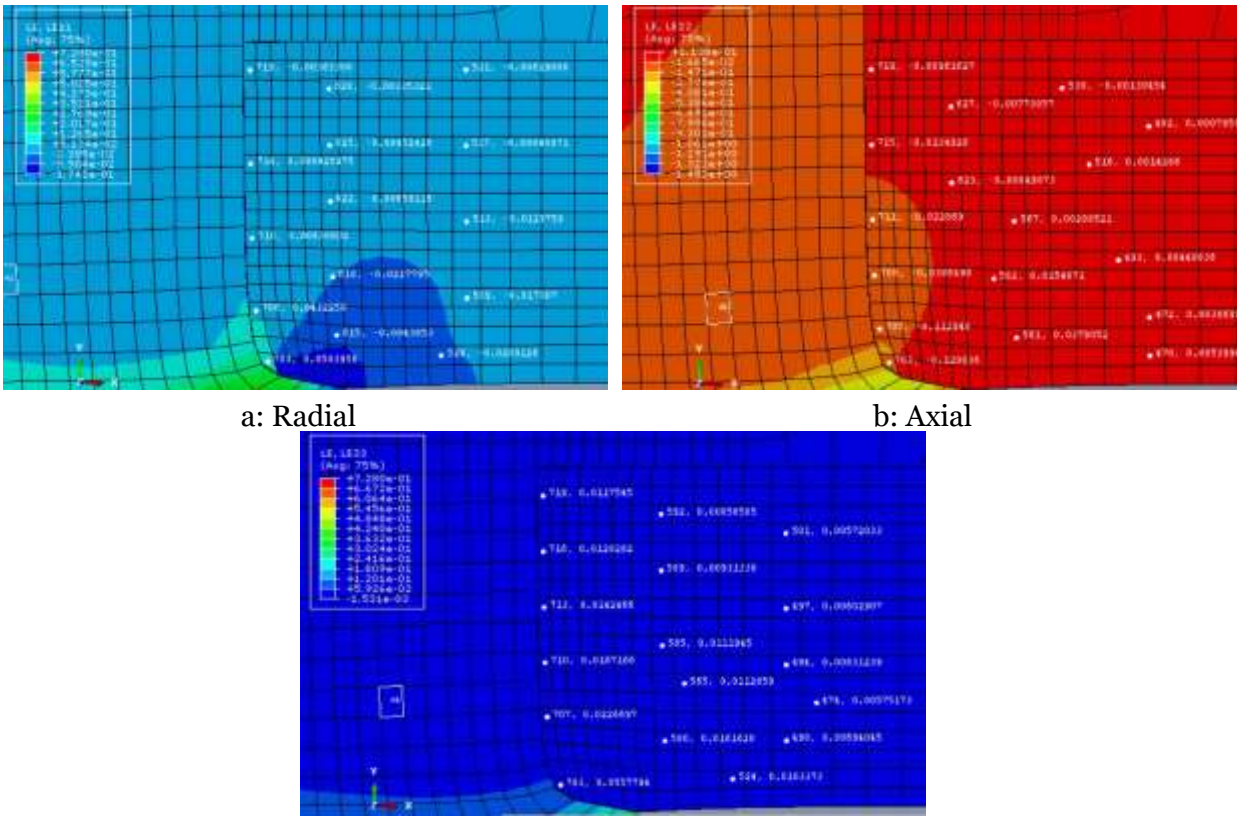

a: Radial b: Axial

c: Hoop

Figure 5.15. Strain distributions within region ‘F’ of the ‘Model 2 QS’ stackup. a: Radial Strain, b: Axial Strain, c: Hoop Strain

Measurements of residual stresses and strains were made at various skin-skin interface and skin-rivet interface element nodes. These interfaces are shown in figure 5.16. First interface is the inner skin region adjacent to the rivet (denoted by 'IR'). X-coordinate is normalized with respect to radius of rivet shank (R_{rivet}). Y-coordinate is normalized with respect to length of rivet shank (L_{shank}). Y-coordinate of IR ranges from 0.55 to 0.77. Second is the inner skin region adjacent to the outer skin (denoted by 'IO'). X-coordinate of IO ranges from 1 to 25. Third is the outer skin region adjacent to the rivet (denoted by 'OR'). Y-coordinate of OR ranges from 0.77 to 1. Fourth is the outer skin region adjacent to the inner skin (denoted by 'OI'). X-coordinate of OI ranges from 1 to 25. Fifth is the rivet region adjacent to the rivet hole which spans both the inner skin's hole region and the outer skin's hole region (denoted by 'RH'). Y-coordinate of RH ranges from 0.3 to 1. In the following plots 'epsilon11', 'epsilon22' and epsilon33' refer to radial strain, axial strain and hoop strain respectively; and 'sigma11', 'sigma22' and sigma33' refer to radial stress, axial stress and hoop stress respectively.

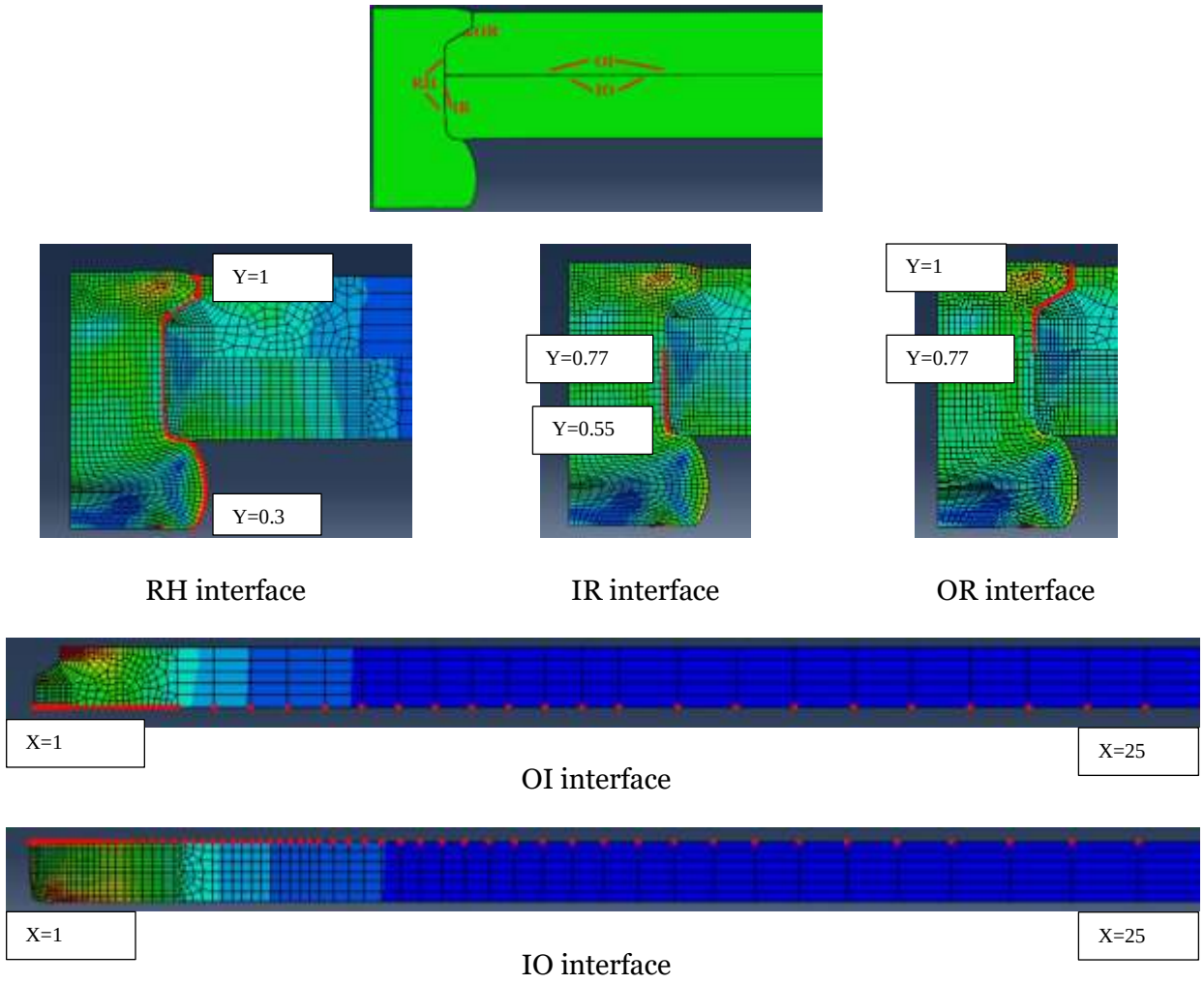

Figure 5.16. Interface residual stresses/strains measurement locations. Measurements were made at the interface nodes (highlighted nodes shown in red).

Referring to figures 5.17 and 5.18, the IR interface residual stress and logarithmic strain distributions are shown. Between normalized Y=0.55 and Y=0.57, the radial strain is positive. Between Y=0.57 and Y=0.77, the radial strain is small in magnitude and both positive and negative. Between normalized Y=0.55 and Y=0.67, the axial strain is negative. Between Y=0.67 and Y=0.77, the radial strain is small in magnitude and both positive and negative. Between Y=0.55 and Y=0.77, the hoop strain is positive. Between Y=0.55 and Y=0.77, the radial stress is

compressive. Between Y=0.55 and Y=0.65, the axial stress is compressive. Between Y=0.65 and Y=0.77, the axial stress is tensile. Between Y=0.55 and Y=0.77, the hoop stress is compressive.

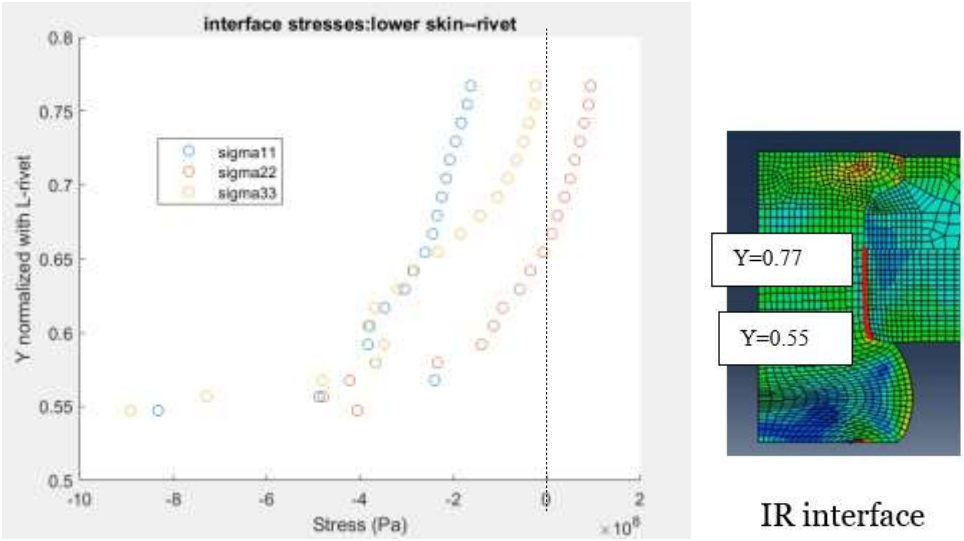

Figure 5.17. Stress distributions within IR interface. Model-2 QS: Chapter 5 quasi-static simulation. X-axis: Pa, Y-axis: non-dimensional.

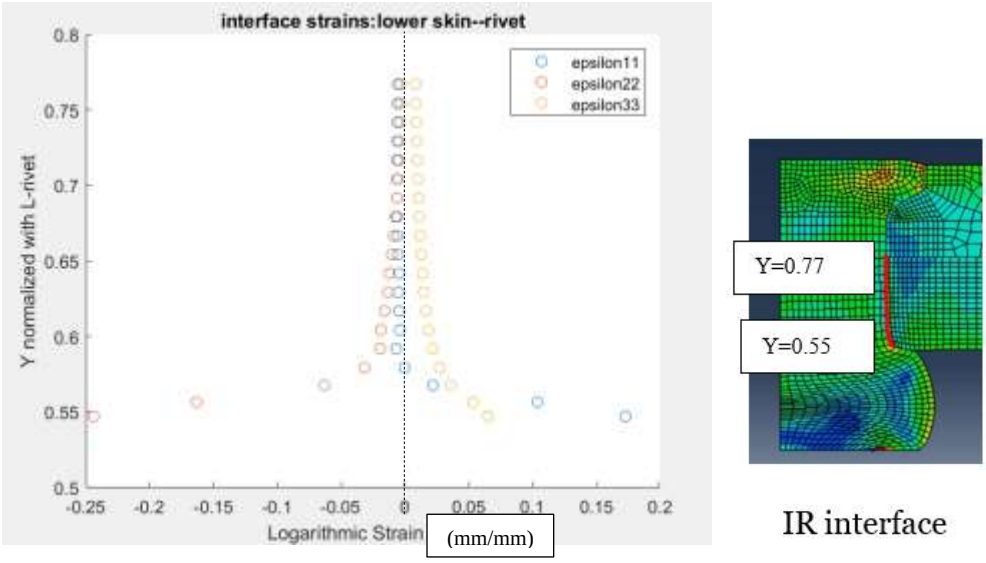

Figure 5.18. Strain distributions within IR interface. Model-2 QS: Chapter 5 quasi-static simulation. X-axis: mm/mm, Y-axis: non-dimensional.

Referring to figures 5.19 and 5.20, the IO interface residual stress and logarithmic strain distributions are shown. The radial strain is negative throughout the IO domain. The axial strain is negative or small in magnitude and positive throughout the IO domain. The hoop strain is positive over the entire IO domain. The residual radial stress is compressive throughout the IO domain. At the hole interface around normalized X=1.0, the axial stress is tensile. At around X=2.0, the axial stress becomes small in magnitude and compressive but becomes small and tensile around X=3.0 and remains like that for the rest of the distribution. At the hole interface around normalized X=1.0, the hoop stress is compressive. The hoop stress becomes tensile around X=3.0 and starts reducing in magnitude thereafter. Starting around X=7.0, it remains small and tensile.

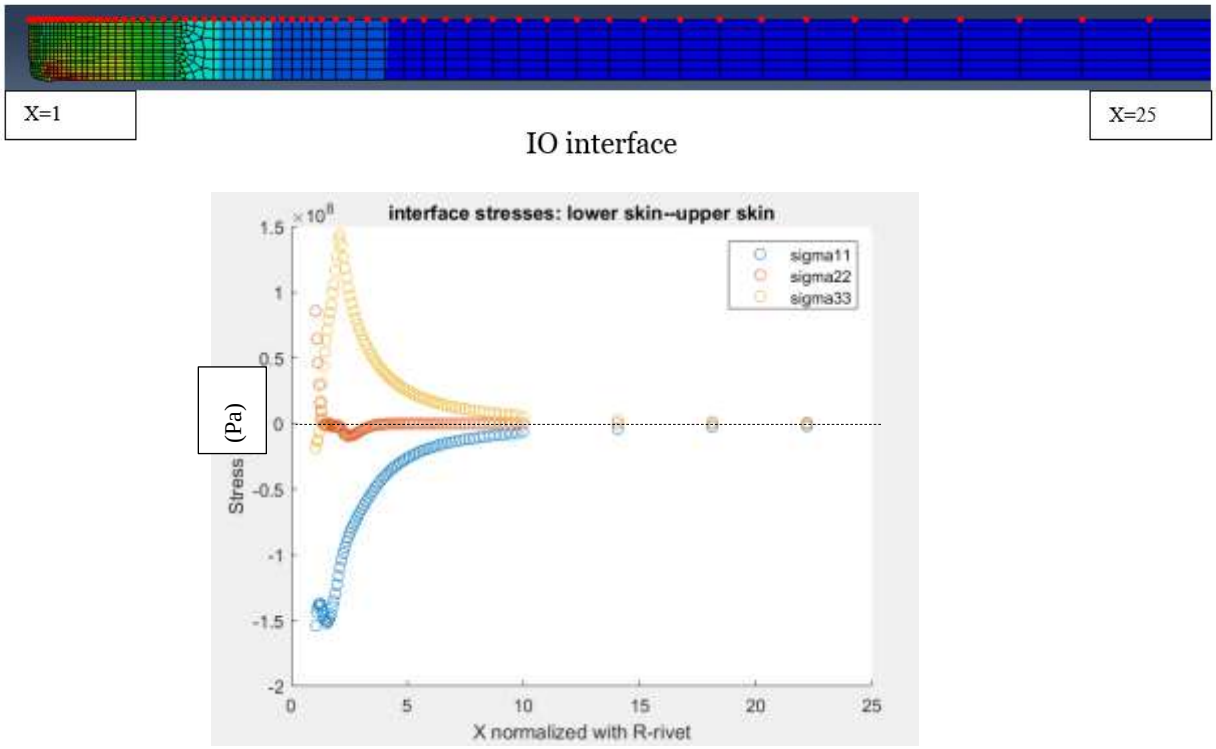

Figure 5.19. Stress distributions within IO interface. Model-2 QS: Chapter 5 quasi-static simulation. X-axis: non-dimensional, Y-axis: Pa.

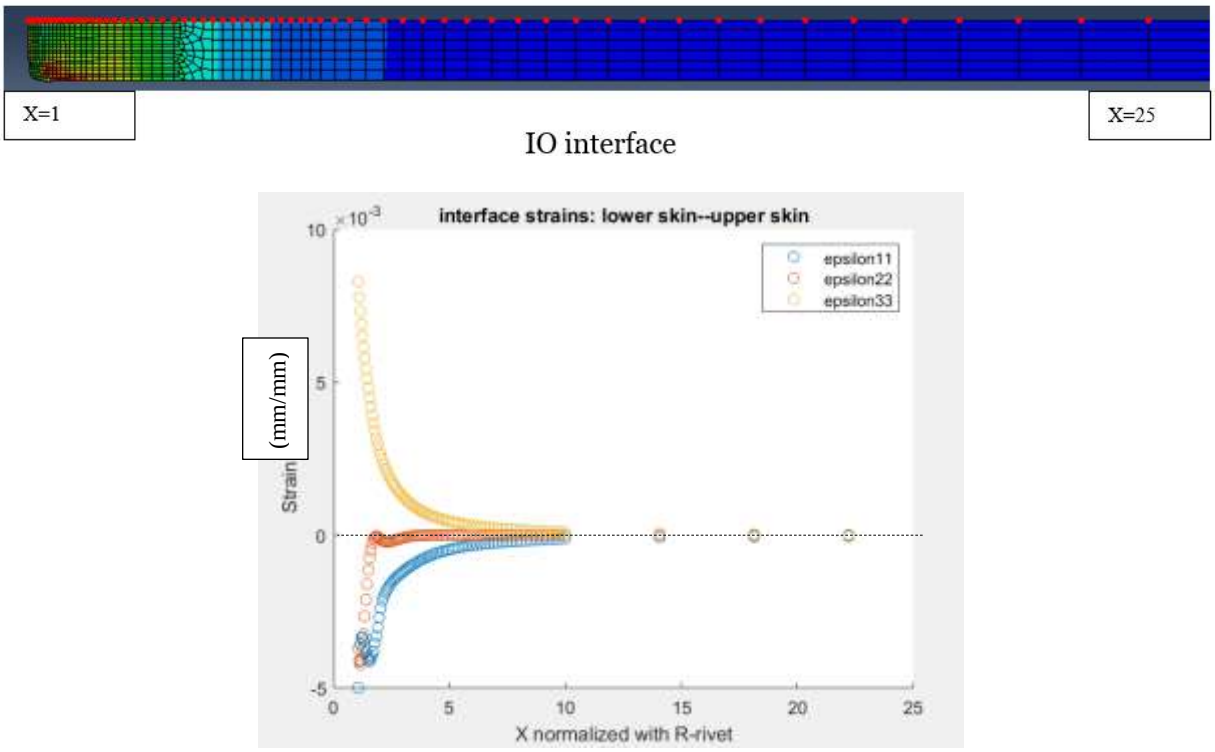

Figure 5.20. Strain distributions within IO interface. Model-2 QS: Chapter 5 quasi-static simulation. X-axis: non-dimensional, Y-axis: mm/mm.

Referring to figures 5.21 and 5.22, the OR interface residual stress and logarithmic strain distributions are shown. Between Y=0.87 and Y=0.90, the radial strain is positive. It is negative everywhere else between Y=0.77 and Y=1.0. The axial strain is negative between Y=0.77 and Y=0.92. The strain is positive everywhere between Y=0.92 and Y=1.0 except it is negative around Y=0.93.

The hoop strain is positive everywhere between Y=0.77 and Y=1.0. The radial stress is compressive everywhere in the OR domain except at Y=0.93. There are many inflections in the axial stress profile in the OR domain between Y=0.77 and Y=1.0. The hoop stress is compressive everywhere in the OR domain except around Y=0.94 and Y=1.0.

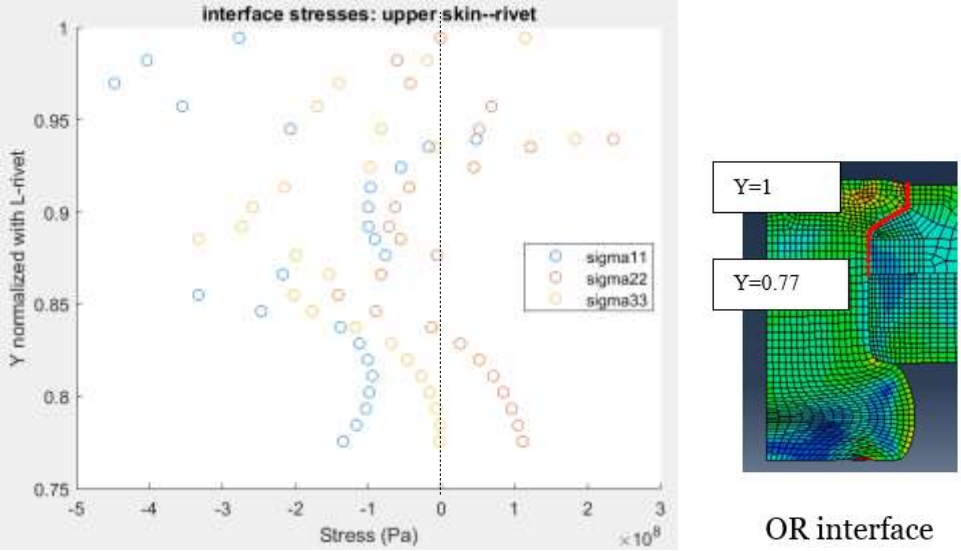

Figure 5.21. Stress distributions within OR interface. Model-2 QS: Chapter 5 quasi-static simulation. X-axis: Pa, Y-axis: non-dimensional.

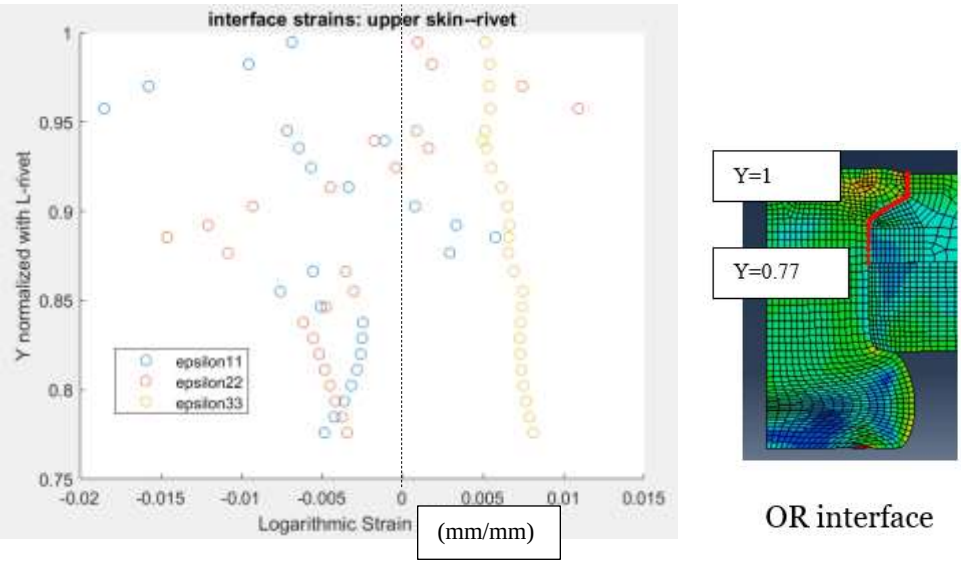

Figure 5.22. Strain distributions within OR interface. Model-2 QS: Chapter 5 quasi-static simulation. X-axis: mm/mm, Y-axis: non-dimensional.

Referring to figures 5.23 and 5.24, the OI interface residual stress and logarithmic strain distributions are shown. The radial strain is negative over the entire OI domain. The axial strain is also negative throughout the OI domain. The hoop strain is positive over the entire OI domain.

The radial stress is compressive across the entire OI domain. The axial stress is tensile at the hole interface near normalized X=1.0. But it becomes compressive at X=3.0. Beyond X=3.0 and for the rest of the OI domain, the axial stress becomes small in magnitude and compressive. The hoop stress is compressive at the hole interface near normalized X=1.0. But it becomes tensile at X=3.0. Beyond X=3.0 and for the rest of the OI domain, the axial stress becomes small in magnitude and tensile.

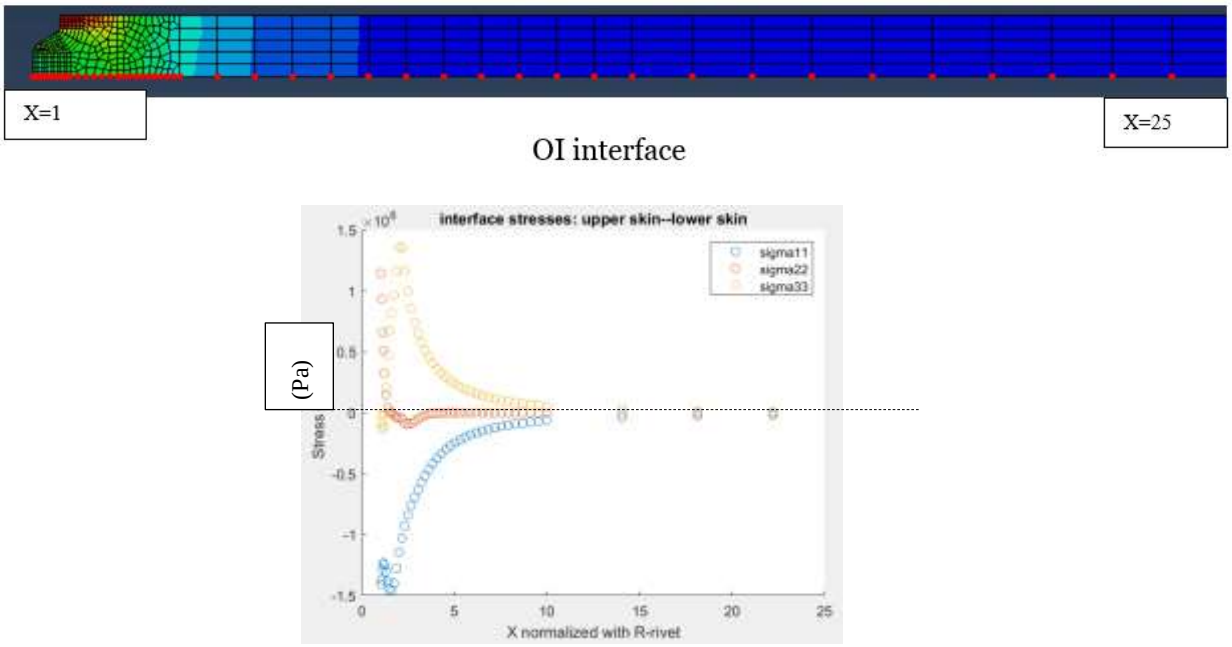

Figure 5.23. Stress distributions within OI interface. Model-2 QS: Chapter 5 quasi-static simulation. X-axis: non-dimensional, Y-axis: Pa.

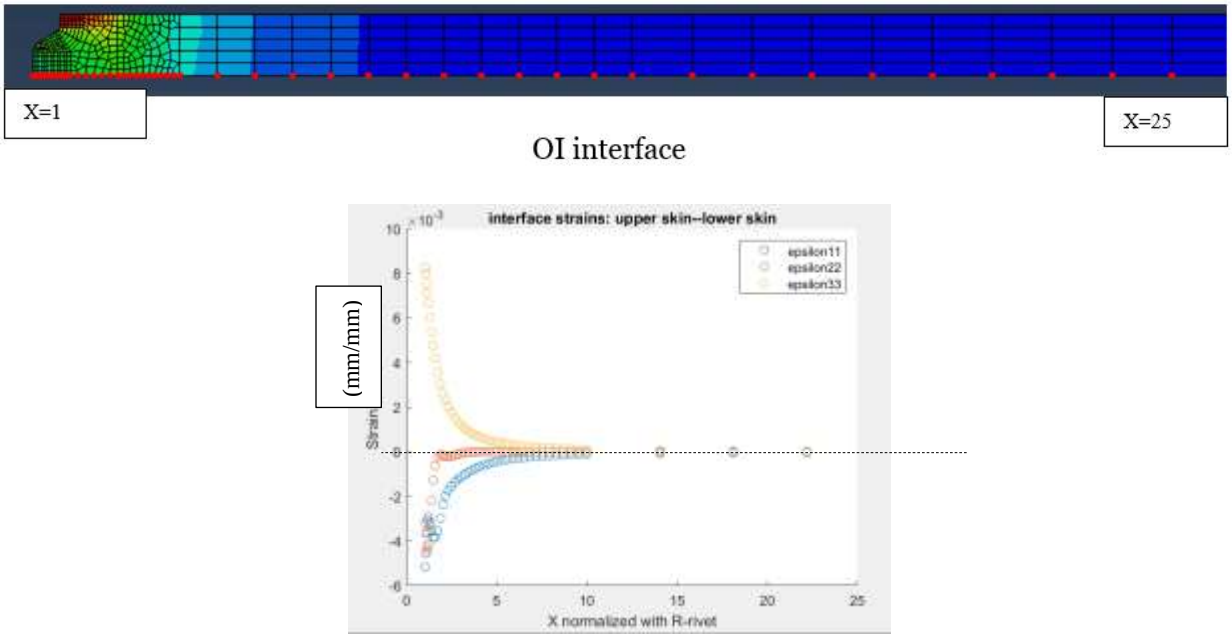

Figure 5.24. Strain distributions within OI interface. Model-2 QS: Chapter 5 quasi-static simulation. X-axis: non-dimensional, Y-axis: mm/mm.

Referring to figures 5.25 and 5.26, the RH interface residual stress and logarithmic strain distributions are shown. Between normalized Y=0.3 and Y=0.55, the residual logarithmic radial strain is negative or small and positive. At Y=0.55, there is an inflection which coincides with the head of the rivet button. Here the strain becomes positive and remains until Y=0.9. Between normalized Y=0.9 to Y=1.0, it is small and negative.

Between normalized Y=0.3 and Y=0.9, the residual logarithmic axial strain is negative. Between normalized Y=0.9 and Y=1.0, it is small and positive. Between Y=0.3 and Y=1.0, the residual logarithmic hoop strain is positive.

Except at Y=0.55 and Y=0.85, the residual radial stress is compressive. The residual axial stress varies between compressive and tensile between Y=0.3 and Y=1.0. The residual hoop stress distribution also varies between compressive and tensile between Y=0.3 and Y=1.0.

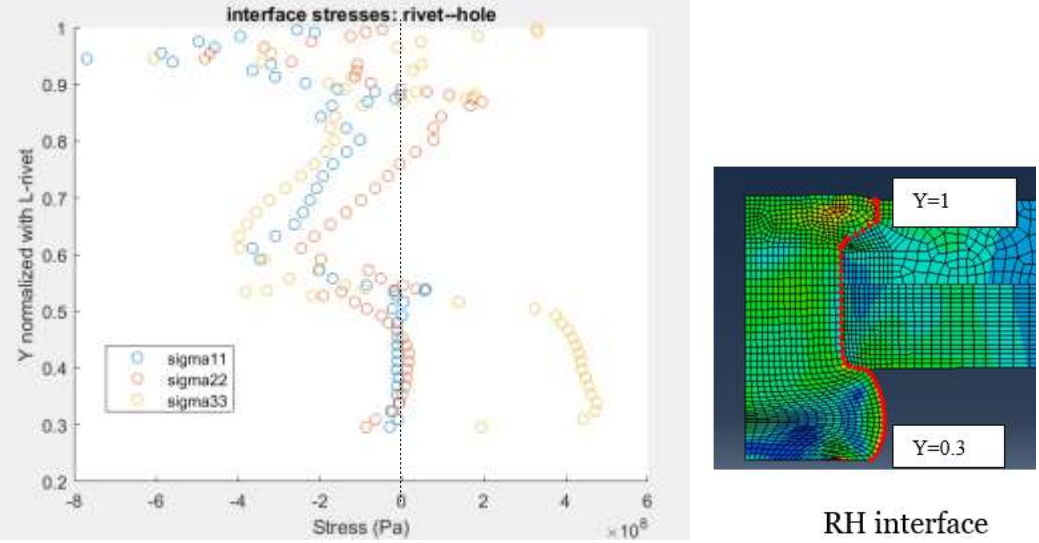

Figure 5.25. Stress distributions within RH interface. Model-2 QS: Chapter 5 quasi-static simulation. X-axis: Pa, Y-axis: non-dimensional.

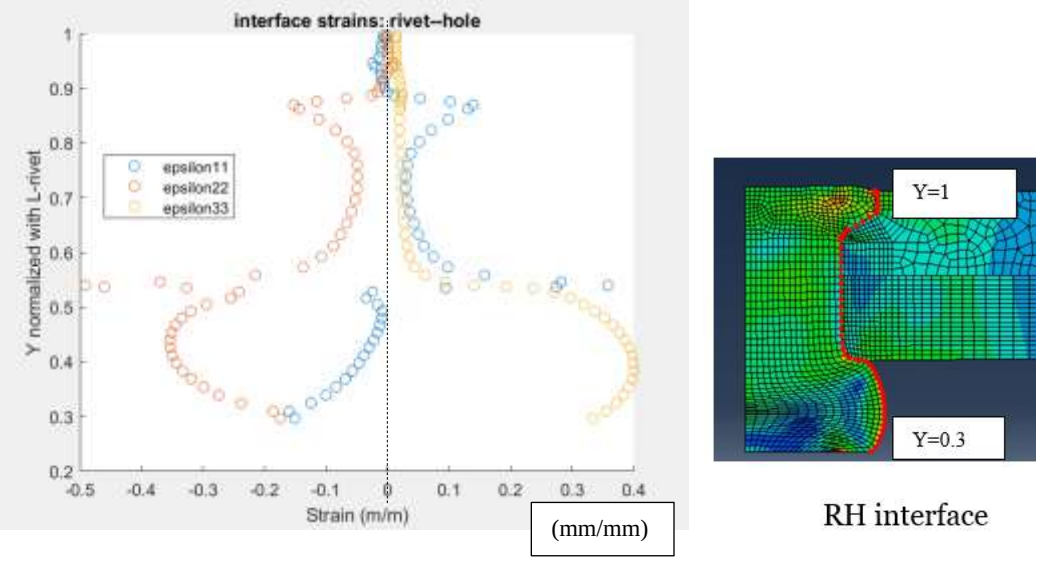

Figure 5.26. Strain distributions within RH interface. Model-2 QS: Chapter 5 quasi-static simulation. X-axis: mm/mm, Y-axis: non-dimensional.

The Von-Mises (V-M) stress in this simulation is a measure of the flow stress at any mesh element under consideration. Stress components can be compared to the V-M stress to evaluate the possibility of crack nucleation. D_b should typically be between 1.4d-1.6d for a joint of good quality. From table 5.2, D_b is 1.48d. All 2425 mesh elements in the FE model were considered and the mesh elements with the *highest stress component magnitudes* were extracted in figure 5.27.

Component	Stress	V-M Stress	Stress/V-M
radial (11)	(Pa)	(Pa)	
Riv 225 pa-SI-1 730	1.87E+08	2.40E+08	0.78
Riv 225 pa-SI-1 1020	-7.49E+08	6.06E+08	-1.24
axial (22)			
Riv 225 pa-SI-1 715	5.02E+08	6.88E+08	0.73
D226 lower pa-1 703	-5.66E+08	3.45E+08	-1.64
hoop (33)			
Riv 225 pa-SI-1 596	5.28E+08	5.36E+08	0.99
Riv 225 pa-SI-1 911	-6.30E+08	5.55E+08	-1.13
shear (12)			
Riv 225 pa-SI-1 734	2.53E+08	5.04E+08	0.50
Riv 225 pa-SI-1 273	-3.58E+08	6.25E+08	-0.57

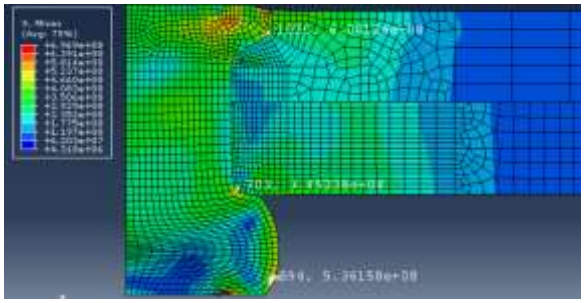

Figure 5.27. Data for Joint Quality Analysis

Highest compressive ratio of stress component/V-M stress in the entire FE mesh is exhibited by mesh element 703 of the inner skin and it is -1.64. This element is located just above the rivet button and is part of region 'F'. Mesh element 1020 of the rivet has the highest compressive stress component of -749 MPa. This element is located just above the rivet wedge and is part of region 'A'. Mesh element 596 of the rivet has the highest tensile ratio of stress component/V-M stress (0.99) and highest tensile stress component (528 MPa). This element is located at the free surface of the rivet button and can be neglected from crack nucleation perspective.

Due to the high (stress/V-M) ratio value of element 703 of inner skin and due to the high magnitude of radial stress of element 1020 of the rivet, these two mesh locations are most critical for crack nucleation because of compression-induced shear. Element 703 of inner skin is more critical than element 1020 of the rivet because of the higher (stress/V-M) ratio (-1.64 vs. -1.24).

5.4 SUMMARY

Two-dimensional quasistatic squeeze riveting FE model was built and simulated. Residual stress and strain results from the simulation were presented and discussed. High magnitude of compressive radial and hoop stresses were observed at the interface between the rivet and the rivet hole. Compressive axial stress was observed at the rivet-upper skin interface at the rivet wedge and the rivet-inner skin interface at the rivet button. Inner skin region adjacent to the rivet button was observed to be most critical location for crack nucleation by compression-induced shearing.

Chapter 6. PARTIAL DYNAMIC MODEL DESIGN AND RESULTS

6.1 INTRODUCTION

In this chapter, FE modeling and analysis of a two-dimensional, percussive riveting model with rivet hammer side fixed is presented and discussed. Because the *rivet hammer side is fixed, energy for rivet deformation is provided by a movable bucking bar. This model is termed as "Partial Dynamic" because the rivet hammer side is held fixed.* In the percussive riveting process, both rivet hammer and bucking bar are movable. It is the next step toward achieving a two-dimensional, full dynamic percussive riveting FE model where both hammer and bucking bar can move. Figure 6.1 shows the strain rate ranges corresponding to various dynamic events.

This work is focused on modeling an unstiffened stack-up as described in section 4.2 and a sample of workfloor implementation is shown in figure 6.2. It is a cold-forming process. The strain rate of this impact event is around 400/s to 1000/s. This causes the rivet material to work harden.

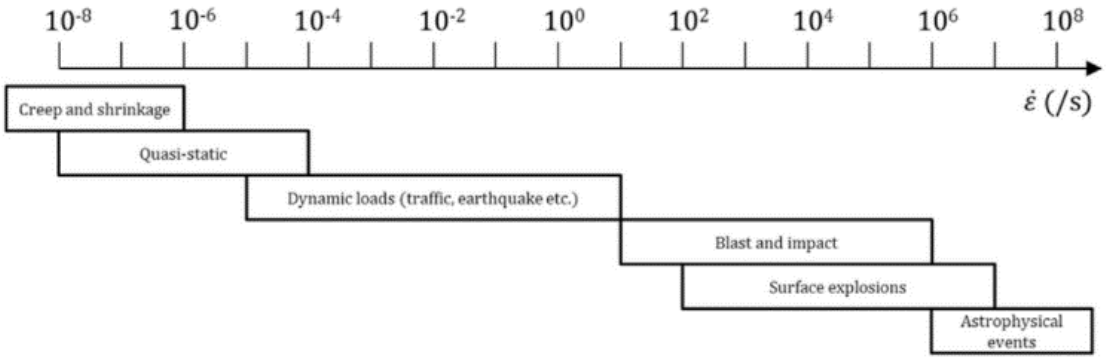

Figure 6.1. Strain rate ranges of dynamic events.

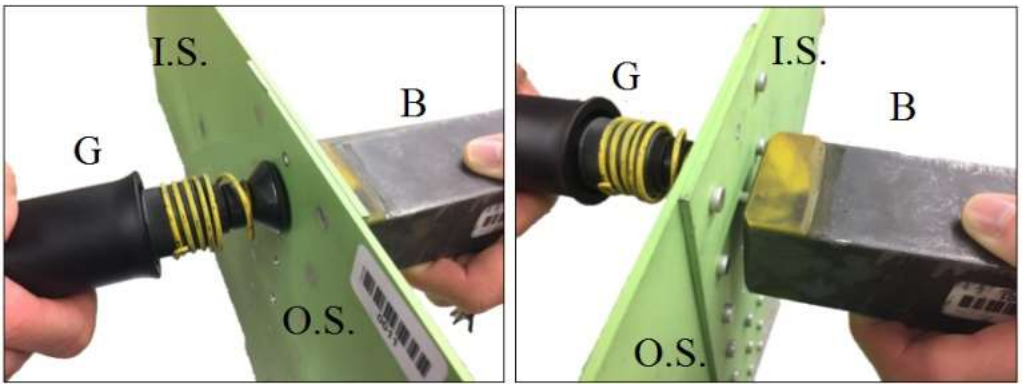

Figure 6.2. Unstiffened stack-up percussive riveting, figure from [Ahn, 4]. G: Percussive Pneumatic Gun, B: Bucking Bar, I.S.: Inner Skin, O.S.: Outer Skin

6.2 Additional Modeling Information

Modeling information of the two-dimensional partial dynamic percussive riveting process has been presented in section 4.2. The partial dynamic percussive riveting process is an intermittent process with a rapid succession of loading and unloading events. The same amount of energy is imparted to the rivet in each hit of the bucking bar. Two simulations were conducted. One with an impact energy of 15 J that will be referred to as "model 1 Dyn" and the other one is a quasistatic simulation that will be referred to as "model 1 QS". D_{shank} is 0.223". It is of interest to study the magnitudes and distributions of the residual stresses and strains after the completion of the riveting process. μ is 0.2 between rivet and sheet surfaces. μ is 0.2 between bucking bar/ rivet die and stackup surfaces. Stick-slip maximum shear stress limit of 269.62 MPa was used.

6.3 Results and Discussion

Since, the modeling effort begins with an axisymmetric condition, it is vital to note that there is no deviation of the hammer, mass or the bucking bar along the X-axis during the simulation. All action takes place along the symmetry axis (Y-axis) of the assembly. In an axisymmetric simulation, both the loading (traction) boundary condition *and* the geometric (displacement) boundary condition must be symmetric. If the components are placed asymmetrically or if the loading does not coincide with axis of symmetry, traction and displacement boundary conditions

no longer remain symmetric. As a result, complicated (and realistic) loading conditions transpire. Axisymmetric analysis is no longer possible under these conditions. A three-dimensional modeling and analysis effort is required. Three-dimensional modeling is discussed in chapter 9.

In the axisymmetric model development, no thickness is prescribed to the mesh elements. It is not required. The biggest issue with studying the percussive riveting process or any other riveting process is the inability to monitor what happens at the rivet- hole interface. Strain gages are placed on the skins at a reasonably close distance from the hole axis [Li, 38]. Consequently, there is some loss in accuracy in these experimental methods. When sectioning riveted joint samples for microstructure study or DIC study, there is a release of stored strain energy. Therefore, actual magnitude of the strain is not observed. This simulation study aims to address this deficiency, especially for the percussive riveting process. Stress and strain distributions were observed across seven regions (regions A through G) as shown in figure 6.3. In figure 6.3, radial gap (circled in yellow) is shown in the 'Model 1 Dyn' stackup between the rivet and the outer skin.

Referring to table 6.1, we can see that R1-R4 of model 1 QS is greater than R1-R4 of model 1 Dyn. This indicates that there is greater radial expansion of rivet material in model 1 QS compared to model 1 Dyn. The button radius of model 1 QS is lesser than that of model 1 Dyn and the button height of model 1 QS is greater than that of model 1 Dyn. The button radius and height indicate that the button is marginally better formed in model 1 Dyn compared to model 1 QS which aids in improving the fatigue strength. In figure 6.3, a radial gap is found between the rivet shank and the non-countersunk region of the outer skin in model 1 Dyn simulation. This indicates poor material filling in the area. This happens because impact energy is imparted by the bucking bar.

Table 6.1. Normalized geometric attribute measurements. R1 is normalized with R_{crown}; R2, R3, R4 and R_b are normalized with R_{shank}; H_b is normalized with L_{rivet}

Material	R_1	R_2	R_3	R_4	R_B	H_B
Model 1 QS	1.013	1.022	1.023	1.063	1.476	0.244
Model 1 Dyn	1.011	1.017	1.017	1.052	1.49	0.239

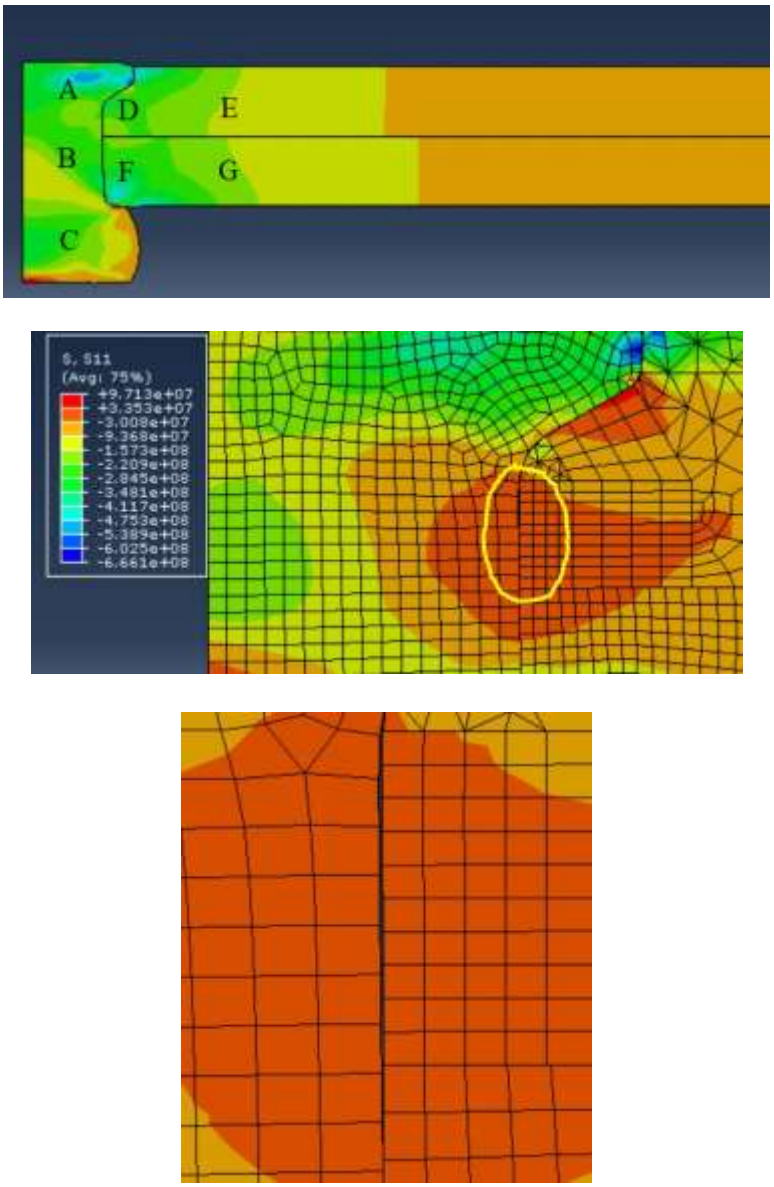

Figure 6.3. Deformed stackup data regions: A- Rivet crown, B- Rivet shank, C- Rivet button, D- Outer Skin adjacent to rivet, E- Outer Skin away from rivet, F- Inner Skin adjacent to rivet, G- Inner Skin away from rivet. Radial Gap (circled in yellow) is found in the 'Model 1 Dyn' stackup between the rivet and the outer skin.

Referring to figure 6.4a, radial stress distribution of region 'A' is shown. All stress and strain data were obtained from the mesh element integration points. For instance, radial stress at integration point# 950 is -223.2 MPa. Radial stress is compressive (~ 630 MPa) adjacent to the

outer skin crown region. It is also compressive near the rivet axis (~ 123 MPa) and in the interior of the rivet button (~ 250 MPa).

Referring to figure 6.4b, axial stress distribution of region 'A' is shown. Axial stress is compressive adjacent to the outer skin crown region (~ 454 MPa). Axial stress magnitude is small near the rivet axis (~ 29 MPa). Stress is found to be either tensile or compressive here. In the interior of the rivet crown, axial stress magnitude is low (~ 70 MPa). There are regions of compressive axial stress and tensile stress in the interior of the rivet crown.

Referring to figure 6.4c, hoop stress distribution of region 'A' is shown. Hoop stress is tensile (~ 500 MPa) at the base of rivet crown at the countersunk region. It is compressive adjacent to the crown region of the outer skin (~ 193 MPa). Hoop stress is tensile near the wedge region (~ 150 MPa) and it is compressive in the interior of the rivet crown (~ 368 MPa) and near the rivet axis (~ 155 MPa).

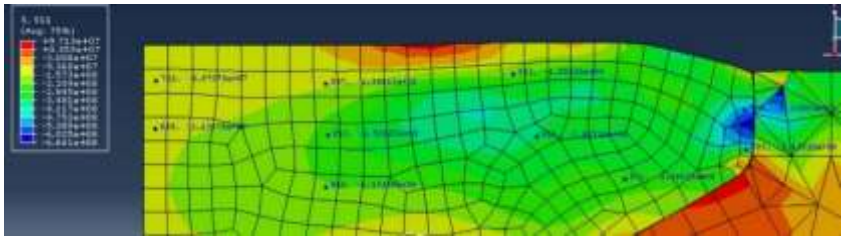
a: Radial


b: Axial

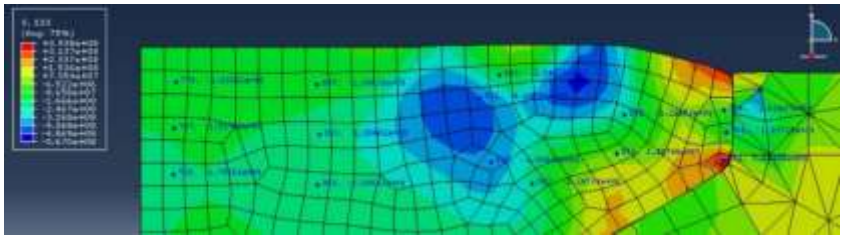
c: Hoop

Figure 6.4. Stress distributions within region 'A' of the 'Model 1 Dyn' stackup. a: Radial Stress, b: Axial Stress, c: Hoop Stress

Referring to figure 6.5a, logarithmic radial strain distribution of region 'A' is shown. Static yield strength of rivet material is 467 MPa and Young's Modulus is 71.7 GPa. This gives an equivalent strain at initial yield of 0.0065. It is seen that the strain is compressive in the rivet crown adjacent to the outer skin crown region (~ 0.014) and adjacent to the wedge region (~ 0.007). In the interior of the rivet crown, there is a band (green color) of tensile strain of higher magnitude (~ 0.067). Between the rivet axis and the band of tensile strain, the strain magnitude is small (< 0.0022).

Referring to figure 6.5b, logarithmic axial strain distribution of region 'A' is shown. Small strain magnitude (~ 0.002) is observed near the rivet axis where material yielding has not taken place. In this region, strain is tensile. Compressive axial strain is found near the outer skin crown region (~ 0.003) and wedge region (~ 0.007). There is a band of compressive axial strain (yellow color) in the interior of the rivet crown (~ 0.1).

Referring to figure 6.5c, logarithmic hoop strain distribution of region 'A' is shown. Small strain magnitude is observed closer to the rivet axis (< 0.001). In the interior of the rivet crown, the strain magnitude increases (~ 0.015), and the strain is tensile in nature. In the region of the rivet adjacent to the outer skin crown region, strain is tensile (~ 0.012).

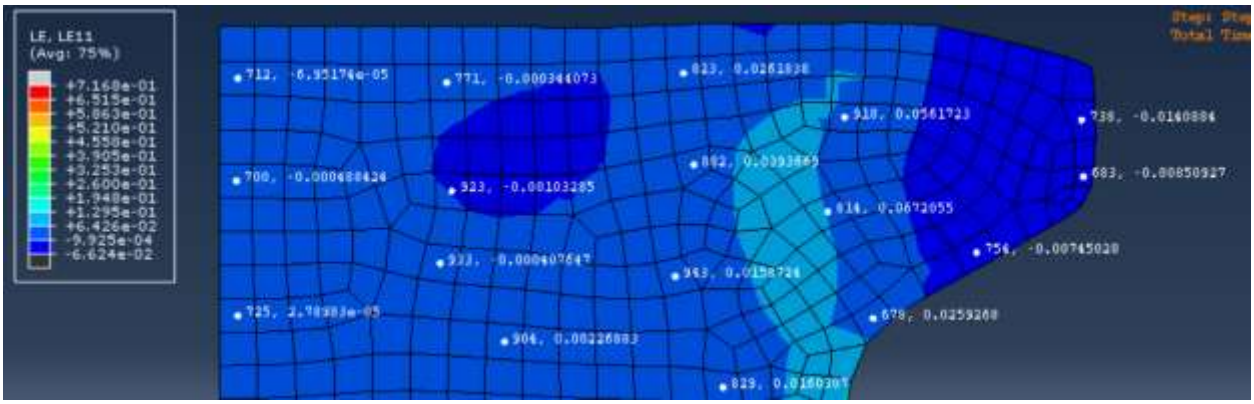

a: Radial

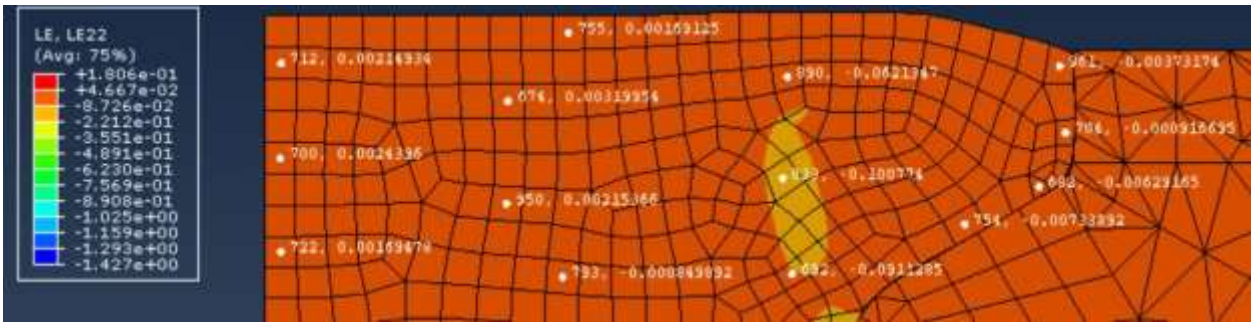

b: Axial

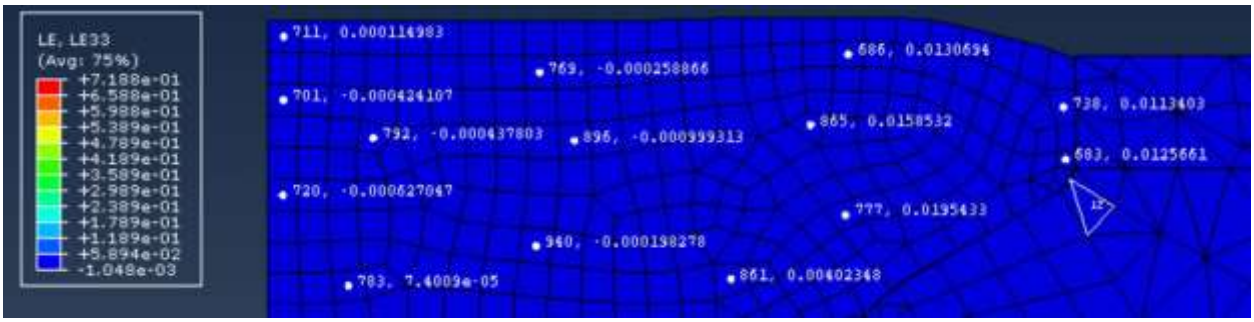

c: Hoop

Figure 6.5. Strain distributions within region 'A' of the 'Model 1 Dyn' stackup. a: Radial Strain, b: Axial Strain, c: Hoop Strain

Referring to figure 6.6a, radial stress distribution of region 'B' is shown. Radial stress is compressive in the region near the base of the rivet crown and rivet axis (~ 175 MPa). It becomes tensile near the head of the rivet button and the rivet axis (~ 63 MPa). It has a small magnitude

at the base of the rivet crown near the outer skin interface where the radial gap was found (~ 20 MPa). It is compressive and of a larger magnitude (~ 424 MPa) near the head of the rivet button at the inner skin interface.

Referring to figure 6.6b, axial stress distribution of region 'B' is shown. Axial stress is compressive in the region near the base of the rivet crown and rivet axis (~ 173 MPa). It becomes tensile near the head of the rivet button and the rivet axis (~ 267 MPa). It is tensile at the base of the rivet crown near the outer skin interface where the radial gap was found (~ 140 MPa). It is compressive near the head of the rivet button at the inner skin interface (~ 300 MPa).

Referring to figure 6.6c, hoop stress distribution of region 'B' is shown. Hoop stress is compressive in the region near the base of the rivet crown and rivet axis (~ 228 MPa). It becomes tensile near the head of the rivet button and the rivet axis (~ 76 MPa). It is tensile and small magnitude (~ 2 MPa) at the base of the rivet crown near the outer skin interface where the radial gap was found. It is compressive near the head of the rivet button at the inner skin interface (~ 413 MPa).

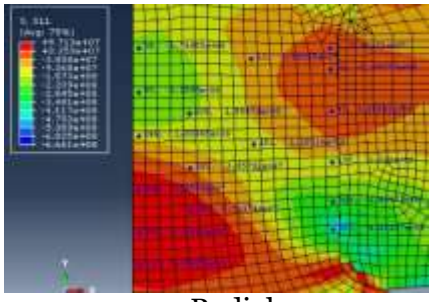

a: Radial

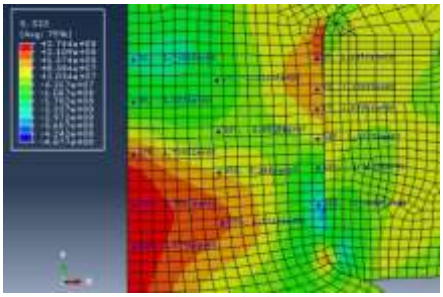

b: Axial

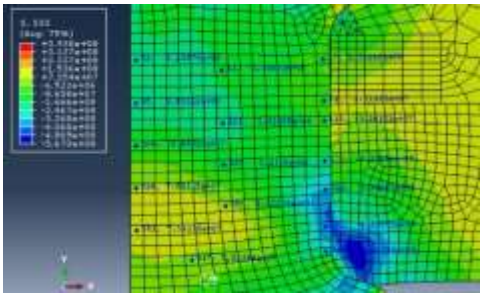

c: Hoop

Figure 6.6. Stress distributions within region 'B' of the 'Model 1 Dyn' stackup. a: Radial Stress, b: Axial Stress, c: Hoop Stress

Referring to figure 6.7a, logarithmic radial strain distribution of region ‘B’ is shown. Radial strain is tensile and of small magnitude (~ 0.001) in the region near the base of the rivet crown and rivet axis. It is tensile and has higher magnitude (~ 0.03) near the head of the rivet button and the rivet axis. It is tensile and has large magnitude (~ 0.09) at the base of the rivet crown near the outer skin interface where the radial gap was found. It is again tensile and has large magnitude (~ 0.2) near the head of the rivet button at the inner skin interface.

Referring to figure 6.7b, logarithmic axial strain distribution of region ‘B’ is shown. Axial strain is compressive and of small magnitude (~ 0.002) in the region near the base of the rivet crown and rivet axis. It is compressive and has higher magnitude (~ 0.04) near the head of the rivet button and the rivet axis. It is compressive and has large magnitude (~ 0.094) at the base of the rivet crown near the outer skin interface where the radial gap was found. It is compressive and has large magnitude (~ 0.16) near the head of the rivet button at the inner skin interface.

Referring to figure 6.7c, logarithmic hoop strain distribution of region ‘B’ is shown. Hoop strain is tensile in the entire rivet shank region. It has a small magnitude (~ 0.002) in the region near the base of the rivet crown and rivet axis. It has a higher magnitude near the head of the rivet button and the rivet axis (~ 0.03). It has a small magnitude (~ 0.012) at the base of the rivet crown near the outer skin interface where the radial gap was found. It has a larger magnitude near the head of the rivet button (~ 0.046) at the inner skin interface.

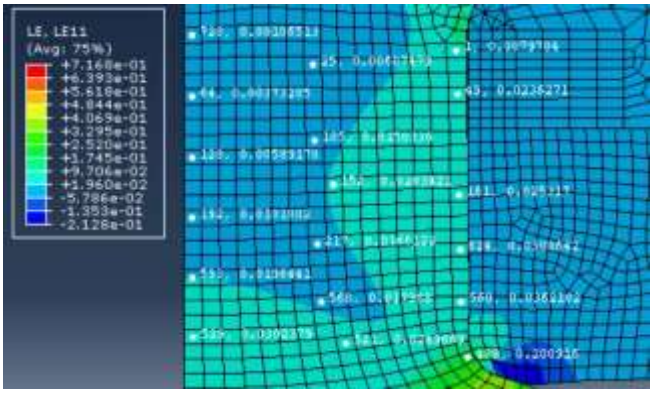

a: Radial

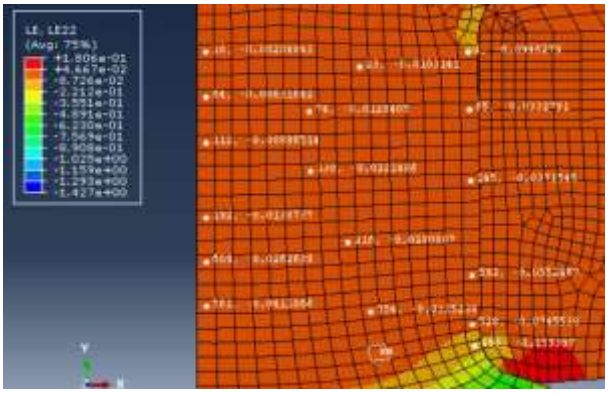

b: Axial

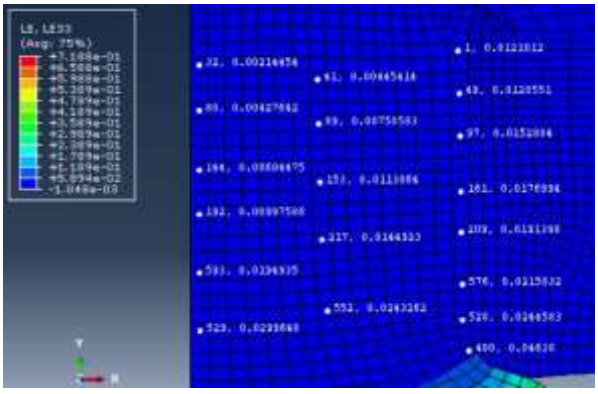

c: Hoop

Figure 6.7. Strain distributions within region ‘B’ of the ‘Model 1 Dyn’ stackup. a: Radial Strain, b: Axial Strain, c: Hoop Strain

Referring to figure 6.8a, radial stress distribution of region ‘C’ is shown. Radial stress is compressive in the rivet button region. Higher magnitude of stress was observed in the interior of the rivet button (~ 200 MPa). A low magnitude of compressive radial stress was found at the free surface of the rivet button (~ 20 MPa).

Referring to figure 6.8b, axial stress distribution of region ‘C’ is shown. Axial stress is tensile and of a high magnitude (~ 235 MPa) at the head of the rivet button near the rivet axis. Axial stress magnitude reduces (~ 61 MPa) near the rivet axis at the bottom of the rivet button. Low magnitude of stress was observed in the interior of the rivet button (~ 50 MPa). A low magnitude of compressive axial stress (~ 30 MPa) was found at the free surface of the rivet button.

Referring to figure 6.8c, hoop stress distribution of region ‘C’ is shown. Hoop stress is compressive at the head of the rivet button near the rivet axis (~ 23 MPa) and near the rivet axis at the bottom of the rivet button (~ 166 MPa). Compressive stress was observed in the interior of the rivet button (~ 208 MPa). High magnitude of tensile hoop stress (~ 370 MPa) was found at the free surface of the rivet button.

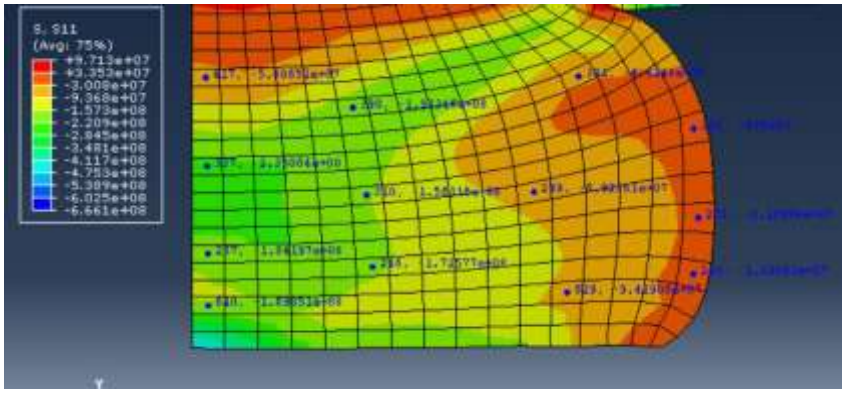

a: Radial

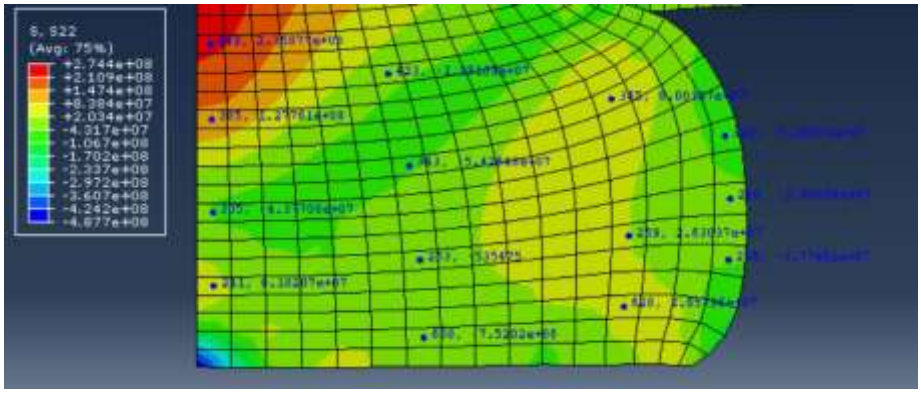

b: Axial

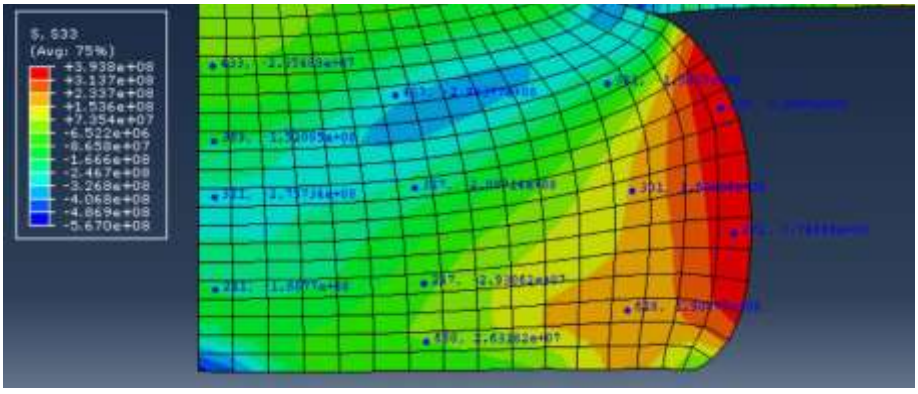

c: Hoop

Figure 6.8. Stress distributions within region ‘C’ of the ‘Model 1 Dyn’ stackup. a: Radial Stress, b: Axial Stress, c: Hoop Stress

Referring to figure 6.9a, logarithmic radial strain distribution of region ‘C’ is shown. Radial strain is tensile in the rivet button. The magnitude is high near the rivet axis toward the base of the rivet button (~ 0.71). The radial strain magnitude at the free surface of the rivet button (~ 0.41) and in the interior of the rivet button (~ 0.08-0.66) is smaller than the one found near the base of the rivet button at the rivet axis.

Referring to figure 6.9b, logarithmic axial strain distribution of region ‘C’ is shown. Axial strain is compressive in the rivet button. The magnitude is high (~ 1.4) near the rivet axis toward the base of the rivet button. The axial strain magnitude at the free surface of the rivet button (~ 0.4) and in the interior of the rivet button (~ 0.8-1.0) is smaller than the one found near the base of the rivet button at the rivet axis.

Referring to figure 6.9c, logarithmic hoop strain distribution of region ‘C’ is shown. Hoop strain is tensile in the rivet button. The magnitude is high near the rivet axis toward the base of the rivet button (~ 0.73). The axial strain magnitude at the free surface of the rivet button (~ 0.4) and in the interior of the rivet button (~ 0.06-0.66) is smaller than the one found near the base of the rivet button at the rivet axis.

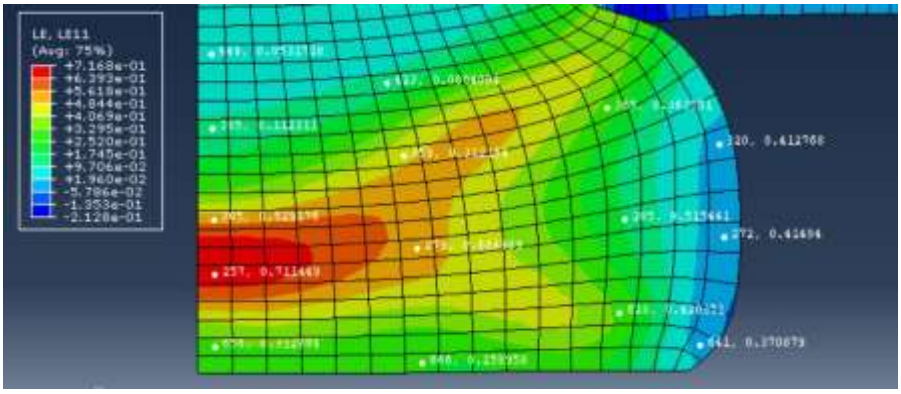

a: Radial

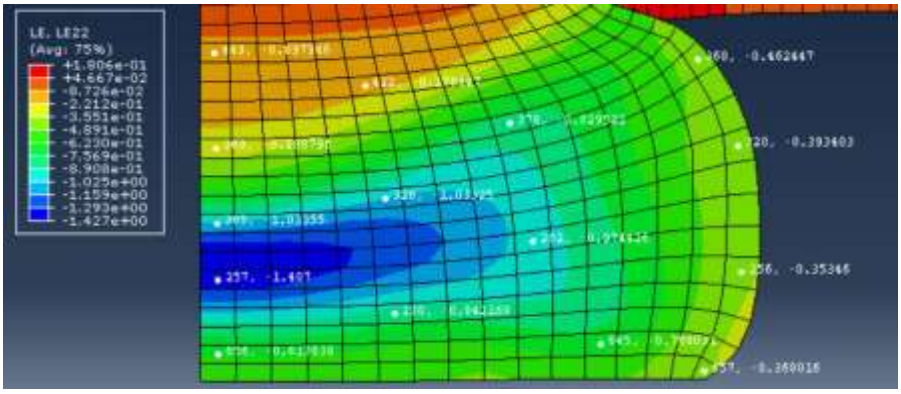

b: Axial

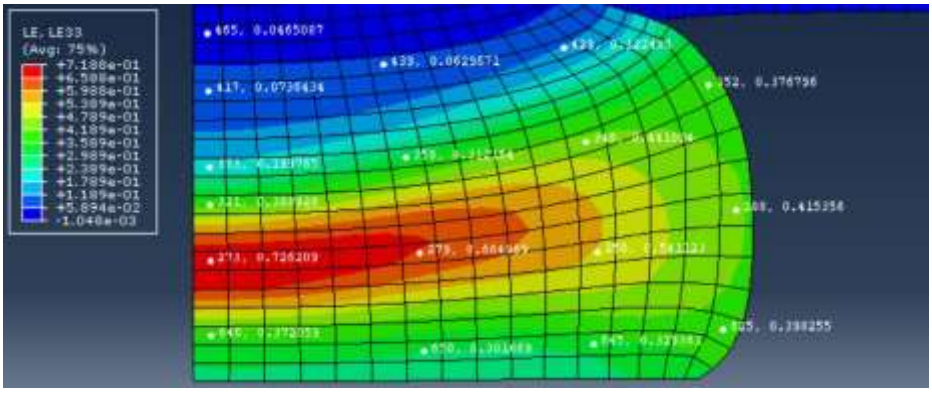

c: Hoop

Figure 6.9. Strain distributions within region 'C' of the 'Model 1 Dyn' stackup. a: Radial Strain, b: Axial Strain, c: Hoop Strain

Referring to figure 6.10a, radial stress distribution of region ‘D’ is shown. Radial stress is compressive in the crown region of the outer skin above the countersink (~ 260 MPa). Radial stress is found to be tensile near the countersink wedge (~ 42 MPa). It is found to be tensile and of low magnitude (~ 40 MPa) at the location where the radial gap was found. It is compressive of larger magnitude (~ 55 MPa) in the interior of the outer skin away from the radial gap.

Referring to figure 6.10b, axial stress distribution of region ‘D’ is shown. Axial stress is both compressive and tensile in the crown region of the outer skin above the countersink (Compressive ~ 66 MPa, Tensile ~ 32 MPa). Axial stress is found to be tensile near the countersink wedge (~ 75 MPa). It is found to be tensile and have low magnitude at the location where the radial gap was found (~ 40-60 MPa). It is found to be tensile and of lower magnitude in the interior of the outer skin away from the radial gap (~ 2-20 MPa).

Referring to figure 6.10c, hoop stress distribution of region ‘D’ is shown. Hoop stress is compressive and tensile in the crown region of the outer skin above the countersink (Compressive ~ 95 MPa, Tensile ~ 61 MPa). Hoop stress is found to be tensile near the countersink wedge (~ 47 MPa). It is found to be tensile and have low magnitude (~ 23 MPa) at the location where the radial gap was found. It is found to be tensile and of higher magnitude (~ 120 MPa) in the interior of the outer skin away from the radial gap.

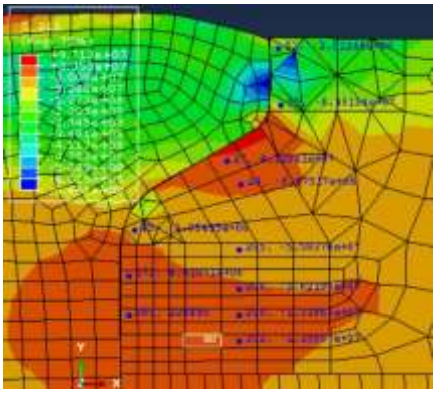

a: Radial

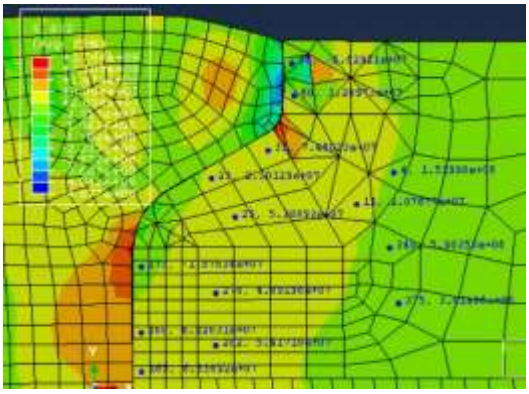

b: Axial

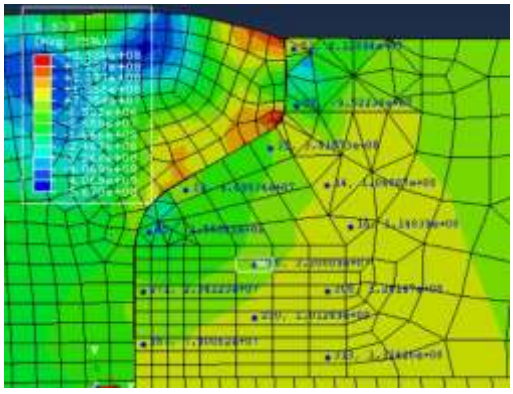

c: Hoop

Figure 6.10. Stress distributions within region ‘D’ of the ‘Model 1 Dyn’ stackup. a: Radial Stress, b: Axial Stress, c: Hoop Stress

Referring to figure 6.11a, logarithmic radial strain distribution of region ‘D’ is shown. Radial strain is compressive and of small magnitude (~ 0.006) in the crown region of the outer skin above the countersink. Radial strain is found to be tensile and compressive of small magnitude near the countersink wedge (< 0.001). It is found to have low magnitude at the location where the radial gap was found (~ 0.0001). It is found to be compressive and of low magnitude (< 0.004) in the interior of the outer skin away from the radial gap.

Referring to figure 6.11b, logarithmic axial strain distribution of region ‘D’ is shown. Axial strain is tensile in the crown region of the outer skin above the countersink (~ 0.027). Axial strain is compressive of small magnitude (~ 0.001) near the countersink wedge. It is compressive and has low magnitude (~ 0.002) at the location where the radial gap was found. It is found to be compressive and of low magnitude (< 0.001) in the interior of the outer skin away from the radial gap. Referring to figure 6.11c, logarithmic hoop strain distribution of region ‘D’ is shown. Hoop strain is tensile and of low magnitude (< 0.004) across region 'D'.

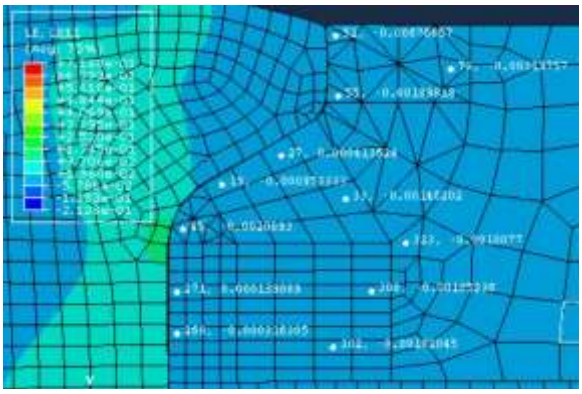

a: Radial

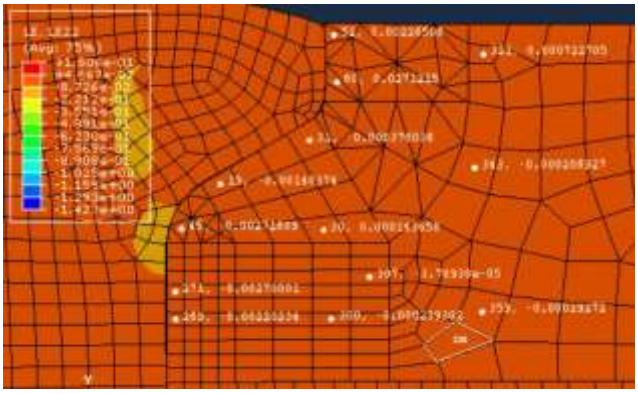

b: Axial

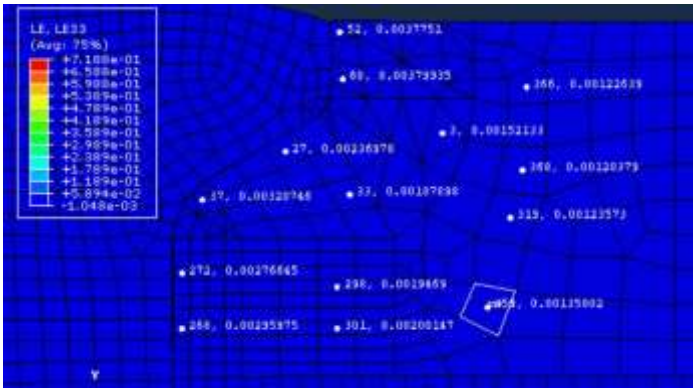

c: Hoop

Figure 6.11. Strain distributions within region ‘D’ of the ‘Model 1 Dyn’ stackup. a: Radial Strain, b: Axial Strain, c: Hoop Strain

Referring to figure 6.12a, radial stress distribution of regions ‘E’ and ‘G’ is shown. Radial stress is compressive across regions 'E' and 'G'. The compressive stress magnitude is higher (~ 60-100 MPa) closer to the rivet-skin interfaces. The magnitude reduces (< 30 MPa) as the distance from the rivet-skin interfaces increases.

Referring to figure 6.12b, axial stress distribution of regions ‘E’ and ‘G’ is shown. Axial stress has a small magnitude across regions 'E' and 'G'. The magnitude is higher closer to the rivet-skin interfaces (~ 15 MPa). The magnitude reduces (< 1 MPa) as the distance from the rivet-skin interfaces increases.

Referring to figure 6.12c, hoop stress distribution of regions ‘E’ and ‘G’ is shown. Hoop stress is tensile across regions 'E' and 'G'. The tensile stress magnitude is higher closer to the rivet-skin interfaces (~ 30-60 MPa). The magnitude reduces (< 25 MPa) as the distance from the rivet-skin interfaces increases.

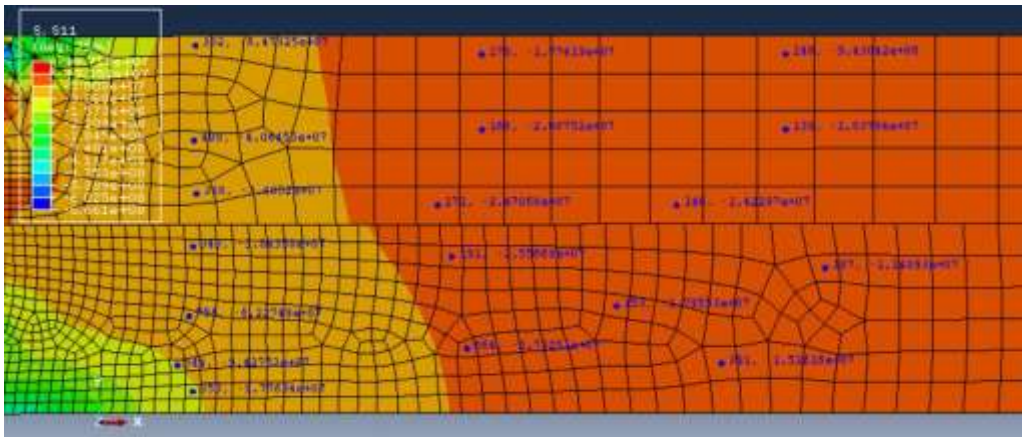

a: Radial

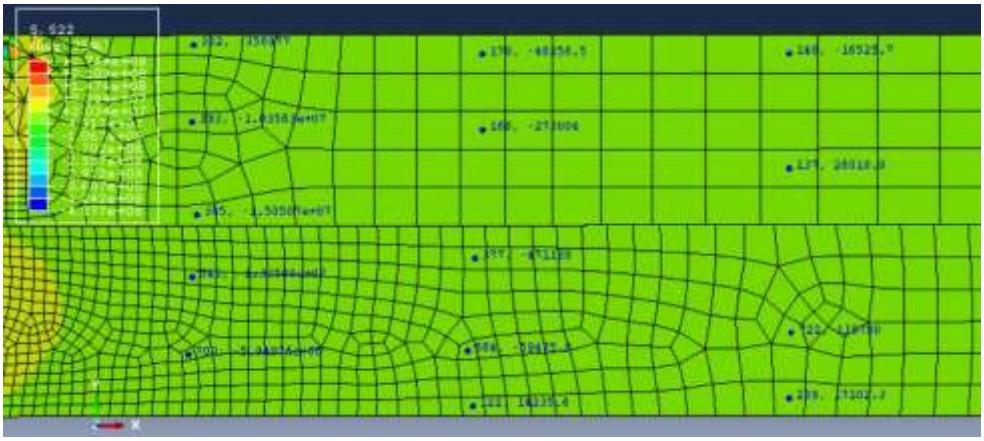

b: Axial

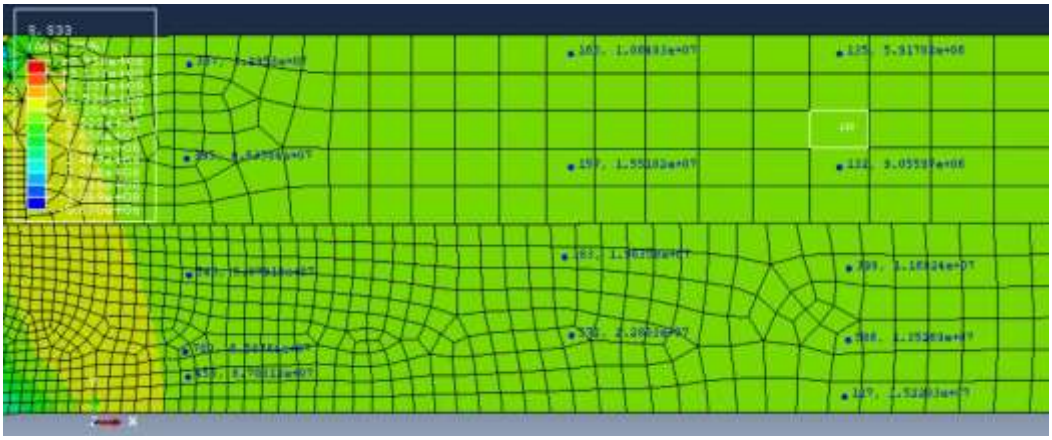

c: Hoop

Figure 6.12. Stress distributions within regions ‘E’ and ‘G’ of the ‘Model 1 Dyn’ stackup. a: Radial Stress, b: Axial Stress, c: Hoop Stress

Referring to figure 6.13a, logarithmic radial strain distribution of regions ‘E’ and ‘G’ is shown. Axial strain is compressive and of low magnitude across regions 'E' and 'G'. The magnitude is relatively higher closer to the rivet-skin interfaces (~ 0.001). The magnitude reduces as the distance from the rivet-skin interfaces increases (< 0.001).

Referring to figure 6.13b, logarithmic axial strain distribution of regions ‘E’ and ‘G’ is shown. Axial strain magnitude is very low in regions ‘E’ and ‘G’. The magnitude reduces (< 0.0001) as the distance from the rivet-skin interfaces increases.

Referring to figure 6.13c, logarithmic hoop strain distribution of regions ‘E’ and ‘G’ is shown. Hoop strain is tensile and of low magnitude across regions 'E' and 'G'. The magnitude is relatively higher closer to the rivet-skin interfaces (~ 0.001). The magnitude reduces (~ 0.0002) as the distance from the rivet-skin interfaces increases.

a: Radial

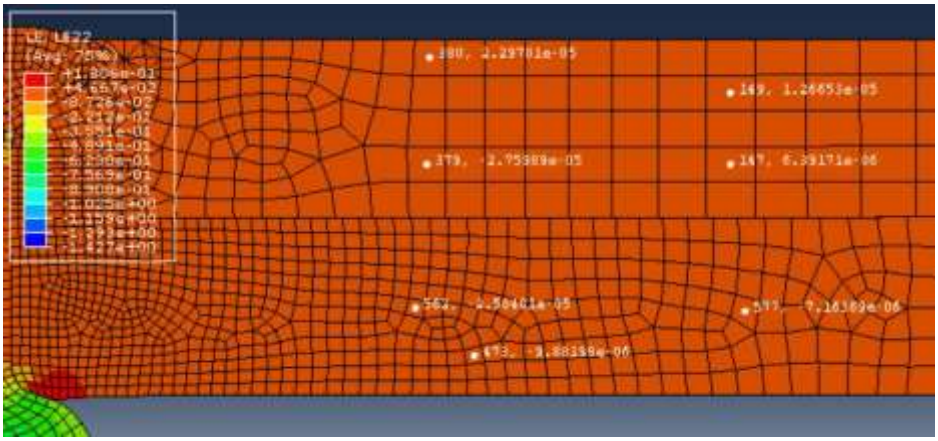

b: Axial

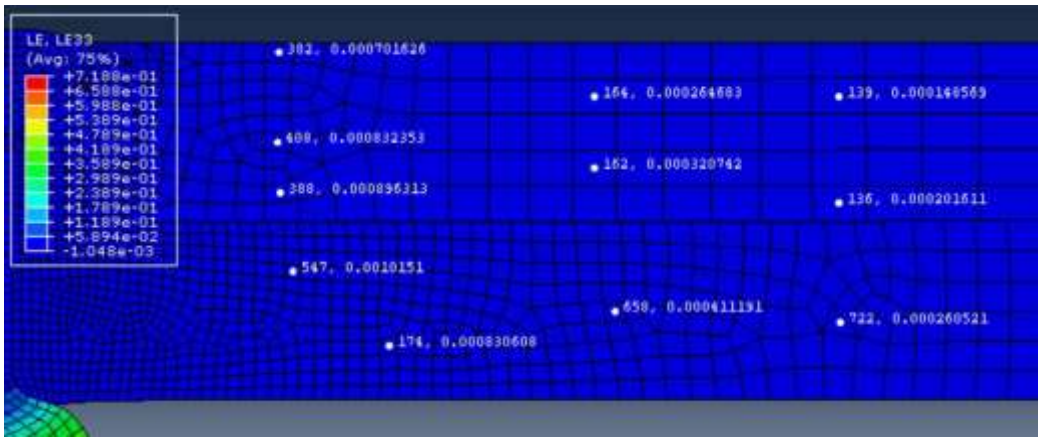

c: Hoop

Figure 6.13. Strain distributions within regions ‘E’ and ‘G’ of the ‘Model 1 Dyn’ stackup. a: Radial Strain, b: Axial Strain, c: Hoop Strain

Referring to figure 6.14a, radial stress distribution of region ‘F’ is shown. Radial stress is compressive across region 'F'. It only becomes tensile near the head of the rivet button (~ 97 MPa). Magnitude of compressive stress reduces (< 70 MPa) in the interior of the region 'F'.

Referring to figure 6.14b, axial stress distribution of region ‘F’ is shown. Axial stress is tensile across region 'F'. It only becomes compressive near the head of the rivet button (~ 90 MPa). Magnitude of tensile stress reduces (~ 4 MPa) in the interior of the region 'F'.

Referring to figure 6.14c, hoop stress distribution of region ‘F’ is shown. Hoop stress is compressive near the head of the rivet button (~ 300 MPa) and in the interior adjacent to the rivet button (~ 100-200 MPa). It becomes tensile further away from the head of the rivet button (~ 130 MPa). But the magnitudes of these tensile stresses are lower than the magnitude of compressive stress found near the head of the rivet button.

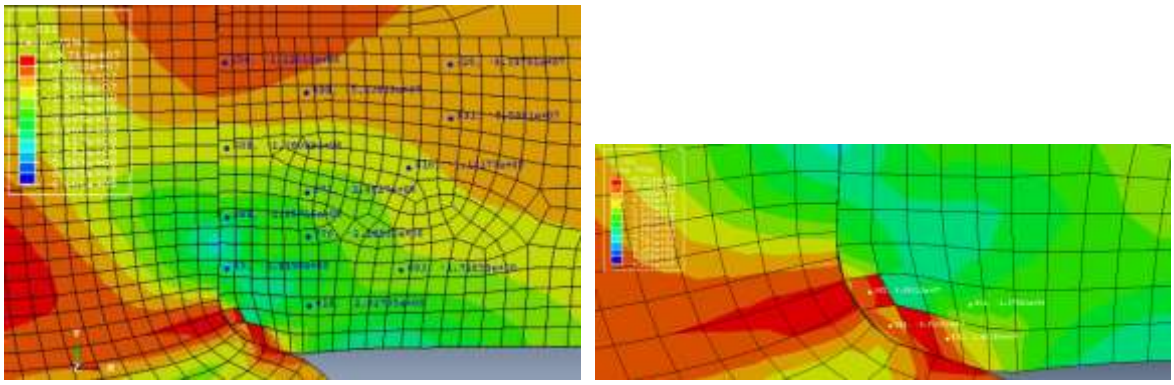

a: Radial

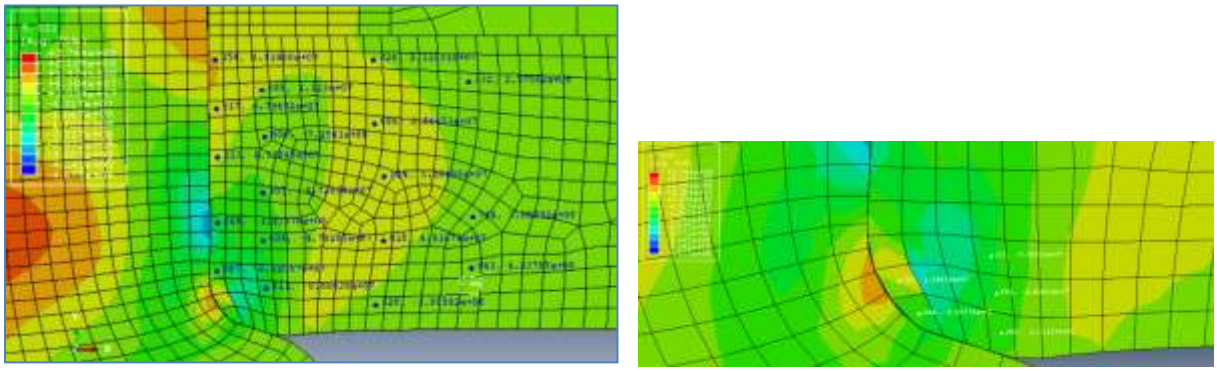

b: Axial

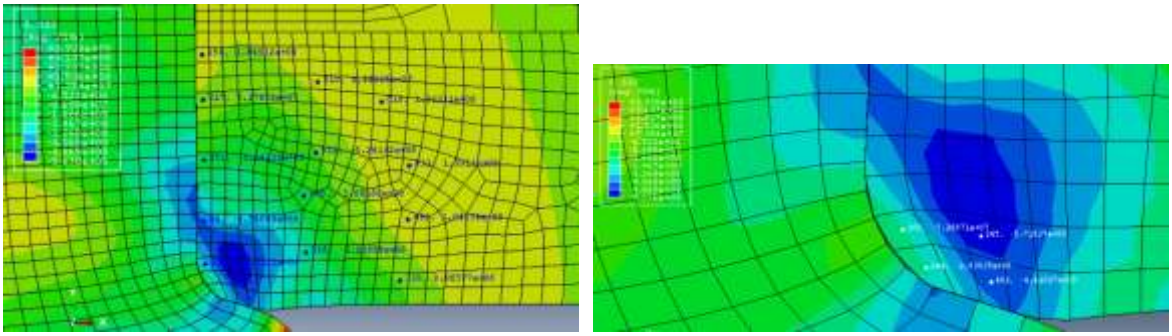

c: Hoop

Figure 6.14. Stress distributions within region ‘F’ of the ‘Model 1 Dyn’ stackup. a: Radial Stress, b: Axial Stress, c: Hoop Stress

Referring to figure 6.15a, logarithmic radial strain distribution of region ‘F’ is shown. The strain is compressive across region ‘F’ except near the head of the rivet button (~ 0.154). The magnitude of strains reduces in region ‘F’ as the distance from the head of the rivet increases.

Referring to figure 6.15b, logarithmic axial strain distribution of region ‘F’ is shown. The strain is both tensile and compressive and of low magnitude (< 0.03) across region ‘F’ except near the head of the rivet button. Near the head of the rivet button tensile and compressive strains of higher magnitude (~ 0.18) are observed.

Referring to figure 6.15c, logarithmic hoop strain distribution of region ‘F’ is shown. The strain is tensile across region ‘F’. The magnitude of the strain reduces away (< 0.008) from the head of the rivet button. Near the head of the rivet button, the strain magnitude is relatively higher (~ 0.05).

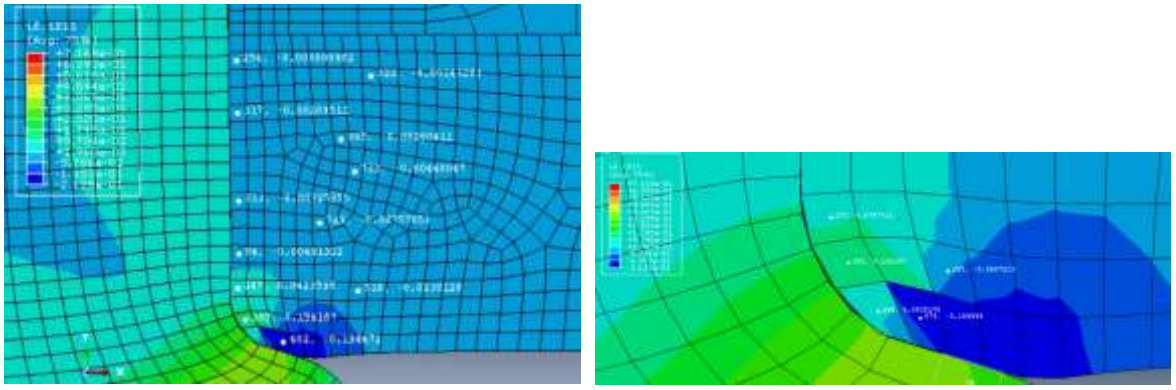

a: Radial

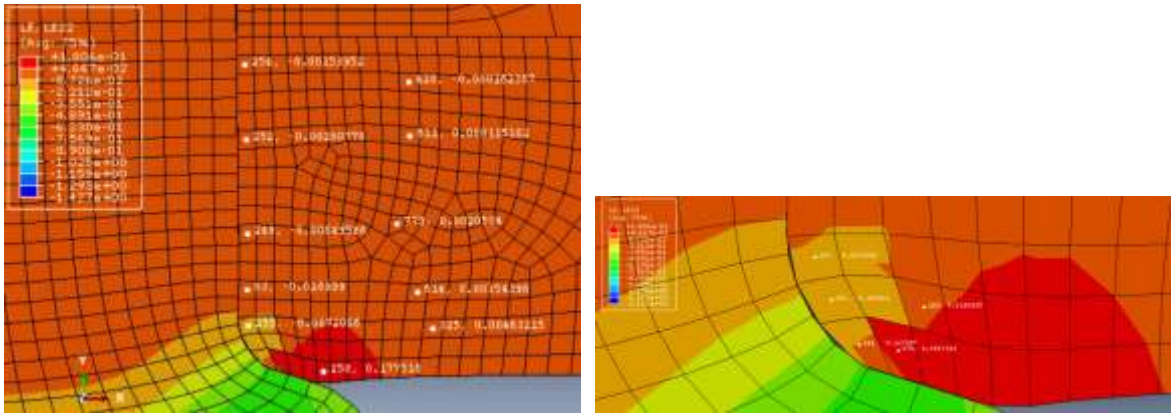

b: Axial

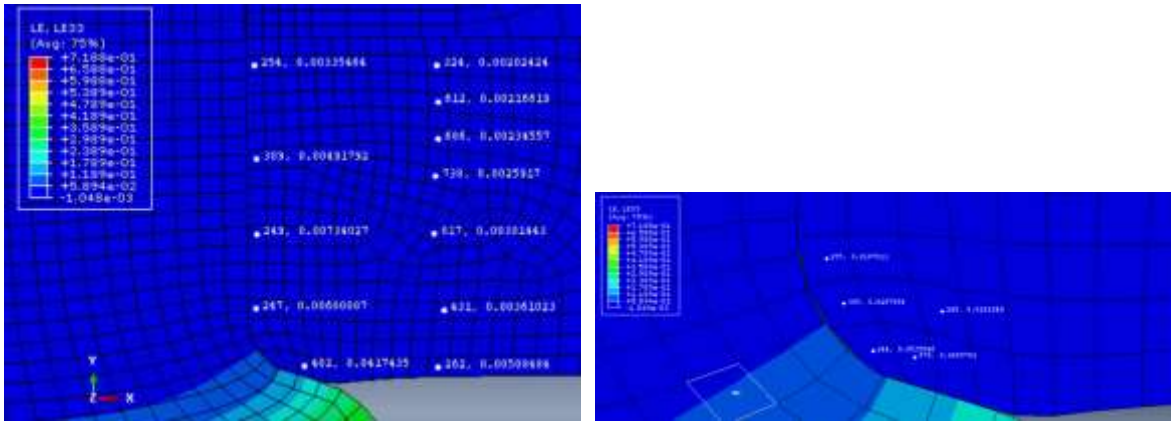

c: Hoop

Figure 6.15. Strain distributions within region 'F' of the 'Model 1 Dyn' stackup. a: Radial Strain, b: Axial Strain, c: Hoop Strain

Measurements of residual stresses and strains were made at various skin-skin interface and skin-rivet interface element nodes. These interfaces are shown in figure 6.16. First interface is the inner skin adjacent to the rivet (denoted by 'IR'). Y-coordinate of IR ranges from 6 mm to 8.5 mm. Second is the inner skin adjacent to the outer skin (denoted by 'IO'). X-coordinate of IO ranges from 2.8 mm to 62 mm. Third is the outer skin adjacent to the rivet (denoted by 'OR'). Y-coordinate of OR ranges from 8.5 mm to 11 mm. Fourth is the outer skin adjacent to the inner skin (denoted by 'OI'). X-coordinate of OI ranges from 2.8 mm to 62 mm. Fifth is the rivet adjacent to the rivet hole which spans both the inner skin's hole region and the outer skin's hole region (denoted by 'RH'). Y-coordinate of RH ranges from 3 mm to 11 mm.

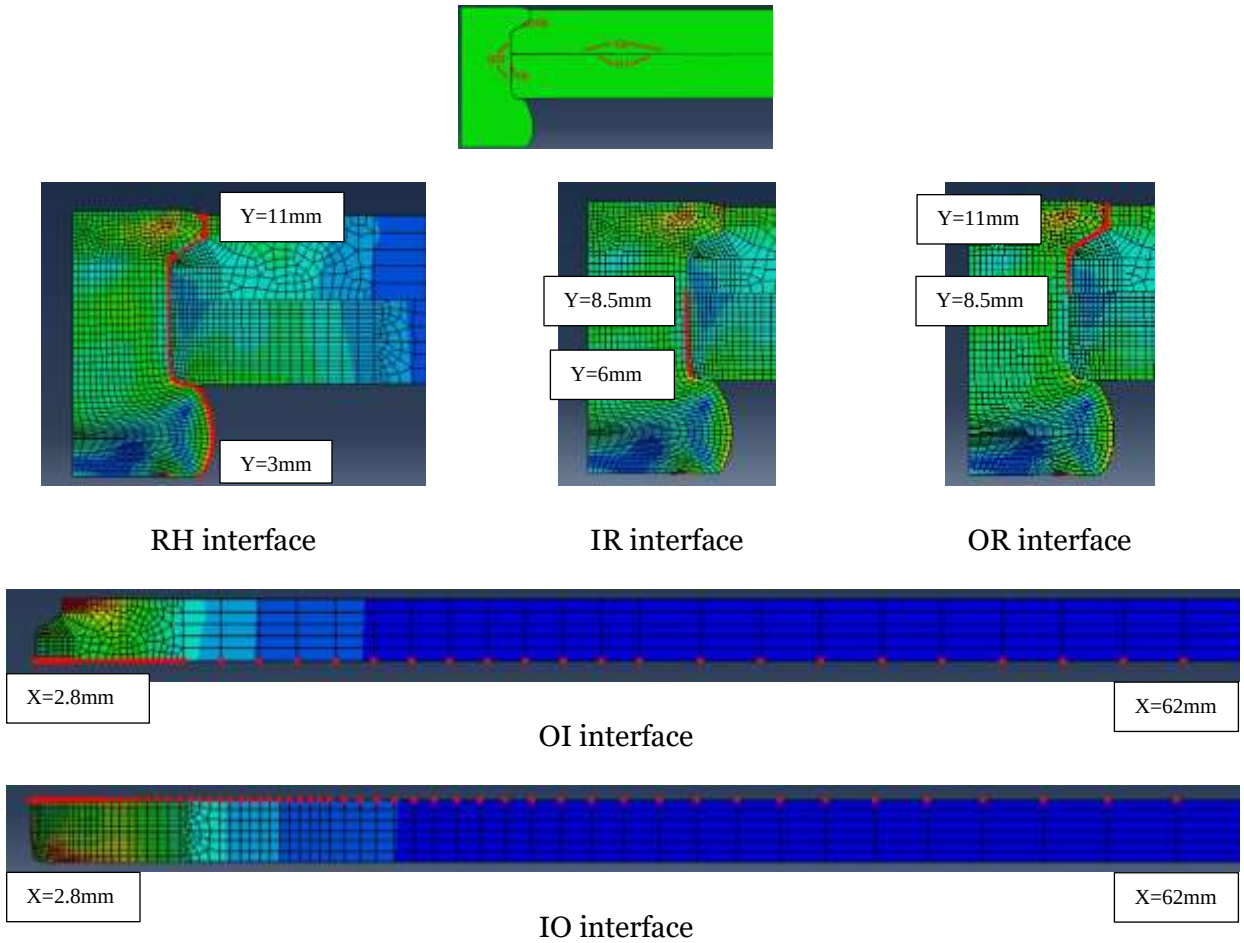

Figure 6.16. Interface residual stresses/strains measurement locations. Measurements were made at the interface nodes (highlighted nodes shown in red).

Referring to figure 6.17a, radial stress distribution of interface 'IR' is shown. The variation of the stress magnitude is large in the area adjacent to the head of the button but it is compressive in nature. But the stress is more compressive in the model 1 QS distribution compared to the model 1 Dyn distribution. The head of the button is one of the stress raisers in the joint.

Referring to figure 6.17b, axial stress distribution of interface 'IR' is shown. The model 1 QS distribution is compressive entirely until Y=7.25 mm but the model 1 Dyn distribution has inflection at Y=6.4 mm from compressive to tensile indicating that the inner skin is in axial tension in this IR region. The distribution of model 1 Dyn becomes tensile from compressive again at Y=7.25 mm. The compressive axial stress acting on the inner skin is greater in the case of model 1 QS compared to model 1 Dyn which can be observed at Y=6.1 mm.

Referring to figure 6.17c, hoop stress distribution of interface 'IR' is shown. Compressive hoop stresses inside the skins are beneficial as described in Chapter 2. The distribution of model 1 QS is entirely compressive. The distribution of model 1 Dyn in compressive until Y=7.65 mm where it turns positive. The stress state at the IR interface is triaxial.

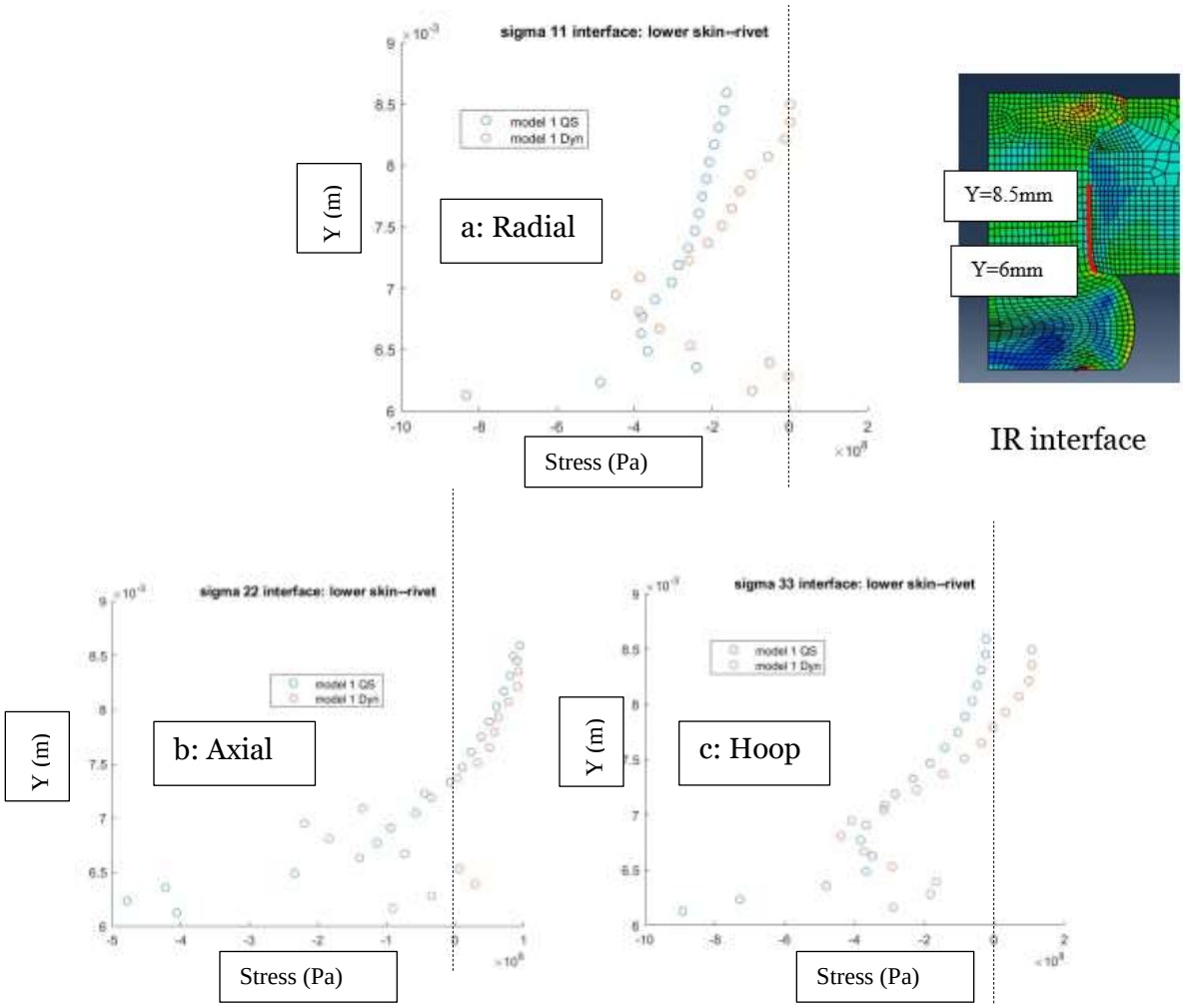

Figure 6.17. Stress distributions within IR interface. a: Radial. b: Axial, c: Hoop. Model-1 QS: Chapter 6 quasi-static simulation, Model-1 Dyn: Chapter 6 partial dynamic simulation. X-axis: Pa, Y-axis: m.

Referring to figure 6.18a, logarithmic radial strain distribution of interface 'IR' is shown. There is greater radial strain in model 1 QS adjacent to the button head compared to model 1 Dyn as can be observed from the R4 values in table 6.1 indicating greater inner skin compression in the former distribution. The distributions are almost the same starting at Y=7 mm. There is not much skin compression that takes place beyond Y=6.7 mm in both distributions.

Referring to figure 6.18b, logarithmic axial strain distribution of interface 'IR' is shown. In both distributions, the axial strain is negative over the entire IR domain. It indicates that portion

of the inner skin corresponding to interface IR is in compression. The magnitude of the compressive strain is greater in the case of model 1 QS compared to model 1 Dyn.

Referring to figure 6.18c, logarithmic hoop strain distribution of interface 'IR' is shown. The strain distributions of both simulations are positive over the whole IR domain. The magnitude of the strain is greater in model 1 QS compared to model 1 Dyn as can be verified from R3 and R4 values from table 6.1. The rivet hole is expanded in radial and hoop directions during the rivet forming process, especially in the inner skin region.

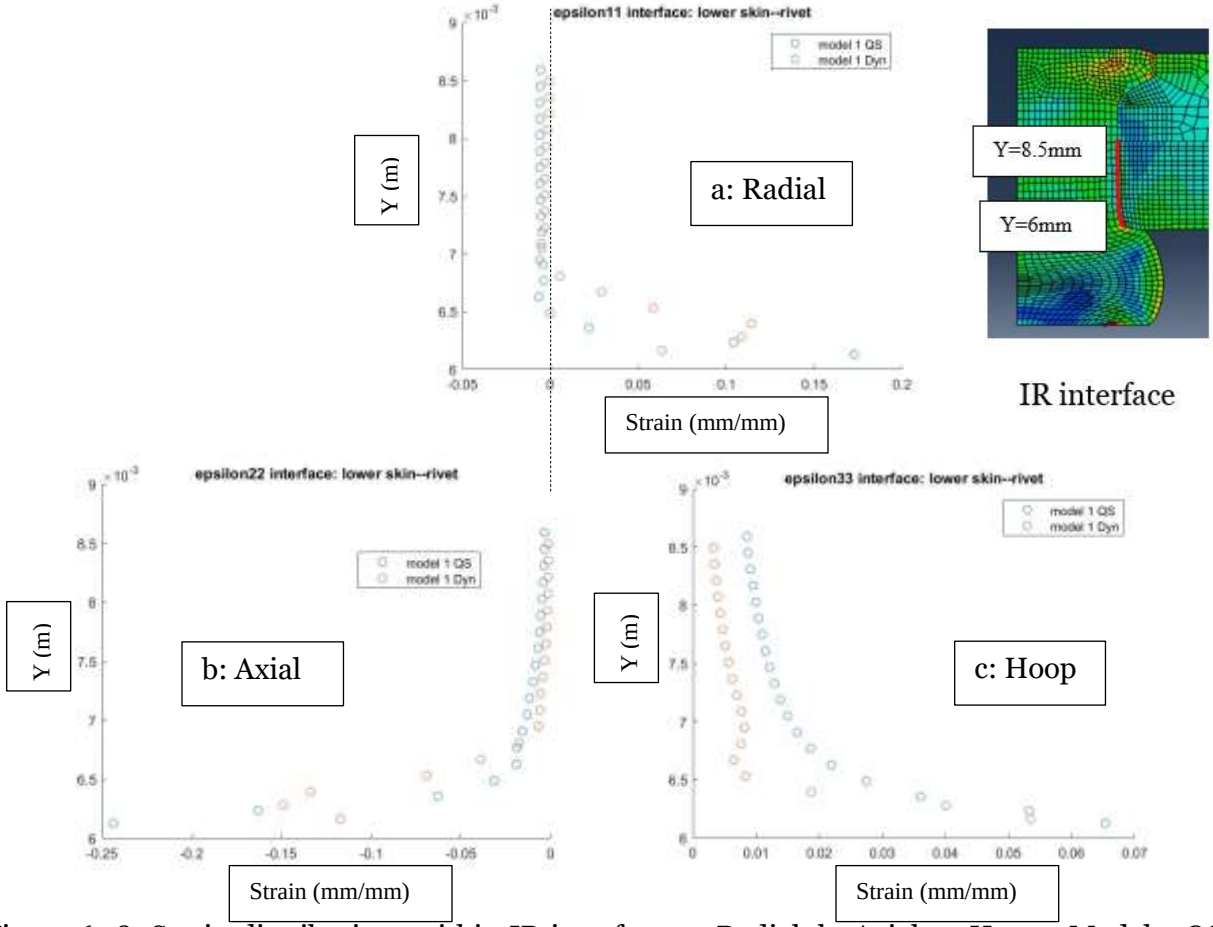

Figure 6.18. Strain distributions within IR interface. a: Radial. b: Axial, c: Hoop. Model-1 QS: Chapter 6 quasi-static simulation, Model-1 Dyn: Chapter 6 partial dynamic simulation. X-axis: mm/mm, Y-axis: m.

Referring to figure 6.19a, radial stress distribution of interface 'IO' is shown. It is entirely compressive for model 1 QS but there is a tensile radial stress region in this interface at X=3 mm. It is compressive for the remaining region. As previously mentioned, a triaxial stress state exists in the inner skin. Observing the lower R3 value of model 1 Dyn, the radial stress magnitude is lower compared to model 1 QS nearer to the skin-rivet interface. The radial stress magnitude reduces as we move away from the skin-rivet interface. The inflections in the stress profiles can be attributed to springback effect.

Referring to figure 6.19b, axial stress distribution of interface 'IO' is shown. Closer to the rivet-skin interface, the axial stress is positive in both distributions. The magnitude is very small away from the interface and the same profile inflection can be seen in both distributions that indicates springback. The axial stress becomes compressive few mm away from the skin-rivet interface and stays compressive for the remaining domain. The magnitude of the compressive axial stress in model 1 Dyn at X=7 mm is greater than the magnitude of compressive axial stress in model 1 QS at X=8mm.

Referring to figure 6.19c, hoop stress distribution of interface 'IO' is shown. The hoop stress in model 1 Dyn is tensile at the skin-rivet interface and is compressive in model 1 QS at the skin-rivet interface. The magnitude reduces as we move away from the skin-rivet interface.

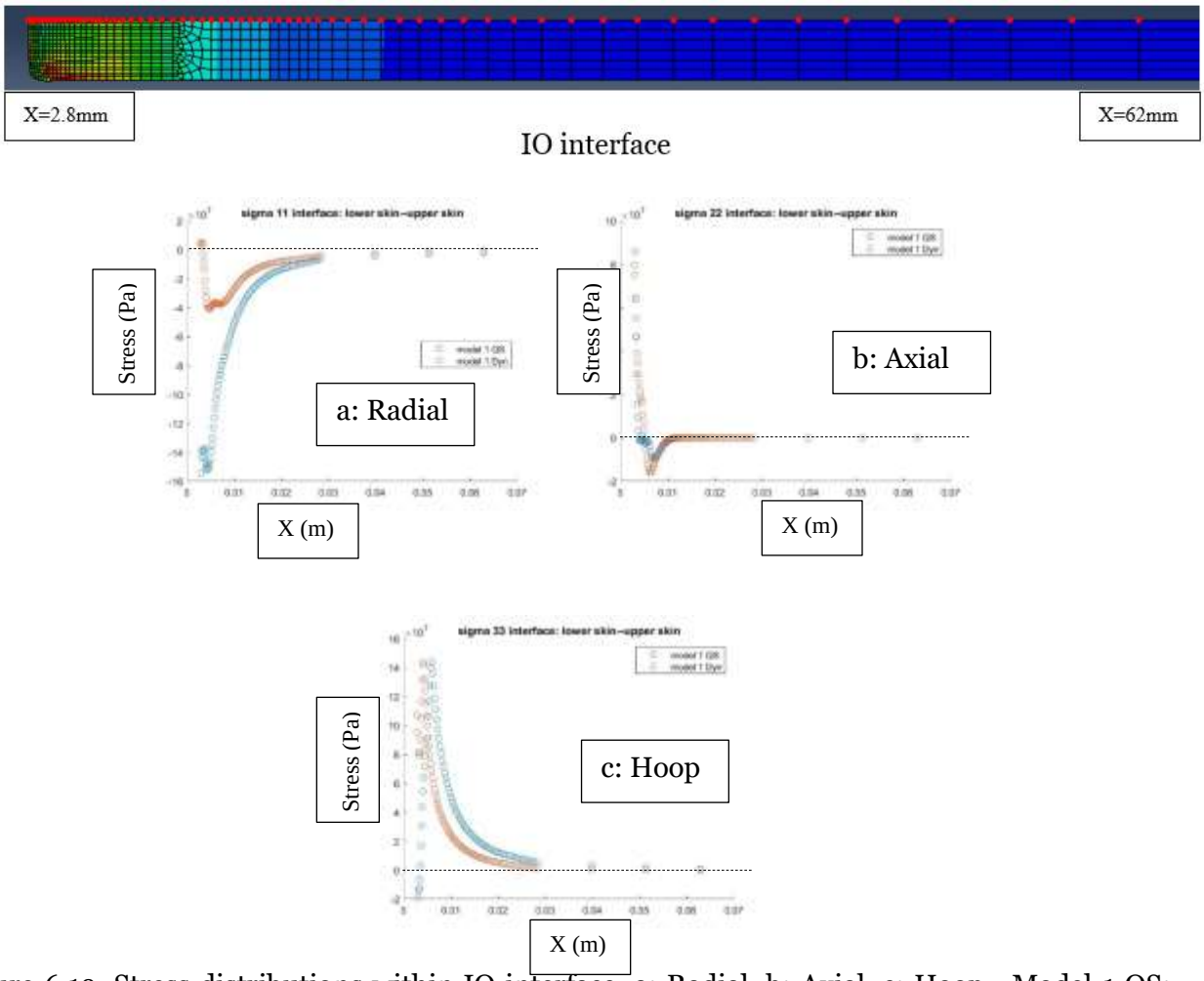

Figure 6.19. Stress distributions within IO interface. a: Radial. b: Axial, c: Hoop. Model-1 QS: Chapter 6 quasi-static simulation, Model-1 Dyn: Chapter 6 partial dynamic simulation. X-axis: m, Y-axis: Pa

Referring to figure 6.20a, logarithmic radial strain distribution of interface 'IO' is shown. Radial strain profile is compressive over the entire domain for both distributions. The maximum magnitude of radial strain of the model 1 QS profile is almost four times greater than the maximum magnitude of the model 1 Dyn profile. This is confirmed by the R3 value of model 1 QS is greater than R3 value of model 1 Dyn. The inflections in the strain profiles correspond to the springback.

Referring to figure 6.20b, logarithmic axial strain distribution of interface 'IO' is shown. Axial strain profile is mostly compressive over the entire domain for both distributions. The maximum magnitude of axial strain of the model 1 QS profile is two times greater than the maximum magnitude of the model 1 Dyn profile.

Referring to figure 6.20c, logarithmic hoop strain distribution of interface 'IO' is shown. Hoop strain profile is tensile over the entire domain for both distributions. The maximum magnitude of hoop strain of the model 1 QS profile is around 2.7 times greater than the maximum magnitude of the model 1 Dyn profile. Tensile hoop strain suggests rivet hole circumferential expansion and skin circumferential expansion.

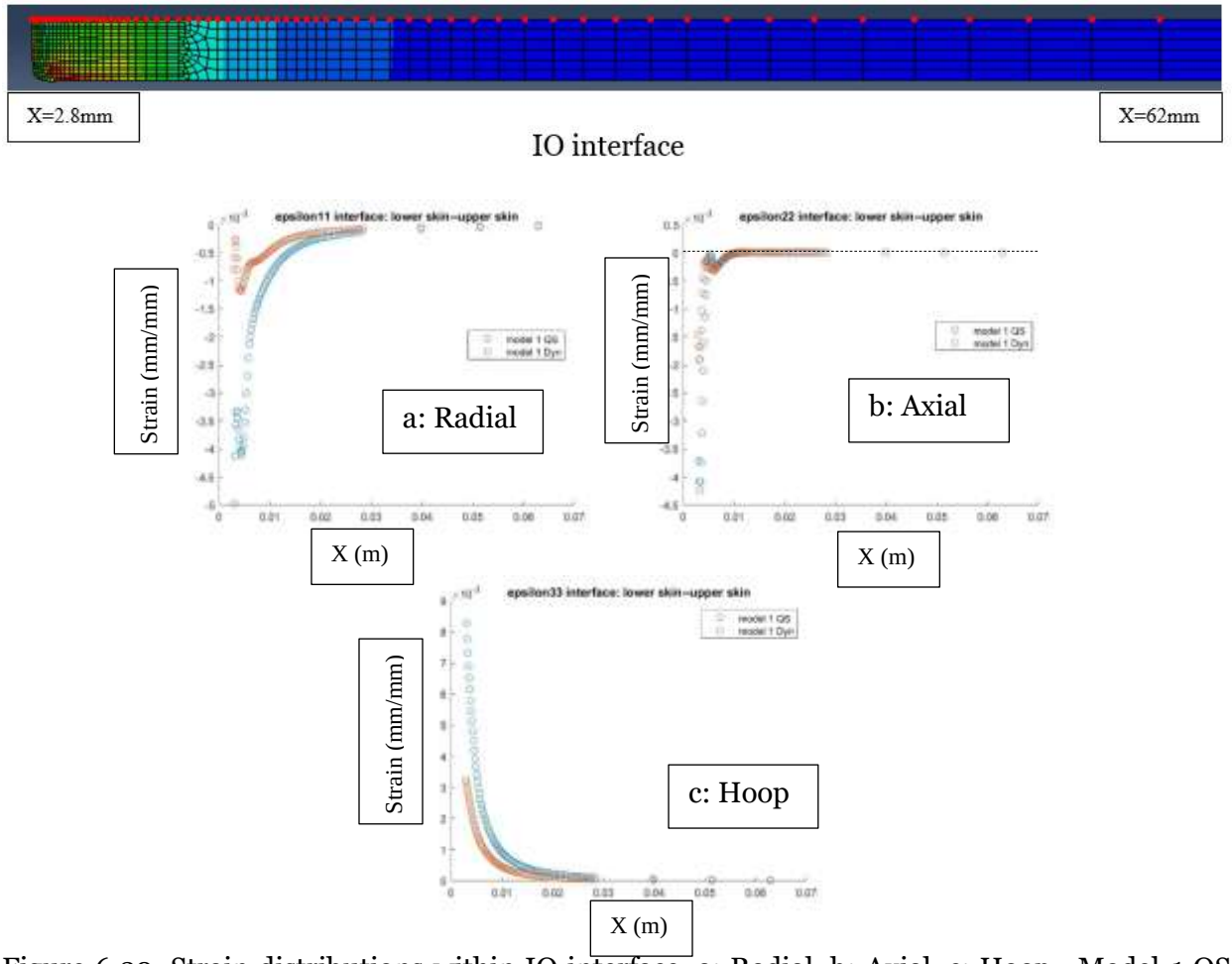

Figure 6.20. Strain distributions within IO interface. a: Radial. b: Axial, c: Hoop. Model-1 QS: Chapter 6 quasi-static simulation, Model-1 Dyn: Chapter 6 partial dynamic simulation. X-axis: m, Y-axis: mm/mm

Referring to figure 6.21a, radial stress distribution of interface 'OR' is shown. Inflections in the stress profiles of both simulations correspond to the countersunk (or crown) area. The two distributions are almost compressive. In the non-countersunk area of the OR interface, the magnitude of the radial stress of model 1 QS is greater than the magnitude of model 1 Dyn. The magnitudes are comparable in the countersunk region.

Referring to figure 6.21b, axial stress distribution of interface 'OR' is shown. The inflections again occur at the countersunk areas. Referring to figure 6.21c, hoop stress distribution of interface 'OR' is shown. The inflections occur at the countersunk areas.

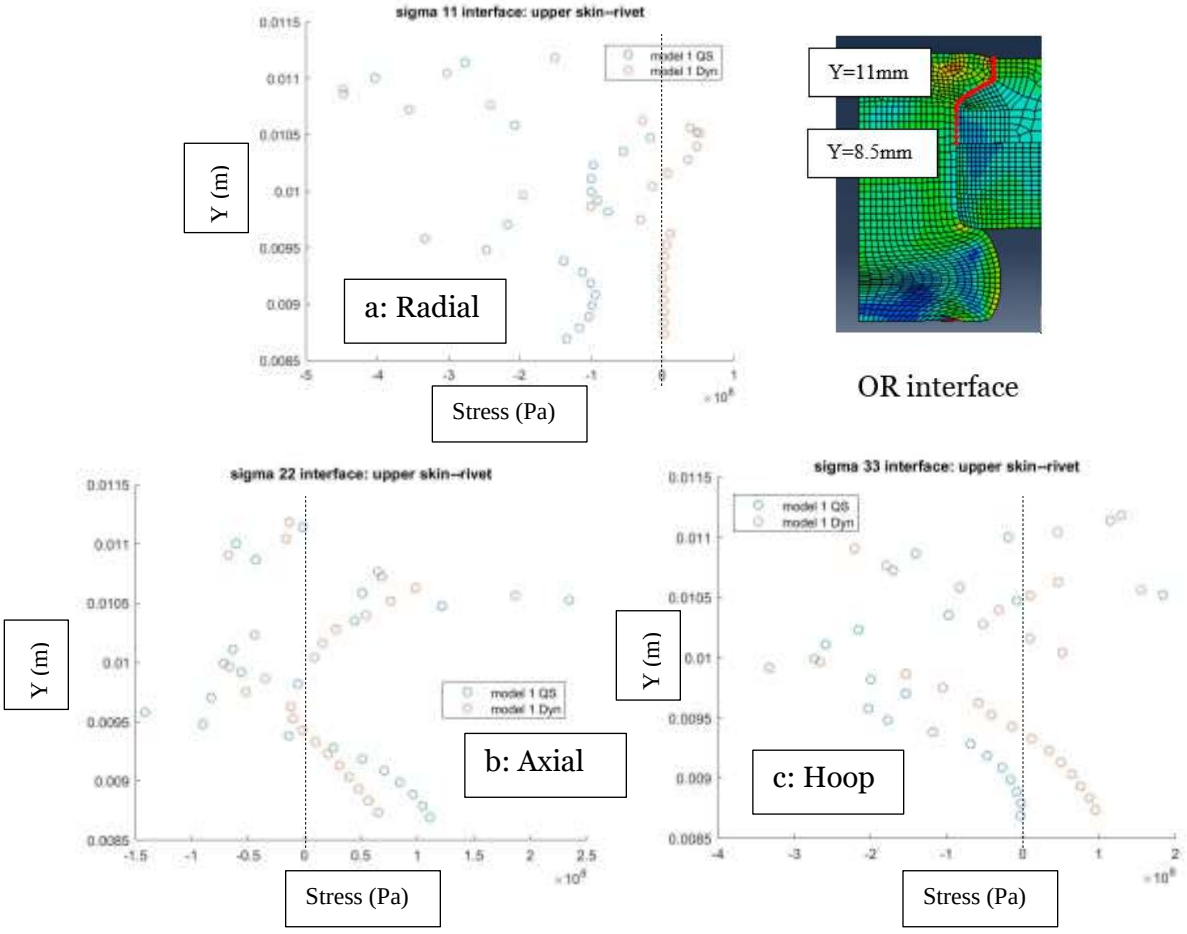

Figure 6.21. Stress distributions within OR interface. a: Radial. b: Axial, c: Hoop. Model-1 QS: Chapter 6 quasi-static simulation, Model-1 Dyn: Chapter 6 partial dynamic simulation. X-axis: Pa, Y-axis: m

Referring to figure 6.22a, logarithmic radial strain distribution of interface 'OR' is shown. The inflections occur at the countersunk areas. The strain is compressive in the whole OR domain. Although, tensile strain is observed in model 1 QS and model 1 Dyn near Y=0.01 m.

Referring to figure 6.22b, logarithmic axial strain distribution of interface 'OR' is shown. The inflections occur at the countersunk areas. The strain is compressive in the non-countersunk area and the strain is tensile in the countersunk area. The magnitude of axial strain of model 1 QS is greater in the non-countersunk area and is approximately the same in the countersunk area.

Referring to figure 6.22c, logarithmic hoop strain distribution of interface 'OR' is shown. Both profiles have tensile hoop strains over the whole OR domain. The magnitude is greater in model 1 QS compared to model 1 Dyn. Values of R1 and R2 in table 6.1 are greater for model 1 QS.

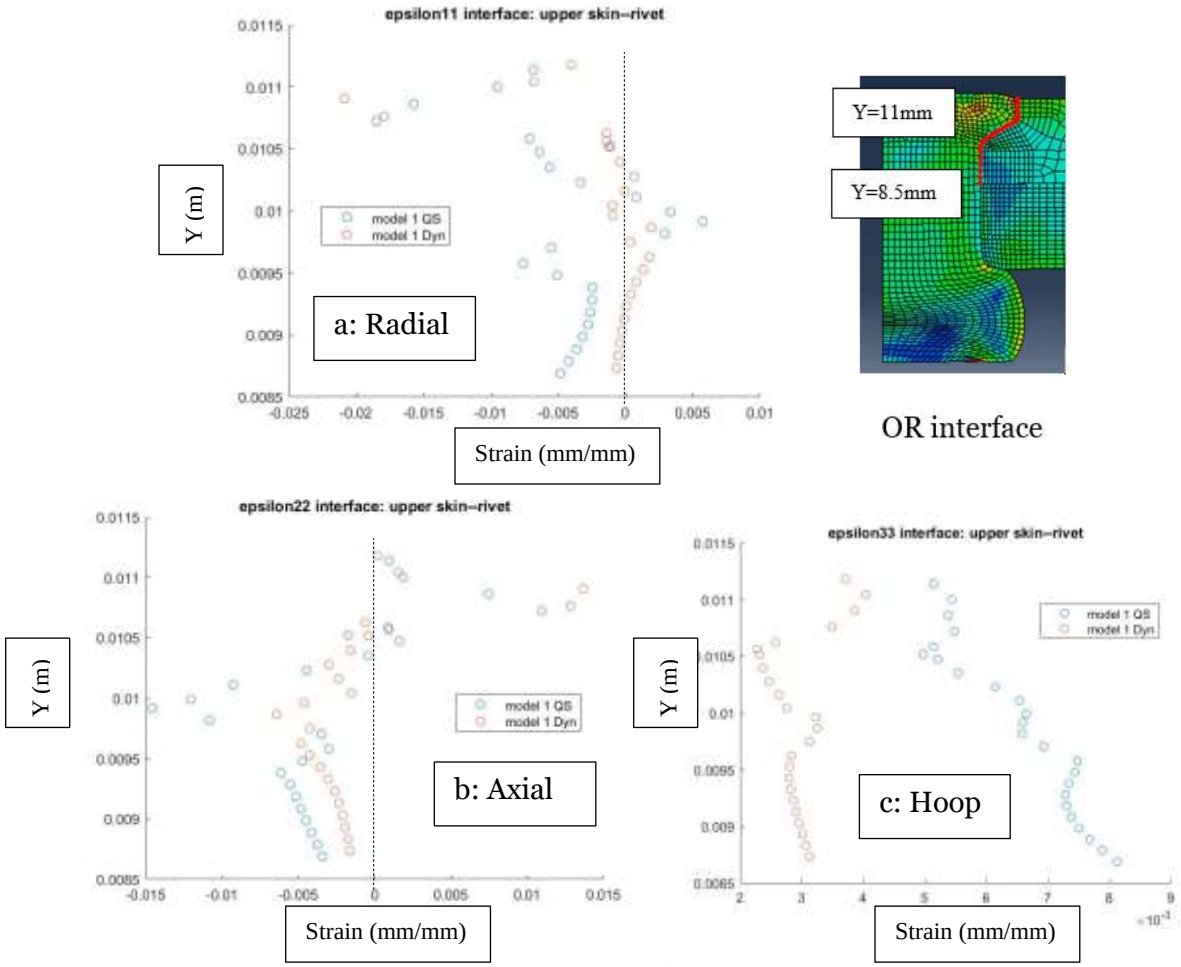

Figure 6.22. Strain distributions within OR interface. a: Radial. b: Axial, c: Hoop. Model-1 QS: Chapter 6 quasi-static simulation, Model-1 Dyn: Chapter 6 partial dynamic simulation. X-axis: mm/mm, Y-axis: m

Referring to figure 6.23a, radial stress distribution of interface 'OI' is shown. The stress is tensile and small in magnitude near the skin-rivet interface in model 1 Dyn where the stress is compressive and large in magnitude near the interface in model 1 QS. Maximum compressive stress magnitude is about four times greater in model 1 QS compared to model 1 Dyn. The stress is compressive for the entire domain in model 1 QS and mostly compressive in model 1 Dyn.

Referring to figure 6.23b, axial stress distribution of interface 'OI' is shown. The stress is tensile and large in magnitude near the rivet-skin interface in both simulations. It turns

compressive a short distance away from the skin-rivet interface. The stress is compressive in both simulations for most of the OI domain. The inflections in the stress profiles correspond to springback.

Referring to figure 6.23c, hoop stress distribution of interface 'OI' is shown. The stress is tensile and large in magnitude near the rivet-skin interface in model 1 Dyn and it is large and compressive near the interface in model 1 QS. It turns tensile a short distance away from the skin-rivet interface in model 1 QS. The stress is tensile in both simulations for most of the OI domain. The inflections in the stress profiles correspond to springback.

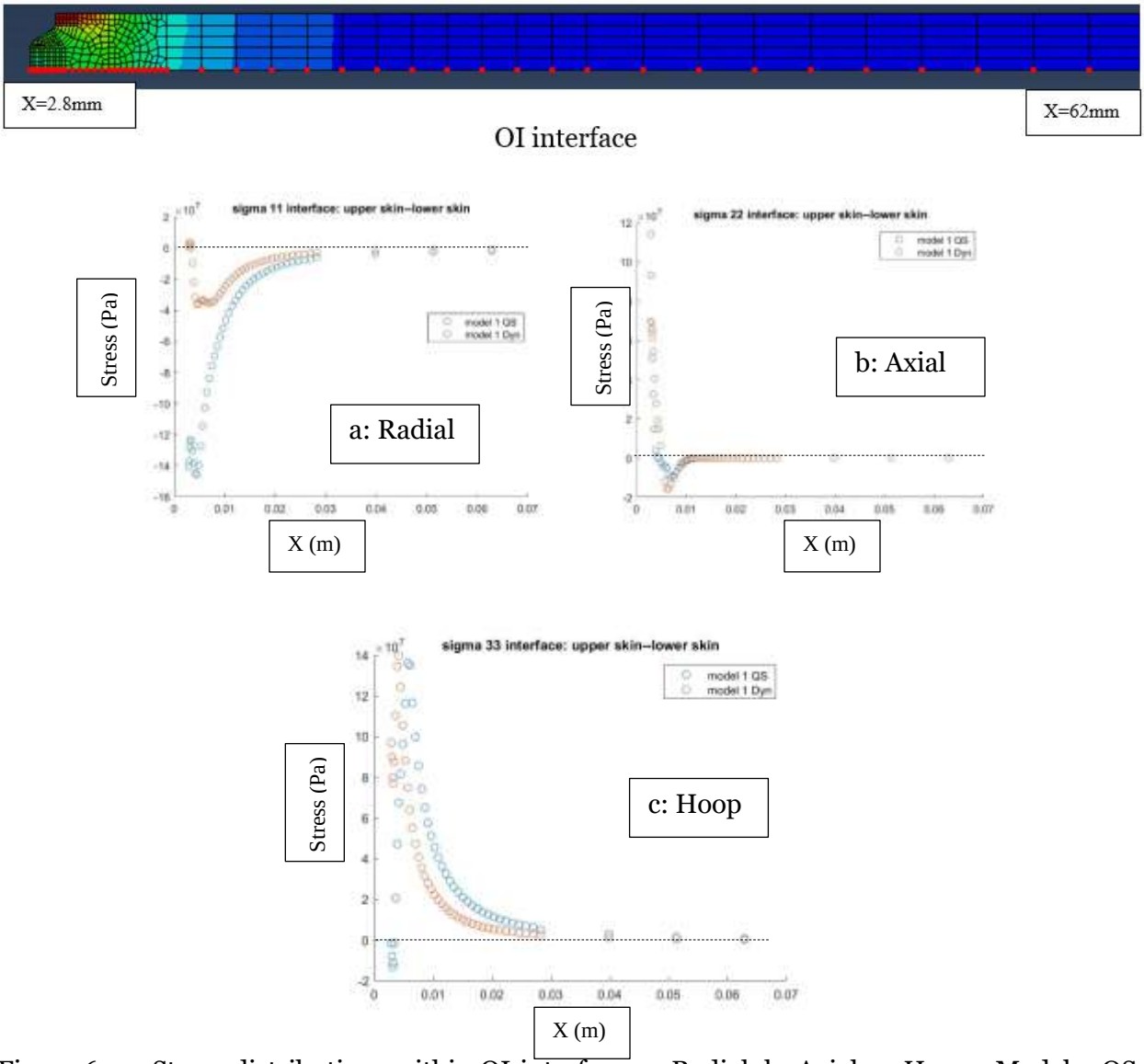

Figure 6.23. Stress distributions within OI interface. a: Radial. b: Axial, c: Hoop. Model-1 QS: Chapter 6 quasi-static simulation, Model-1 Dyn: Chapter 6 partial dynamic simulation. X-axis: m, Y-axis: Pa

Referring to figure 6.24a, logarithmic radial strain distribution of interface 'OI' is shown. The strain is compressive and five times larger in magnitude near the rivet-skin interface in model 1 QS compared to model 1 Dyn. The strain is compressive in both simulations for the entire OI domain. The inflections in the strain profiles correspond to springback. The magnitudes of the strains reduce as we move away from the skin-rivet interface.

Referring to figure 6.24b, logarithmic axial strain distribution of interface 'OI' is shown. The strain is tensile and 2.5 times larger in magnitude near the rivet-skin interface in model 1 QS compared to model 1 Dyn. The strain is compressive in both simulations for the entire OI domain. The magnitudes of the strains reduce as we move away from the skin-rivet interface.

Referring to figure 6.24c, logarithmic hoop strain distribution of interface 'OI' is shown. The strain is tensile and 2.7 times larger in magnitude near the rivet-skin interface in model 1 QS compared to model 1 Dyn. The strain is tensile in both simulations for the entire OI domain. The magnitudes of the strains reduce as we move away from the skin-rivet interface.

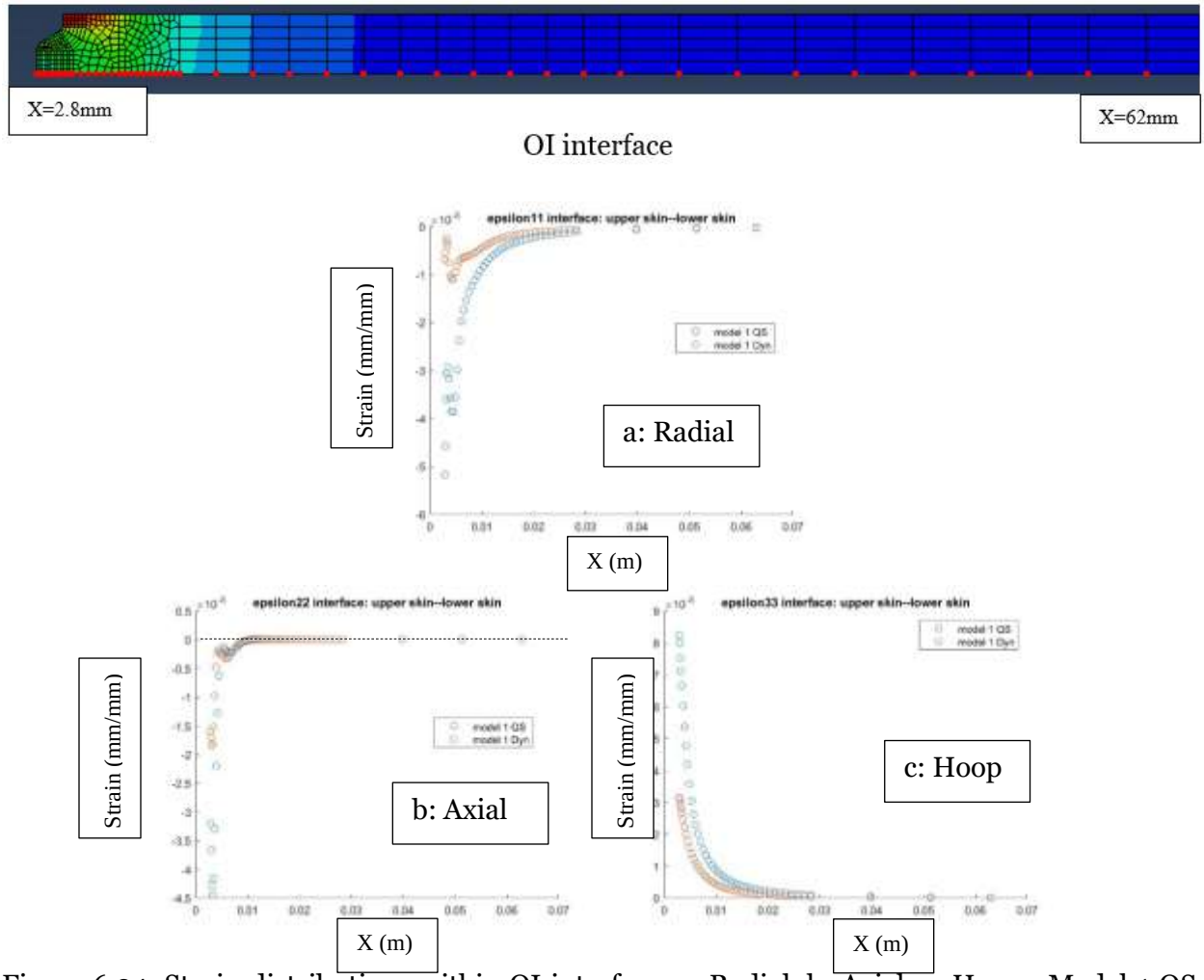

Figure 6.24. Strain distributions within OI interface. a: Radial. b: Axial, c: Hoop. Model-1 QS: Chapter 6 quasi-static simulation, Model-1 Dyn: Chapter 6 partial dynamic simulation. X-axis: m, Y-axis: mm/mm

Referring to figure 6.25, radial stress, axial stress and hoop stress distributions of interface 'RH' are shown respectively. There are inflections in both profiles for all three stress components at the same regions: rivet button head and the countersunk areas. Radial stress is mostly compressive for both model 1 QS and model 1 Dyn at the RH interface. Axial stress is compressive in the rivet button area and rivet crown area.

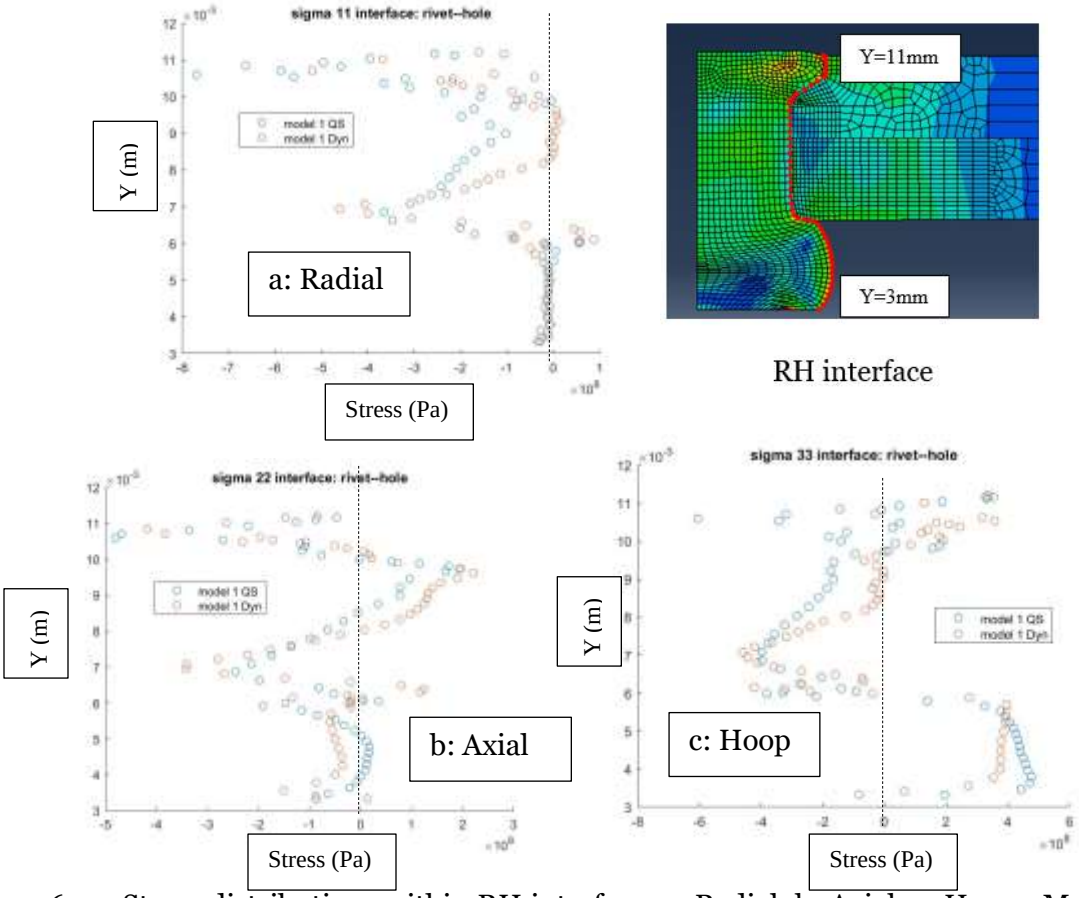

Figure 6.25. Stress distributions within RH interface. a: Radial. b: Axial, c: Hoop. Model-1 QS: Chapter 6 quasi-static simulation, Model-1 Dyn: Chapter 6 partial dynamic simulation. X-axis: Pa, Y-axis: m

Referring to figures 6.26a and 6.26b, logarithmic radial strain and axial strain distributions of interface 'RH' are shown, respectively. There are inflections in both profiles for both strain components at the same regions: rivet button head and the countersunk areas.

Referring to figures 6.26c, logarithmic hoop strain distribution of interface ‘RH’ is shown. It is entirely tensile for both model 1 QS and model 1 Dyn. The strain magnitude of model 1 Dyn is higher in the rivet button area and the magnitude of model 1 QS is higher in the rivet-skin area. It is almost the same in the rivet-countersunk area for both model 1 QS and model 1 Dyn.

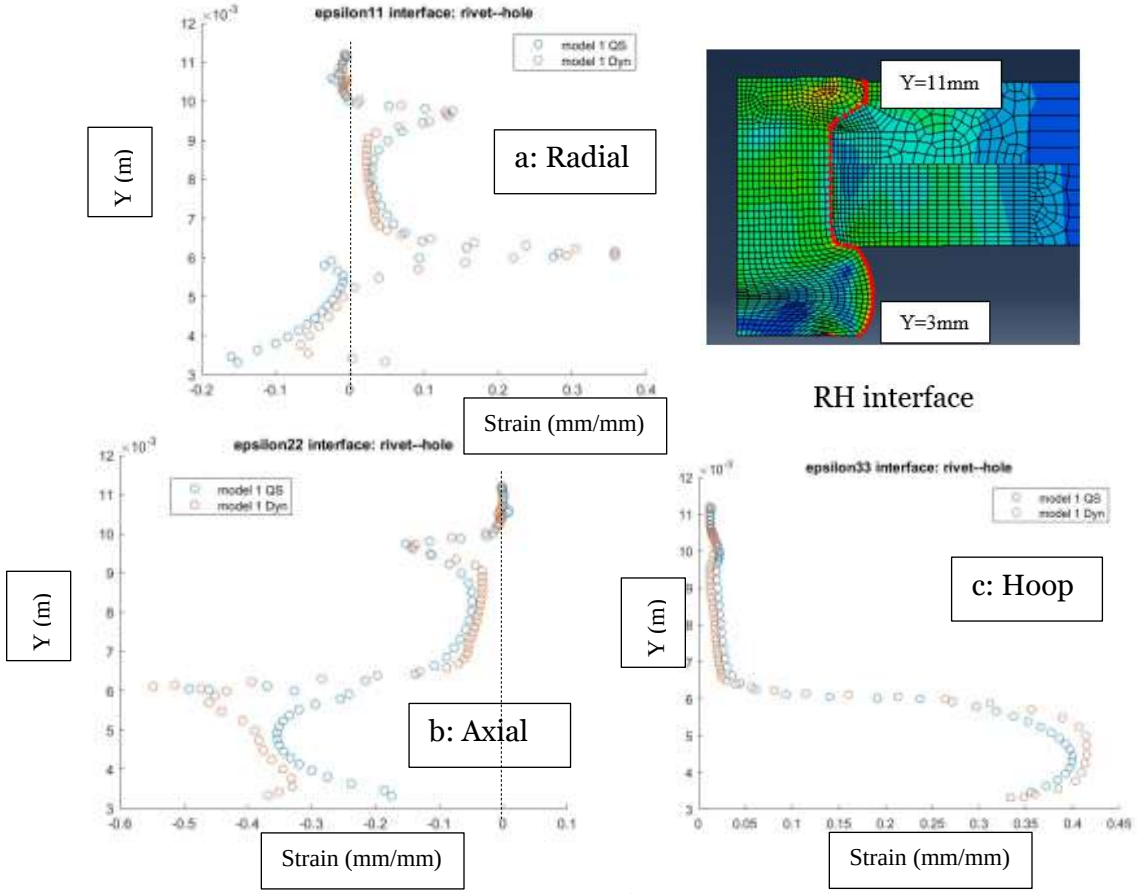

Figure 6.26. Strain distributions within RH interface. a: Radial. b: Axial, c: Hoop. Model-1 QS: Chapter 6 quasi-static simulation, Model-1 Dyn: Chapter 6 partial dynamic simulation. X-axis: mm/mm, Y-axis: m

Stress components are compared to the V-M stress to evaluate the possibility of crack nucleation. D_b is between 1.4d-1.6d for a joint of good quality. From table 6.1, D_b of Model 1 QS is 1.476d and D_b of Model 1 Dyn is 1.49d. Figure 6.27 shows stress levels at *mesh elements with the highest magnitude of the stress components* within model 1 QS and model 1 Dyn FE meshes.

Component	Stress	V-M Stress	Stress/V-M
radial (11)	(Pa)	(Pa)	
D226 upper pa-1 1	2.10E+08	1.49E+08	1.41
Riv 223 pa-SI-1 749	-8.63E+08	5.93E+08	-1.46
axial (22)			
Riv 223 pa-SI-1 657	4.13E+08	4.00E+08	1.03
D226 lower pa-1 305	-5.50E+08	4.65E+08	-1.18
hoop (33)			
Riv 223 pa-SI-1 304	4.85E+08	4.97E+08	0.98
D226 lower pa-1 244	-8.91E+08	1.08E+09	-0.83
shear (12)			
D226 lower pa-1 244	5.64E+08	1.08E+09	0.52
Riv 223 pa-SI-1 608	-3.41E+08	6.63E+08	-0.51

Model 1 QS

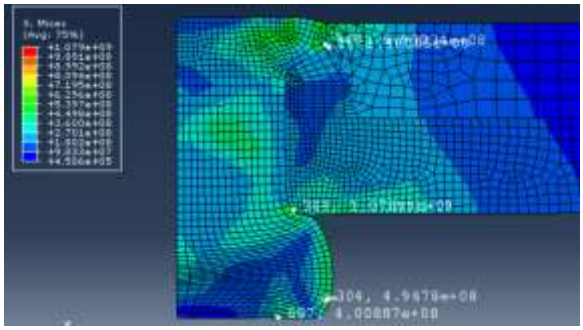

Model 1 QS

Component	Stress	V-M Stress	Stress/V-M
radial (11)	(Pa)	(Pa)	
D226 upper pa-1 1	1.35E+08	1.87E+08	0.72
Riv 223 pa-SI-1 704	-6.98E+08	4.91E+08	-1.42
axial (22)			
Riv 223 pa-SI-1 593	2.76E+08	1.94E+08	1.42
Riv 223 pa-SI-1 672	-4.88E+08	3.90E+08	-1.25
hoop (33)			
Riv 223 pa-SI-1 681	5.04E+08	5.64E+08	0.89
D226 lower pa-1 535	-6.08E+08	3.18E+08	-1.91
shear (12)			
Riv 223 pa-SI-1 198	1.77E+08	3.54E+08	0.50
Riv 223 pa-SI-1 448	-2.45E+08	4.96E+08	-0.49

Model 1 Dyn

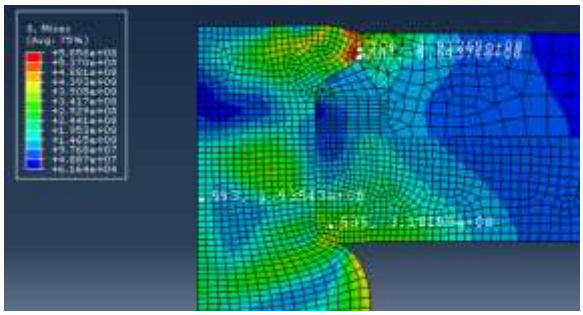

Model 1 Dyn

Figure 6.27. Data for Joint Quality Analysis

In model 1 QS, highest compressive ratio of stress component/V-M stress in the entire FE mesh is exhibited by mesh element 749 of the rivet and it is -1.46. This element is located just above the rivet wedge and is part of region 'A'. Mesh element 244 of the inner skin has the highest compressive stress component of -891 MPa. This element is located just above the rivet button and is part of region 'F'. Mesh element 1 of the outer skin has the highest tensile ratio of stress component/V-M stress (1.41). This element is located just above the wedge surface of the outer

skin and is part of region ‘D’. Mesh element 244 of the inner skin has highest tensile stress component (564 MPa), although it is the shear stress component. Rivet elements with high (stress/V-M) ratios—element 304 and 657—are at the free surface of the rivet button. So, these are not part of the crack nucleation discussion.

Due to the high (stress/V-M) ratio value of element 749 of the rivet and due to the high magnitude of radial stress of element 244 of the inner skin, these two mesh locations are most critical for crack nucleation because of compression-induced shear. Element 749 of the rivet is more critical than element 244 of the inner skin because of the higher (stress/V-M) ratio (-1.46 vs. -0.83).

In model 1 Dyn, highest compressive ratio of stress component/V-M stress in the entire FE mesh is exhibited by mesh element 535 of the inner skin and it is -1.91. This element is part of region ‘F’ and is near rivet shank. Mesh element 704 of the rivet has the highest compressive stress component of -698 MPa. This element is located at the rivet crown and is part of region ‘A’. Mesh element 593 of the rivet has the highest tensile ratio of stress component/V-M stress (1.42). This element is located at the rivet axis and is part of region ‘B’. Mesh element 681 of the rivet has highest tensile stress component (504 MPa). This element is located just above the rivet wedge and is part of region ‘A’. Element 535 of inner skin and element 593 of rivet are in the interior of their respective parts. So, these are not critical from crack nucleation perspective.

Due to the high (stress/V-M) ratio value of element 704 of the rivet and due to the high magnitude of hoop stress of element 681 of the rivet, these two mesh locations are most critical for crack nucleation. Element 681 of the rivet is more critical than element 704 of the rivet because of the presence of high tensile hoop stress.

6.4 SUMMARY

Two-dimensional partial dynamic riveting FE model was built and simulated. Residual stress and strain results from the simulation were presented and discussed. A gap was observed between the rivet shank the outer skin below the countersink wedge. This resulted in tensile stresses below the countersink wedge. Compressive stress was observed in this location in the quasistatic squeeze simulation. Tensile axial stress was observed at the rivet-upper skin interface at the rivet wedge and compressive axial stress was observed at the rivet-inner skin interface at the rivet button. In the partial dynamic percussive simulation, rivet crown region adjacent to the rivet wedge observed to be most critical for crack nucleation.

Chapter 7. FULL DYNAMIC MODEL DESIGN AND RESULTS

7.1 INTRODUCTION

In this chapter, FE modeling and analysis of a two-dimensional, dynamic percussive riveting model is presented and discussed. In this model, *both rivet hammer and bucking bar are free to move*. Hence, *this model is termed as "Full Dynamic"*. In this chapter, the full dynamic percussive simulation results are compared with quasistatic squeeze simulation results.

7.2 ADDITIONAL MODELING INFORMATION

The axisymmetric percussive (or dynamic) simulation for this repeated-impact riveting process was performed as per the method described in this section 4.3 and is referred to as "Model 2 Dyn". Geometric dimensions used are shown in table 4.4. The results are compared with the quasistatic simulation that has the same geometric dimensions. This quasistatic simulation is referred to as "Model 2 QS". Geometric dimensions from table 4.1 were considered. Refer to table 5.1 for the values of CL and TR for the "Model 2 Dyn" simulation. μ is 0.25 between rivet and sheet surfaces. μ is 0.2 between bucking bar/ rivet die and stackup surfaces. Stick-slip maximum shear stress limit of 269.62 MPa was used. +950 N push force b_Y and -1600 N push force h_Y were used in this simulation.

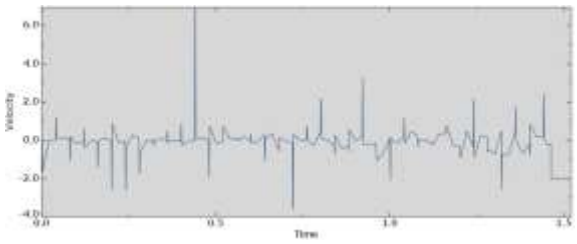

Figure 7.1. "Model 2 Dyn" simulation Bucking Bar Axial Velocity-Time Profile. X-axis: seconds, Y-axis: [m/s]

The percussive simulations are completed in eighty load steps—40 load steps and 40 unloading steps. Each load-unload cycle takes 40 ms to complete. The total simulation time scale is 1.6 seconds. The axial velocity profile of the bucking bar (shown in figure 7.1) over the duration of Model 2 Dyn simulation indicates the back-and-forth motion of the bucking bar.

7.3 Results and Discussion

The percussive riveting process is a multiple-impact process and the joint is formed over the span of a number of strokes. For the set of percussive riveting simulation in this chapter, about forty strokes were needed to attain target button height and diameters. Target button height is 25-30% of L_{shank} and target button diameter was 1.45-1.5 of D_{shank}. The measured geometric attributes (shown in figure 5.3) of the simulation are given in table 7.1.

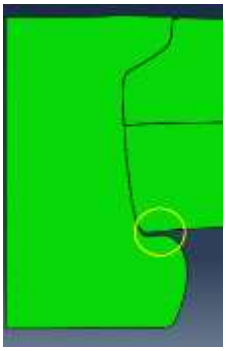

Figure 7.2. Axial Gap found in Percussive Simulation (circled in yellow).

Table 7.1. Normalized geometric attribute measurements. R_1 normalized with R_{crown}; R_2, R_3, R_4, R_{button} normalized with R_{shank}; Gap normalized with $t_{inner\text{-}Skin}$; H_{button} normalized with L_{shank}

Normalized	R_1	R_2	R_3	R_4	Gap	H_{button}	R_{button}
Model 2 QS	1.01	1.016	1.017	1.044	--	0.286	1.48
Model 2 Dyn	1.033	1.023	1.025	1.152	0.034	0.253	1.504

It is seen that the values of R_1-R_4 are all greater for the percussive simulation compared to the quasistatic simulation. This is because there is *greater radial expansion of the rivet shank in the percussive riveting process compared to the quasistatic squeeze riveting process*. Referring to figure 7.2, there exists a gap between the inner skin and the top of the rivet button in the case of percussive simulation. The axial gap is around 3-4% of the thickness of the inner skin of the simulation stackup. There is miniscule axial gap in the quasistatic simulation of the order of few μm. *The rivet button of percussive simulation is found to be of larger radius compared to the quasistatic simulation and the button height is also smaller compared to quasistatic simulation.* The *larger* values of R_1-R_4 and R_{button} of percussive simulations occur because of significant stress wave propagation effects, these effects are absent in the quasistatic riveting process.

Also, *larger* values of R_1-R_4 and R_{button} of percussive simulations are observed because of the *absence of heat transfer by convection*. Only *conduction* is allowed as input in the coupled structural-thermal simulations. This leads to a *higher temperature rise* than what is expected in the actual process. Another reason is the *repeated contact* between the rivet and the skins at the interfaces between the rivet and skins because of *multiple hammer strokes* causes the *deformation and temperature* at these interfaces to *exceed* what is observed in the quasistatic *squeeze riveting* process.

It is possible to achieve same H_{button} and R_{button} for both quasistatic and percussive techniques but R_1 and R_4 will be larger in the case of percussive process because of enhanced radial material flow in the crown region and in the rivet region adjacent to the inner skin resulting from impact energy induced stress-wave propagation and higher temperature rise.

Figure 7.3 displays the evolution the rivet forming over the span of the entire “Model 2 Dyn” simulation. First several hits result in only small plastic deformation of the rivet. Gradually, the rivet shank contacts the hole wall surfaces and the rivet deformation increases along with hole expansion. This is followed by incremental button formation. The rivet button exhibits a triaxial stress state. The radial expansion of the hole is seen to be non-uniform along the hole axis. The

expansion is found to be more in the inner skin region compared to the outer skin region as can be verified using the R_4 and R_3 from table 7.1 of the percussive simulation, "Model 2 Dyn". Also, there is *relative motion* between the rivet and the skins in the percussive simulation. This motion is not restricted in the simulation. This eventually results in *larger* R_1-R_4 values compared to the quasistatic squeeze simulation.

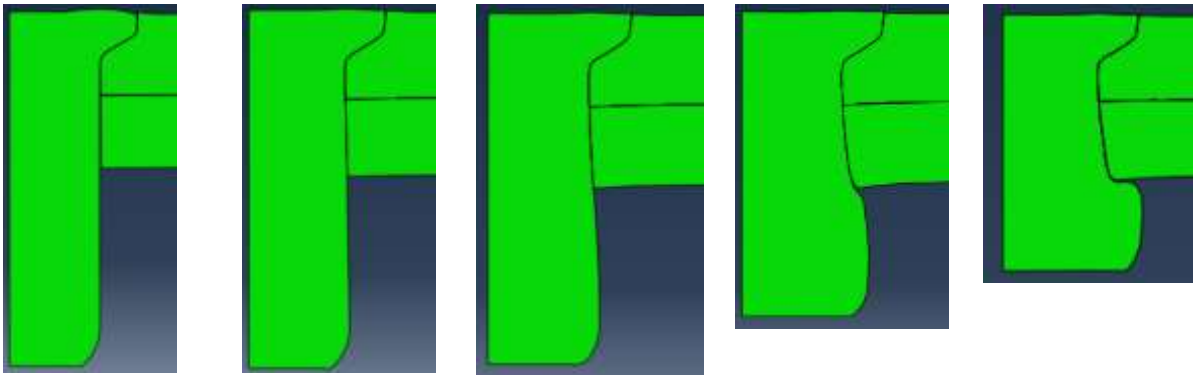

After 1st Hit | After 10th Hit | After 20th Hit | After 30th Hit | End of simulation

Figure 7.3. Rivet Deformation Evolution of the "Model 2 Dyn" Stackup over the span of entire simulation.

Distributions of strains and stresses in the vicinity of the rivet are shown in figures 7.4 and 7.5, respectively. It is observed that the levels of strains in the crown region of the rivet and the outer skin and the region of the inner skin adjacent to the top of the rivet button are higher in the percussive joint compared to the quasistatic squeeze joint.

Referring to table 7.1 and figure 7.6, the values of R_1-R_4 are all greater in model 2 Dyn compared to model 2 QS. This indicates *greater radial expansion* of the rivet from crown to the head of the rivet button. The rivet button diameter of model 2 Dyn is greater than model 2 QS. The rivet button height of model 2 Dyn is smaller than model 2 QS. There is an axial gap between the head of the rivet button and the inner surface of the inner skin. This will lead to a difference in the stress profiles of model 2 QS and model 2 Dyn in the interfaces that cover this area.

MODEL 2 DYN ε_{11} plot MODEL 2 DYN ε_{22} plot MODEL 2 DYN ε_{33} plot

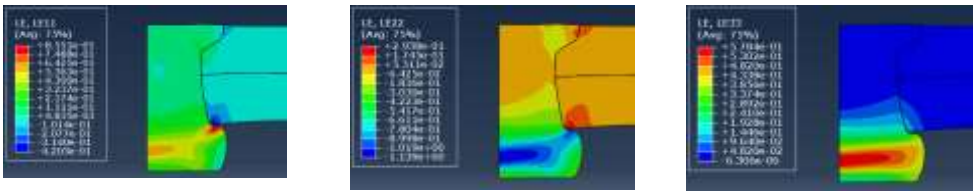

MODEL 2 QS ε_{11} plot MODEL 2 QS ε_{22} plot MODEL 2 QS ε_{33} plot

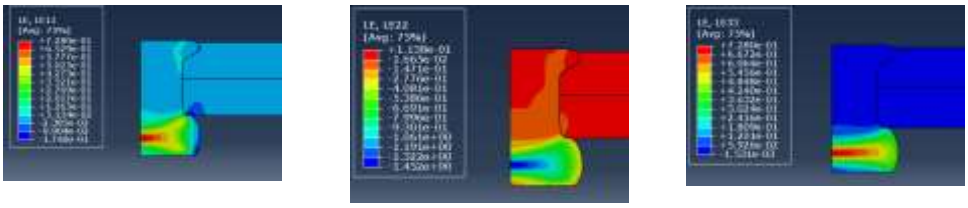

Figure 7.4. Residual Logarithmic Strain Distributions of the Two Simulations.

MODEL 2 DYN σ_{11} plot MODEL 2 DYN σ_{22} plot MODEL 2 DYN σ_{33} plot

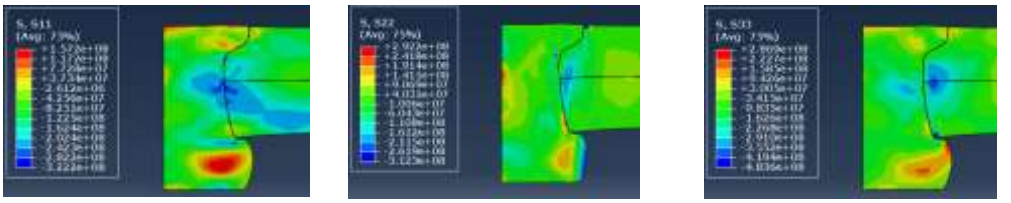

MODEL 2 QS σ_{33} plot MODEL 2 QS σ_{22} plot MODEL 2 QS σ_{11} plot

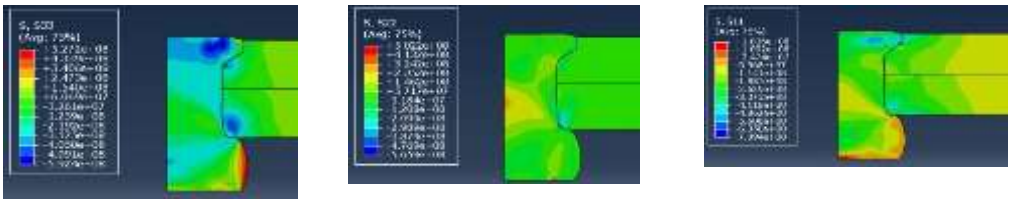

Figure 7.5. Residual Stress Distributions of the Two Simulations.

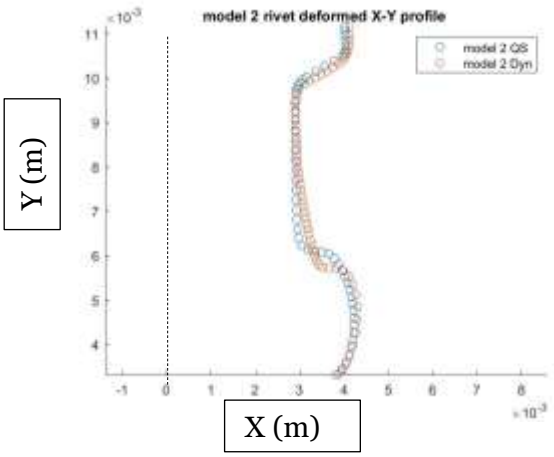

Figure 7.6. Deformed rivet X-Y profile at the interface of rivet and rivet hole at the end of riveting process. Model 2 QS: quasi-static profile, Model 2 Dyn: full dynamic profile. X-axis: m, Y-axis: m

Figure 7.7. Deformed stackup data regions: A- Rivet crown, B- Rivet shank, C- Rivet button, D- Outer Skin adjacent to rivet, E- Outer Skin away from rivet, F- Inner Skin adjacent to rivet, G- Inner Skin away from rivet.

Residual stresses and strains of “Model 2 Dyn” simulation were extracted from the seven regions of the deformed stackup indicated in figure 7.7. Referring to figure 7.8a, radial stress distribution in region ‘A’ model 2 Dyn is shown. Radial stress is tensile adjacent to the crown of the upper skin (~ 32 MPa). It is also tensile adjacent to the wedge region (~ 67 MPa). At the head of the crown near the rivet axis, stress is tensile (~ 131 MPa). At the base of the crown near the rivet axis, stress is compressive (~ 63 MPa). Within the interior of the region 'A', there are areas of both tensile and compressive stresses. These *tensile* stresses are *not desirable* for a good quality joint.

Referring to figure 7.8b, axial stress distribution in region ‘A’ of model 2 Dyn is shown. Axial stress is both tensile and compressive adjacent to the crown of the upper skin (Tensile~ 24 MPa, Compressive ~ 11 MPa). It is *compressive* adjacent to the wedge region (~ 96 MPa). This is *desirable* in a good quality joint. At the head of the crown near the rivet axis, stress is tensile (~ 18 MPa). At the base of the crown near the rivet axis, stress is compressive (~ 211 MPa). At the base of the crown below the wedge, the stress is observed to be tensile (~ 201 MPa). Within the interior of the region 'A', there are areas of both tensile and compressive stresses.

Referring to figure 7.8c, hoop stress distribution in region ‘A’ of model 2 Dyn is shown. Hoop stress is *both tensile and compressive* adjacent to the crown of the upper skin (Tensile~ 11 MPa, Compressive ~ 52 MPa). Hoop stress needs to be *entirely compressive in this region* of a good quality joint. It is compressive adjacent to the wedge region (~ 60 MPa). At the head of the crown near the rivet axis, stress is tensile (~ 107 MPa). At the base of the crown near the rivet axis, stress is compressive (~ 105 MPa). Within the interior of the region 'A', there are areas of both tensile and compressive stresses.

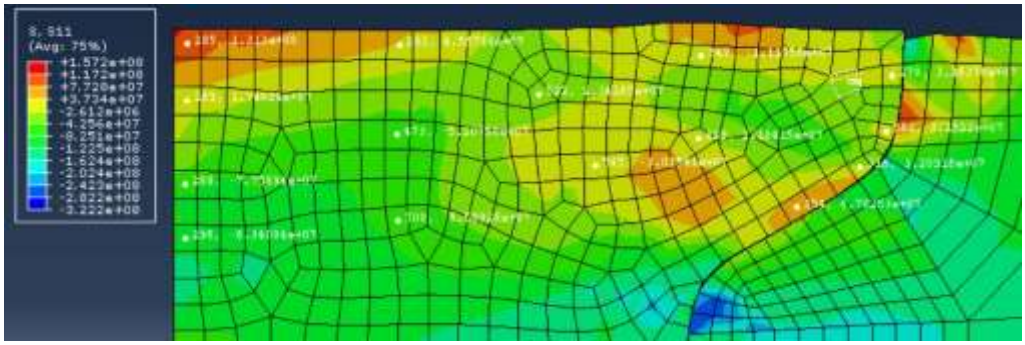

a: Radial

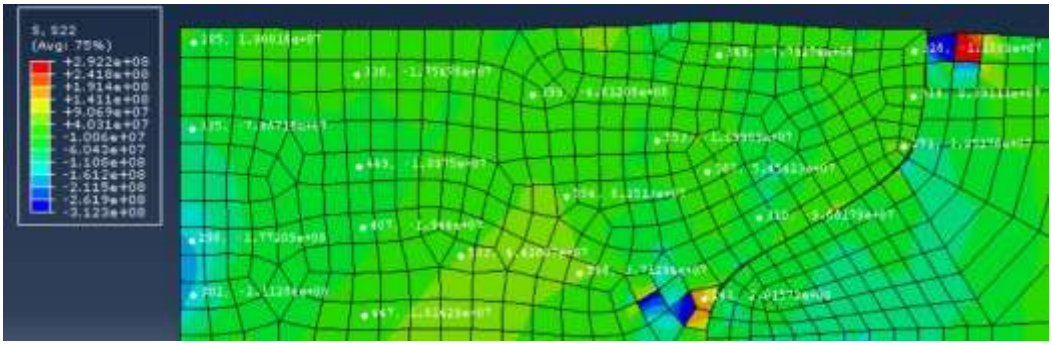

b: Axial

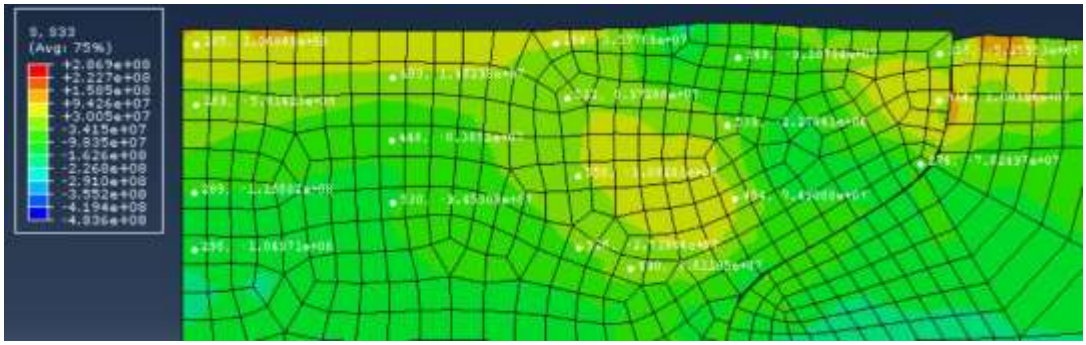

c: Hoop

Figure 7.8. Stress distributions within region ‘A’ of the ‘Model 2 Dyn’ stackup. a: Radial Stress, b: Axial Stress, c: Hoop Stress

Referring to figure 7.9a, logarithmic radial strain distribution in region ‘A’ of model 2 Dyn is shown. Radial strain is compressive adjacent to the crown of the upper skin (~ 0.1). It is tensile adjacent to the wedge region (~0.09). At the head of the crown near the rivet axis, strain is tensile (~ 0.0045). At the base of the crown near the rivet axis, strain is tensile (~ 0.014). At the base of the crown below the wedge, the strain is observed to be tensile (~0.175). Within the interior of the region 'A', the strain is observed to be tensile.

Referring to figure 7.9b, logarithmic axial strain distribution in region ‘A’ of model 2 Dyn is shown. Axial strain is tensile adjacent to the crown of the upper skin (~0.117). It is compressive adjacent to the wedge region (~ 0.08). At the head of the crown near the rivet axis, strain is tensile (~0.014). At the base of the crown near the rivet axis, strain is compressive (~0.008). At the base

of the crown below the wedge, the strain is observed to be compressive (~0.2). Within the interior of the region 'A', the strain is observed to be compressive.

Referring to figure 7.9c, logarithmic hoop strain distribution in region ‘A’ of model 2 Dyn is shown. The hoop strain is tensile across region ‘A’. Magnitude is greater adjacent to the outer skin (~ 0.04) compared to magnitude near the rivet axis (~ 0.02).

a: Radial

b: Axial

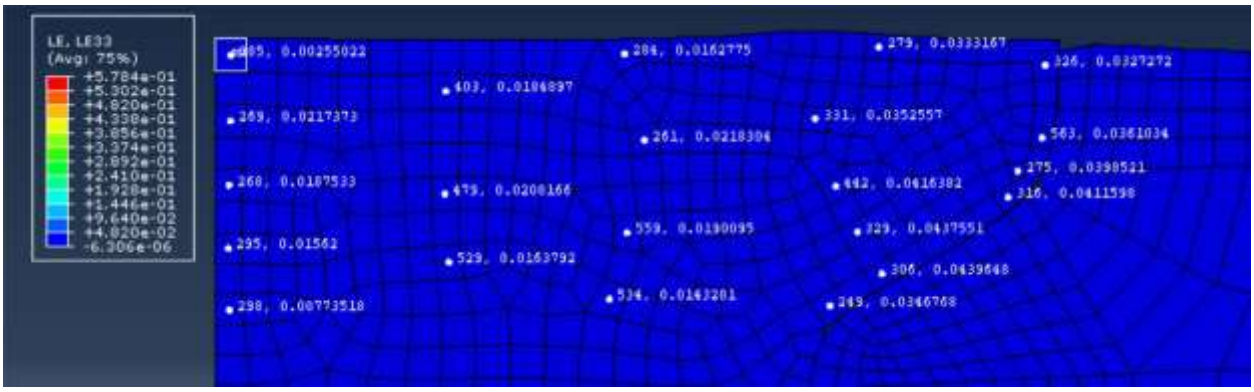

c: Hoop

Figure 7.9. Strain distributions within region 'A' of the 'Model 2 Dyn' stackup. a: Radial Strain, b: Axial Strain, c: Hoop Strain

Referring to figure 7.10a, radial stress distribution in region 'B' of model 2 Dyn is shown. Radial stress is compressive (~ 200 MPa) adjacent to skins *except* near the head of the rivet button (~ 50.5 MPa). It is compressive in the interior of region 'B'. It is also compressive near the rivet axis. Although, there is a small area of tensile stress near the rivet axis below region 'A' (~ 23 MPa).

Referring to figure 7.10b, axial stress distribution in region 'B' of model 2 Dyn is shown. Axial stress is compressive (~ 100 MPa) adjacent to skins *except* near the head of the rivet button (~ 200 MPa). It is tensile in the interior of region 'B' except adjacent to the rivet button head. It is also tensile near the rivet axis (~ 217 MPa).

Referring to figure 7.10c, hoop stress distribution in region 'B' of model 2 Dyn is shown. Hoop stress is compressive across region 'B' *except* near the head of the rivet button adjacent to the inner skin (~ 133 MPa). In the percussive simulation, there is a gap between the rivet and the inner skin near the head of the rivet button. This gap can be attributed to *large strains* in this region because of *temperature rise* due to *repeated impact*. There is thermally induced softening in this region which leads to *higher* material flow. This *gap* is *not desirable* in a good quality joint. But the *gap formation* is *unavoidable* in a coupled structural-thermal numerical simulation with

no convective heat transfer. Due to the *different curvature* of the *skins* because of the application of the rivet hammer (1600 N) and bucking bar (950 N) *constraint forces* of *different magnitude*, R_4 of model 2 Dyn is greater than that of R_4 of model 2 QS. There is no rivet hammer in model 2 QS.

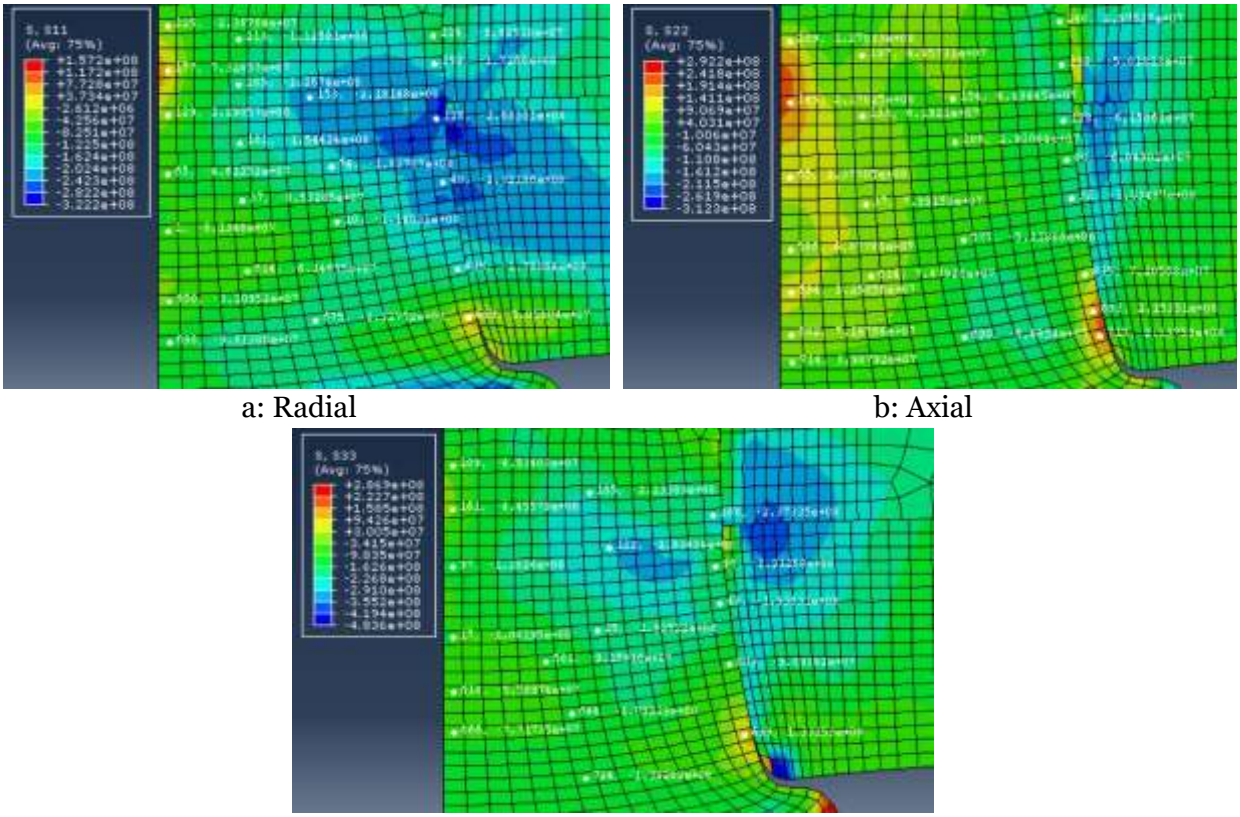

a: Radial b: Axial

c: Hoop

Figure 7.10. Stress distributions within region 'B' of the 'Model 2 Dyn' stackup. a: Radial Stress, b: Axial Stress, c: Hoop Stress

Referring to figure 7.11a, logarithmic radial strain distribution in region 'B' of model 2 Dyn is shown. Strain is tensile across region 'B'. Magnitude is higher (~ 0.12) near the head of the rivet button compared to the interior of region 'B' (~ 0.03) and compared to area near base of the region 'A' (~ 0.004).

Referring to figure 7.11b, logarithmic axial strain distribution in region ‘B’ of model 2 Dyn is shown. Strain is compressive across region ‘B’ except near the rivet axis at the base of region ‘A’ (~ 0.011). Magnitude of compressive strain is higher near the head of the rivet button (~0.31) compared to the interior of region ‘B’ (~ 0.08).

Referring to figure 7.11c, logarithmic hoop strain distribution in region ‘B’ of model 2 Dyn is shown. Strain is tensile across region ‘B’. Magnitude is higher near the head of the rivet button (~ 0.122) compared to the interior of region ‘B’ (~ 0.04) and compared to area near base of the region ‘A’ (~ 0.002).

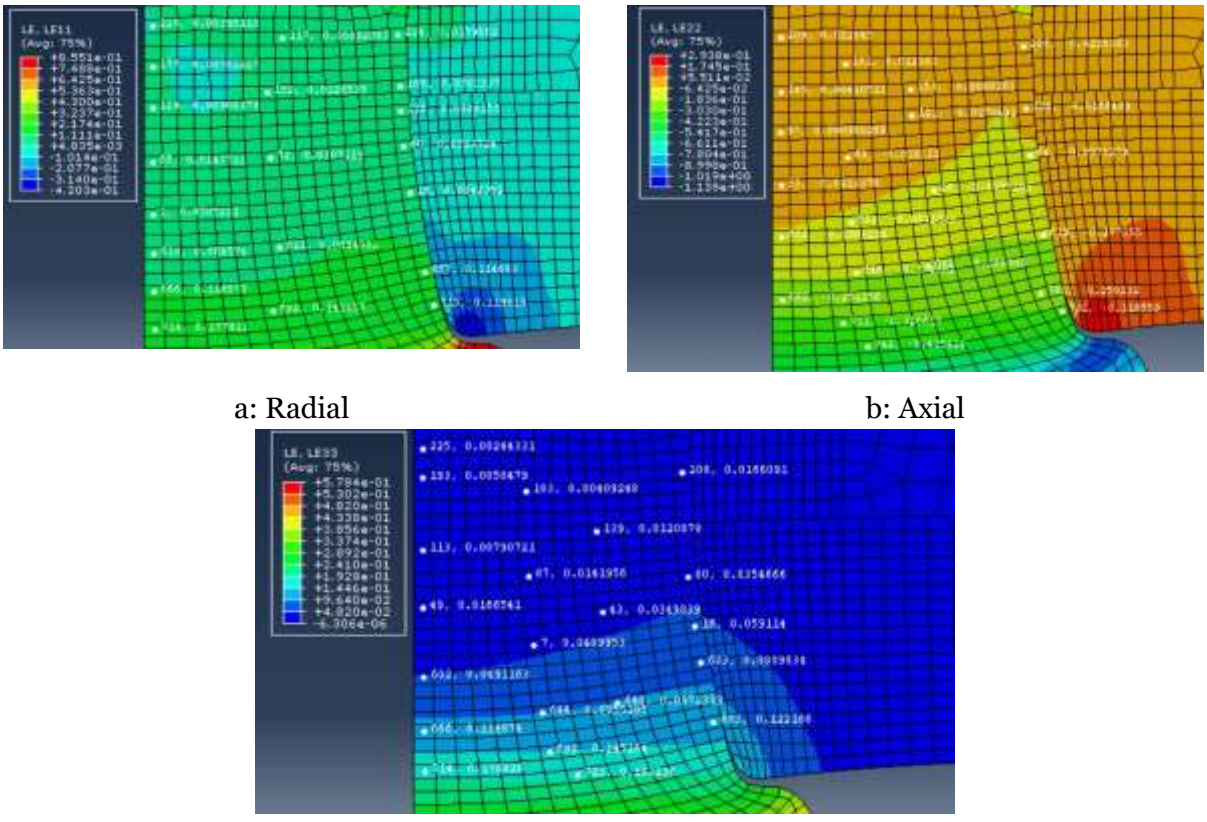

a: Radial

b: Axial

c: Hoop

Figure 7.11. Strain distributions within region ‘B’ of the ‘Model 2 Dyn’ stackup. a: Radial Strain, b: Axial Strain, c: Hoop Strain

Referring to figure 7.12a, radial stress distribution in region ‘C’ of model 2 Dyn is shown. Radial stress is compressive across region 'C', although there is a large area in the interior of region 'C' where the stress is tensile (~ 161 MPa). Stress is mostly compressive (~20 MPa) at the free surface of the rivet button.

Referring to figure 7.12b, axial stress distribution in region ‘C’ of model 2 Dyn is shown. Axial stress is compressive across region 'C', although there is a large area in the interior of region 'C' (~188 MPa) and an area near the rivet axis at the base of the rivet button (~105 MPa) where the stress is tensile. Stress is compressive at the free surface of the rivet button (~260 MPa).

Referring to figure 7.12c, hoop stress distribution in region ‘C’ of model 2 Dyn is shown. Stress is compressive near the rivet axis (~150 MPa), across a large area in the interior of region ‘C’, and near the head of the rivet button (~131 MPa). But there is also a large area in the interior of region ‘C’ (~187 MPa) and at the free surface of the rivet button (~236 MPa) where the hoop stress is tensile.

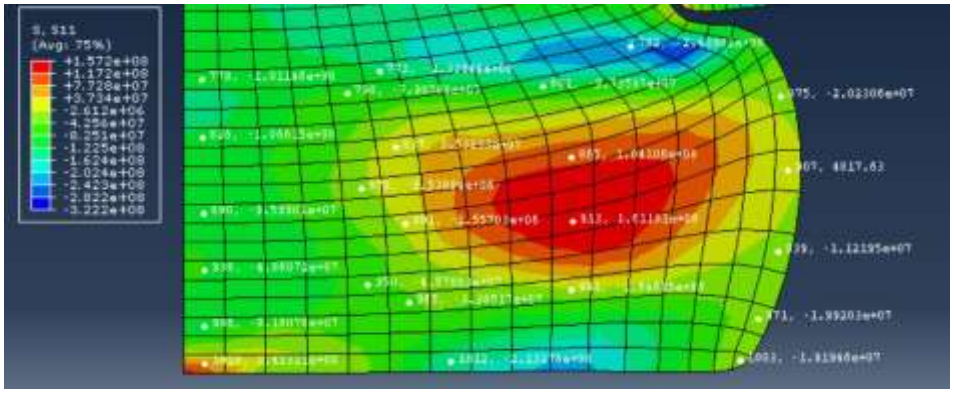

a: Radial

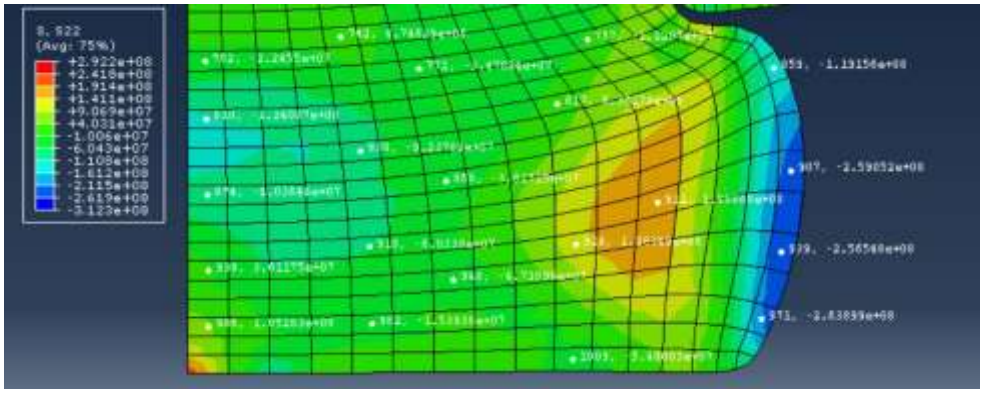

b: Axial

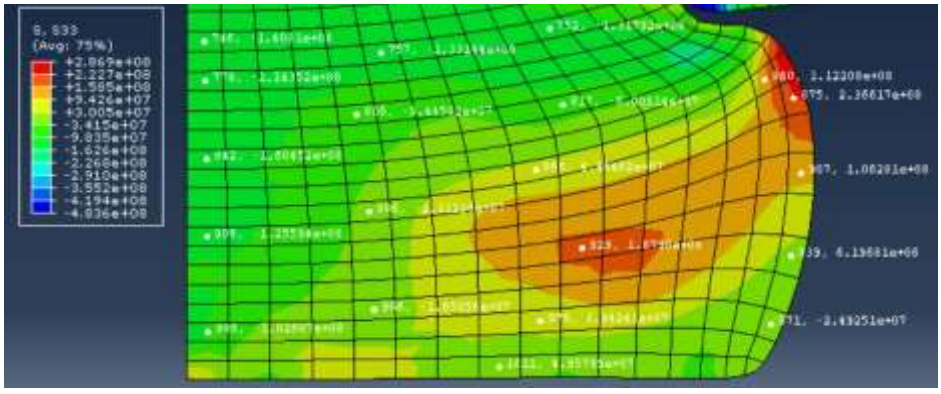

c: Hoop

Figure 7.12. Stress distributions within region ‘C’ of the ‘Model 2 Dyn’ stackup. a: Radial Stress, b: Axial Stress, c: Hoop Stress

Referring to figure 7.13a, logarithmic radial strain distribution in region ‘C’ of model 2 Dyn is shown. Strain is tensile across region ‘C’ except in a small area near the base of the rivet button at the free surface where the strain is compressive (~ 0.02).

Referring to figure 7.13b, logarithmic axial strain distribution in region ‘C’ of model 2 Dyn is shown. Axial strain is compressive across region ‘C’. There is region (color blue) that stretches from the rivet axis to the head of the rivet button where high magnitude of strain (~ 1) is observed. Areas outside this band in region ‘C’ have a lower axial strain magnitude (~ 0.4-0.6).

Referring to figure 7.13c, logarithmic hoop strain distribution in region ‘C’ of model 2 Dyn is shown. Hoop strain is tensile across region ‘C’. Strain is found to have a higher magnitude (> 0.5) in the central area of region ‘C’ (color red and orange).

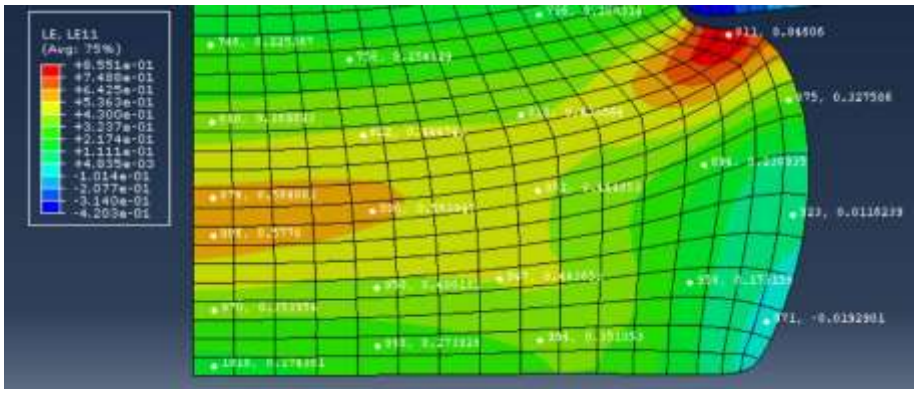

a: Radial

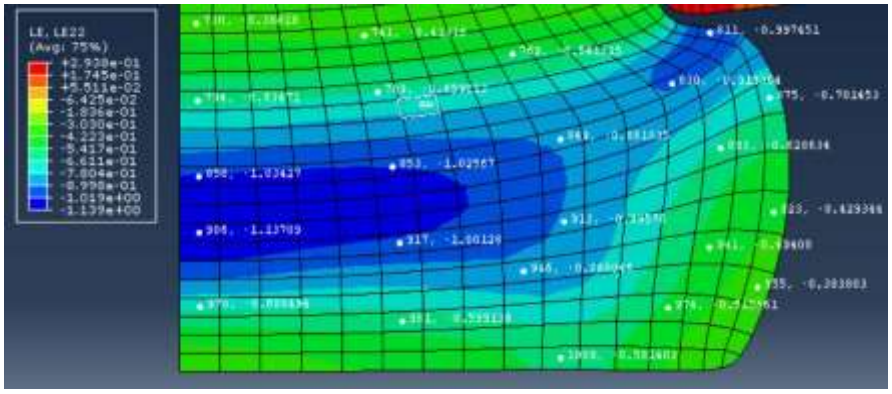

b: Axial

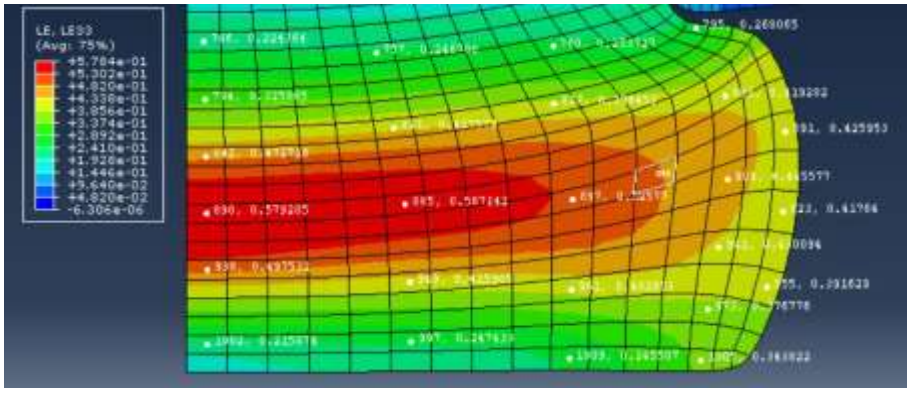

c: Hoop

Figure 7.13. Strain distributions within region 'C' of the 'Model 2 Dyn' stackup. a: Radial Strain, b: Axial Strain, c: Hoop Strain

Referring to figure 7.14a, radial stress distribution in region ‘D’ of model 2 Dyn is shown. Radial stress is tensile in the area adjacent to the rivet crown (~ 162 MPa). This is not desirable in a good quality joint. Stress is compressive in the wedge area (~ 36 MPa) and below the wedge area (~ 324 MPa). Stress is compressive adjacent to the rivet shank (~ 125-170 MPa). The radial stress is compressive in the interior of region 'D'.

Referring to figure 7.14b, axial stress distribution in region ‘D’ of model 2 Dyn is shown. Axial stress is compressive in the area adjacent to the rivet crown (~ 305 MPa). Stress is compressive in the wedge area (~ 46 MPa) and below the wedge area (~ 75 MPa). Stress is tensile adjacent to the rivet shank (~ 33-88 MPa). The axial stress is compressive in the interior of region 'D'.

Referring to figure 7.14c, hoop stress distribution in region ‘D’ of model 2 Dyn is shown. Hoop stress is tensile in the area adjacent to the rivet crown (~ 100 MPa). This is not desirable in a good quality joint. Stress is compressive in the wedge area (~ 152 MPa) and below the wedge area (~ 16 MPa). Stress is compressive adjacent to the rivet shank (~ 75 MPa). The hoop stress is compressive in the interior of region 'D'.

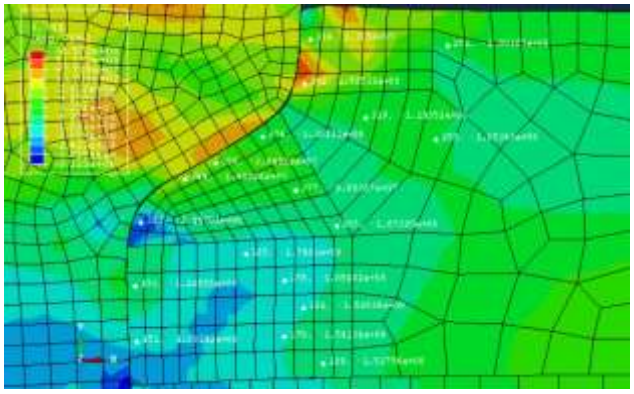

a: Radial

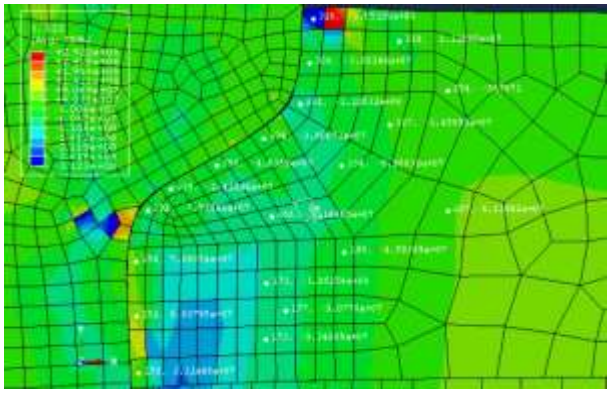

b: Axial

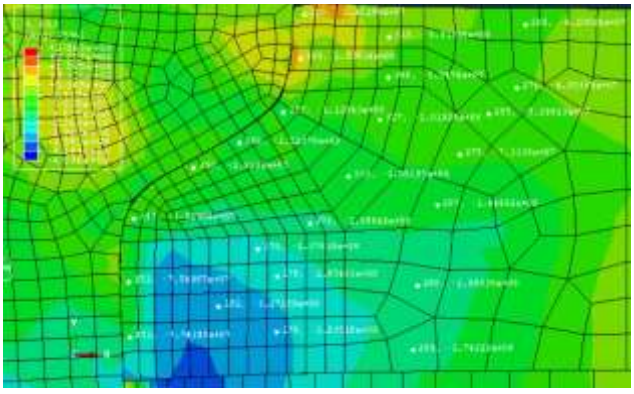

c: Hoop

Figure 7.14. Stress distributions within region ‘D’ of the ‘Model 2 Dyn’ stackup. a: Radial Stress, b: Axial Stress, c: Hoop Stress

Referring to figure 7.15a, logarithmic radial strain distribution in region ‘D’ of model 2 Dyn is shown. Radial strain is compressive in the area adjacent to the rivet crown (~ 0.16). Strain is tensile in the wedge area (~ 0.05) and below the wedge area (~ 0.01). Strain is tensile adjacent to the rivet shank (~ 0.037). The radial strain is compressive in the interior area of region 'D' adjacent to rivet crown and wedge. The radial strain is tensile of small magnitude in the interior area of region 'D' adjacent to the rivet shank (~ 0.001).

Referring to figure 7.15b, logarithmic axial strain distribution in region ‘D’ of model 2 Dyn is shown. Axial strain is tensile in the area adjacent to the rivet crown (~ 0.12). Strain is compressive in the wedge area (~ 0.05) and below the wedge area (~ 0.02). Strain is compressive adjacent to the rivet shank (~ 0.038). The axial strain is tensile in the interior area of region 'D' adjacent to rivet crown and wedge. The axial strain is compressive in the interior area of region 'D' adjacent to the rivet shank (~ 0.014).

Referring to figure 7.15c, logarithmic hoop strain distribution in region ‘D’ of model 2 Dyn is shown. Hoop strain is tensile across region 'D'. The magnitude is higher near the rivet-skin interface (~ 0.01-0.03) compared to the magnitude away from the rivet-skin interface (<0.012).

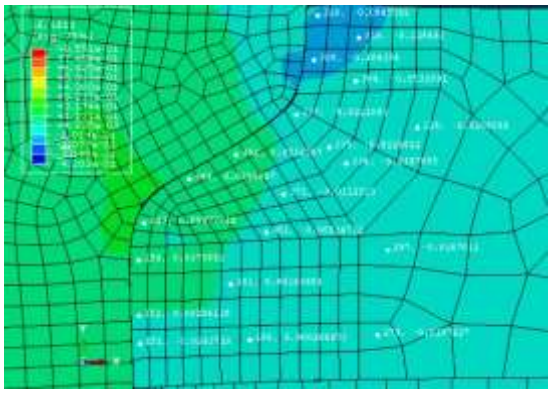

a: Radial

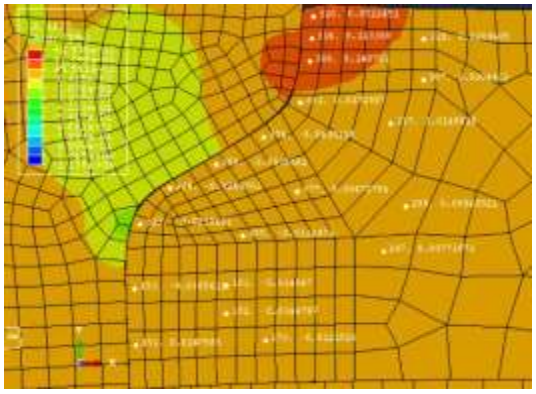

b: Axial

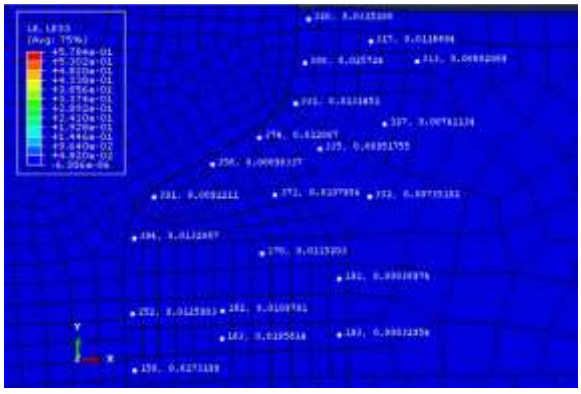

c: Hoop

Figure 7.15. Strain distributions within region ‘D’ of the ‘Model 2 Dyn’ stackup. a: Radial Strain, b: Axial Strain, c: Hoop Strain

Referring to figure 7.16a, radial stress distribution within regions ‘E’ and ‘G’ of Model-2 Dyn simulation is shown. Radial stress is compressive across regions 'E' and 'G'. The magnitude is higher in the areas adjacent to regions 'D' and 'F' (~ 100 MPa) compared to the magnitude in the areas away from these regions (~ 10-50 MPa).

Referring to figure 7.16b, axial stress distribution within regions ‘E’ and ‘G’ of Model-2 Dyn is simulation is shown. The magnitude of compressive and tensile axial stresses in regions ‘E’ and ‘G’ is small (< 15 MPa).

Referring to figure 7.16c, hoop stress distribution within regions ‘E’ and ‘G’ of Model-2 Dyn simulation is shown. Hoop stress is tensile across regions 'E' and 'G'. The magnitude is higher in the areas adjacent to regions 'D' and 'F' (~ 70 MPa) compared to the magnitude in the areas away from these regions (~ 30 MPa).

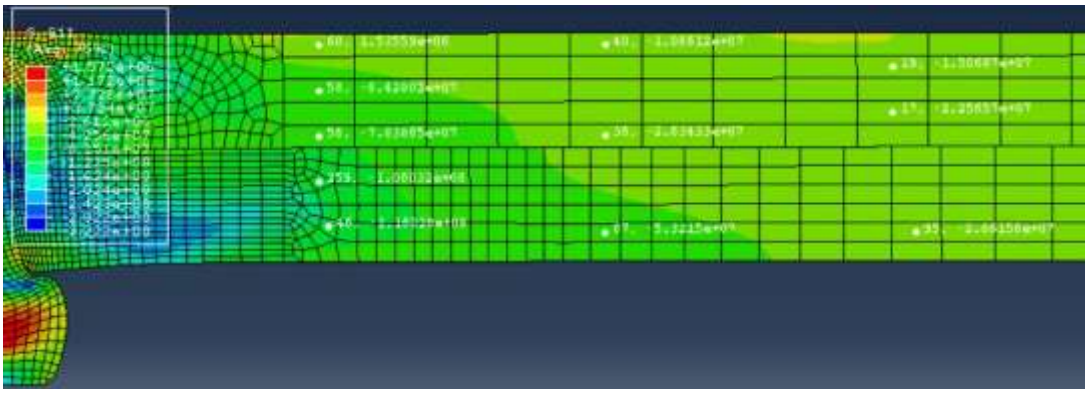

a: Radial

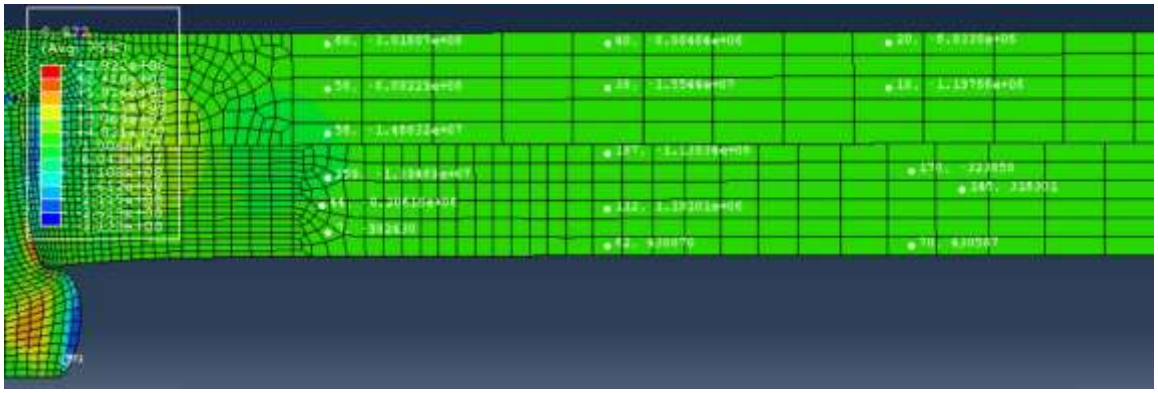

b: Axial

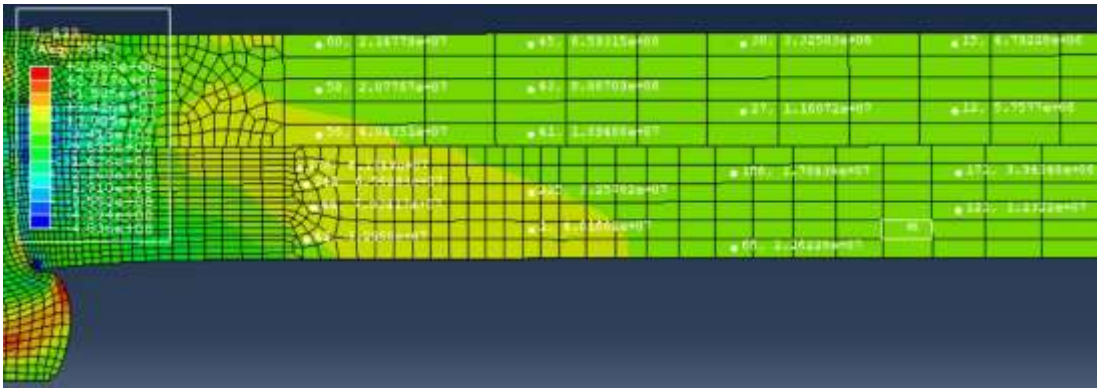

c: Hoop

Figure 7.16. Stress distributions within regions ‘E’ and ‘G’ of the ‘Model 2 Dyn’ stackup. a: Radial Stress, b: Axial Stress, c: Hoop Stress

Referring to figure 7.17a, logarithmic radial strain distribution within regions ‘E’ and ‘G’ of Model-2 Dyn simulation is shown. The radial strain is compressive and has small magnitude across regions ‘E’ and ‘G’ (<0.003).

Referring to figure 7.17b, logarithmic axial strain distribution within regions ‘E’ and ‘G’ of Model-2 Dyn simulation is shown. The axial strain is tensile and has small magnitude across regions ‘E’ and ‘G’ (<0.001). Axial strain is tensile because of the tie constraint used in the Model 2 Dyn (full dynamic percussive) simulation.

Referring to figure 7.17c, logarithmic hoop strain distribution within regions ‘E’ and ‘G’ of Model-2 Dyn simulation is shown. The hoop strain is tensile and has small magnitude across regions ‘E’ and ‘G’ (<0.003).

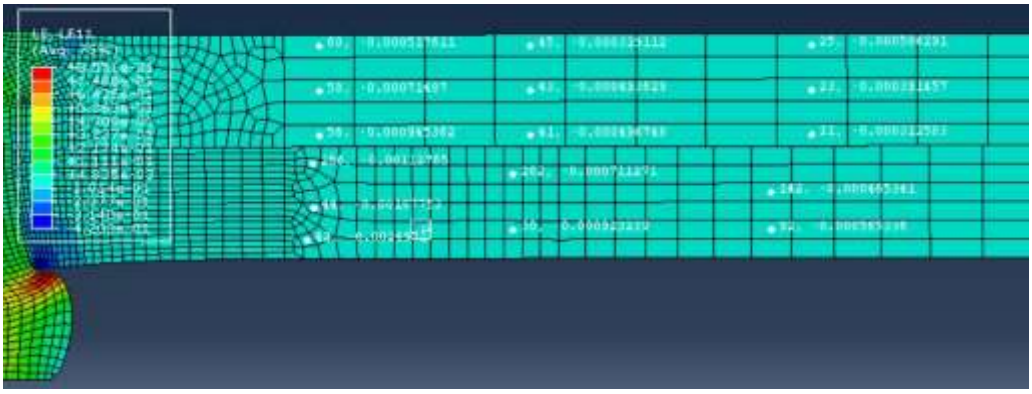

a: Radial

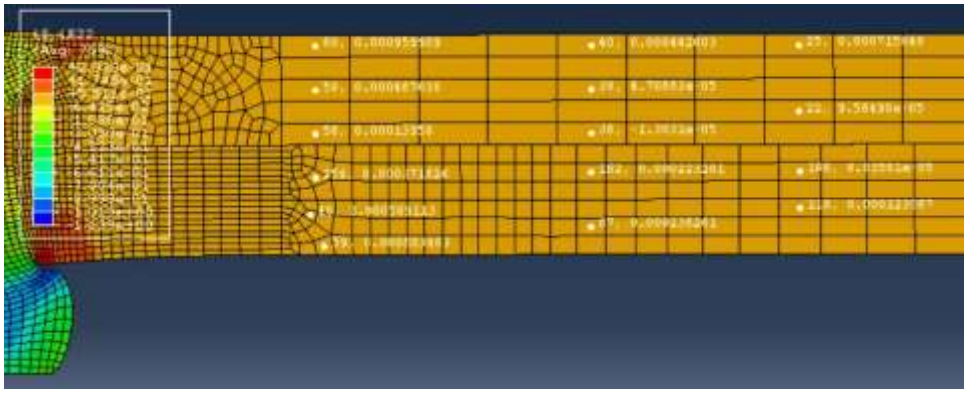

b: Axial

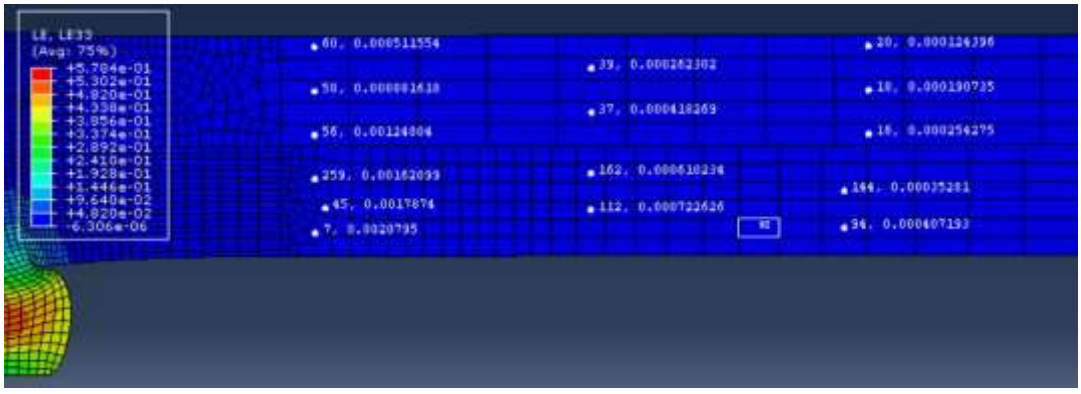

c: Hoop

Figure 7.17. Strain distributions within regions ‘E’ and ‘G’ of the ‘Model 2 Dyn’ stackup. a: Radial Strain, b: Axial Strain, c: Hoop Strain

Referring to figure 7.18a, radial stress distribution within region ‘F’ of Model-2 Dyn simulation is shown. Radial stress is compressive across region ‘F’. Magnitude is higher in the area of region ‘F’ adjacent to region ‘D’ near the rivet shank (~ 309 MPa).

Referring to figure 7.18b, axial stress distribution within region ‘F’ of Model-2 Dyn simulation is shown. Axial stress is compressive in area of region ‘F’ adjacent to the rivet shank (~ 150 MPa). Tensile stresses are found in the interior of region ‘F’ (~ 40 MPa).

Referring to figure 7.18c, hoop stress distribution within region ‘F’ of Model-2 Dyn simulation is shown. Hoop stress is compressive across region ‘F’. There is small area of tensile hoop stress adjacent to the rivet shank near region ‘D’ (~ 100 MPa) and adjacent to the head of the rivet button (~174 MPa).

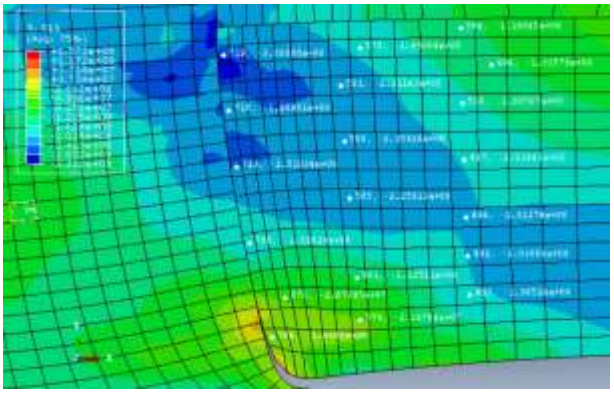

a: Radial

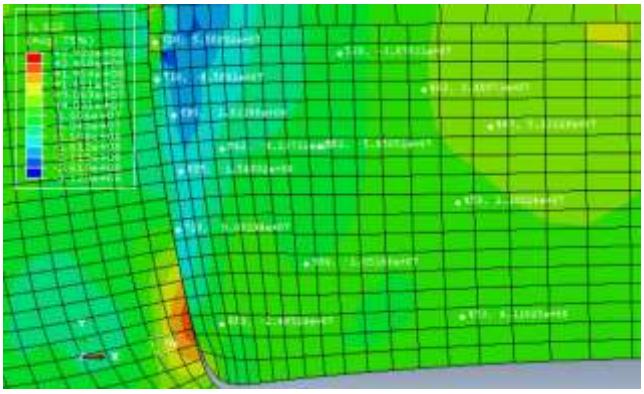

b: Axial

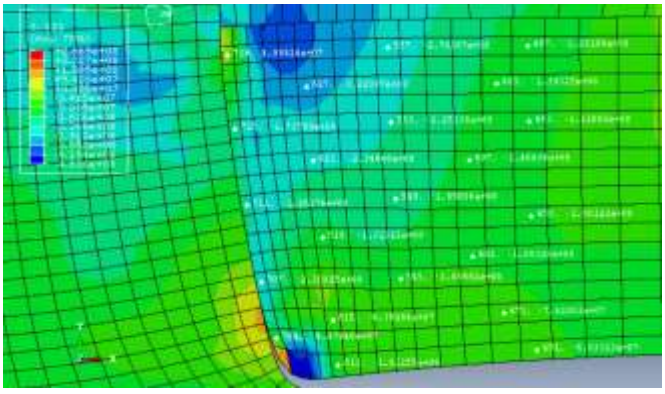

c: Hoop

Figure 7.18. Stress distributions within region ‘F’ of the ‘Model 2 Dyn’ stackup. a: Radial Stress, b: Axial Stress, c: Hoop Stress

Referring to figure 7.19a, logarithmic radial strain distribution within region ‘F’ of Model-2 Dyn simulation is shown. Radial strain is compressive across region ‘F’. The magnitude is higher near the head of the rivet button (~ 0.05) compared to other areas in region ‘F’.

Referring to figure 7.19b, logarithmic axial strain distribution within region ‘F’ of Model-2 Dyn simulation is shown. Axial strain is tensile across region ‘F’. The magnitude is higher near the head of the rivet button (~ 0.29) compared to other areas in region ‘F’.

Referring to figure 7.19c, logarithmic hoop strain distribution within region ‘F’ of Model-2 Dyn simulation is shown. Hoop strain is tensile across region ‘F’. The magnitude is higher near the head of the rivet button (~ 0.1-0.15) compared to other areas in region ‘F’.

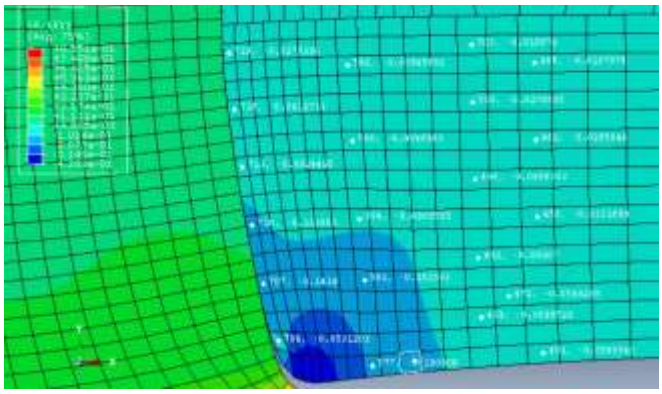

a: Radial

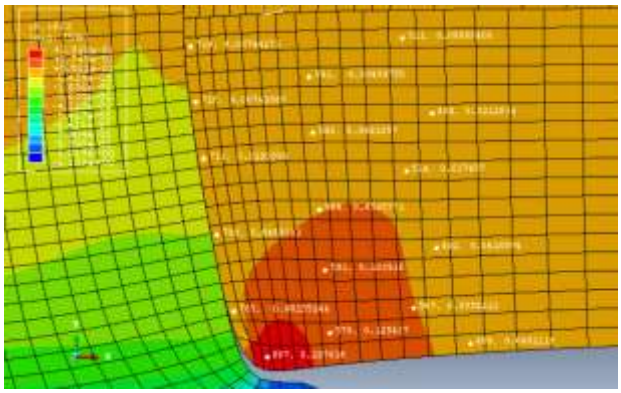

b: Axial

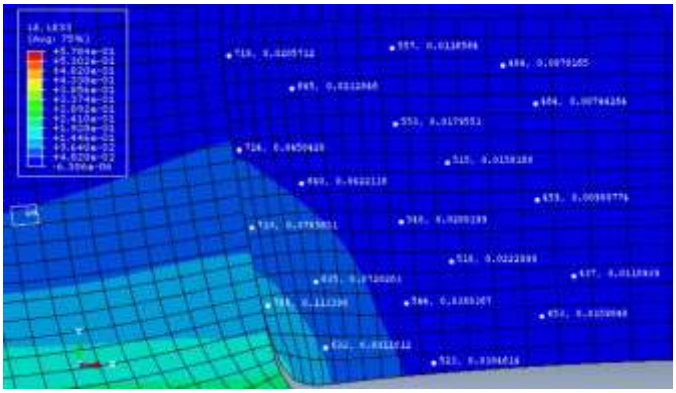

c: Hoop

Figure 7.19. Strain distributions within region ‘F’ of the ‘Model 2 Dyn’ stackup. a: Radial Strain, b: Axial Strain, c: Hoop Strain

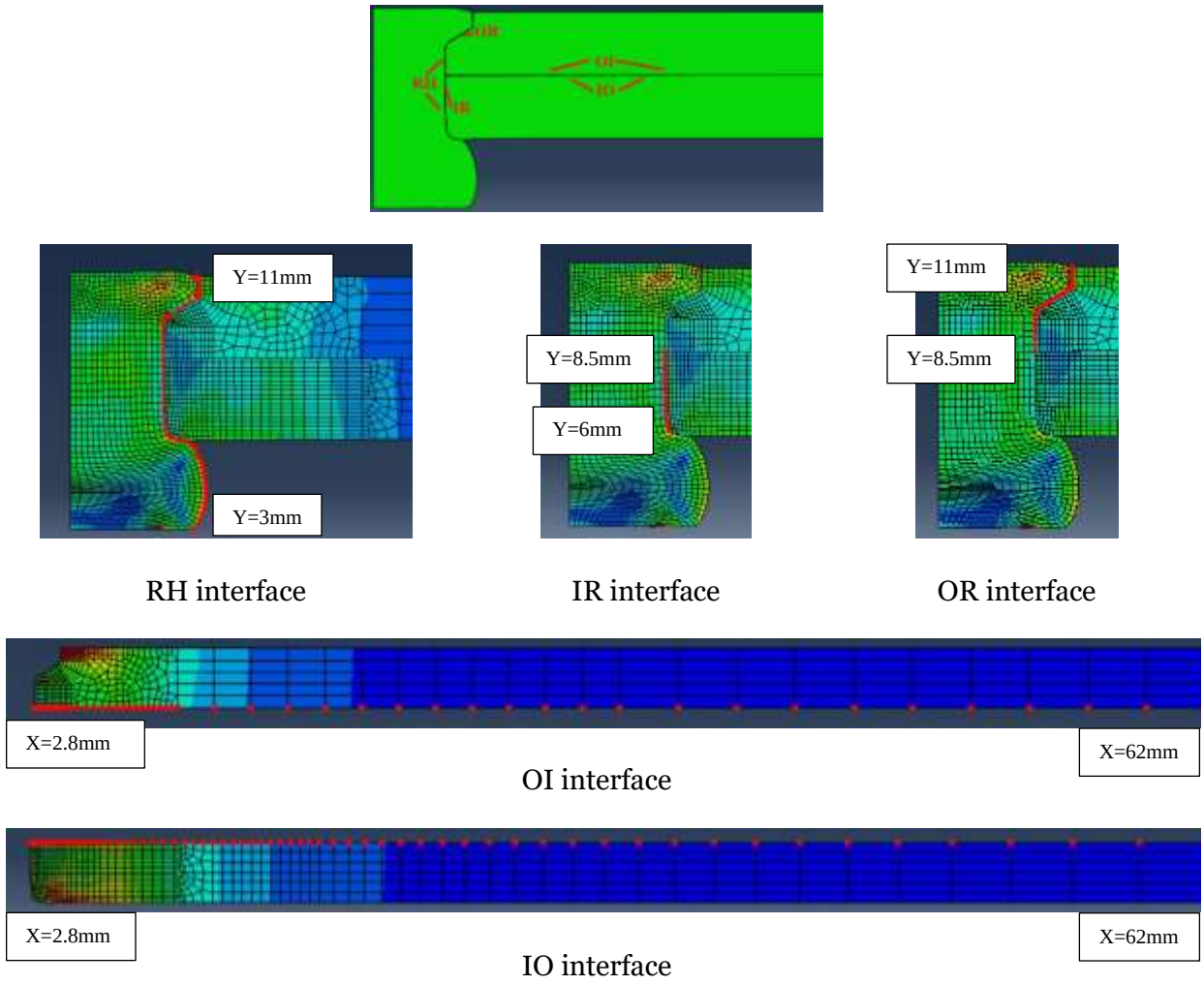

Figure 7.20. Interface residual stresses/strains measurement locations. Measurements were made at the interface nodes (highlighted nodes shown in red).

Measurements of residual stresses and strains were made at various skin-skin interface and skin-rivet interface element nodes. These interfaces are shown in Figure 7.20. First interface is the inner skin region adjacent to the rivet (denoted by 'IR'). Y-coordinate of IR ranges from 6 mm to 8.5 mm. Second is the inner skin region adjacent to the outer skin (denoted by 'IO'). X-coordinate of IO ranges from 2.8 mm to 62 mm. Third is the outer skin region adjacent to the rivet (denoted by 'OR'). Y-coordinate of OR ranges from 8.5 mm to 11 mm. Fourth is the outer skin region adjacent to the inner skin (denoted by 'OI'). X-coordinate of OI ranges from 2.8 mm

to 62 mm. Fifth is the rivet region adjacent to the rivet hole which spans both the inner skin's hole region and the outer skin's hole region (denoted by 'RH'). Y-coordinate of RH ranges from 3 mm to 11 mm.

Referring to figure 7.21a, radial stress distribution at interface IR of model 2 QS and model 2 Dyn is shown. Near the head of the button at Y=6 mm the radial stress is marginally compressive in model 2 Dyn and highly compressive in model 2 QS. Higher up along IR interface the radial stresses are compressive and toward the IO interface near Y=8 mm compressive stresses in model 2 Dyn are higher in magnitude compared to model 2 QS.

Referring to figure 7.21b, axial stress distribution at interface IR of model 2 QS and model 2 Dyn is shown. Near the head of the button at Y=6 mm the axial stress is tensile in model 2 Dyn and highly compressive in model 2 QS. Higher up along IR interface the axial stresses are compressive in model 2 Dyn and tensile in model 2 QS. Toward the IO interface near Y=8 mm the stress becomes tensile in model 2 Dyn and marginally compressive in model 2 QS.

Referring to figure 7.21c, hoop stress distribution at interface IR of model 2 QS and model 2 Dyn is shown. Near the head of the button at Y=6 mm the hoop stress is tensile in model 2 Dyn and compressive in model 2 QS. Higher up along IR interface the axial stresses are compressive in model 2 Dyn and in model 2 QS. Toward the IO interface near Y=8 mm the stress becomes tensile in model 2 Dyn and stress remains compressive in model 2 QS.

As explained previously, tensile stresses were observed near head of the rivet button at Y=6 mm because of the gap found at the IR interface. This occurs because of temperature rise due to repeated impact. There is thermally induced softening in this region which leads to higher material flow. Gap formation is unavoidable in a coupled structural-thermal numerical simulation with no convective heat transfer. *Higher magnitude of strains* at this interface can be explained by this *same phenomenon*.

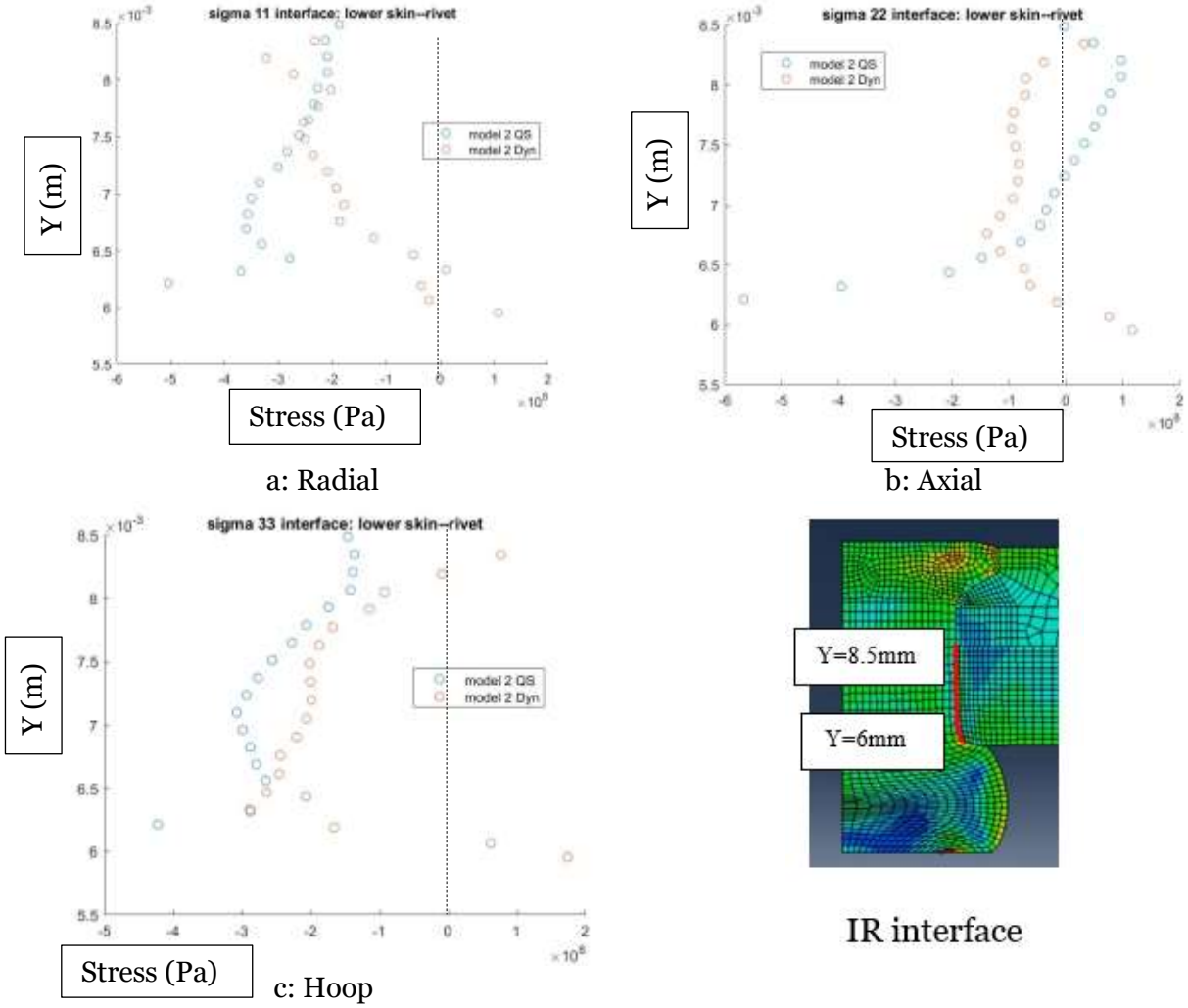

Figure 7.21. Stress distributions within IR interface. a: Radial. b: Axial, c: Hoop. Model-2 QS: Chapter 7 quasi-static simulation, Model-2 Dyn: Chapter 7 full dynamic simulation. X-axis: Pa, Y-axis: m.

Referring to figure 7.22a, logarithmic radial strain distribution at interface IR of model 2 QS and model 2 Dyn is shown. Near the head of the button at Y=6 mm the radial strain is positive in model 2 QS and negative in model 2 Dyn. Higher up along IR interface the radial strain remains negative in model 2 Dyn and positive in model 2 QS. As can be observed in table 7.1, R4 and R3 values of model 2 Dyn are larger than model 2 QS.

Referring to figure 7.22b, logarithmic axial strain distribution at interface IR of model 2 QS and model 2 Dyn is shown. Near the head of the button at Y=6 mm the axial strain is negative in model 2 QS and positive in model 2 Dyn. Higher up along IR interface the axial strain remains negative in model 2 QS and positive in model 2 Dyn.

Referring to figure 7.22c, logarithmic hoop strain distribution at interface IR of model 2 QS and model 2 Dyn is shown. The hoop strain is positive in both model 2 QS and model 2 Dyn but the magnitude is higher in the latter distribution over the entire IR interface indicating a greater hole expansion in model 2 Dyn compared to model 2 QS that can be verified using table 7.1.

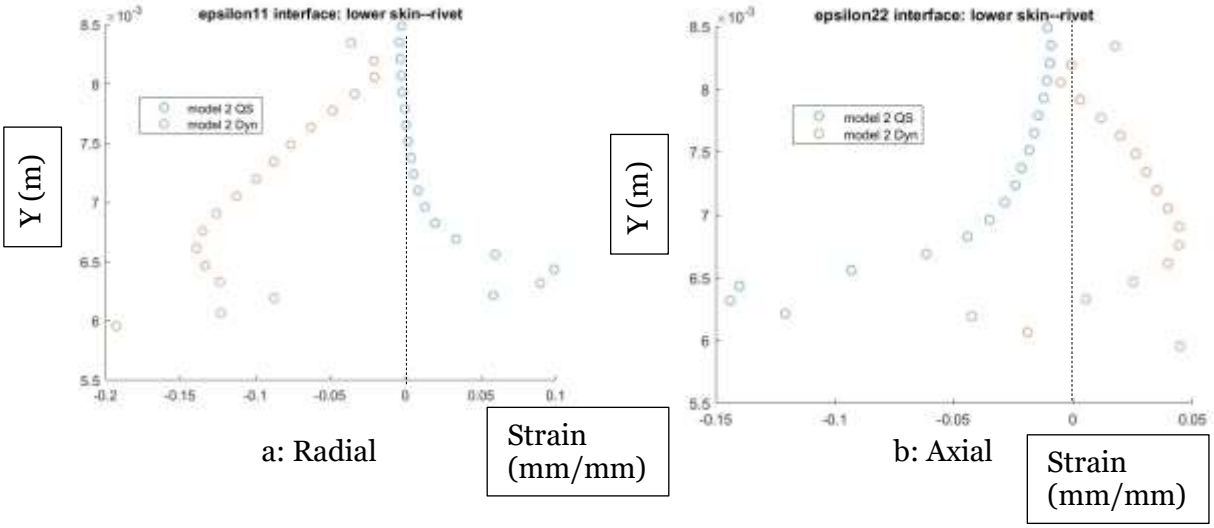

a: Radial

b: Axial

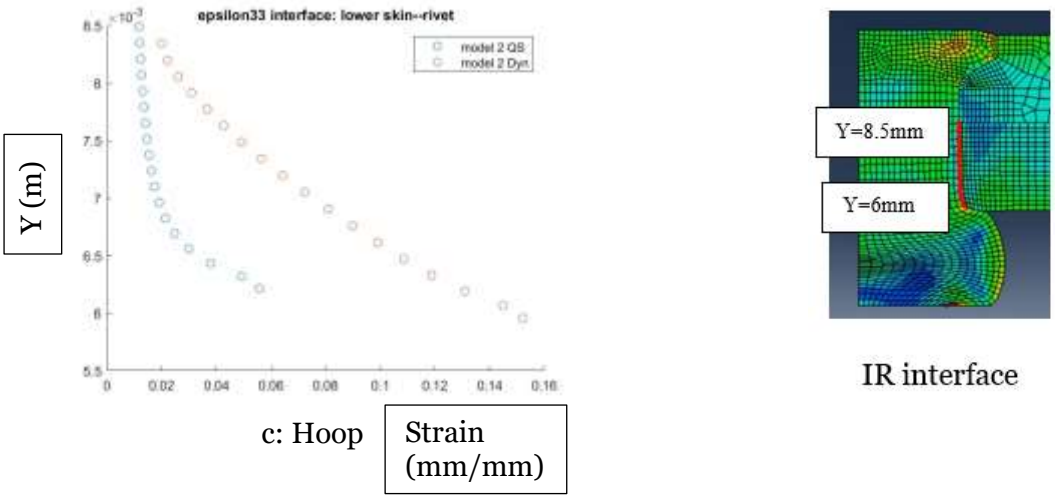

Figure 7.22. Strain distributions within IR interface. a: Radial. b: Axial, c: Hoop. Model-2 QS: Chapter 7 quasi-static simulation, Model-2 Dyn: Chapter 7 full dynamic simulation. X-axis: mm/mm, Y-axis: m.

Referring to figure 7.23a, radial stress distribution at interface IO of model 2 QS and model 2 Dyn is shown. At the skin-rivet interface near X=3 mm, the stress is more compressive in model 2 Dyn compared to model 2 QS. The stress remains compressive in both distributions over the entire IO domain. The inflections in the stress distributions indicate springback.

Referring to figure 7.23b, axial stress distribution at interface IO of model 2 QS and model 2 Dyn is shown. At the skin-rivet interface near X=3 mm, the stress is more compressive in model 2 Dyn compared to model 2 QS. The stress remains compressive in both distributions for a short distance from the skin-rivet interface but it oscillates between compression and tension away from the skin-rivet interface. The value of stress in both distributions is small and tensile further away from skin-rivet interface. Oscillation is *larger* is model 2 Dyn because of the *tie constraint* that is used between the two skins.

Referring to figure 7.23c, hoop stress distribution at interface IO of model 2 QS and model 2 Dyn is shown. At the skin-rivet interface near X=3 mm, the stress is more compressive in model 2 Dyn compared to model 2 QS. The stress remains compressive in both distributions for a short distance away for the skin-rivet interface. The area of compressive hoop stress region of model 2

Dyn is greater than the area of model 2 QS. The inflections in the stress distributions indicate springback. The stress is small in magnitude in both distributions further away from the skin-rivet interface.

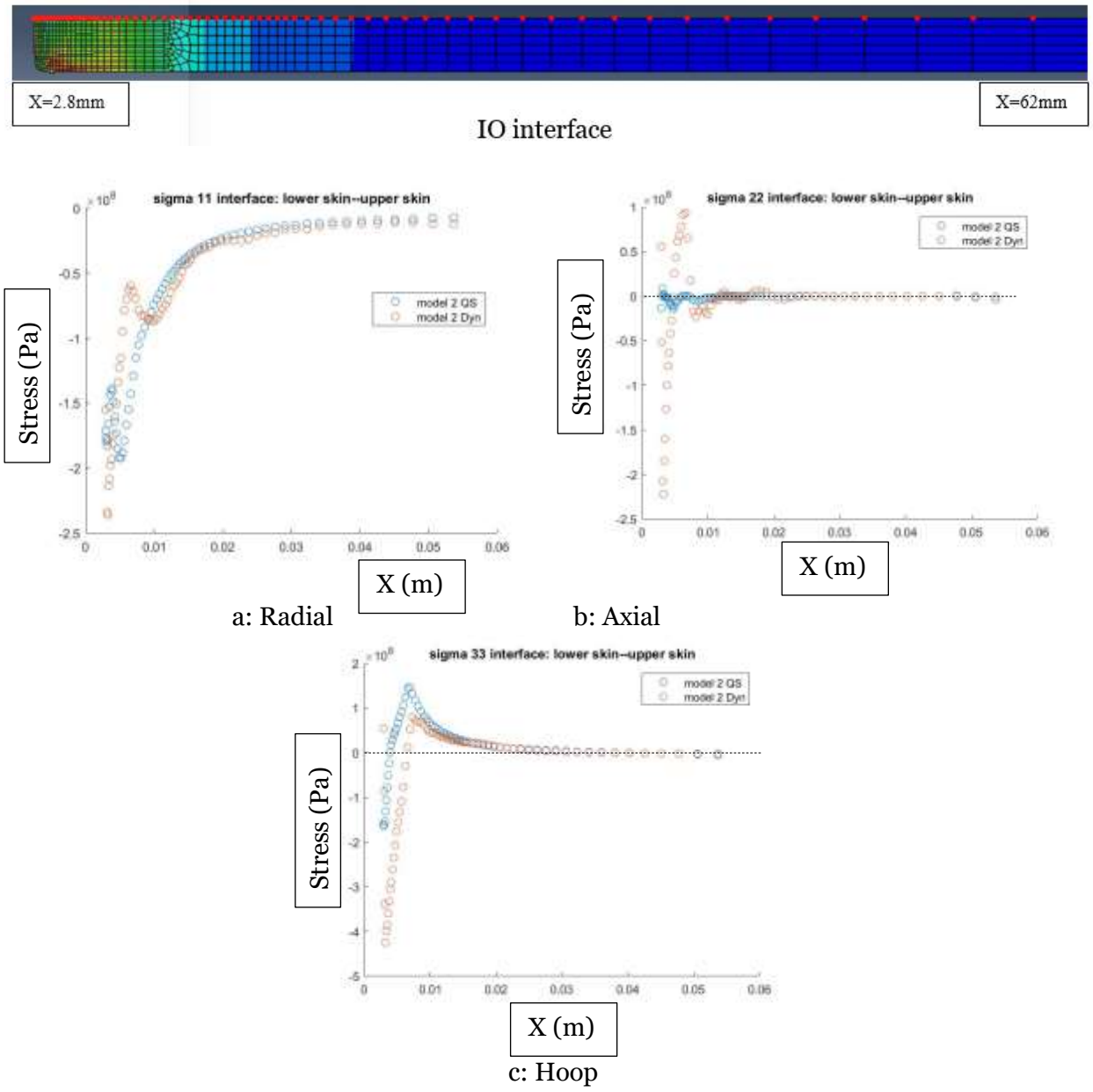

Figure 7.23. Stress distributions within IO interface. a: Radial. b: Axial, c: Hoop. Model-2 QS: Chapter 7 quasi-static simulation, Model-2 Dyn: Chapter 7 full dynamic simulation. X-axis: m, Y-axis: Pa

Referring to figure 7.24a, logarithmic radial strain distribution at interface IO of model 2 QS and model 2 Dyn is shown. At the skin-rivet interface near X=3 mm, the strain is more compressive in model 2 Dyn compared to model 2 QS. The strain remains compressive in both distributions for the entire IO domain. Around X=5 mm there are inflections in both profiles corresponding to springback. The stress is small in magnitude in both distributions further away from the skin-rivet interface.

Referring to figure 7.24b, logarithmic axial strain distribution at interface IO of model 2 QS and model 2 Dyn is shown. At the skin-rivet interface near X=3 mm, the strain is compressive in model 2 QS and tensile in model 2 QS. There is an inflection near the skin-rivet interface where the strain becomes negative from positive and becomes positive again in model 2 Dyn at X=5mm. The strain remains compressive in model 2 QS distributions for the entire IO domain. The magnitude is small further away from the skin-rivet interface. It oscillates between positive and negative in the case of model 2 Dyn and further away from the skin-rivet interface but the magnitude is small.

Referring to figure 7.24c, logarithmic hoop strain distribution at interface IO of model 2 QS and model 2 Dyn is shown. At the skin-rivet interface near X=3 mm, the strain is tensile in model 2 QS and model 2 QS. The strain is 1.7 times greater at the skin-rivet interface in model 2 Dyn compared to model 2 QS. The strain remains positive in both distributions for the entire IO domain. The magnitude is small further away from the skin-rivet interface in both distributions.

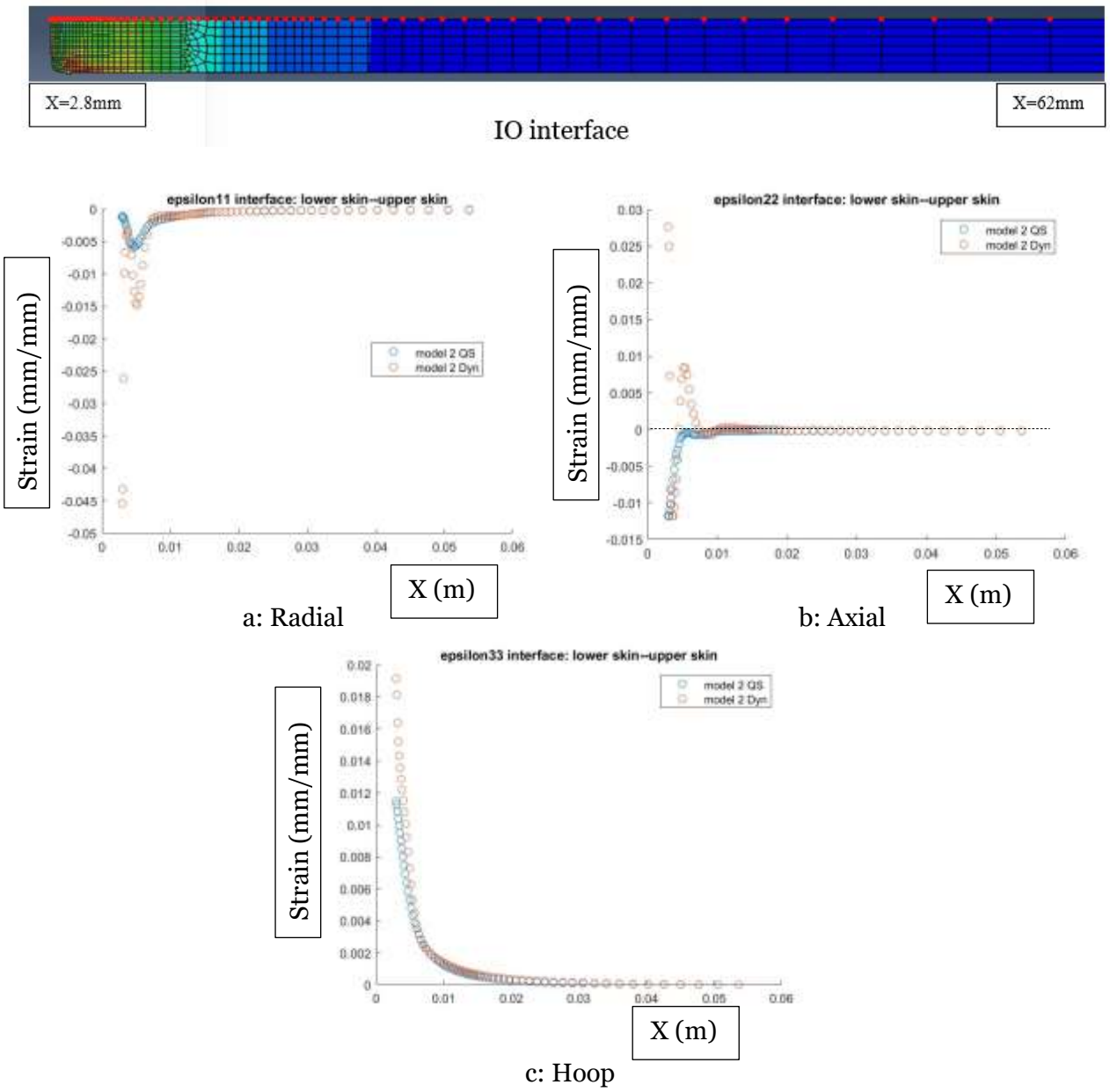

Figure 7.24. Strain distributions within IO interface. a: Radial. b: Axial, c: Hoop. Model-2 QS: Chapter 7 quasi-static simulation, Model-2 Dyn: Chapter 7 full dynamic simulation. X-axis: m, Y-axis: mm/mm

Referring to figure 7.25a, radial stress distribution at interface OR of model 2 QS and model 2 Dyn is shown. The stress remains negative in both distributions for the entire OR domain except it turns positive in the crown region of model 2 Dyn but the area is small. Magnitude of maximum compressive stress in model 2 QS is two times the magnitude of maximum compressive stress in model 2 Dyn.

Referring to figure 7.25b, axial stress distribution at interface OR of model 2 QS and model 2 Dyn is shown. There are inflections in both stress profiles and the stress remains negative in both distributions for the entire OR domain except it turns positive in the crown region of model 2 Dyn. The stress profile of model 2 QS is comparatively more compressive. Magnitude of maximum compressive stress in model 2 QS is 2.5 times the magnitude of maximum compressive stress in model 2 Dyn.

Referring to figure 7.25c, hoop stress distribution at interface OR of model 2 QS and model 2 Dyn is shown. There are inflections in both stress profiles and the stress remains negative in both distributions for the entire OR domain except it turns positive in the crown region of model 2 Dyn and model 2 QS. Magnitude of maximum compressive stress in model 2 QS is 3 times the magnitude of maximum compressive stress in model 2 Dyn.

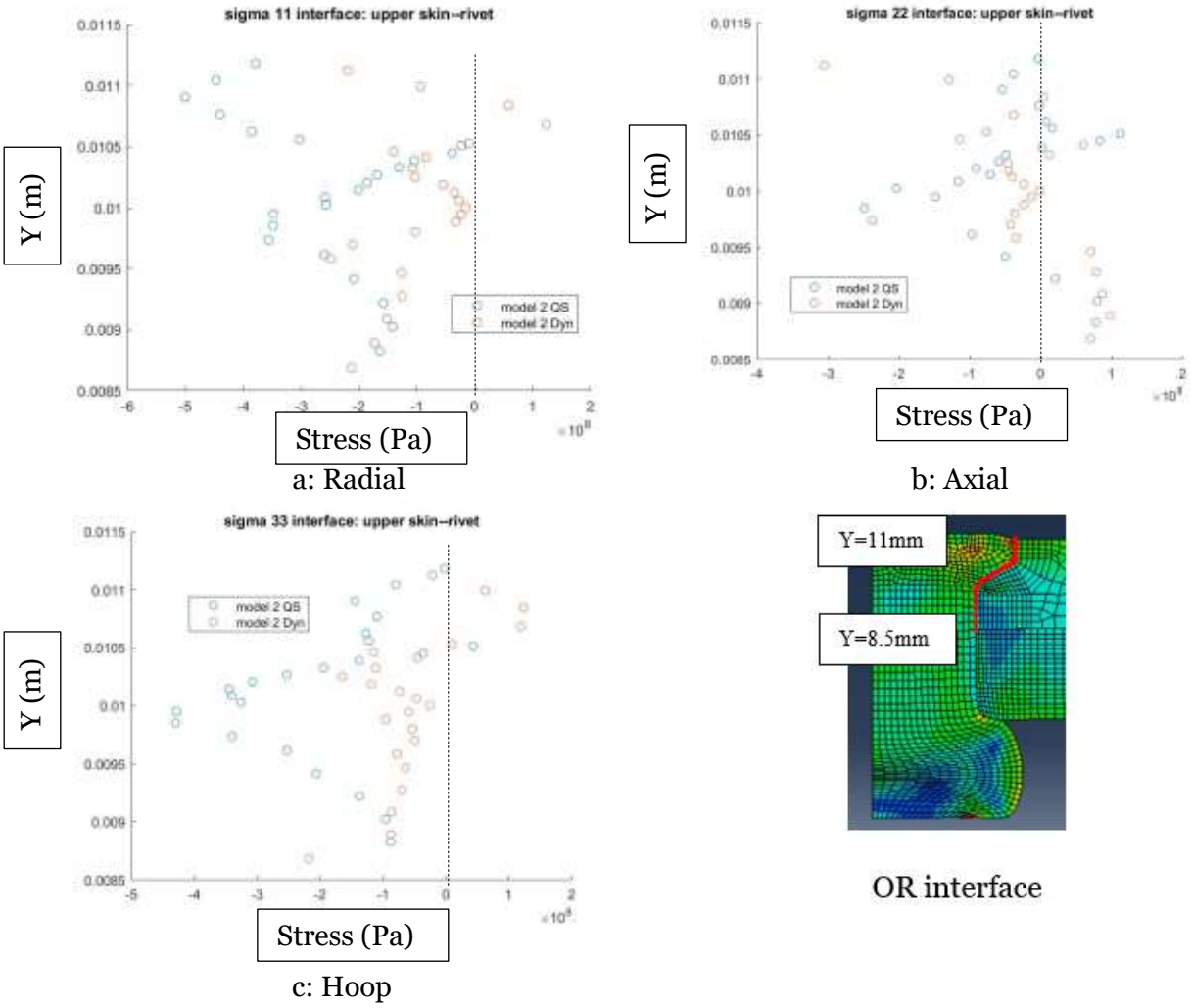

Figure 7.25. Stress distributions within OR interface. a: Radial. b: Axial, c: Hoop. Model-2 QS: Chapter 7 quasi-static simulation, Model-2 Dyn: Chapter 7 full dynamic simulation. X-axis: Pa, Y-axis: m

Referring to figure 7.26a, logarithmic radial strain distribution at interface OR of model 2 QS and model 2 Dyn is shown. There are inflections in model 2 Dyn strain profile and the strain remains negative in model 2 QS for the entire OR domain. The strain profile of model 2 Dyn is positive below Y=0.0103 and negative above Y=0.0103. Above Y=0.0103, it is the countersunk area. The maximum magnitude of model 2 Dyn strain is over 5 times the maximum magnitude of model 2 QS strain.

Referring to figure 7.26b, logarithmic axial strain distribution at interface OR of model 2 QS and model 2 Dyn is shown. There are inflections in both strain profiles. The strain profile of both distributions is negative below Y=0.0103 and positive above Y=0.0103. Above Y=0.0103, it is the countersunk area.

Referring to figure 7.26c, logarithmic hoop strain distribution at interface OR of model 2 QS and model 2 Dyn is shown. There are inflections in both strain profiles and the strains remain positive for the entire OR domain. The maximum magnitude of the model 2 Dyn profile is 2.7 times the maximum magnitude of model 2 QS profile.

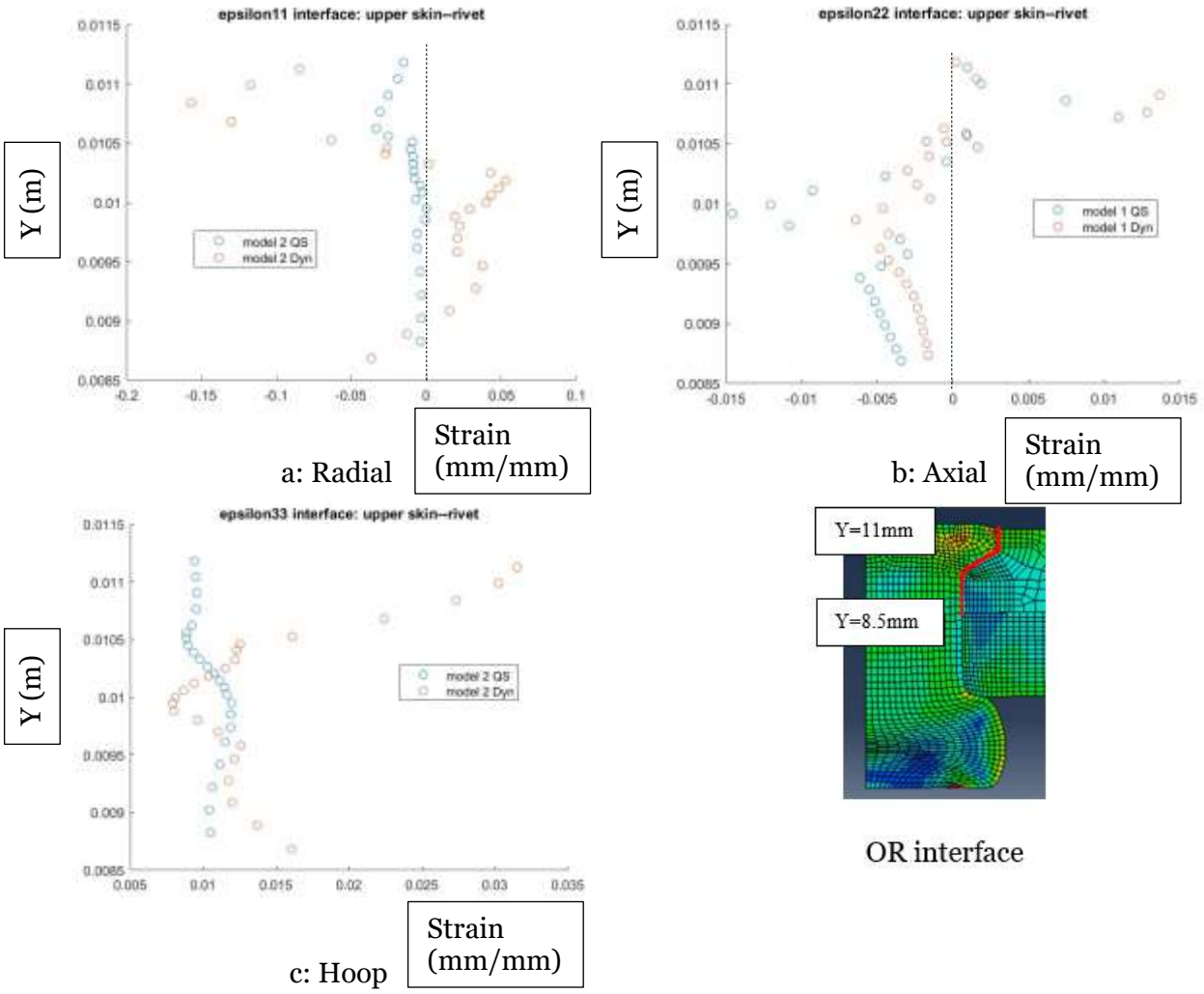

Figure 7.26. Strain distributions within OR interface. a: Radial. b: Axial, c: Hoop. Model-2 QS: Chapter 7 quasi-static simulation, Model-2 Dyn: Chapter 7 full dynamic simulation. X-axis: mm/mm, Y-axis: m

Referring to figure 7.27a, radial stress distribution at interface OI of model 2 QS and model 2 Dyn is shown. There are inflections in both stress profiles and the stresses remain compressive for the entire OI domain. The maximum magnitude of the model 2 Dyn profile is 1.3 times the maximum magnitude of model 2 QS profile. Away from the skin-rivet interface at X=3mm stress magnitudes of both distributions become small. Inflections in the profiles indicate springback.

Referring to figure 7.27b, axial stress distribution at interface OI of model 2 QS and model 2 Dyn is shown. There are inflections in both stress profiles. Oscillation of model 2 Dyn stress profile is more conspicuous compared to model 2 QS. Away from the skin-rivet interface at X=3mm stress magnitudes of both distributions become small.

Referring to figure 7.27c, hoop stress distribution at interface OI of model 2 QS and model 2 Dyn is shown. There are inflections in both stress profiles. The compressive hoop stress region of model 2 Dyn is greater than the same region in model 2 QS. Away from the skin-rivet interface at X=3mm stress magnitudes of both distributions become small. Inflection in the stress profiles indicates springback.

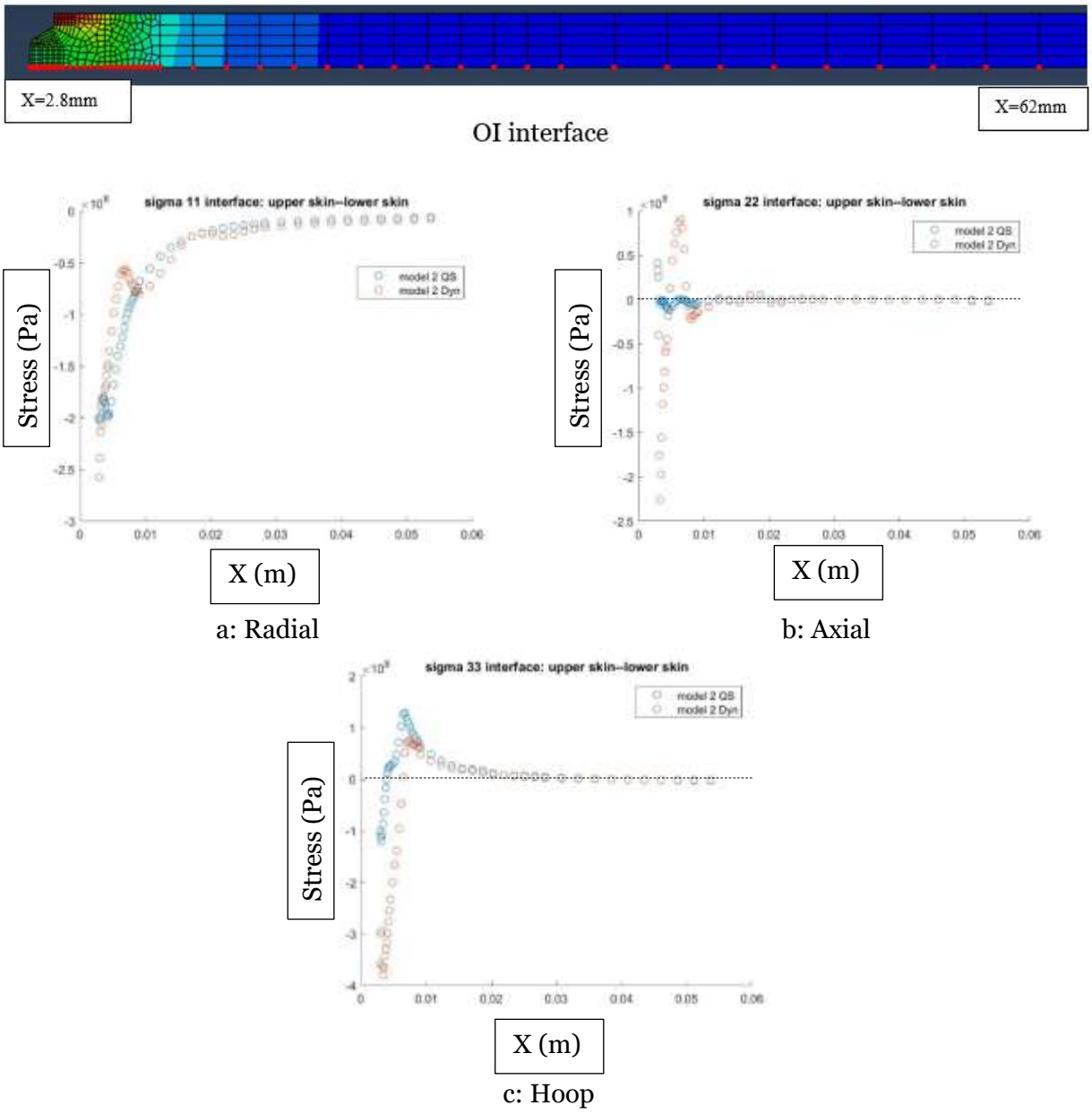

Figure 7.27. Stress distributions within OI interface. a: Radial. b: Axial, c: Hoop. Model-2 QS: Chapter 7 quasi-static simulation, Model-2 Dyn: Chapter 7 full dynamic simulation. X-axis: m, Y-axis: Pa

Referring to figure 7.28a, logarithmic radial strain distribution at interface OI of model 2 QS and model 2 Dyn is shown. There are inflections in both strain profiles. The strain profile of model 2 QS is entirely negative. It is almost entirely negative in the case of model 2 Dyn except at X=5 mm. Away from the skin-rivet interface at X=3mm strain magnitudes of both distributions become small. Maximum strain magnitude of model 2 Dyn is 7 times the maximum strain magnitude of model 2 QS.

Referring to figure 7.28b, logarithmic axial strain distribution at interface OI of model 2 QS and model 2 Dyn is shown. There are inflections in both strain profiles. Inflection of the model 2 Dyn profile is greater than model 2 QS profile. Away from the skin-rivet interface at X=3mm strain magnitudes of both distributions become small.

Referring to figure 7.28c, logarithmic hoop strain distribution at interface OI of model 2 QS and model 2 Dyn is shown. Both strain profiles are entirely positive. Away from the skin-rivet interface at X=3mm strain magnitudes of both distributions become small. Maximum magnitude of model 2 Dyn strain is 1.6 times maximum magnitude of model 2 QS strain.

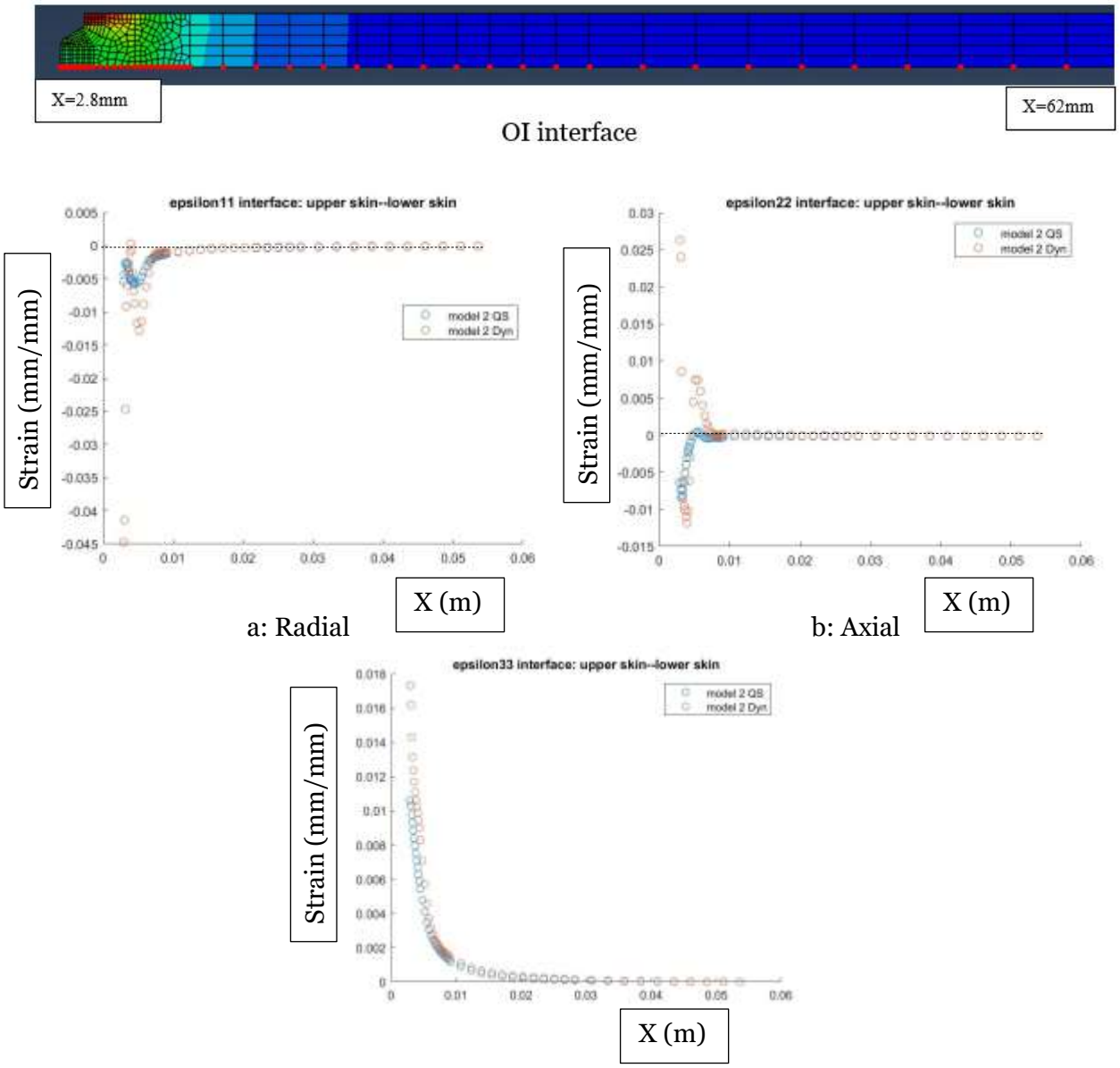

Figure 7.28. Strain distributions within OI interface. a: Radial. b: Axial, c: Hoop. Model-2 QS: Chapter 7 quasi-static simulation, Model-2 Dyn: Chapter 7 full dynamic simulation. X-axis: m, Y-axis: mm/mm

Referring to figure 7.29a, radial stress distribution at interface RH of model 2 QS and model 2 Dyn is shown. There are profile inflections at Y=6 mm corresponding to the head of the rivet button and Y=10.5 mm corresponding to the rivet crown. At the Y=6 mm location, both stress profiles become tensile. Both profiles are entirely negative in the regions of RH adjacent to the inner skin and non-countersunk region of the outer skin. In the crown region the model 2 QS profile is entirely compressive and the model 2 Dyn profile is tensile or marginally compressive.

Referring to figure 7.29b, axial stress distribution at interface RH of model 2 QS and model 2 Dyn is shown. There are profile inflections at Y=6 mm corresponding to the head of the rivet button and Y=10.5 mm corresponding to the rivet crown. In the button region between Y=3 mm and Y=6 mm, model 2 QS profile is tensile and model 2 Dyn profile is compressive. Between Y=6 mm and Y=8.6 mm, the RH region is adjacent to the inner skin. Here the model 2 QS profile is compressive and the model 2 Dyn profile is both compressive and tensile. Above Y=10 mm in the rivet crown region, the model 2 QS profile is both tensile and compressive while the model 2 Dyn profile is entirely tensile.

Referring to figure 7.29c, hoop stress distribution at interface RH of model 2 QS and model 2 Dyn is shown. There are profile inflections across the entire RH domain. In the button region between Y=3 mm and Y=6 mm, model 2 QS profile is tensile and model 2 Dyn profile is mostly tensile. Between Y=6 mm and Y=8.6 mm, the RH region is adjacent to the inner skin. Here both stress profiles are mostly compressive. Above Y=8.6 mm in the remaining RH region, both stress profiles are both tensile and compressive.

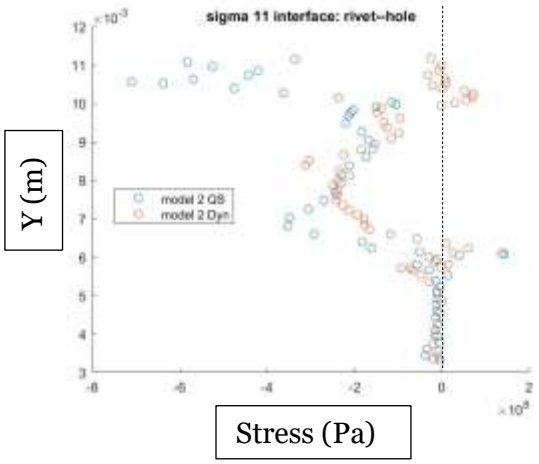

a: Radial

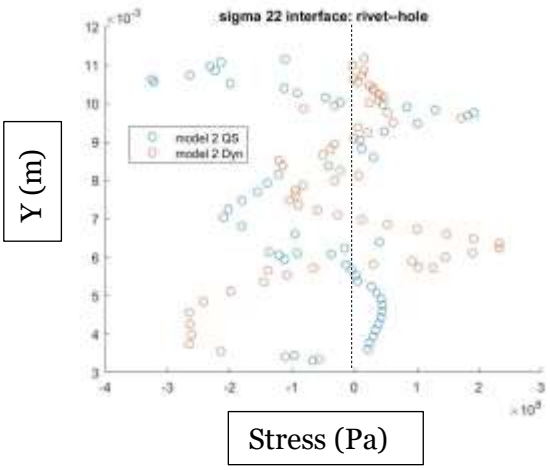

b: Axial

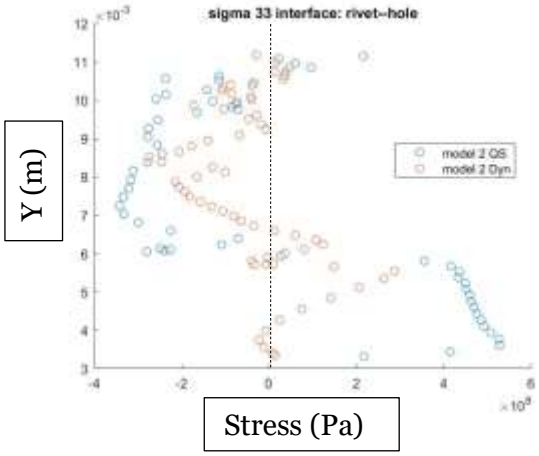

c: Hoop

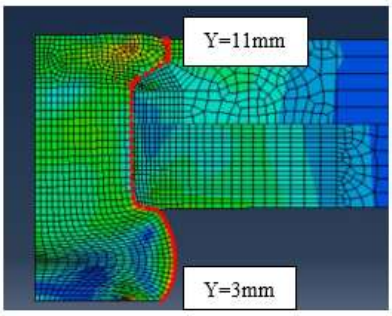

RH interface

Figure 7.29. Stress distributions within RH interface. a: Radial. b: Axial, c: Hoop. Model-2 QS: Chapter 7 quasi-static simulation, Model-2 Dyn: Chapter 7 full dynamic simulation. X-axis: Pa, Y-axis: m

Referring to figure 7.30a, logarithmic radial strain distribution at interface RH of model 2 QS and model 2 Dyn is shown. There are profile inflections at Y=6 mm and Y=10 mm. In the button region between Y=3 mm and Y=6 mm, model 2 QS profile is mostly positive and model 2 Dyn profile is mostly negative. Between Y=6 mm and Y=10 mm, both strain profiles are positive. Above Y=10 mm in the remaining RH region, model 2 QS strain profile is positive and model 2 Dyn strain profile is both positive and negative.

Referring to figure 7.30b, logarithmic axial strain distribution at interface RH of model 2 QS and model 2 Dyn is shown. There are profile inflections again at Y=6 mm and Y=10 mm. In the button region between Y=3 mm and Y=8.65 mm, both strain profiles are negative. Above Y=8.65 mm in the remaining RH region, model 2 QS strain profile is negative and model 2 Dyn strain profile is both positive and negative.

Referring to figure 7.30c, logarithmic hoop strain distribution at interface RH of model 2 QS and model 2 Dyn is shown. Both strain profiles are entirely positive over the RH domain. The model 2 Dyn profile has a greater magnitude compared to the model 2 QS profile in the rivet button region, inner skin region and countersunk outer skin region. The magnitudes of both profiles are approximately the same in the non-countersunk region of the outer skin.

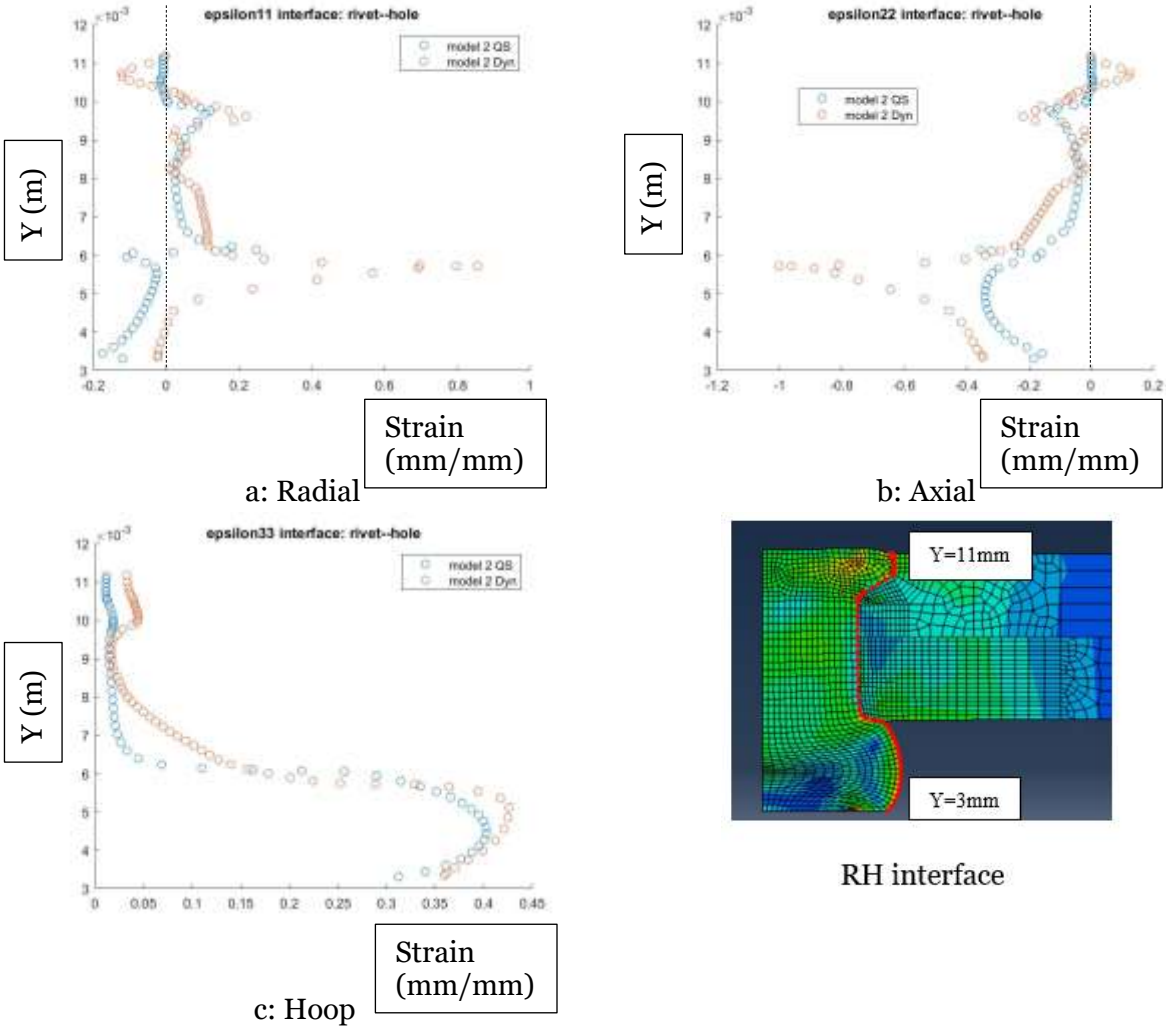

Figure 7.30. Strain distributions within RH interface. a: Radial. b: Axial, c: Hoop. Model-2 QS: Chapter 7 quasi-static simulation, Model-2 Dyn: Chapter 7 full dynamic simulation. X-axis: mm/mm, Y-axis: m

From table 7.1, D_b of Model 2 QS is 1.48d and D_b of Model 2 Dyn is 1.504d. Figure 7.31 shows stress levels at mesh elements with the *highest magnitude of the stress components* within the *entire FE mesh*.

Component	Stress	V-M Stress	Stress/V-M
radial (11)	(Pa)	(Pa)	
Riv 225 pa-SI-1 730	1.87E+08	2.40E+08	0.78
Riv 225 pa-SI-1 1020	-7.49E+08	6.06E+08	-1.24
axial (22)			
Riv 225 pa-SI-1 715	5.02E+08	6.88E+08	0.73
D226 lower pa-1 703	-5.66E+08	3.45E+08	-1.64
hoop (33)			
Riv 225 pa-SI-1 596	5.28E+08	5.36E+08	0.99
Riv 225 pa-SI-1 911	-6.30E+08	5.55E+08	-1.13
shear (12)			
Riv 225 pa-SI-1 734	2.53E+08	5.04E+08	0.50
Riv 225 pa-SI-1 273	-3.58E+08	6.25E+08	-0.57

Model 2 QS

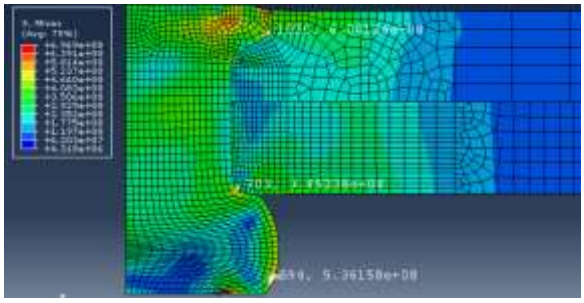

Model 2 QS

Component	Stress	V-M Stress	Stress/V-M
radial (11)	(Pa)	(Pa)	
D226 upper pa-1 321	2.52E+08	4.31E+07	5.85
D226 upper pa-1 396	-4.62E+08	1.84E+08	-2.51
axial (22)			
D226 upper pa-1 321	2.92E+08	4.31E+07	6.78
Riv 225 pa-SI-1 323	-3.12E+08	4.74E+07	-6.59
hoop (33)			
D226 upper pa-1 321	2.96E+08	4.31E+07	6.87
D226 lower pa-1 667	-5.06E+08	4.67E+08	-1.08
shear (12)			
Riv 225 pa-SI-1 797	1.19E+08	3.73E+08	0.32
D226 upper pa-1 380	-1.11E+08	2.32E+08	-0.48

Model 2 Dyn

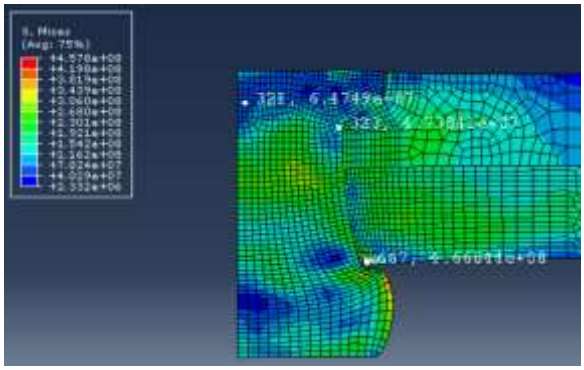

Model 2 Dyn

Figure 7.31. Data for Joint Quality Analysis

In model 2 Dyn, highest compressive ratio of stress component/V-M stress in the entire FE mesh is exhibited by mesh element 323 of the rivet and it is -6.59. This element is located just below the rivet wedge and is part of region 'A'. Mesh element 667 of the inner skin has the highest compressive stress component of -506 MPa. This element is located just above the rivet button and is part of region 'F'. Mesh element 321 of the rivet has the highest tensile ratio of stress component/V-M stress (6.87) and highest tensile stress component (296 MPa). This element is located near the rivet axis and is part of region 'A'.

Mesh element 321 of the rivet is less critical for crack nucleation because it is in the interior of the rivet. Mesh element 667 of the inner skin and mesh element 323 of the rivet are critical. Mesh element 667 of inner skin-- because of its higher hoop stress magnitude (506 MPa) -- is the more critical element for crack nucleation compared to mesh element 323 of the rivet.

In model 2 QS, element 703 of inner skin was shown to be most critical. This discussion can be found in section 5.3

7.4 SUMMARY

Two-dimensional full dynamic percussive riveting FE model was built and simulated. Residual stress and strain results from the simulation were presented and discussed. An axial gap was observed between the head of the rivet button and the inner surface of the inner skin. Tensile stresses were observed in the percussive riveting stackup at the countersink wedge region and near the head of the rivet button. These tensile stresses are not desirable in a good quality joint. The dynamic percussive riveting stackup was found to be most critical for crack nucleation inside the inner skin because of compression-induced shearing. Two observations from the percussive simulation are the formation of the gap between the rivet and inner skin and the higher deformations at the rivet-skin interfaces because of stress wave propagation and thermally induced softening.

The gap and the higher rivet deformations are ascribed to the inability to include convective heat transfer in the numerical simulation framework, resulting in higher temperature rise than what is expected. Another reason for the gap and large rivet deformations are because of the free relative motion of the rivet inside the rivet hole. A third reason for the high rivet deformation is due to the different curvature of the skins under the application of the unequal rivet hammer (1600 N) and bucking bar (950 N) constraint forces. This causes R_4 of model 2 Dyn to be greater than that of R_4 of model 2 QS.

Chapter 8. DESIGN OF EXPERIMENTS OF FULL DYNAMIC MODEL

8.1 INTRODUCTION

In this chapter, the full dynamic percussive simulation results are compared with quasistatic squeeze simulation results. Three-factor, two-level analyses were performed in two separate sets. One set focuses on the effects of CL (clearance ratio), TR (skin thickness ratio), and μ (friction coefficient). The other set focuses on the effects of KE (rivet hammer impact energy), b_Y (bucking bar constraint force), and h_Y (rivet hammer constraint force). R_1, R_2, R_3, R_4, R_B, H_B and axial gap were measured and the effects of the six factors on these parameters were modeled. Parameter models and the measured residual strains and stresses at stackup contact interfaces will be presented and discussed.

8.2 DOE DEVELOPMENT

Relevant modeling information is discussed in section 4.3. In the following discussion of the DOE, one axisymmetric quasistatic simulation (QS) and sixteen axisymmetric percussive simulations were performed. As mentioned before, three attributes were considered for analysis set 1 (AS1 simulations), CL, TR, and μ. Three geometric attributes were considered for analysis set 2 (AS2 simulations), KE, b_Y, and h_Y. Refer to tables 8.1, 8.2, and 8.3 for the attributes of QS, AS1 and AS2 simulations respectively. Residual stress/strain distributions of simulations AS1-8 and AS2-8 are discussed in detail in section 8.3.2. These simulations are indicated in tables 8.2 and 8.3 with bold lettering.

Table 8.1. Attributes of QS simulation model

CL	TR	μ
0.9956	1	0.25

Table 8.2. Analysis set 1 parameter values. KE=21 J, b_Y= +950 N, h_Y= -1600 N

AS1-	Parameter		
	TR	CL	μ
1	0.9	0.9867	0.25
2	0.9	0.9867	0.35
3	0.9	0.9956	0.25
4	0.9	0.9956	0.35
5	1.0	0.9867	0.25
6	1.0	0.9867	0.35
7	1.0	0.9956	0.25
8	**1.0**	**0.9956**	**0.35**

Table 8.3. Analysis set 2 parameter values. TR= 1.0, CL= 0.9912, μ= 0.25

AS2-	Parameter		
	KE, J	b_Y, N	h_Y, N
1	15	+950	-1600
2	15	+950	-2400
3	15	+1450	-1600
4	15	+1450	-2400
5	21	+950	-1600
6	21	+950	-2400
7	21	+1450	-1600
8	**21**	**+1450**	**-2400**

All AS1 percussive simulations are completed in eighty load steps—40 load steps and 40 unloading steps while the number of strokes of each AS2 simulation is different ranging from 33 to 55 strokes. Each percussive load-unload cycle takes 40 ms to complete. This indicates a rivet hammer strike frequency of 25 Hz. μ is 0.2 between bucking bar/ rivet die and stackup surfaces. μ for all other mating surfaces is shown in tables 8.1, 8.2, and 8.3. The shear stress limit used to initiate slipping between mating surfaces is 269.62 MPa. Geometric dimensions in the percussive simulations are shown in table 8.4 normalized with D_{shank} of the respective stackups. Simulation 'QS' is the same as simulation 'Model 2 QS' from chapter 7. Simulation AS1-7 is the same as simulation 'Model 2 Dyn' from chapter 7.

Table 8.4. Dimensions of analysis sets 1 and 2 stackups normalized using respective D_{SHANK} values

	AS1-				AS2-
	1,2	3,4	5,6	7,8	1-8
D_{SHANK} (in.)	0.223	0.225	0.223	0.225	0.224
Normalized quantity					
Hole Diameter	1.013	1.0044	1.013	1.0044	1.0089
Inner Skin Diameter	9.475	9.393	9.475	9.393	9.4323
t_{INNER}	0.403	0.4	0.4484	0.4444	0.4464
Outer Skin Diameter	9.475	9.393	9.475	9.393	9.4323
t_{OUTER}	0.448	0.4444	0.4484	0.4444	0.4464
L_{RIVET}	1.9775	1.9603	1.9775	1.9603	1.9685
L_{SHANK}	1.699	1.6848	1.699	1.6848	1.6919
Rivet Countersink	0.277	0.2755	0.277	0.2755	0.2766
D_{CROWN}	1.399	1.3959	1.399	1.3959	1.3972
Crown Hole	1.408	1.396	1.408	1.396	1.4018
Bucking Bar	8.951	8.873	8.951	8.873	8.9104
Bucking Bar Length	31.39	31.117	31.39	31.117	31.2478
Deformable Die	6.726	6.6678	6.726	6.6678	6.696

8.3 RESULTS AND DISCUSSION

8.3.1 *Rivet Deformation Parameter Modeling*

ANOVA technique was used to model the geometric deformation parameters. These parameters were obtained as responses from the AS1 and AS2 simulations. From the fit statistics of the models, the *kinetic energy* of the *rivet hammer impact* (KE) and *Skin thickness ratio* (TR) were found to *significantly* impact R_B and H_B. Friction Coefficient between stackup parts (μ) was found to *significantly* impact Gap between rivet and inner skin. The detailed analysis is given in the appendix. KE, TR and μ need to be carefully controlled to obtain joints of good quality. The need to reduce the gap is of utmost importance. It is observed that an *increase in μ* leads to a *reduction in the gap,* an *increase in KE* leads to an *increase in* R_B and a *reduction in* H_B*, and* an *increase in TR* leads to a *reduction in* R_B and an *increase in* H_B.

8.3.2 *Residual Stress and Strain Distributions at Stackup Interfaces*

Target button height is 25-30% of L_{SHANK} and target button diameter was 1.45-1.5 D_{SHANK}. In table 8.5, the values of R_1-R_4 are all greater for the AS1-7 simulation compared to AS1 QS simulation. This is because there is greater radial expansion of the rivet shank in the percussive riveting process compared to the quasistatic squeeze riveting process. There exists a gap between the inner skin and the top of the rivet button in the case of percussive simulations after the final unloading step of the simulation is completed. This gap is discussed in section 7.3. The rivet button of AS1-7 is found to be of larger radius compared to QS simulation and the button height is also smaller compared to QS. The values of R_1-R_4 and R_B of AS1-7 are larger because of significant stress wave propagation effects, these effects are absent in the quasistatic riveting process.

Table 8.5. Normalized geometric measurements of QS and AS1-7

Normalized	R_1	R_2	R_3	R_4	R_B	H_B	Gap
QS	1.01	1.016	1.017	1.044	1.48	0.286	--
AS1-7	1.033	1.023	1.025	1.152	1.504	0.253	0.034

Residual strain and stress distributions of two simulations (AS1-8 and AS2-8) are discussed in the following discussion. Seven regions of the deformed stackup shown in figure 8.1 are the areas of interest for studying the stress and strain distributions in these two simulations.

Figure 8.1. Deformed stackup data regions: A- Rivet crown, B- Rivet shank, C- Rivet button, D- Outer Skin adjacent to rivet, E- Outer Skin away from rivet, F- Inner Skin adjacent to rivet, G- Inner Skin away from rivet.

Referring to figure 8.2a, radial stress distributions in region ‘A’ of AS1-8 and AS2-8 are shown. Radial stress is tensile and compressive adjacent to the crown of the upper skin in AS1-8. Stress is compressive adjacent to the crown of the upper skin in AS2-8. It is compressive adjacent to the wedge region in both AS1-8 and AS2-8. At the head of the crown near the rivet axis, stress is tensile in both AS1-8 and AS2-8. At the base of the crown near the rivet axis, stress is compressive in both simulations. Within the interior of the region 'A', there is an area of tensile stress adjacent to the wedge region in AS1-8. Stress is entirely compressive in the interior of region 'A' of AS2-8.

Referring to figure 8.2b, axial stress distributions in region ‘A’ of AS1-8 and AS2-8 are shown. Axial stress is tensile adjacent to the crown of the upper skin in AS1-8. Stress is compressive adjacent to the crown of the upper skin in AS2-8. It is compressive adjacent to the wedge region in both simulations. At the head of the crown near the rivet axis, stress is tensile in both simulations. At the base of the crown near the rivet axis, stress is compressive in both cases. At the base of the crown below the wedge, the stress is observed to be compressive in AS1-8 and tensile in AS2-8. Within the interior of the region 'A' in both simulations, there are areas of both tensile and compressive stresses.

Referring to figure 8.2c, hoop stress distributions in region ‘A’ of AS1-8 and AS2-8 are shown. Hoop stress is tensile in AS1-8 and compressive in AS2-8 adjacent to the crown of the upper skin. It is compressive adjacent to the wedge region in both simulations. At the head of the crown near the rivet axis, stress is tensile in AS1-8 and compressive in AS2-8. At the base of the crown near the rivet axis, stress is compressive in both simulations. Within the interior of the region 'A', there is an area of tensile stress located by the wedge in AS2-8. In AS1-8, stress is compressive across interior of region 'A'.

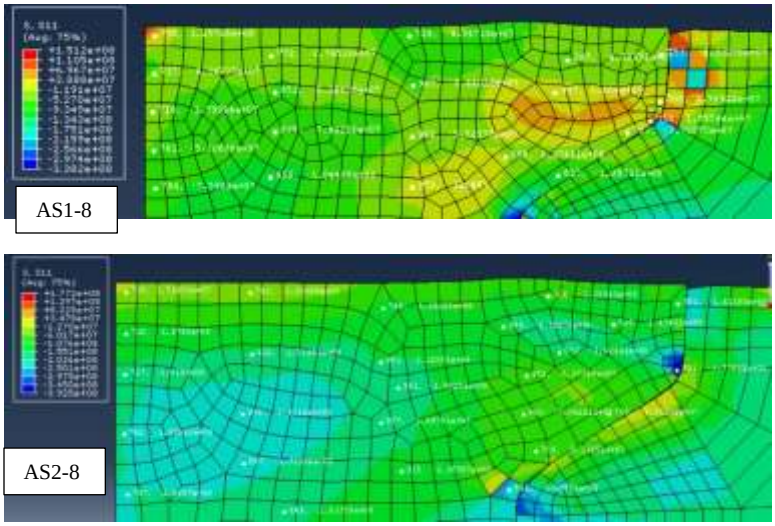

a1: AS1 Radial (top) a2: AS2 Radial (bottom)

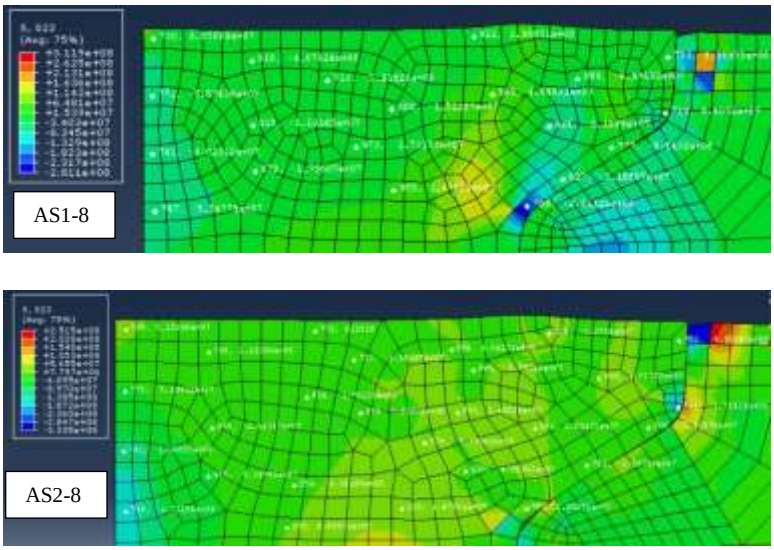

b1: AS1 Axial (top) b2: AS2 Axial (bottom)

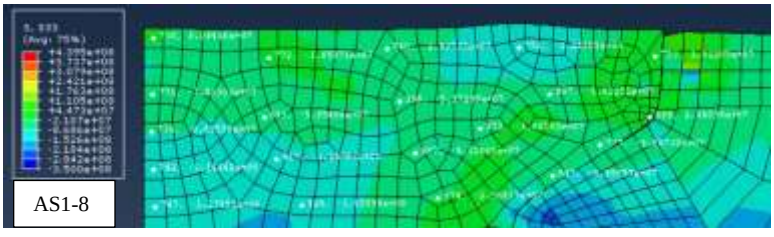

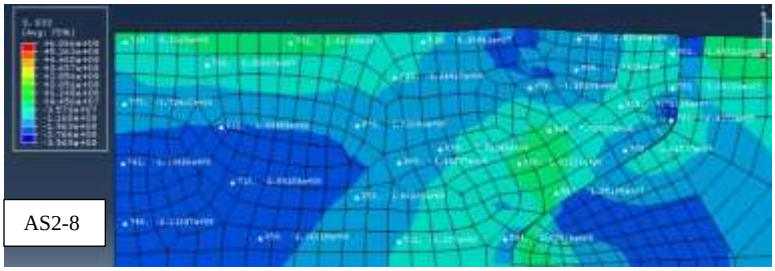

c1: AS1 Hoop (top) c2: AS2 Hoop (bottom)

Figure 8.2. Stress distributions within region ‘A’ of the AS1-8 and AS2-8 simulation stackups. a: Radial Stress, b: Axial Stress, c: Hoop Stress

Referring to figure 8.3a, logarithmic radial strain distributions in region ‘A’ of AS1-8 and AS2-8 are shown. Radial strain is compressive adjacent to the crown of the upper skin in both simulations. It is tensile adjacent to the wedge region in both simulations. At the head of the crown near the rivet axis, strain is compressive in both simulations. At the base of the crown near the rivet axis, strain is tensile in both simulations. At the base of the crown below the wedge, the strain is observed to be tensile in both simulations. Within the interior of the region 'A', the strain is observed to be tensile in both simulations.

Referring to figure 8.3b, logarithmic axial strain distributions in region ‘A’ of AS1-8 and AS2-8 are shown. Axial strain is tensile adjacent to the crown of the upper skin in both simulations. It is compressive adjacent to the wedge region in both simulations. At the head of the crown near the rivet axis, strain is tensile in both simulations. At the base of the crown near the rivet axis, strain is tensile in both simulations. At the base of the crown below the wedge, the strain is observed to be compressive in both simulations. Within the interior of the region 'A', there are areas of tensile and compressive strain in both simulations.

Referring to figure 8.3c, logarithmic hoop strain distributions in region ‘A’ of AS1-8 and AS2-8 are shown. The hoop strain is tensile across region ‘A’ in both simulations. Strain is compressive

at the top of the rivet crown near the rivet axis in both simulations. Magnitude is greater adjacent to the outer skin compared to magnitude near the rivet axis in both simulations.

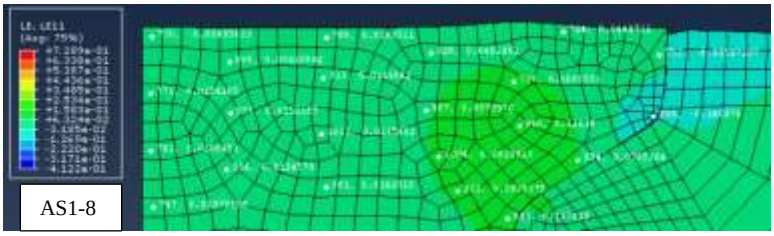

a1: AS1 Radial (top) a2: AS2 Radial (bottom)

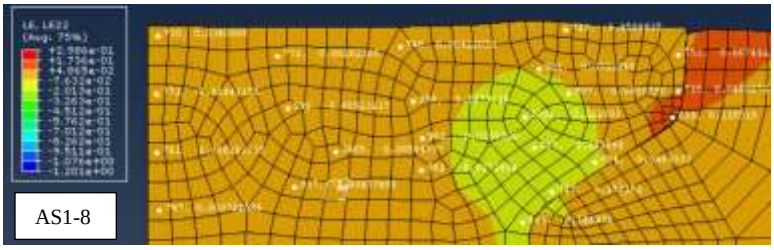

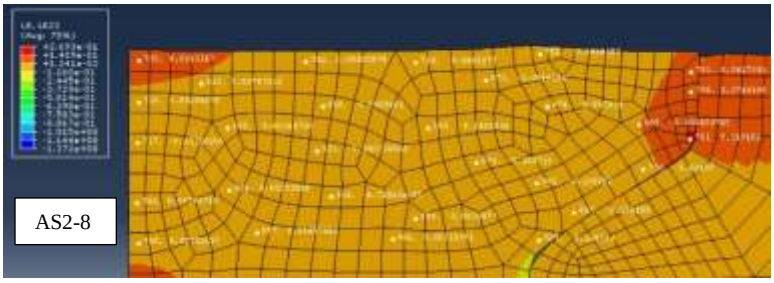

b1: AS1 Axial (top) b2: AS2 Axial (bottom)

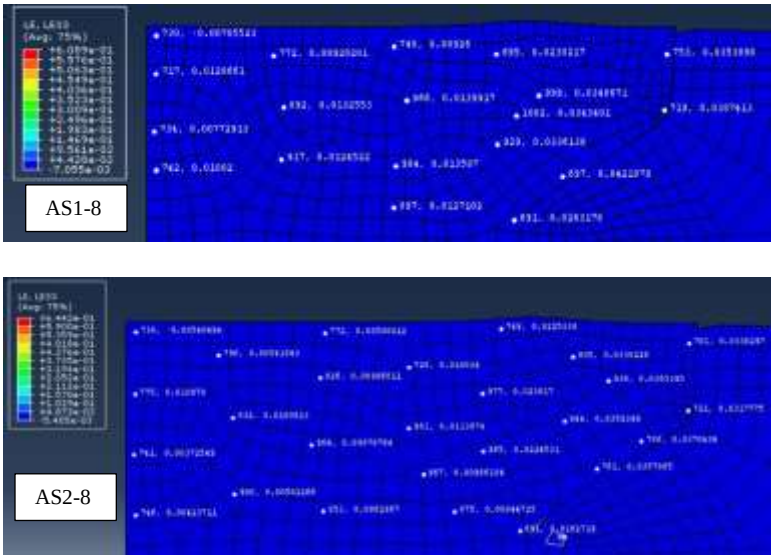

c1: AS1 Hoop (top) c2: AS2 Hoop (bottom)

Figure 8.3. Strain distributions within region ‘A’ of the AS1-8 and AS2-8 simulation stackups. a: Radial Strain, b: Axial Strain, c: Hoop Strain

Referring to figure 8.4a, radial stress distributions in region ‘B’ of AS1-8 and AS2-8 are shown. Radial stress is compressive adjacent to skins in both simulations except near the head of the rivet button and at the top of the rivet-inner skin interface in AS2-8. It is compressive in the interior of region 'B'. It is compressive near the rivet axis in AS2-8. There is an area near the top of region 'B' where stress is tensile in AS1-8.

Referring to figure 8.4b, axial stress distributions in region ‘B’ of AS1-8 and AS2-8 are shown. Axial stress is compressive adjacent to skins except near the head of the rivet button and near the outer skin in AS1-8. It is tensile near the rivet inner-skin interface and head of the rivet button in AS2-8. It is tensile in the most areas of interior of region 'B'. It is also tensile near the rivet axis.

Referring to figure 8.4c, hoop stress distributions in region ‘B’ of AS1-8 and AS2-8 are shown. Hoop stress is compressive across region ‘B’. It is tensile at the head of the rivet button in AS1-8. It is tensile at the top of the rivet- inner skin interface and at the head of the rivet button.

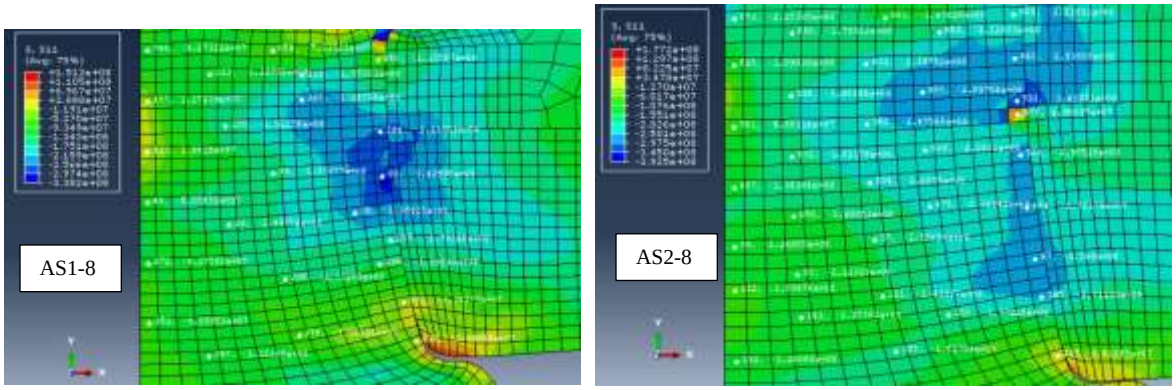

a1: AS1 Radial (left) a2: AS2 Radial (right)

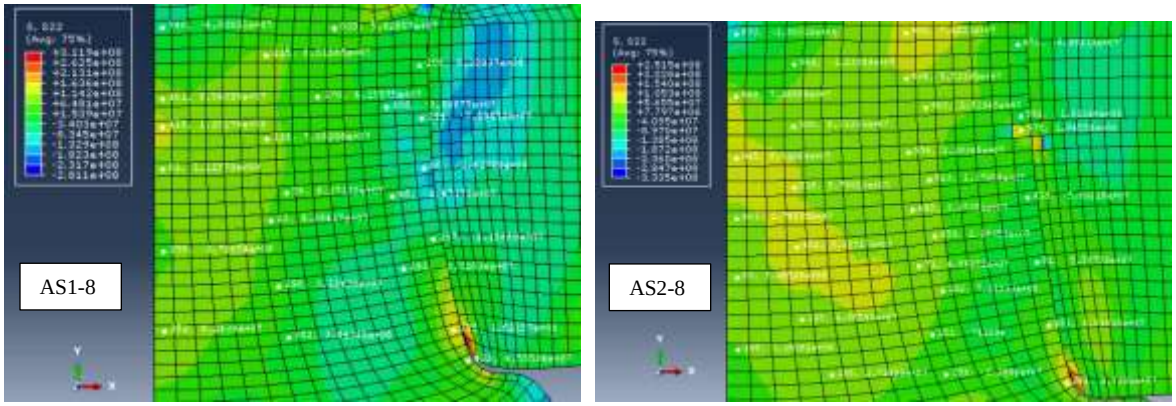

b1: AS1 Axial (left) b2: AS2 Axial (right)

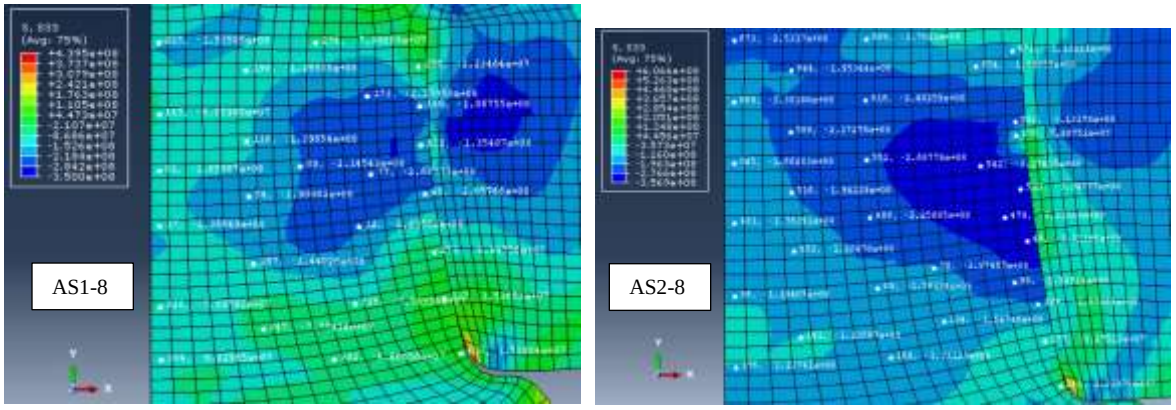

c1: AS1 Hoop (left) c2: AS2 Hoop (right)

Figure 8.4. Stress distributions within region 'B' of the AS1-8 and AS2-8 simulation stackups. a: Radial Stress, b: Axial Stress, c: Hoop Stress

Referring to figure 8.5a, logarithmic radial strain distributions in region ‘B’ of AS1-8 and AS2-8 are shown. Strain is tensile across region ‘B’ in both simulations. Magnitude is higher near the head of the rivet button compared to the interior of region ‘B’ and compared to area near base of the region ‘A’.

Referring to figure 8.5b, logarithmic axial strain distributions in region ‘B’ of AS1-8 and AS2-8 are shown. Strain is compressive across region ‘B’ except near the rivet axis at the base of region ‘A’ in both simulations. Magnitude of compressive strain is higher near the head of the rivet button compared to the interior of region ‘B’ in both simulations.

Referring to figure 8.5c, logarithmic hoop strain distributions in region ‘B’ of AS1-8 and AS2-8 are shown. Strain is tensile across region ‘B’ in both simulations. Magnitude is higher near the head of the rivet button compared to the interior of region ‘B’ and compared to area near base of the region ‘A’ in both simulations.

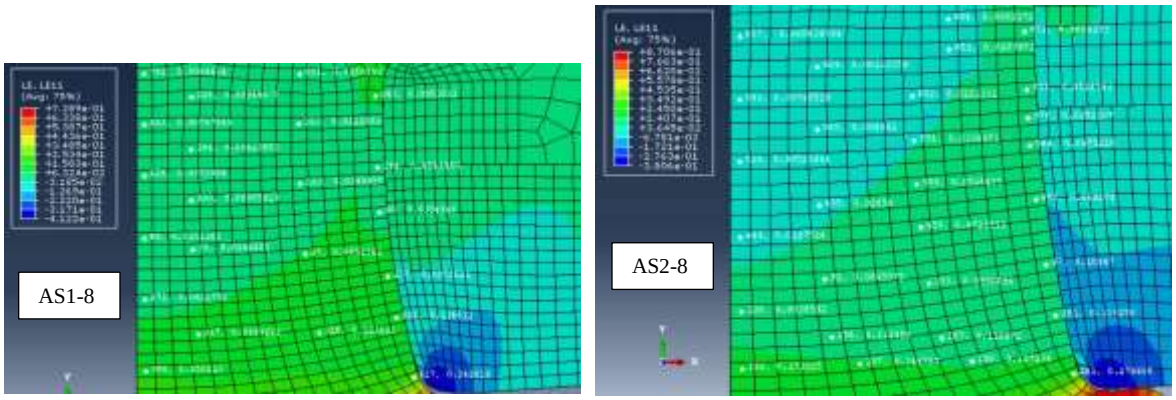

a1: AS1 Radial (left) a2: AS2 Radial (right)

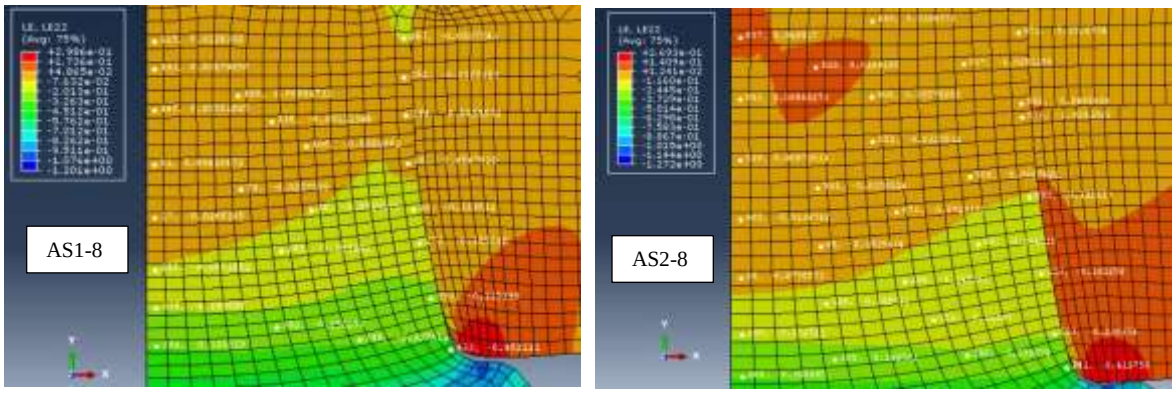

b1: AS1 Axial (left) b2: AS2 Axial (right)

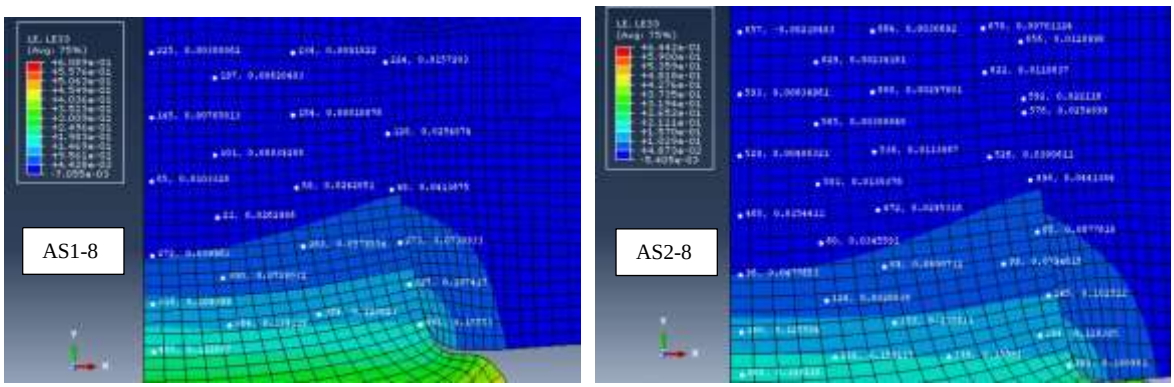

c1: AS1 Hoop (left) c2: AS2 Hoop (right)

Figure 8.5. Strain distributions within region ‘B’ of the AS1-8 and AS2-8 simulation stackups. a: Radial Strain, b: Axial Strain, c: Hoop Strain

Referring to figure 8.6a, radial stress distributions in region ‘C’ of AS1-8 and AS2-8 are shown. Radial stress is compressive across region 'C' in both simulations. Tensile stress is observed at the head of the rivet button. In both simulations, there is a large area near the free surface of the rivet button in the interior of region 'C' where the stress is tensile.

Referring to figure 8.6b, axial stress distributions in region ‘C’ of AS1-8 and AS2-8 are shown. Axial stress is tensile at the top of region 'C', from rivet axis to the rivet button free surface in both simulations. Stress is compressive at the free surface of the rivet button in both simulations. There

is a large area in the interior of region 'C' near the free surface where the stress is tensile in both simulations.

Referring to figure 8.6c, hoop stress distributions in region ‘C’ of AS1-8 and AS2-8 are shown. Stress is compressive near the rivet axis in both simulations. Stress is compressive across a large area in the interior of region ‘C’ and near the head of the rivet button in both simulations. There is also a large area in the interior of region ‘C’ near the free surface of the rivet button where the hoop stress is tensile in both simulations. Stress is tensile at the rivet button free surface.

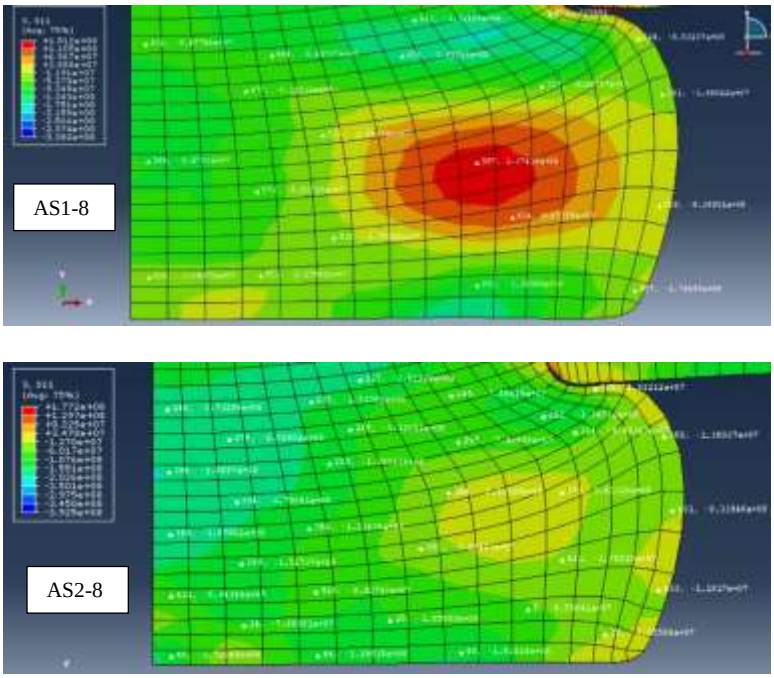

a1: AS1 Radial (top) a2: AS2 Radial (bottom)

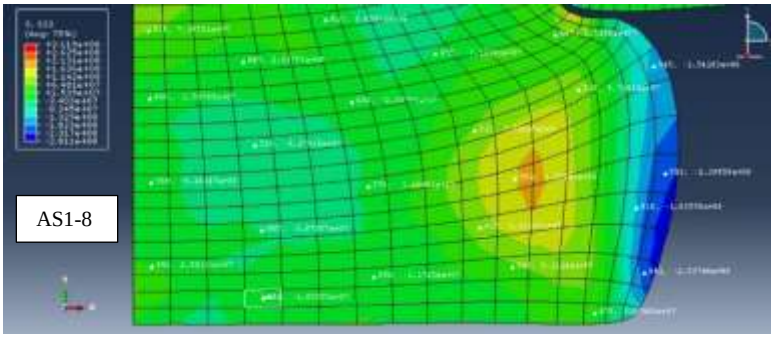

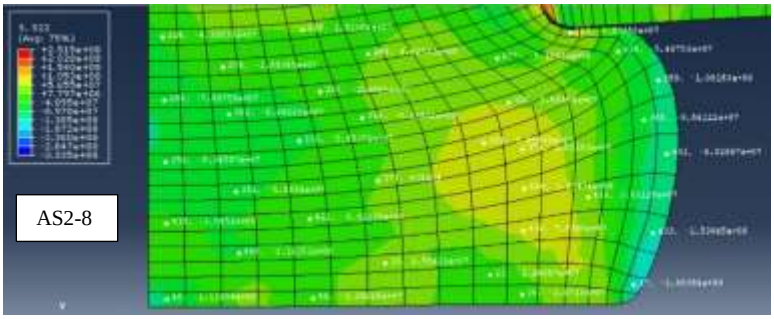

b1: AS1 Axial (top) b2: AS2 Axial (bottom)

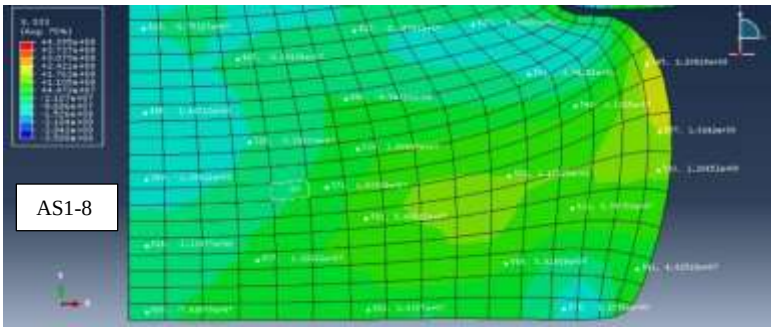

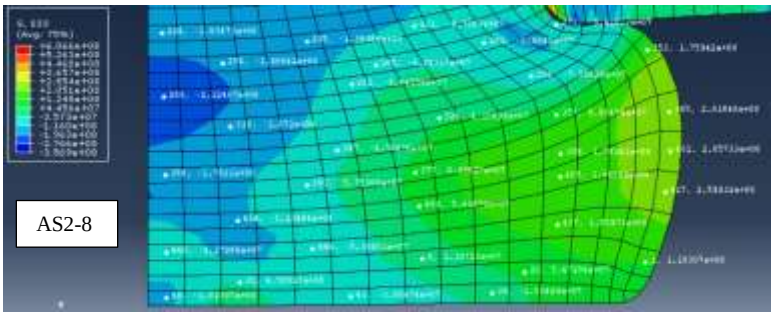

c1: AS1 Hoop (top) c2: AS2 Hoop (bottom)

Figure 8.6. Stress distributions within region 'C' of the AS1-8 and AS2-8 simulation stackups. a: Radial Stress, b: Axial Stress, c: Hoop Stress

Referring to figure 8.7a, logarithmic radial strain distributions in region ‘C’ of AS1-8 and AS2-8 are shown. In both simulations, strain is tensile across region ‘C’ except in the area near the base of the rivet button at the free surface where the strain is compressive.

Referring to figure 8.7b, logarithmic axial strain distributions in region ‘C’ of AS1-8 and AS2-8 are shown. Axial strain is compressive across region ‘C’ in both simulations. There is region that stretches from the rivet axis to the head of the rivet button where high magnitude of compressive strain is observed in both simulations. Areas outside this band in region ‘C’ have a lower axial strain magnitude.

Referring to figure 8.7c, logarithmic hoop strain distributions in region ‘C’ of AS1-8 and AS2-8 are shown. Hoop strain is tensile across region ‘C’ in both simulations. Strain is found to have a higher magnitude in the central area of region ‘C’ in both simulations.

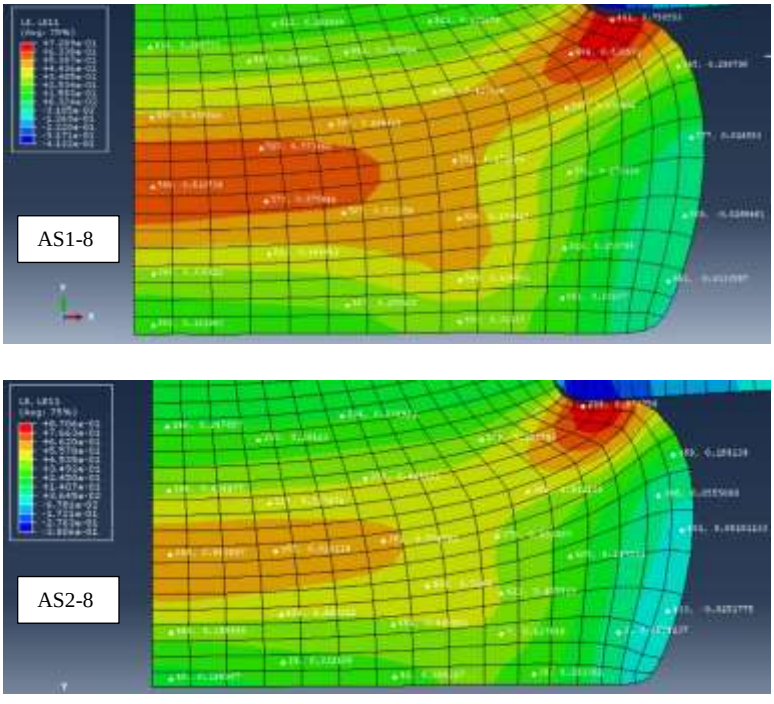

a1: AS1 Radial (top) a2: AS2 Radial (bottom)

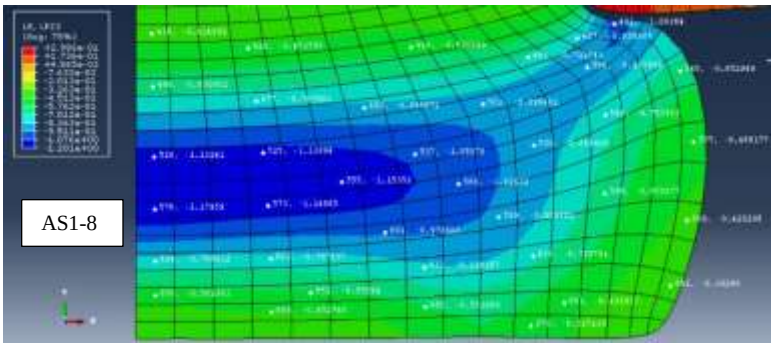

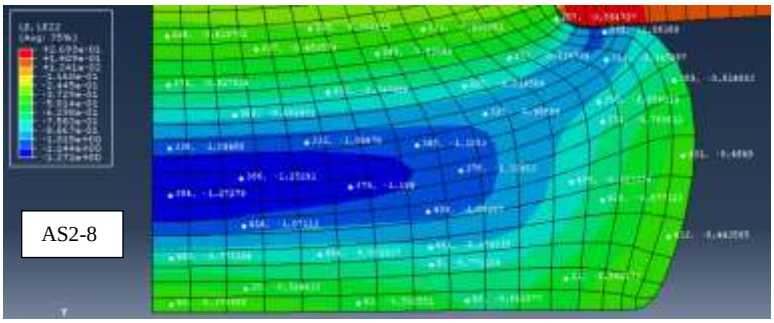

b1: AS1 Axial (top) b2: AS2 Axial (bottom)

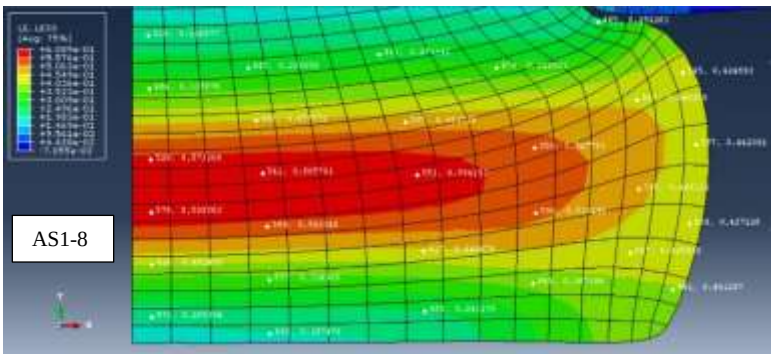

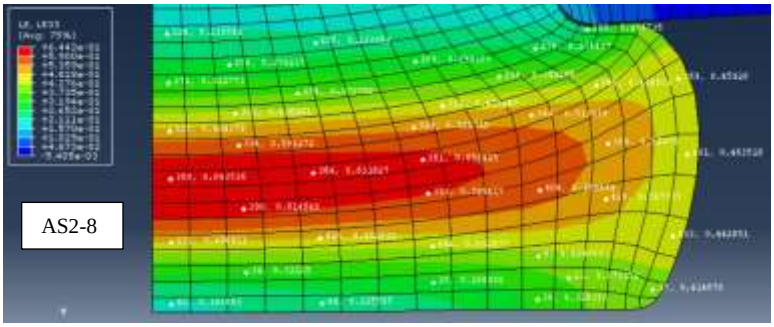

c1: AS1 Hoop (top) c2: AS2 Hoop (bottom)

Figure 8.7. Strain distributions within region 'C' of the AS1-8 and AS2-8 simulation stackups. a: Radial Strain, b: Axial Strain, c: Hoop Strain

Referring to figure 8.8a, radial stress distributions in region ‘D’ of AS1-8 and AS2-8 are shown. Radial stress is tensile in the area adjacent to the rivet crown in AS1-8. It is compressive in the same area in AS2-8. Stress is tensile and compressive in the wedge area and below the wedge area in both simulations. Stress is compressive adjacent to the rivet shank in both simulations. The radial stress is compressive in the interior of region 'D' in both simulations.

Referring to figure 8.8b, axial stress distributions in region ‘D’ of AS1-8 and AS2-8 are shown. Axial stress is compressive in the area adjacent to the rivet crown in both simulations. Stress is compressive in the wedge area in AS1-8. It is tensile and compressive in the wedge area in AS2-8. Stress is tensile and compressive below the wedge area in both simulations. Stress is tensile adjacent to the rivet shank in both simulations. The axial stress is compressive in the interior of region 'D'. It becomes tensile some distance further away from the rivet-upper skin interface.

Referring to figure 8.8c, hoop stress distributions in region ‘D’ of AS1-8 and AS2-8 are shown. Hoop stress is compressive in the area adjacent to the rivet crown in both simulations. Stress is compressive in the wedge area in both simulations. Stress is compressive below the wedge area in AS1-8 and tensile below the wedge area in AS2-8. Stress is compressive adjacent to the rivet shank in both simulations. The hoop stress is compressive in the interior of region 'D' in both simulations.

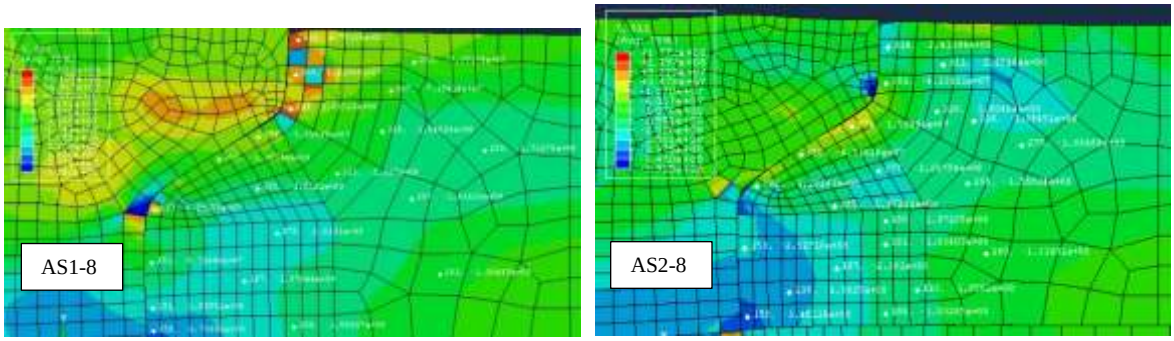

a1: AS1 Radial (left) a2: AS2 Radial (right)

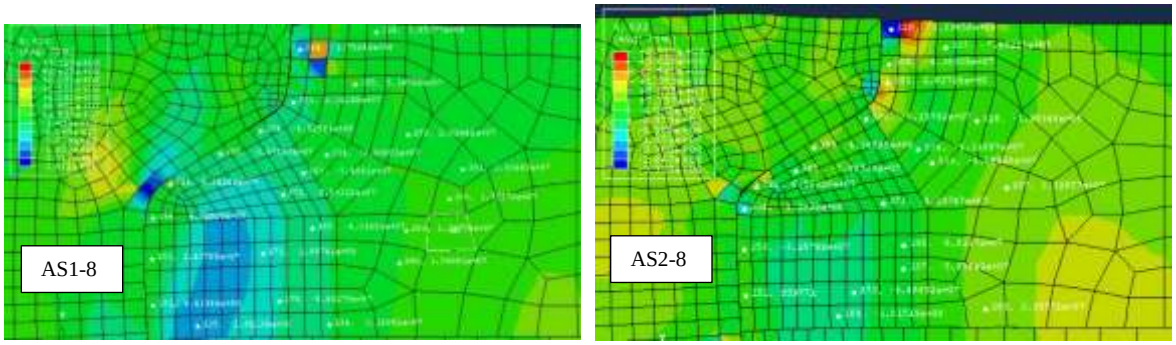

b1: AS1 Axial (left) b2: AS2 Axial (right)

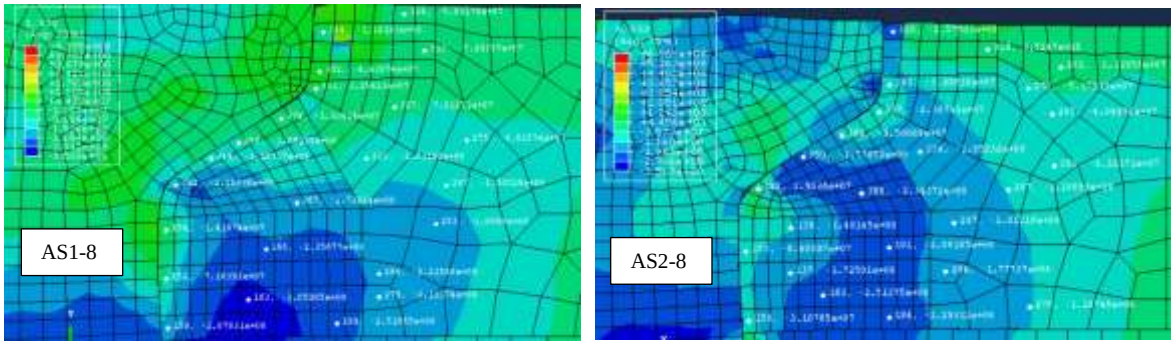

c1: AS1 Hoop (left) c2: AS2 Hoop (right)

Figure 8.8. Stress distributions within region 'D' of the AS1-8 and AS2-8 simulation stackups. a: Radial Stress, b: Axial Stress, c: Hoop Stress

Referring to figure 8.9a, logarithmic radial strain distributions in region 'D' of AS1-8 and AS2-8 are shown. Radial strain is compressive in the area adjacent to the rivet crown in both simulations. Strain is tensile in the wedge area and below the wedge area in both simulations. In

both simulations, strain is tensile adjacent to the rivet shank except adjacent to inner skin. The radial strain is compressive in the interior area of region 'D' adjacent to rivet crown and wedge. The radial strain is compressive in AS1-8 and tensile in AS2-8 in the interior area of region 'D' adjacent to the rivet shank.

Referring to figure 8.9b, logarithmic axial strain distributions in region ‘D’ of AS1-8 and AS2-8 are shown. Axial strain is tensile in the area adjacent to the rivet crown in both simulations. Strain is compressive in the wedge area and below the wedge area in both simulations. Strain is compressive adjacent to the rivet shank in both simulations. The axial strain is tensile in the interior area of region 'D' adjacent to rivet crown in both simulations.

Referring to figure 8.9c, logarithmic hoop strain distributions in region ‘D’ of AS1-8 and AS2-8 are shown. Hoop strain is tensile across region 'D' in both simulations. The magnitude is higher near the rivet-skin interface compared to the magnitude away from the rivet-skin interface in both simulations.

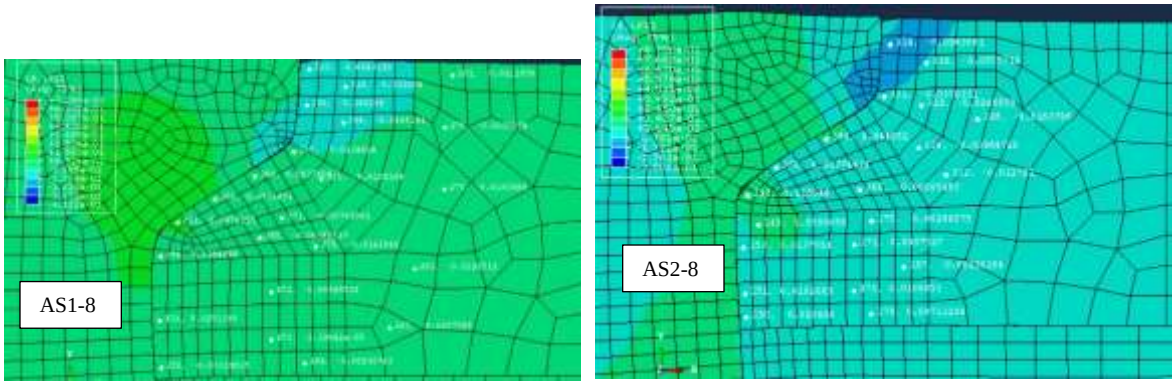

a1: AS1 Radial (left) a2: AS2 Radial (right)

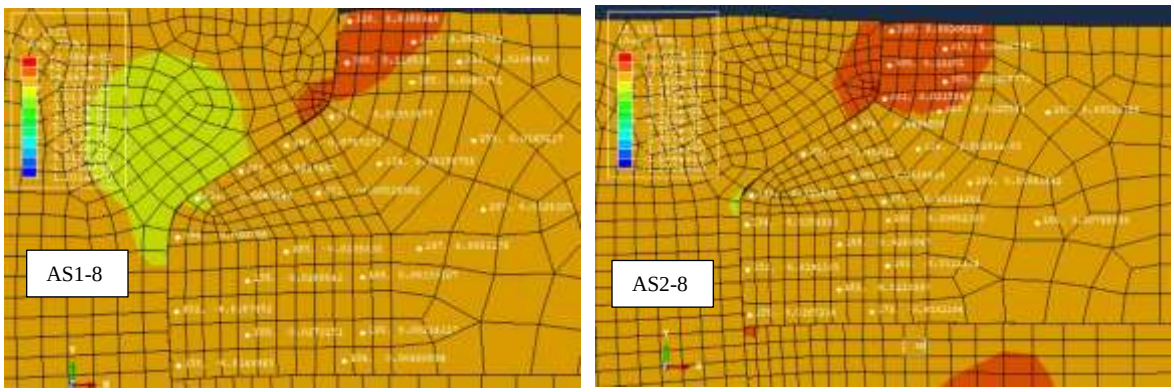

b1: AS1 Axial (left) b2: AS2 Axial (right)

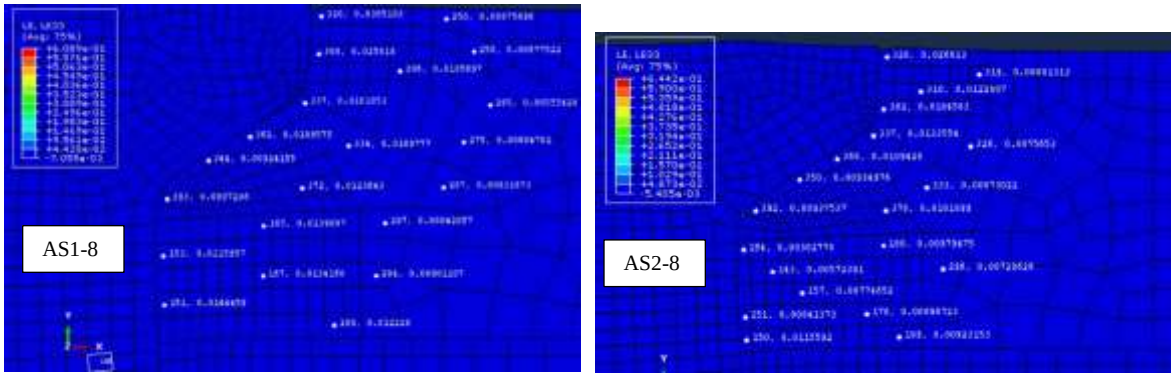

c1: AS1 Hoop (left) c2: AS2 Hoop (right)

Figure 8.9. Strain distributions within region ‘D’ of the AS1-8 and AS2-8 simulation stackups. a: Radial Strain, b: Axial Strain, c: Hoop Strain

Referring to figure 8.10a, radial stress distributions in regions ‘E’ and 'G' of AS1-8 and AS2-8 are shown. Radial stress is compressive across regions 'E' and 'G' in both simulations. In both simulations, the magnitude is higher in the areas adjacent to regions 'D' and 'F' compared to the magnitude in the areas away from these regions.

Referring to figure 8.10b, axial stress distributions in regions ‘E’ and 'G' of AS1-8 and AS2-8 are shown. In both simulations, the magnitude of compressive and tensile axial stresses in regions ‘E’ and ‘G’ is small.

Referring to figure 8.10c, hoop stress distributions in regions ‘E’ and 'G' of AS1-8 and AS2-8 are shown. In both simulations, hoop stress is tensile across regions 'E' and 'G'. The magnitude is

higher in the areas adjacent to regions 'D' and 'F' compared to the magnitude in the areas away from these regions in both simulations.

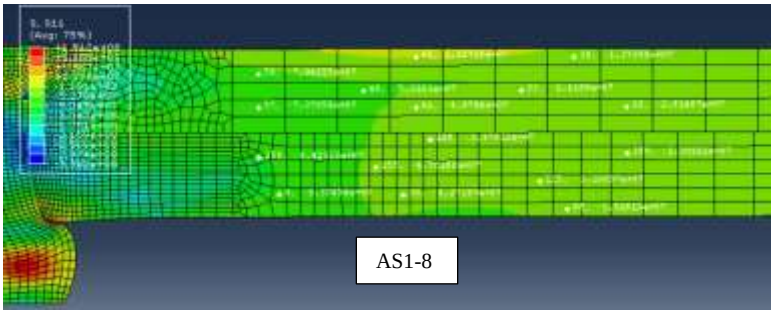

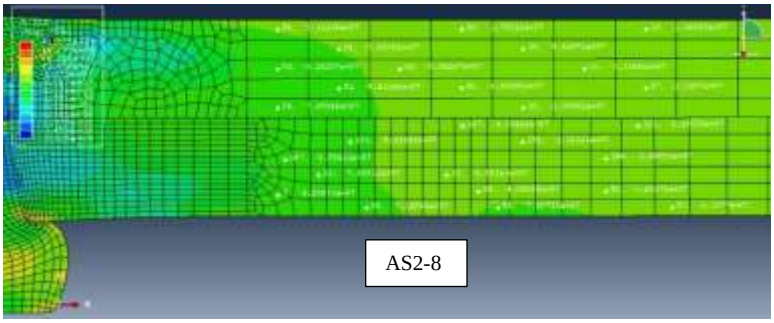

a1: AS1 Radial (top) a2: AS2 Radial (bottom)

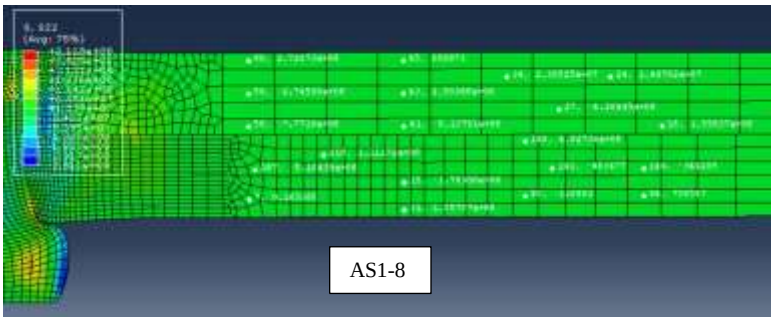

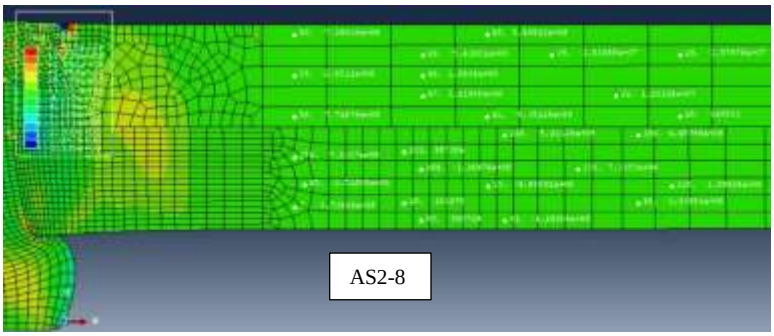

b1: AS1 Axial (top) b2: AS2 Axial (bottom)

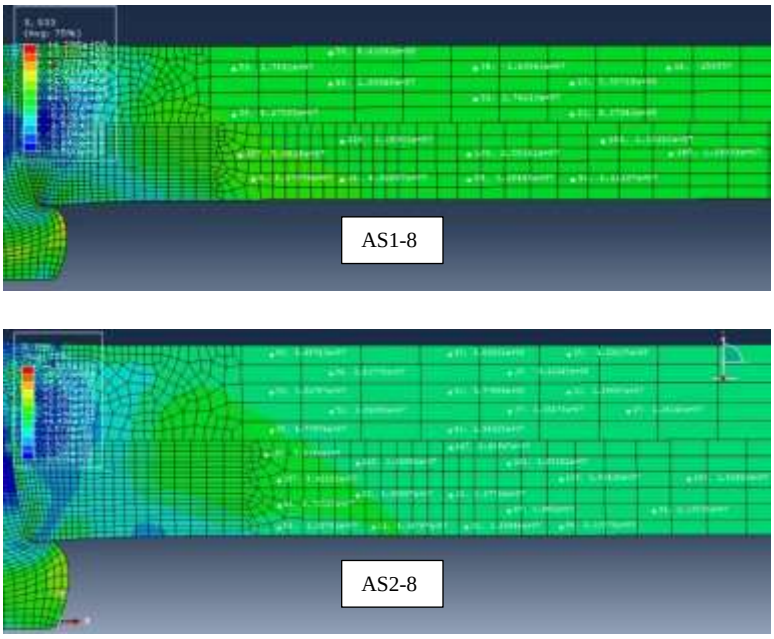

C1: AS1 Hoop (top) c2: AS2 Hoop (bottom)

Figure 8.10. Stress distributions within regions ‘E’ and ‘G’ of the AS1-8 and AS2-8 simulation stackups. A: Radial Stress, b: Axial Stress, c: Hoop Stress

Referring to figure 8.11a, logarithmic radial strain distributions within regions ‘E’ and ‘G’ of AS1-8 and AS2-8 simulation are shown. The radial strain is compressive and has small magnitude across regions ‘E’ and ‘G’ in both simulations. Magnitude of strain reduces with increasing distance from rivet axis in both simulations.

Referring to figure 8.11b, logarithmic axial strain distributions within regions ‘E’ and ‘G’ of AS1-8 and AS2-8 simulation are shown. The axial strain is tensile and has small magnitude across regions ‘E’ and ‘G’ in both simulations. Axial strain is tensile because of the tie constraint used in the AS1-8 and AS2-8 (full dynamic percussive) simulations. Strain magnitude reduces in both simulations with increasing distance from rivet axis.

Referring to figure 8.11c, logarithmic hoop strain distributions within regions ‘E’ and ‘G’ of AS1-8 and AS2-8 simulation are shown. The hoop strain is tensile and has small magnitude across

regions ‘E’ and ‘G’ in both simulations. The strain magnitude reduces with increasing distance from rivet axis in both simulations.

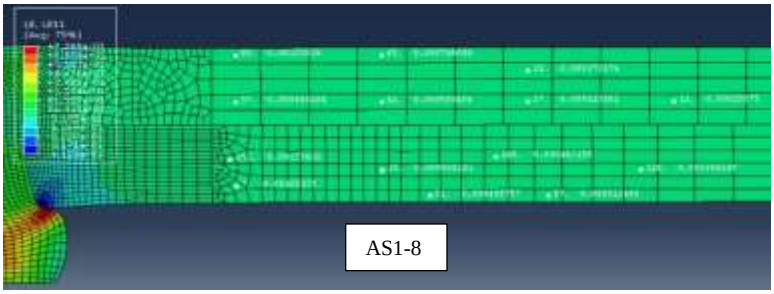

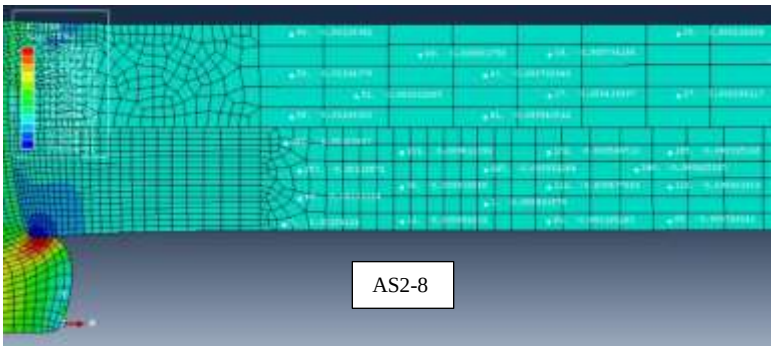

a1: AS1 Radial (top) a2: AS2 Radial (bottom)

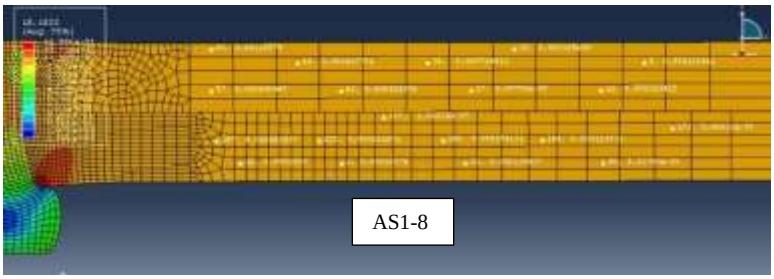

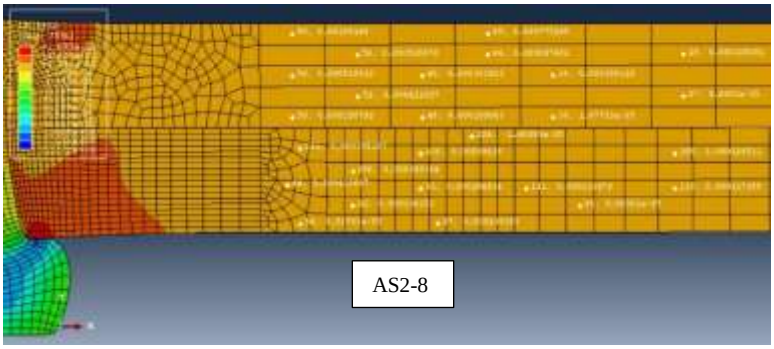

b1: AS1 Axial (top) b2: AS2 Axial (bottom)

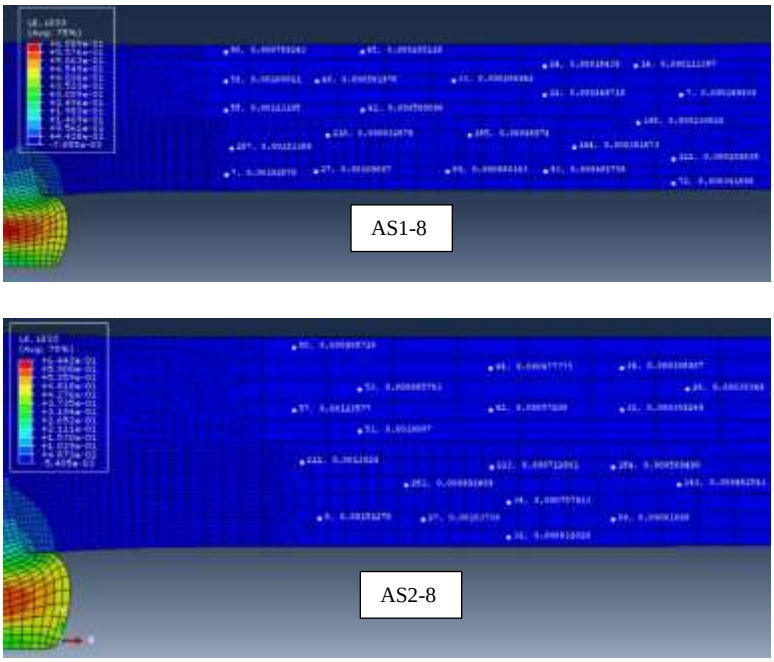

c1: AS1 Hoop (top) c2: AS2 Hoop (bottom)

Figure 8.11. Strain distributions within regions ‘E’ and ‘G’ of the AS1-8 and AS2-8 simulation stackups. a: Radial Strain, b: Axial Strain, c: Hoop Strain

Referring to figure 8.12a, radial stress distributions in region 'F' of AS1-8 and AS2-8 are shown. Radial stress is compressive across region ‘F’. Tensile stress is observed near the head of the rivet button in both simulations. Tensile stress is observed in AS2-8 in the area near the rivet shank at the inner skin-outer skin.

Referring to figure 8.12b, axial stress distributions in region 'F' of AS1-8 and AS2-8 are shown. There are areas of tensile and compressive stress in region 'F' in both simulations. At two locations near rivet shank in both simulations, head of the rivet button and inner skin- outer skin interface, tensile stress is observed.

Referring to figure 8.12c, hoop stress distributions in region 'F' of AS1-8 and AS2-8 are shown. Hoop stress is compressive across region ‘F’ in both simulations. There is small area of tensile hoop stress adjacent to the rivet shank near region ‘D’ and near head of the rivet button in both simulations.

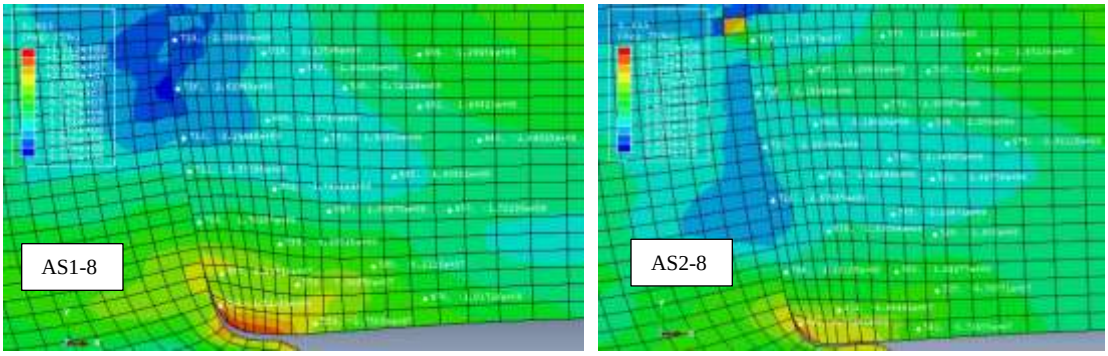

a1: AS1 Radial (left) a2: AS2 Radial (right)

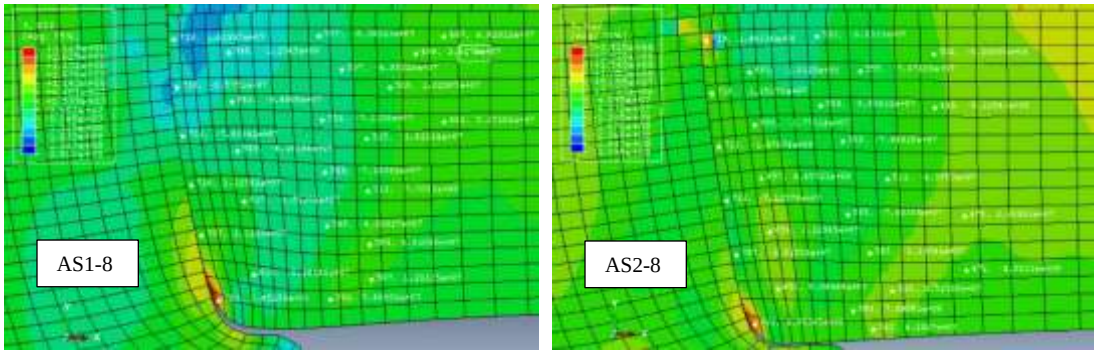

b1: AS1 Axial (left) b2: AS2 Axial (right)

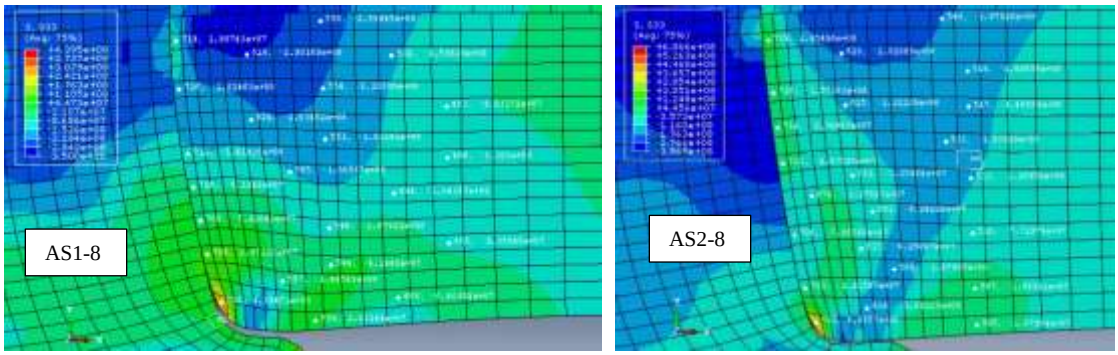

c1: AS1 Hoop (left) c2: AS2 Hoop (right)

Figure 8.12. Stress distributions within region 'F' of the AS1-8 and AS2-8 simulation stackups. a: Radial Stress, b: Axial Stress, c: Hoop Stress

Referring to figure 8.13a, logarithmic radial strain distributions within region ‘F’ of AS1-8 and AS2-8 simulation are shown. Radial strain is compressive across region ‘F’ in both simulations. The magnitude is higher near the head of the rivet button compared to other areas in region ‘F’ in both simulations. There is an area in AS1-8 near the rivet shank at the inner skin-outer skin interface where tensile strain of small magnitude is observed.

Referring to figure 8.13b, logarithmic axial strain distributions within region ‘F’ of AS1-8 and AS2-8 simulation are shown. Axial strain is tensile across region ‘F’. The magnitude is higher near the head of the rivet button compared to other areas in region ‘F’ in both simulations. There are areas near the rivet shank and near the inner skin-outer skin interface where compressive strains are observed in both simulations.

Referring to figure 8.13c, logarithmic hoop strain distributions within region ‘F’ of AS1-8 and AS2-8 simulation are shown. Hoop strain is tensile across region ‘F’ in both simulations. The magnitude is higher near the head of the rivet button compared to other areas in region ‘F’ in both simulations.

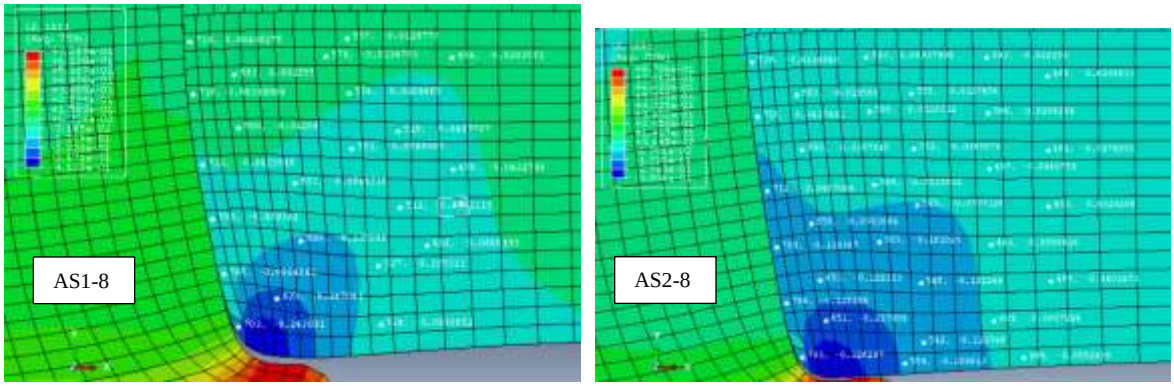

a1: AS1 Radial (top) a2: AS2 Radial (bottom)

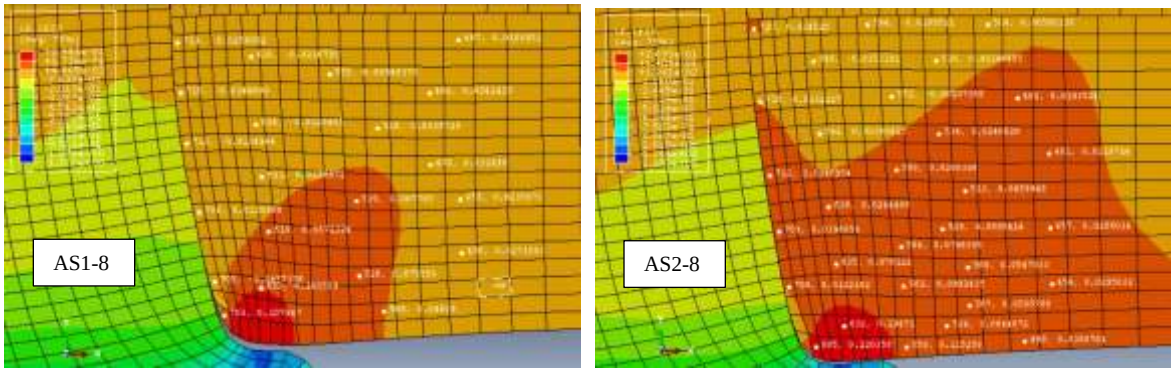

b1: AS1 Axial (top) b2: AS2 Axial (bottom)

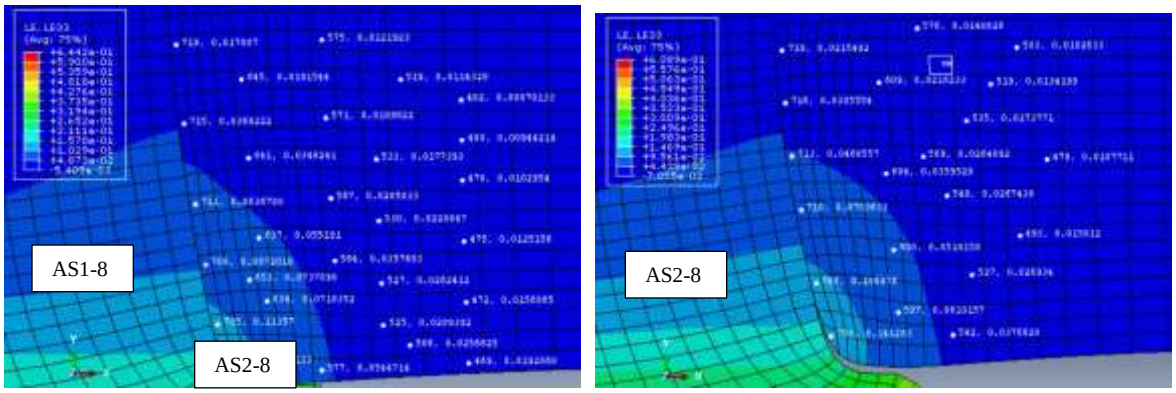

c1: AS1 Hoop (top) c2: AS2 Hoop (bottom)

Figure 8.13. Strain distributions within region 'F' of the AS1-8 and AS2-8 simulation stackups. a: Radial Strain, b: Axial Strain, c: Hoop Strain

Measurements of residual stresses and strains were made at various skin-skin interface and skin-rivet interface element nodes. These interfaces are shown in Figure 8.14. X-coordinate is normalized with respect to radius of rivet shank (R_{rivet}). Y-coordinate is normalized with respect to length of rivet shank (L_{shank}). First interface is the inner skin region adjacent to the rivet (denoted by 'IR'). Normalized Y-coordinate of IR ranges from 0.55 to 0.75. Second is the inner skin region adjacent to the outer skin (denoted by 'IO').

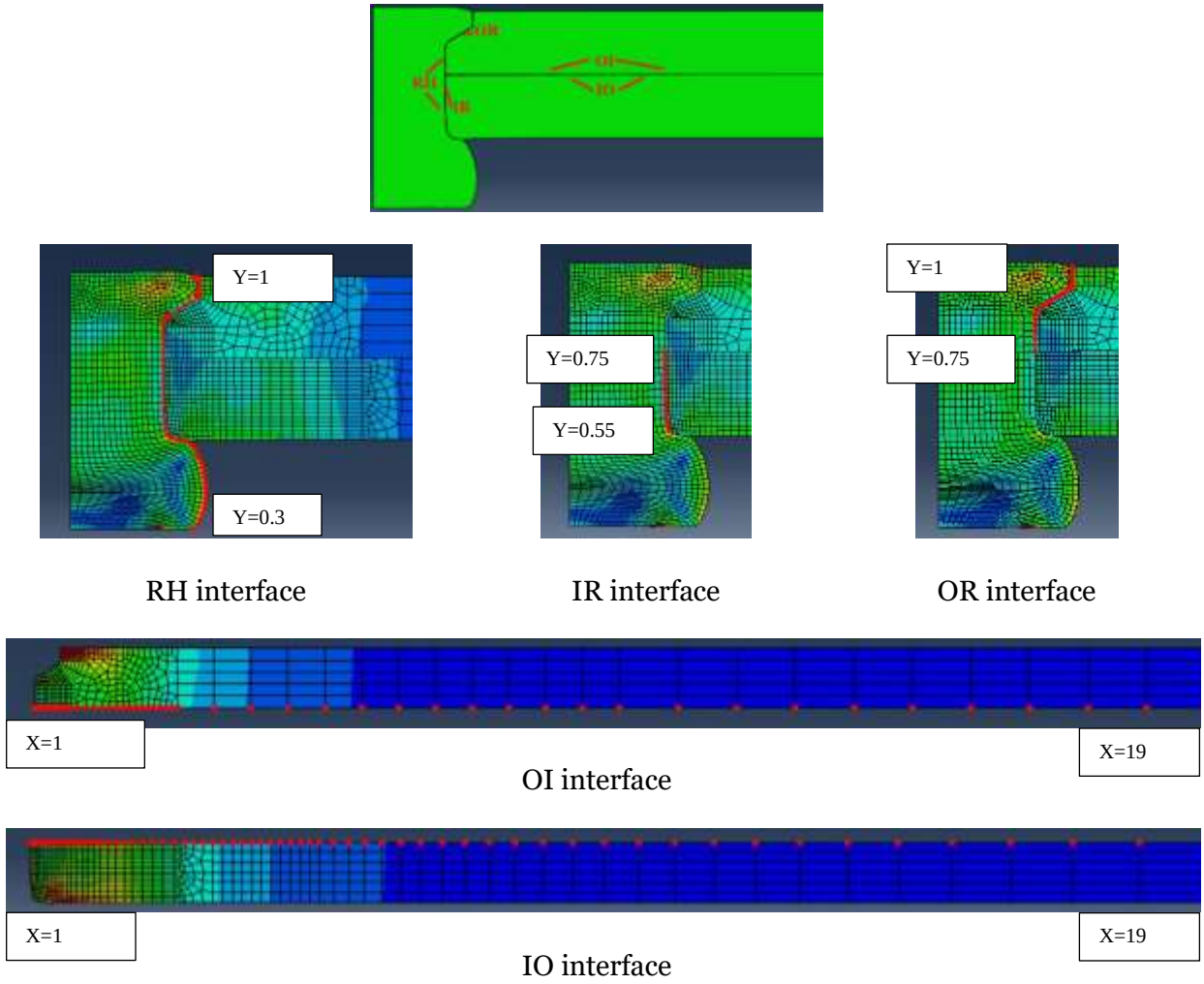

Figure 8.14. Interface residual stresses/strains measurement locations. Measurements were made at the interface nodes (highlighted nodes shown in red).

Normalized X-coordinate of IO ranges from 1 to 19. Third is the outer skin region adjacent to the rivet (denoted by 'OR'). Normalized Y-coordinate of OR ranges from 0.75 to 1. Fourth is the

outer skin region adjacent to the inner skin (denoted by 'OI'). Normalized X-coordinate of OI ranges from 1 to 19. Fifth is the rivet region adjacent to the rivet hole which spans both the inner skin's hole region and the outer skin's hole region (denoted by 'RH'). Normalized Y-coordinate of RH ranges from 0.3 to 1.

Referring to figure 8.15, the residual radial stress distributions of the quasistatic-percussive comparison and the two analysis sets-- QS and AS1-7, Analysis set 1 in the middle, Analysis set 2 on the right-- are shown at interface IR. Near the head of the button at Y=0.53 the radial stress is tensile in AS1-7 and highly compressive in QS from figure 8.15a. Higher up along IR interface the radial stresses are compressive and toward the IO interface near Y=0.75 compressive stresses in AS1-7 are higher in magnitude compared to QS. Y=0.75 corresponds to the location of the outer surface of the inner skin or the IR interface. Y=0.75 is where both skins mate against each other. From figure 8.15b and 8.15c, the radial stress trend is found to be tensile near Y=0.53 in AS1 and AS2 simulations but as we proceed toward Y=0.75, it becomes compressive in all simulations.

Referring to figure 8.15d, axial stress distribution at interface IR of QS and AS1-7 is shown. Near the head of the button at Y=0.53 the axial stress is tensile in AS1-7 and highly compressive in QS. Higher up along IR interface the axial stresses are compressive in AS1-7 and tensile in QS. Toward the IO interface near Y=0.75 the stress becomes tensile in AS1-7 and marginally compressive in QS. From figure 8.15e and 8.15f, the axial stress trend is found to be mostly tensile near Y=0.53 in AS1 and AS2 simulations. Between Y=0.56 and Y=0.65, the axial stresses of all simulations become compressive and remain mostly compressive until Y=0.7. For some simulations it turns tensile between Y=0.7 and Y=0.75.

Referring to figure 8.15g, hoop stress distribution at interface IR of QS and AS1-7 is shown. Near the head of the button at Y=0.53 the hoop stress is tensile in AS1-7 and compressive in QS. Higher up along IR interface the axial stresses are compressive both models. Toward the IO interface near Y=0.75 the stress becomes tensile in AS1-7 and remains compressive in QS. From figure 8.15h and 8.15i, the hoop stress trend is found to be mostly tensile near Y=0.53 in AS1 and

AS2 simulations. Between Y=0.56 and Y=0.73, the hoop stresses of all simulations become compressive and mostly remain compressive. Beyond Y=0.73, some distributions become tensile and other remain compressive.

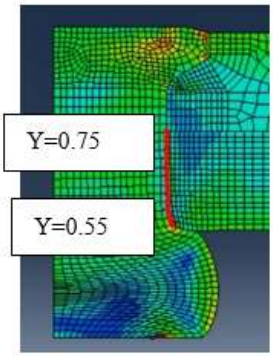

IR interface

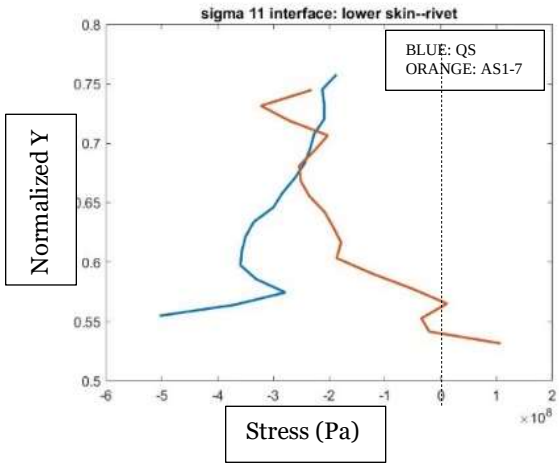

a: QS and AS 1-7 radial stress

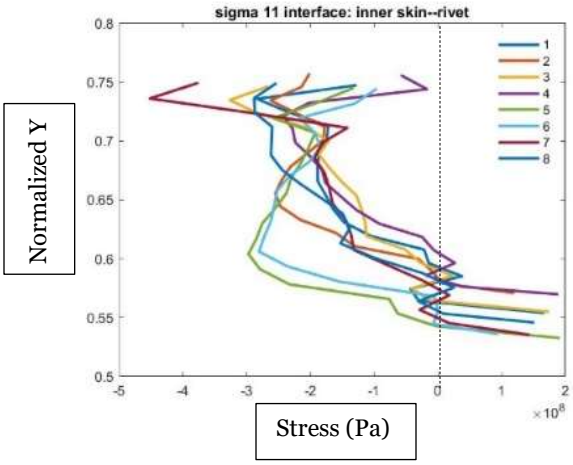

b: AS1 radial stress

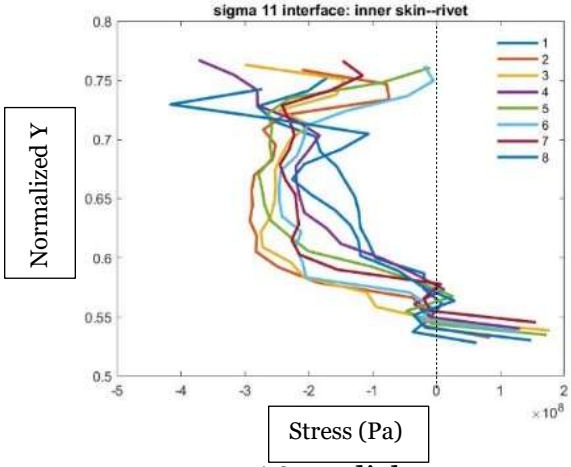

c: AS2 radial stress

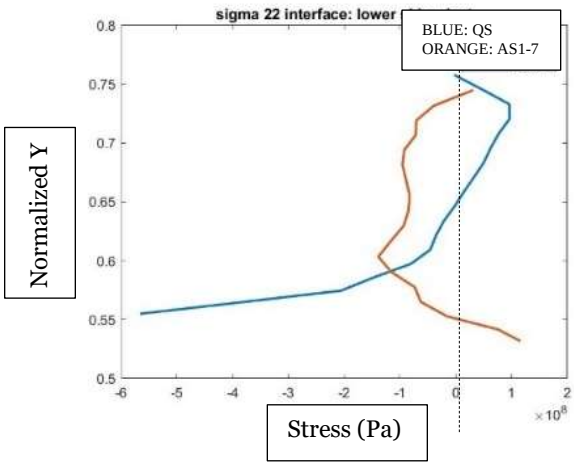

d: QS and AS1-7 axial stress

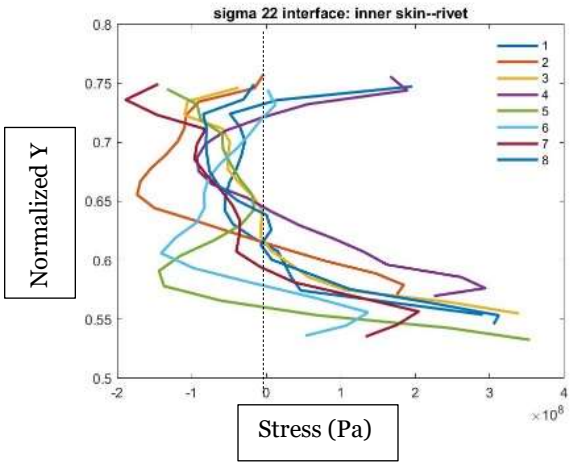

e: AS1 axial stress

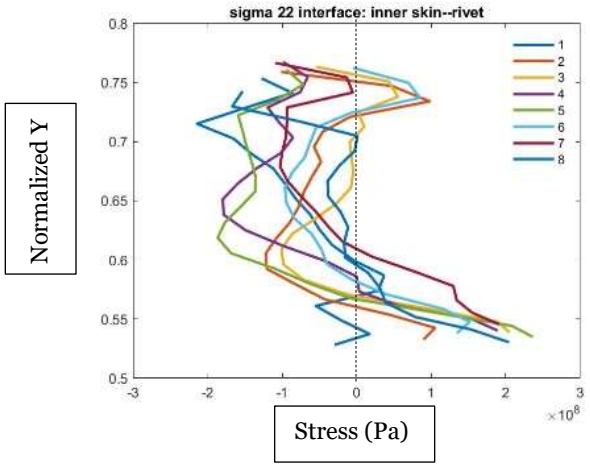

f: AS2 axial stress

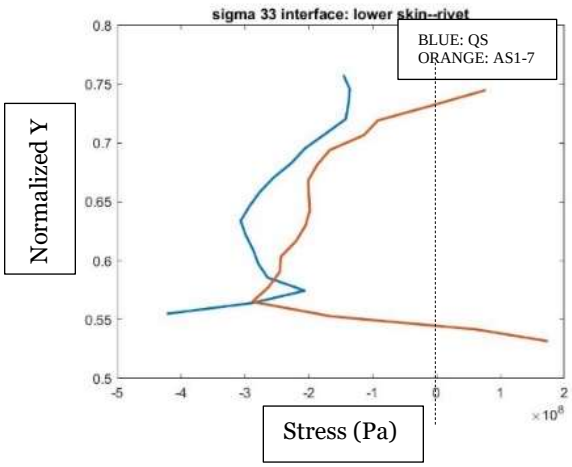

g: QS and AS1-7 hoop stress

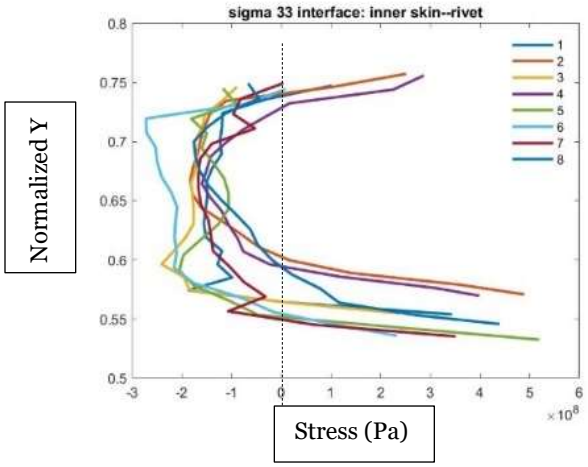

h: AS1 hoop stress

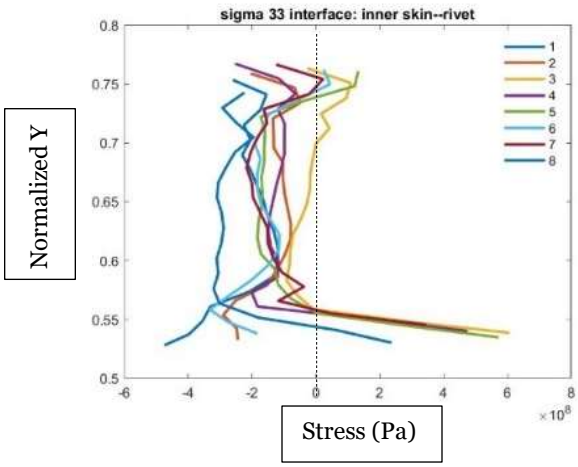

i: AS2 hoop stress

Figure 8.15. Residual stress distributions of QS, AS1 and AS2 simulations at the IR interface.

Referring to figure 8.16a, logarithmic radial strain distribution at interface IR of QS and AS1-7 is shown. Near the head of the button at Y=0.53 the radial strain is positive in QS and negative in AS1-7. Higher up along IR interface the radial strain remains negative in AS1-7 and positive in QS. As can be observed in table 8.5, R_4 and R_3 values of AS1-7 are larger than QS. From figure 8.16b and 8.16c, the radial strain trend in AS1 and AS2 simulations is found to be negative near Y=0.53. Between Y=0.53 and Y=0.75, the radial strains of almost all simulations remain negative. Inflections in the profiles can be observed near Y=0.57, Y=0.6, and Y=0.72.

Referring to figure 8.16d, logarithmic axial strain distribution at interface IR of QS and AS1-7 is shown. Near the head of the button at Y=0.53 the axial strain is negative in QS and positive in AS1-7. Although there are inflections in the profiles at Y=0.55, Y=0.6, and Y=0.72, the axial strain remains negative in QS and positive in AS1-7. From figure 8.16e and 8.16f, in AS1 and AS2 simulations, the axial strain trend is found to be positive for some and negative for others near Y=0.53. There are three inflections in the axial strain trends over the IR domain. The behavior of all distributions is similar and can be visualized as a '∑' pattern between Y=0.53 and Y=0.75.

Referring to figure 8.16g, logarithmic hoop strain distribution at interface IR of QS and AS1-7 is shown. The hoop strain is positive in both QS and AS1-7 over the entire IR domain but the magnitude is higher in AS1-7 indicating a greater hole expansion in AS1-7 compared to QS that can be verified using table 8.5. From figure 8.16h and 8.16i, in AS1 and AS2 simulations, the hoop strain distribution is found to be positive for all simulations for the entire IR domain. The strains are greater at Y= 0.53 than at Y=0.75 in all simulations which corresponds to a higher R_4 compared to R_3.

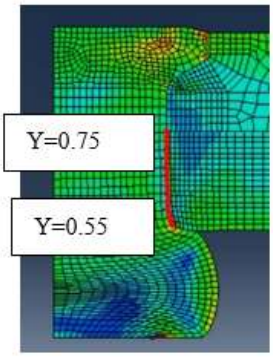

IR interface

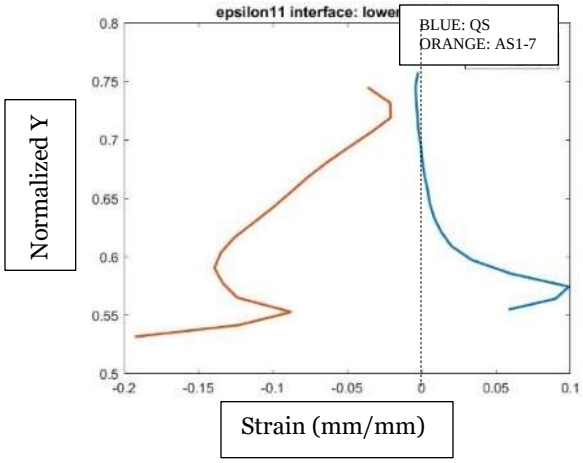

a: QS and AS 1-7 radial strain

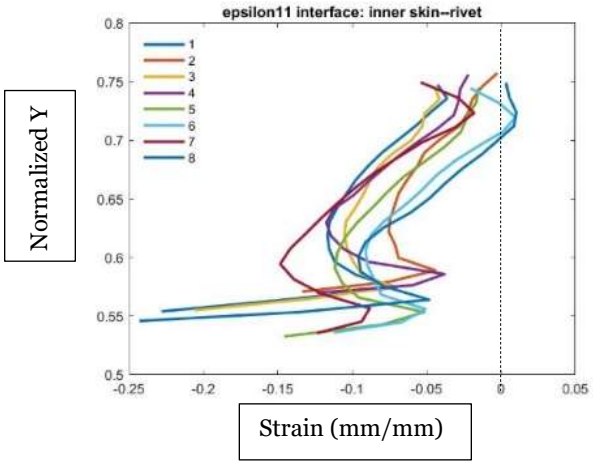

b: AS1 radial strain

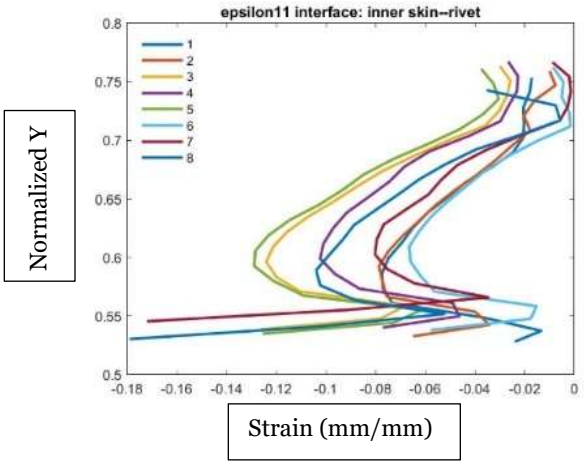

c: AS2 radial strain

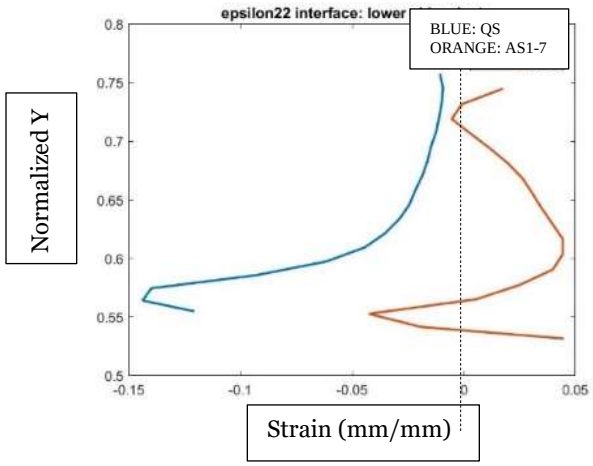

d: QS and AS1-7 axial strain

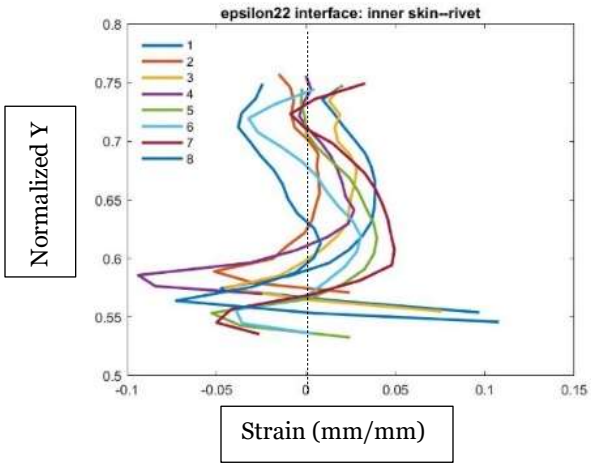

e: AS1 axial strain

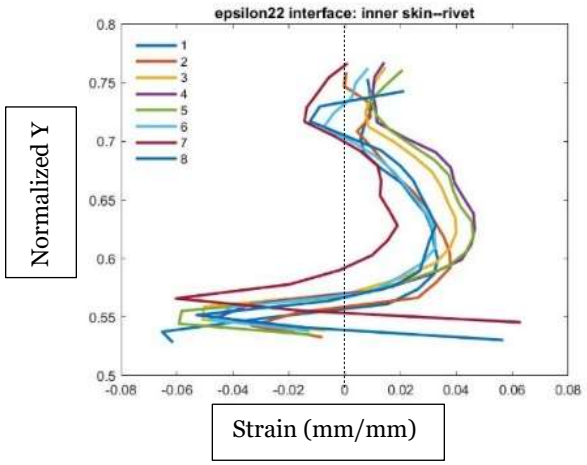

f: AS2 axial strain

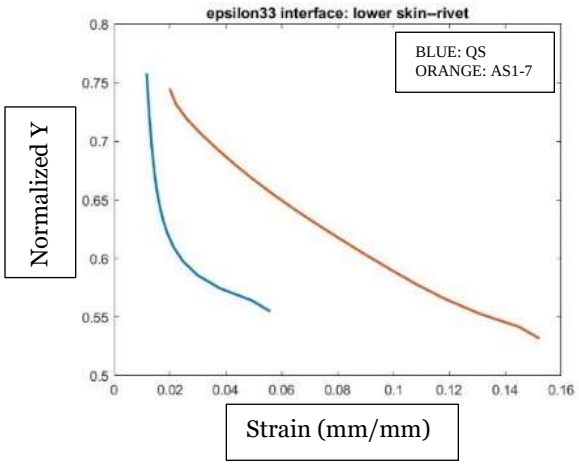

g: QS and AS1-7 hoop strain

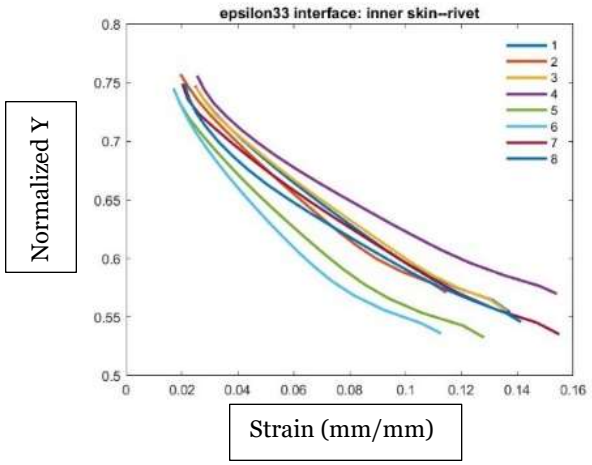

h: AS1 hoop strain

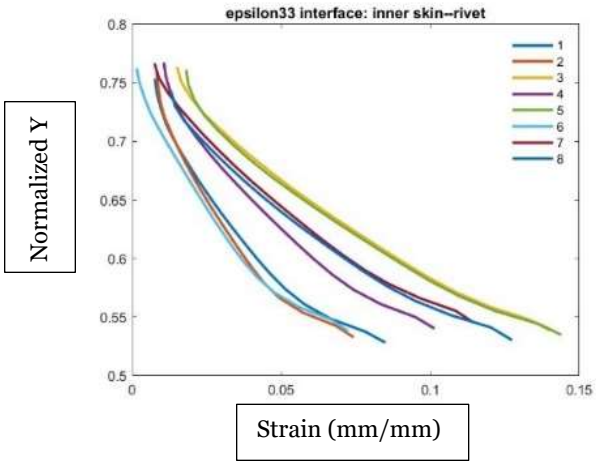

i: AS2 hoop strain

Figure 8.16. Residual strain distributions of QS, AS1 and AS2 simulations at the IR interface.

Referring to figure 8.17a, radial stress distribution at interface IO of QS and AS1-7 is shown. At the skin-rivet interface near X=1, the stress is more compressive in AS1-7 compared to QS. The stress remains compressive in both distributions over the entire IO domain. The inflections in the AS1-7 stress distribution at X=4 indicates springback [Rans, 14]. From figure 8.17b and 8.17c, the radial stress is found to be compressive for almost all AS2 and AS1 simulations near X=1. There are three inflections in the radial stress trends over the IO domain. These are near X=1, X=3, and X=4. The inflection at X=4 corresponds to springback. The behavior of all distributions is similar and the radial stress remains compressive for the entire IO domain for almost all simulations.

Referring to figure 8.17d, axial stress distribution at interface IO of QS and AS1-7 is shown. At the skin-rivet interface near X=1, the stress is more compressive in AS1-7 compared to QS. The stress remains compressive in both distributions for a short distance from the skin-rivet interface but it oscillates between compression and tension away from the skin-rivet interface. The value of stress in both distributions is small and tensile further away from skin-rivet interface. From figure 8.17e and 8.17f, the axial stress is found to be compressive for almost all AS1 and AS2 simulations near X=1. There are multiple inflections in the axial stress trends over the IO domain. The behavior of all distributions is similar. Like the radial stress distributions, the magnitude of the axial stress reduces in all distributions beyond X=8.

Referring to figure 8.17g, hoop stress distribution at interface IO of QS and AS1-7 is shown. Near X=1, the stress is more compressive in AS1-7 compared to QS. The stress remains compressive in both distributions for a short distance away from the skin-rivet interface. The area of compressive hoop stress region of AS1-7 is greater than the area of QS. The inflection in the stress distribution near X=3 indicates springback. The stress is small in magnitude in both distributions further away from the skin-rivet interface. From figure 8.17h and 8.17i, the hoop stress is found to be compressive for AS1 and AS2 simulations near X=1. There are two major inflections in the hoop stress trends over the IO domain at around X=1 and X=3. The behavior of all distributions is similar. Like the radial and axial stress distributions, the magnitude of the hoop stress reduces in all distributions beyond X=7.

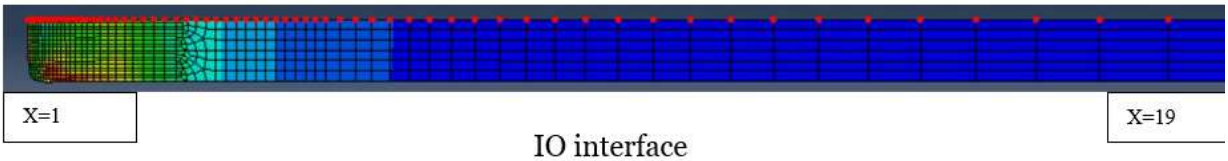

IO interface

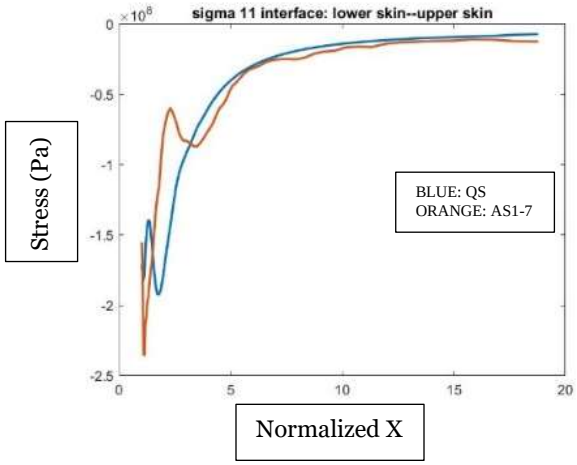

a: QS and AS 1-7 radial stress

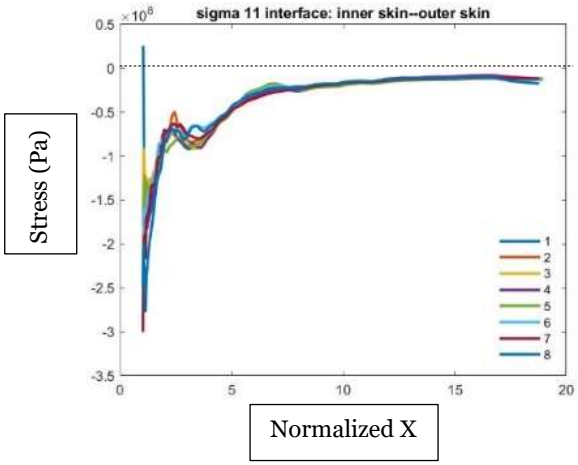

b: AS1 radial stress

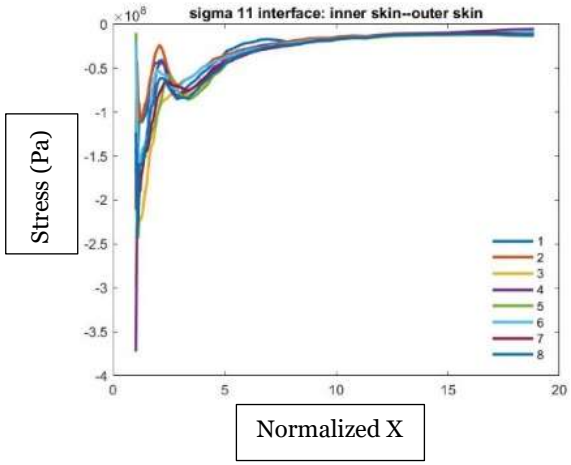

c: AS2 radial stress

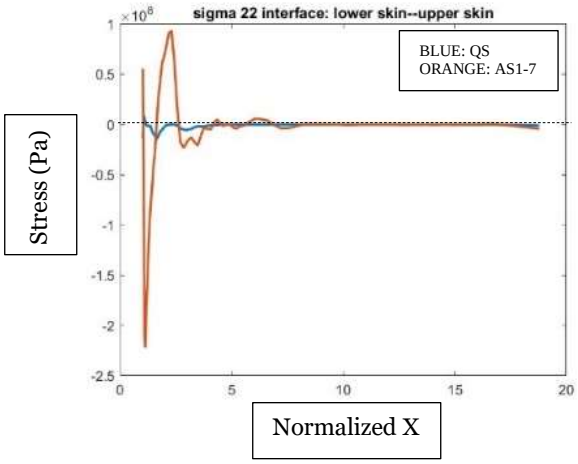

d: QS and AS1-7 axial stress

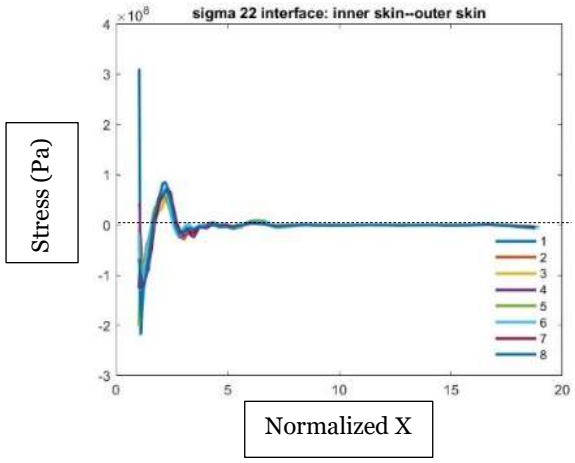

e: AS1 axial stress

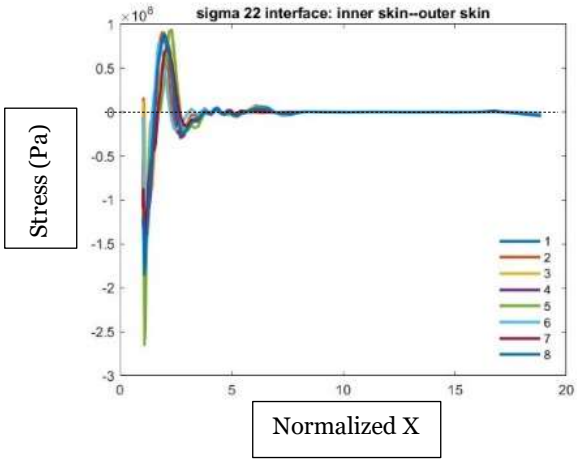

f: AS2 axial stress

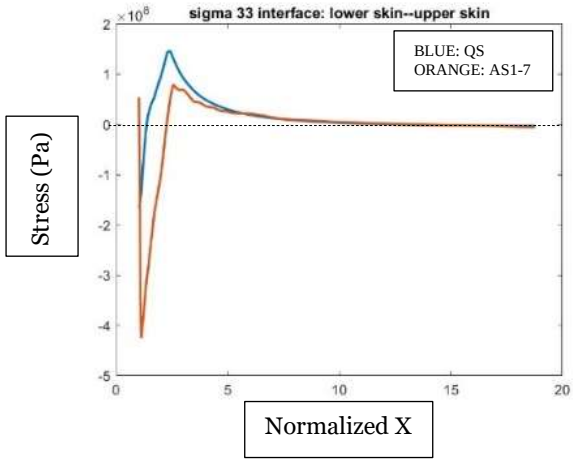

g: QS and AS1-7 hoop stress

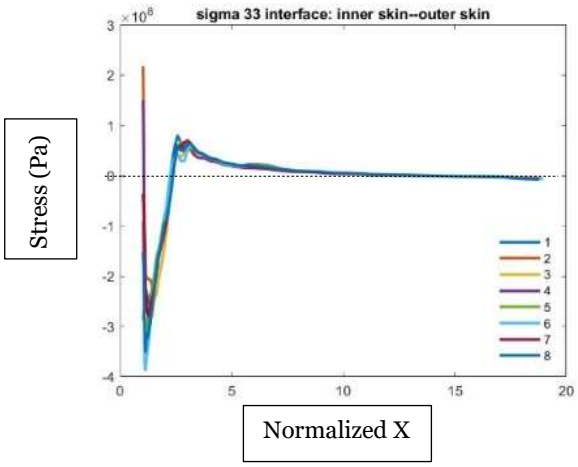

h: AS1 hoop stress

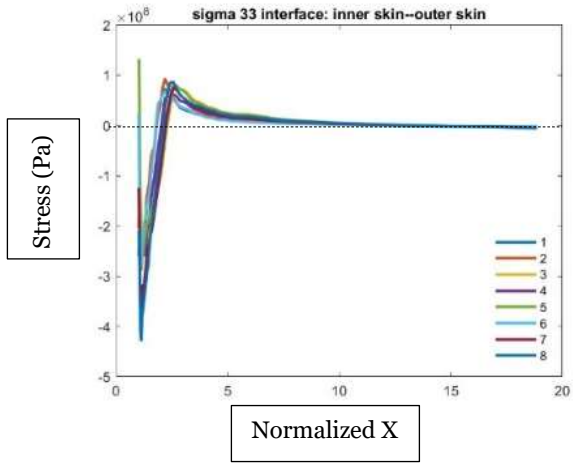

i: AS2 hoop stress

Figure 8.17. Residual stress distributions of QS, AS1 and AS2 simulations at the IO interface.

Referring to figure 8.18a, logarithmic radial strain distribution at interface IO of QS and AS1-7 is shown. At the skin-rivet interface near X=1, the strain is more compressive in AS1-7 compared to QS. The strain remains compressive in both distributions for the entire IO domain. Around X=2 there are inflections in both profiles. The strain is small in magnitude in both distributions further away from the skin-rivet interface. From figure 8.18b and 8.18c, the radial strain is found to negative for some AS2 and AS1 simulations and positive for others near X=1. There are two major inflections in the radial strain trends over the IO domain at around X=1 and X=2. The behavior of all distributions is similar. The magnitude of the radial strain reduces in all distributions beyond X=3.

Referring to figure 8.18d, logarithmic axial strain distribution at interface IO of QS and AS1-7 is shown. At the skin-rivet interface near X=1, the strain is negative in QS and tensile in AS1-7. There is an inflection near the skin-rivet interface where the strain becomes negative from positive and becomes positive again in AS1-7 at X=1. The strain remains compressive in QS distributions for the entire IO domain. The magnitude is small further away from the skin-rivet interface. It oscillates between positive and negative in the case of AS1-7 and further away from the skin-rivet interface but the magnitude is small. From figure 8.18e and 8.18f, the axial strain in AS1 and AS2 is found to be positive for all simulations near X=1. There are two major inflections and one minor inflection in the axial strain trends over the IO domain. The major inflections are near X=1 and X=2. The minor inflection is near X=3. The behavior of all distributions is similar. The magnitude of the axial strain reduces in all distributions beyond X=4.

Referring to figure 8.18g, logarithmic hoop strain distribution at interface IO of QS and AS1-7 is shown. At the skin-rivet interface near X=1, the strain is tensile in QS and AS1-7. The strain is 1.7 times greater at the skin-rivet interface in AS1-7 compared to QS. The strain remains positive in both distributions for the entire IO domain. The magnitude is small further away from the skin-rivet interface in both distributions. From figure 8.18h and 8.18i, the hoop strain is found to be positive for all simulations near X=1. There are no major inflections in the hoop strain trends over

the IO domain. The hoop strain remains positive over the entire IO domain in all distributions. The magnitude of the hoop strain reduces in all distributions beyond X=3.

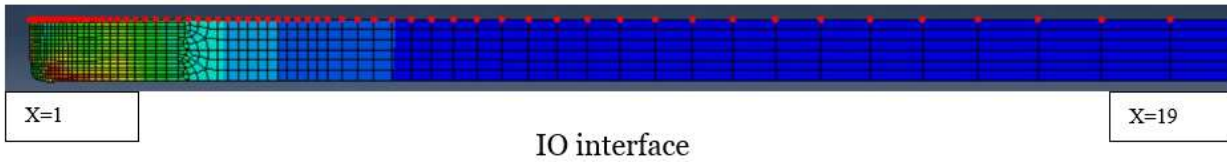

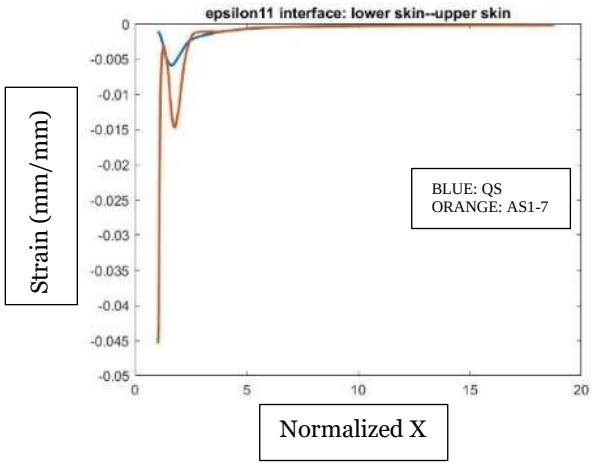

a: QS and AS 1-7 radial strain

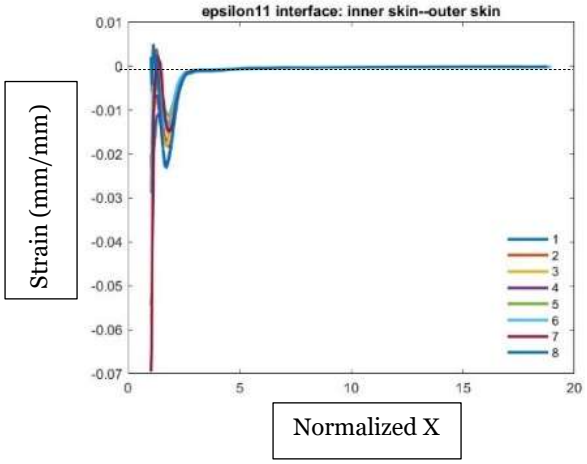

b: AS1 radial strain

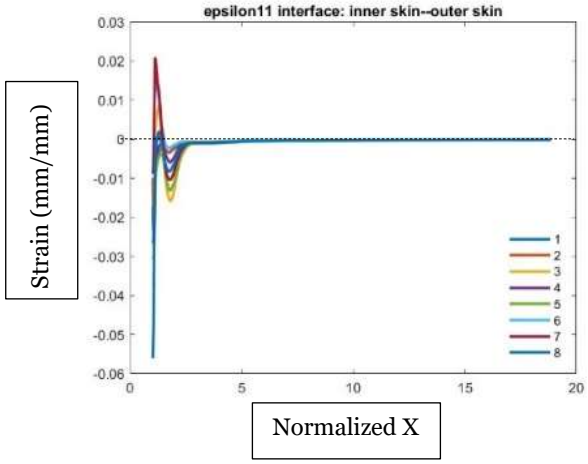

c: AS2 radial strain

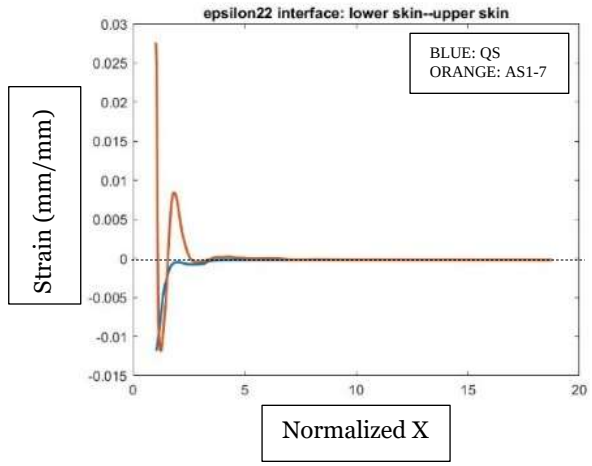

d: QS and AS1-7 axial strain

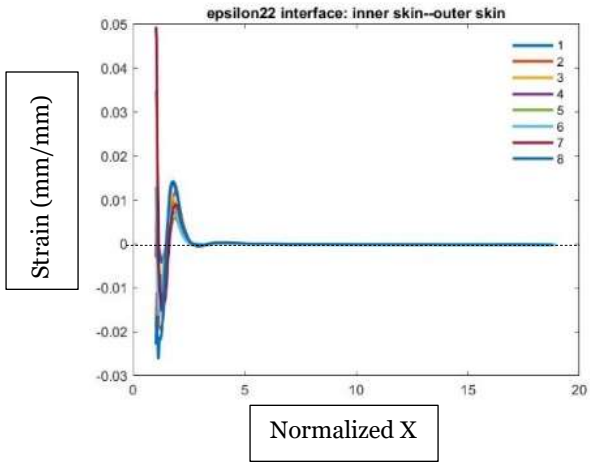

e: AS1 axial strain

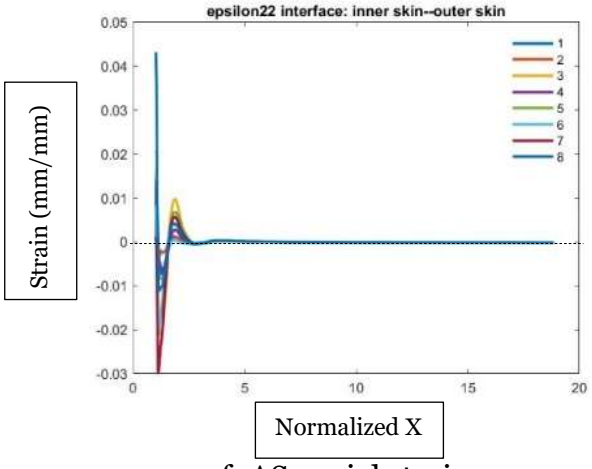

f: AS2 axial strain

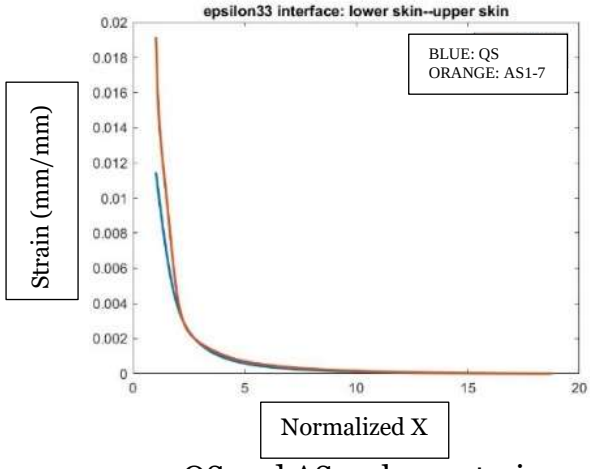

g: QS and AS1-7 hoop strain

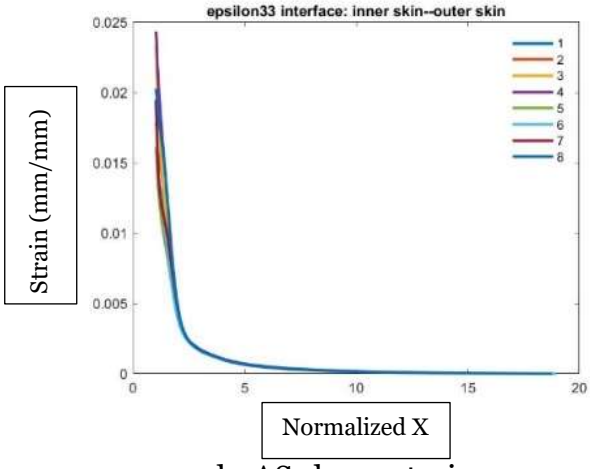

h: AS1 hoop strain

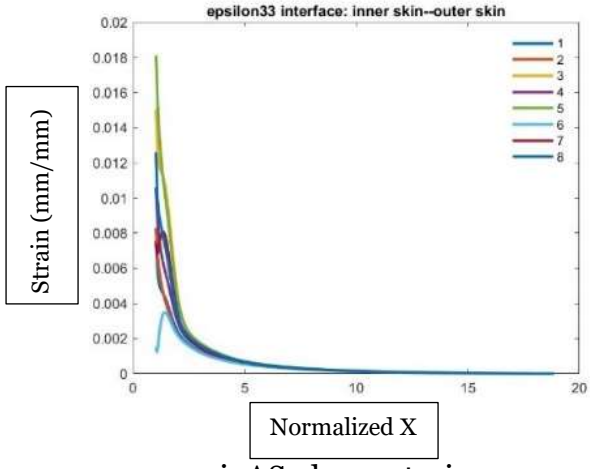

i: AS2 hoop strain

Figure 8.18. Residual strain distributions of QS, AS1 and AS2 simulations at the IO interface.

Referring to figure 8.19a, radial stress distribution at interface OR of QS and AS1-7 is shown. The stress remains negative in both distributions for the entire OR domain except it turns positive in the crown region of AS1-7 but the region is small and is located near Y=0.95. Magnitude of maximum compressive stress in QS is two times the magnitude of maximum compressive stress in AS1-7. From figure 8.19b and 8.19c, the radial stress is found to be compressive or small and tensile for all simulations near Y=0.75. Radial stress switches signs at Y=0.9 and Y=0.95 for some distributions. Y=0.9 corresponds to base of the countersink and Y=0.95 corresponds to base of the rivet crown.

Referring to figure 8.19d, axial stress distribution at interface OR of QS and AS1-7 is shown. There are inflections in both stress profiles. The stress profile of QS is comparatively more compressive below Y=0.92 and the profile of AS1-7 is comparatively more compressive above Y=0.92. Magnitude of maximum compressive stress in AS1-7 is 1.2 times the magnitude of maximum compressive stress in QS. From figure 8.19e and 8.19f, the axial stress is found to be compressive some percussive simulations and found to be tensile for others near Y=0.75. There are several inflections in the axial stress trends over the OR domain. The locations of major inflections correspond to the base of the countersink near Y=0.9 and the base of the crown near Y=0.94.

Referring to figure 8.19g, hoop stress distribution at interface OR of QS and AS1-7 is shown. There are inflections in both stress profiles and the stress remains negative in both distributions for the entire OR domain except it turns positive in the crown region of AS1-7 and QS near Y=0.95. Magnitude of maximum compressive stress in QS is 2 times the magnitude of maximum compressive stress in AS1-7. From figure 8.19h and 8.19i, the hoop stress is found to be compressive for almost all percussive distributions near Y=0.75. There are several inflections in the hoop stress trends over the OR domain. The locations of major inflections again correspond to the base of the countersink near Y=0.87 and the base of the crown near Y=0.95.

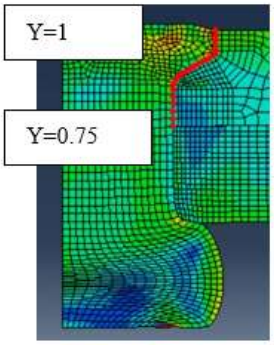

OR interface

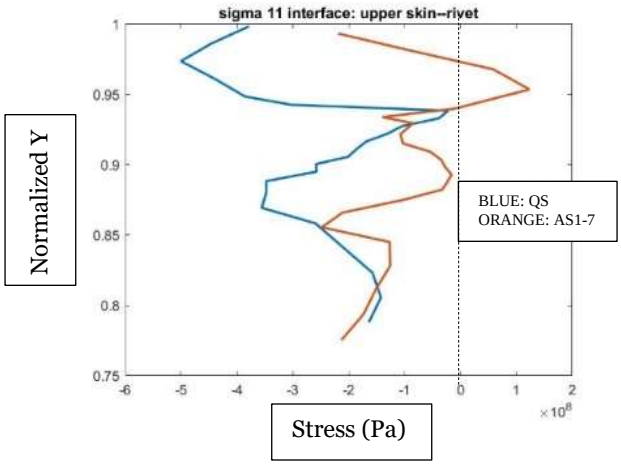

a: QS and AS 1-7 radial stress

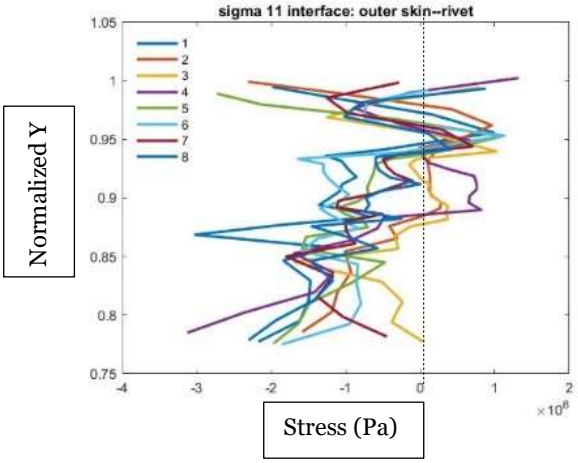

b: AS1 radial stress

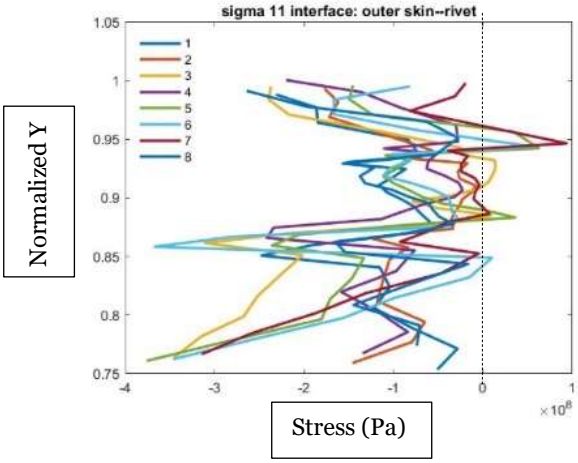

c: AS2 radial stress

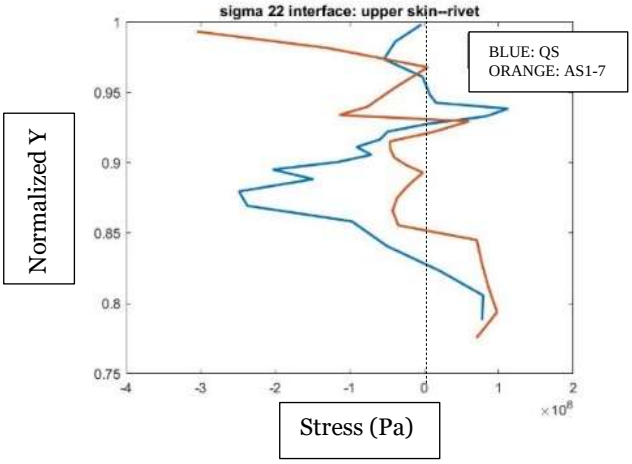

d: QS and AS1-7 axial stress

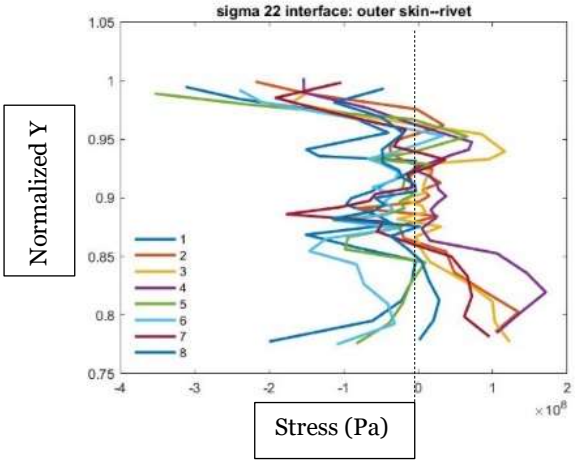

e: AS1 axial stress

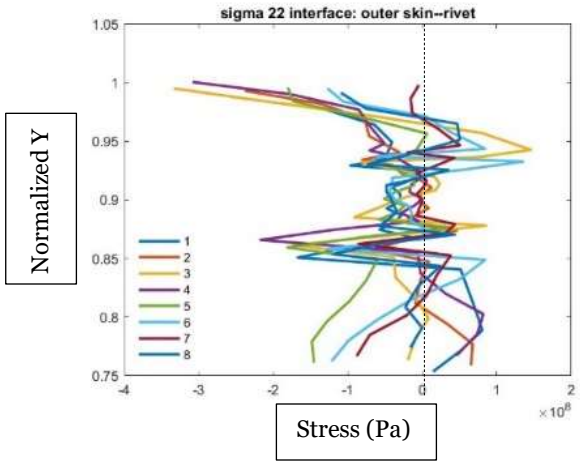

f: AS2 axial stress

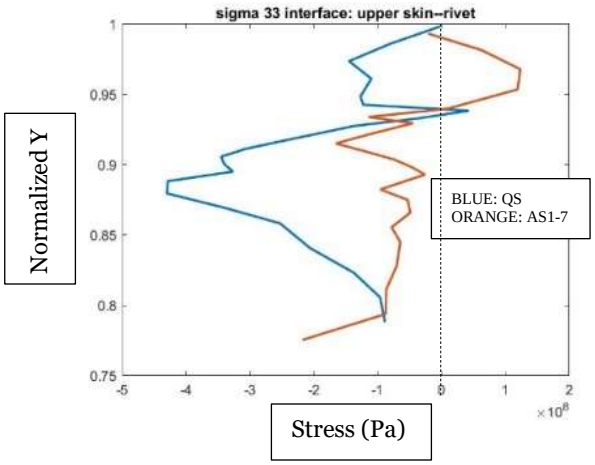

g: QS and AS1-7 hoop stress

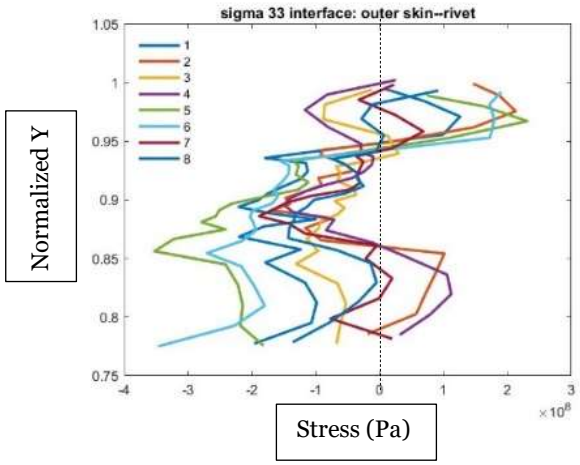

h: AS1 hoop stress

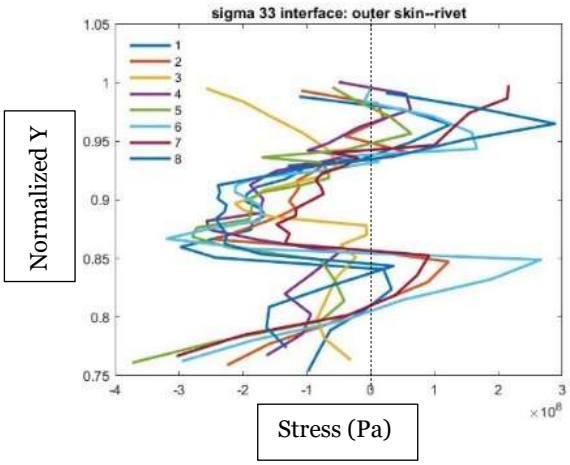

i: AS2 hoop stress

Figure 8.19. Residual stress distributions of QS, AS1 and AS2 simulations at the OR interface.

Referring to figure 8.20a, logarithmic radial strain distribution at interface OR of QS and AS1-7 is shown. There are inflections in AS1-7 strain profile near Y=0.9 and near Y=0.97. The strain remains negative or marginally positive in QS for the entire OR domain. The maximum magnitude of AS1-7 strain is over 5 times the maximum magnitude of QS strain. From figure 8.20b and 8.20c, the radial strain is found to be negative for almost all AS1 and AS2 simulations near Y=0.75. There are two major inflections in the radial strain trends over the OR domain and these are near Y=0.87 and Y=0.95. The behavior of all distributions is similar.

Referring to figure 8.20d, logarithmic axial strain distribution at interface OR of QS and AS1-7 is shown. There are inflections in both strain profiles. The strain profile of AS1-7 is negative between Y=0.78 and Y=0.92. It is positive elsewhere. The strain profile of QS is negative below Y=0.92. It is positive above Y=0.92. It roughly mirrors the radial strain distribution from figure 8.20a about the Y-axis. From figure 8.20e and 8.20f, the axial strain is found to be positive for some AS1 and AS2 distributions near Y=0.75 and negative for others. Major inflections in the axial strain trends over the OR domain are at Y=0.87 and Y=0.95. The behavior of all distributions is similar and percussive axial strain distributions almost mirror the radial strain distributions from figure 8.20 b and 8.20c about the Y-axis.

Referring to figure 8.20g, logarithmic hoop strain distribution at interface OR of QS and AS1-7 is shown. There are inflections in both strain profiles and the strains remain positive for the entire OR domain. The maximum magnitude of the AS1-7 profile is 2.7 times the maximum magnitude of QS profile. The hoop strain of AS1-7 is smaller than QS between Y=0.86 and Y=0.91. This corresponds to the transition zone from the rivet shank to the rivet countersink wedge region. From figure 8.20h and 8.20i, the hoop strain is found to be positive for all percussive simulations near Y=0.75. There is one inflection in the hoop strain trends over the OR domain at Y=0.87. The behavior of all distributions is similar. The hoop strain in all distributions is positive over the entire OR domain.

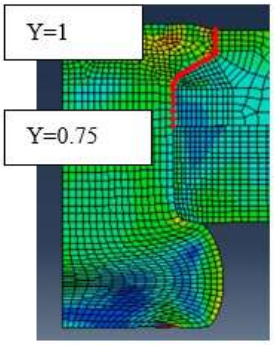

OR interface

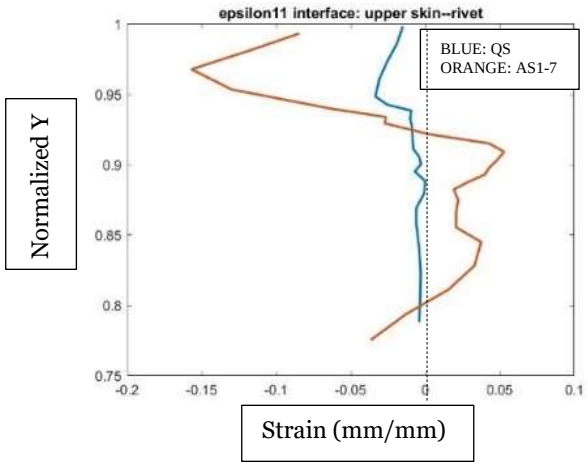

a: QS and AS 1-7 radial strain

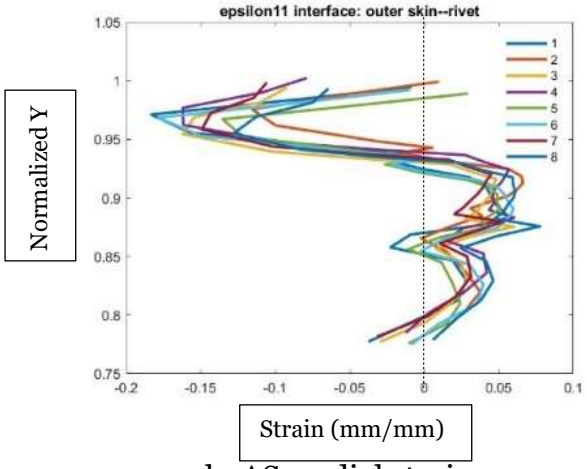

b: AS1 radial strain

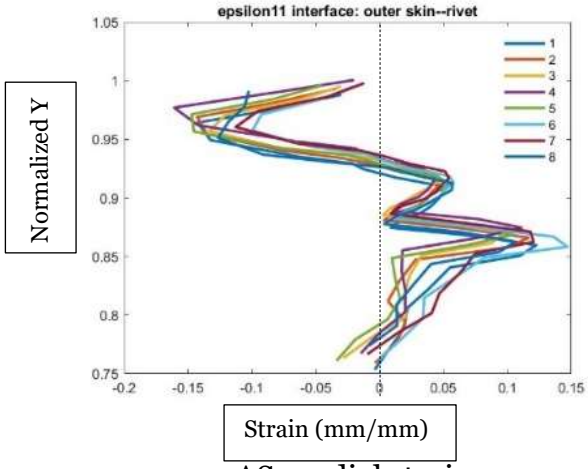

c: AS2 radial strain

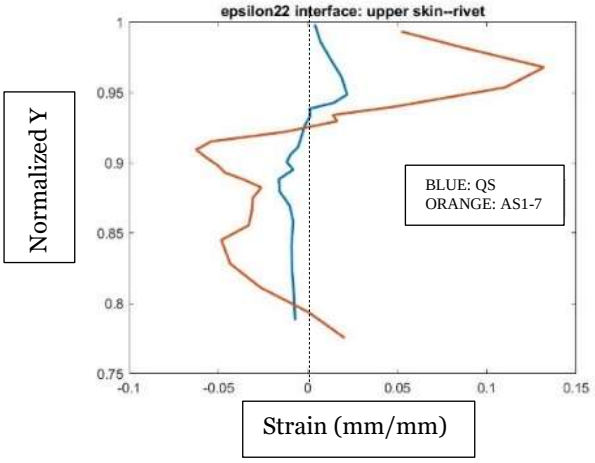

d: QS and AS1-7 axial strain

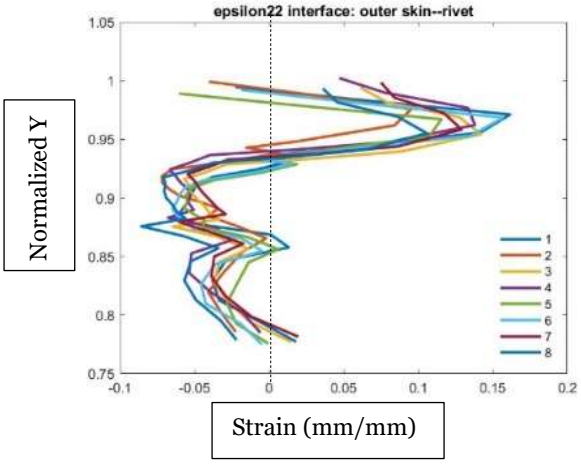

e: AS1 axial strain

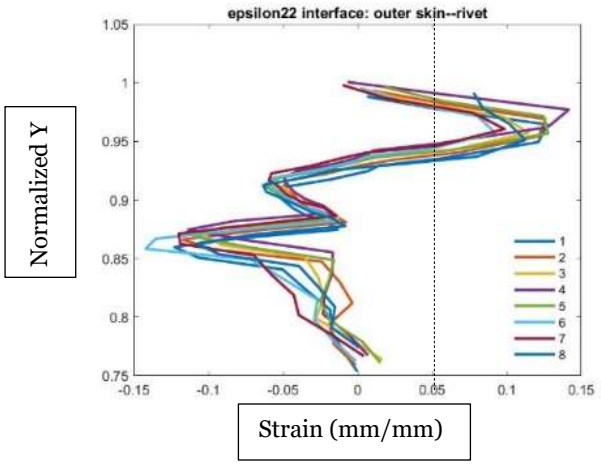

f: AS2 axial strain

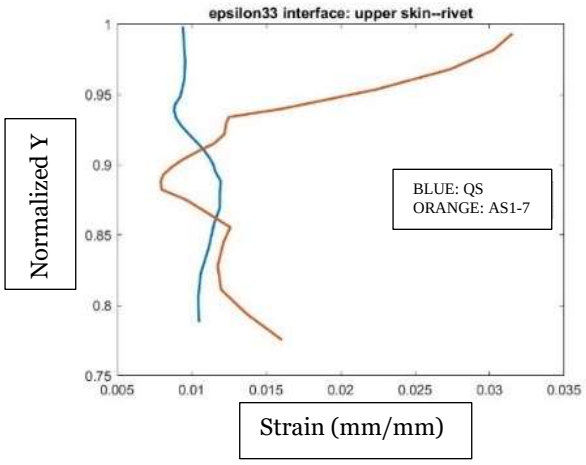

g: QS and AS1-7 hoop strain

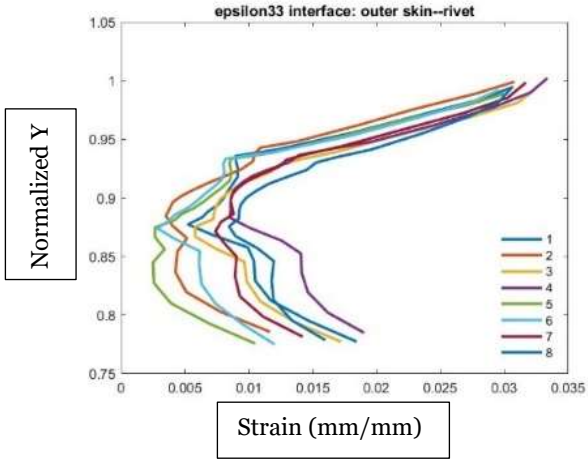

h: AS1 hoop strain

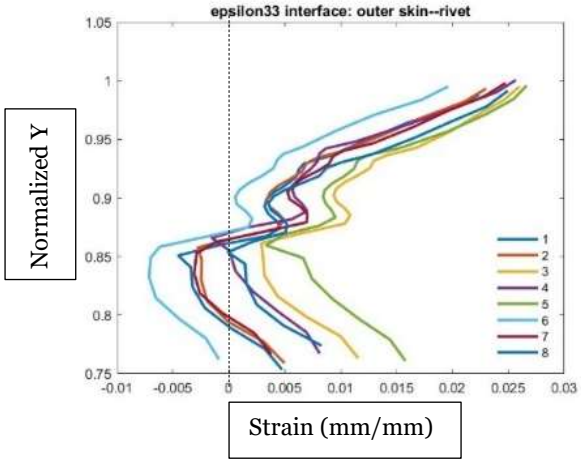

i: AS2 hoop strain

Figure 8.20. Residual strain distributions of QS, AS1 and AS2 simulations at the OR interface.

Referring to figure 8.21a, radial stress distribution at interface OI of QS and AS1-7 is shown. There are inflections in both stress profiles and the stresses remain compressive for the entire OI domain. The maximum magnitude of the AS1-7 stress is 1.3 times the maximum magnitude of QS stress. Away from the skin-rivet interface beyond X=10 stress magnitudes of both distributions become small. Inflections in the AS1-7 profile at X=3 indicates springback. From figure 8.21b and 8.21c, the radial stress is found to be compressive for all percussive simulations near X=1. The inflection in the radial stress trends over the OI domain at approximately X=3 that corresponds to springback. The radial stress is compressive for the entire OI domain in all distributions.

Referring to figure 8.21d, axial stress distribution at interface OI of QS and AS1-7 is shown. There are inflections in both stress profiles. Inflections of AS1-7 stress profile are more conspicuous compared to QS. Away from the skin-rivet interface at X=5 stress magnitudes of both distributions become small. From figure 8.21e and 8.21f, the axial stress is found to be compressive for some percussive simulations and tensile for others near X=1. There are two inflections in the axial stress trends over the OI domain at approximately X=1 and X=2. The stress magnitude becomes small in all distributions beyond X=5.

Referring to figure 8.21g, hoop stress distribution at interface OI of QS and AS1-7 is shown. There are inflections in both stress profiles. The compressive hoop stress region of AS1-7 is greater than the same region in QS. Away from the skin-rivet interface beyond X=9 stress magnitudes of both distributions become small. Inflection in the stress profiles indicates springback. From figure 8.21h and 8.21i, the hoop stress is found to be compressive in some distributions and found to be tensile in other distributions near X=1. There is one inflection in the hoop stress trends over the OI domain at approximately X=3. The magnitude becomes small in all distributions beyond X=9.

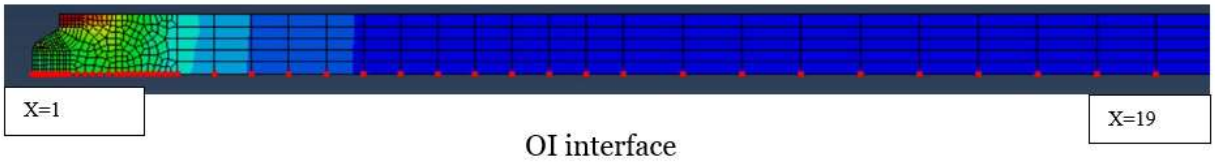

OI interface

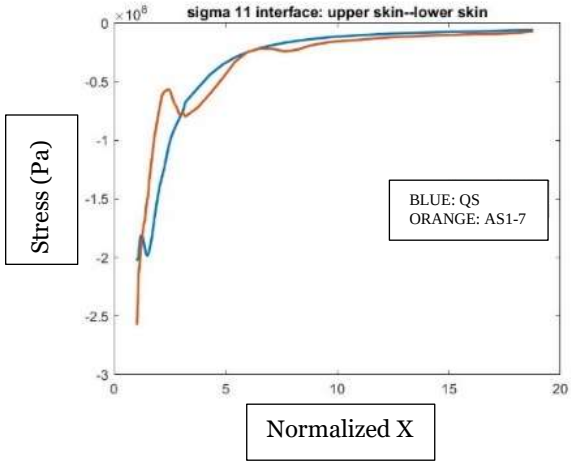

a: QS and AS 1-7 radial stress

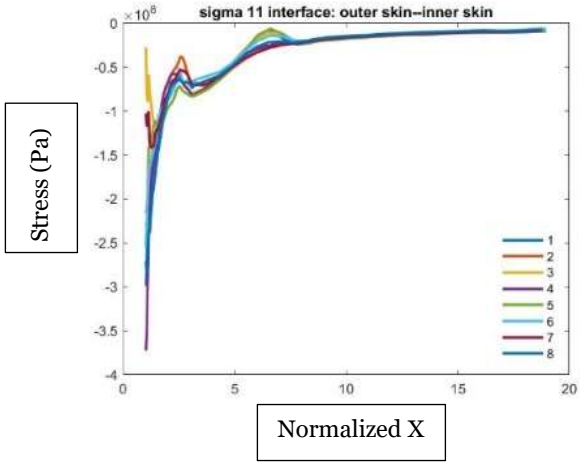

b: AS1 radial stress

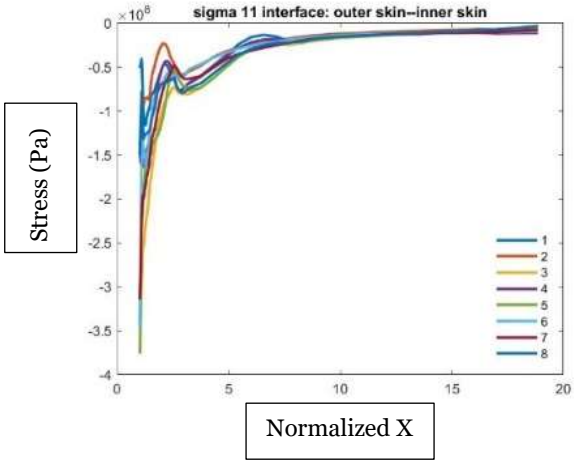

c: AS2 radial stress

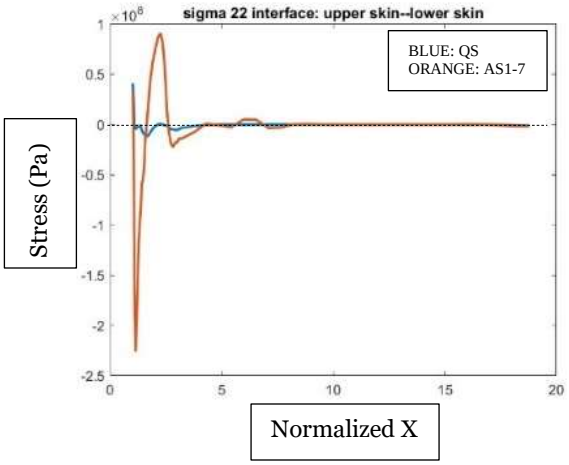

d: QS and AS1-7 axial stress

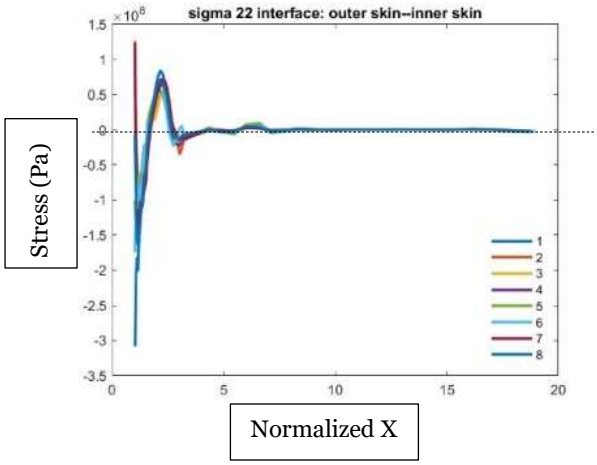

e: AS1 axial stress

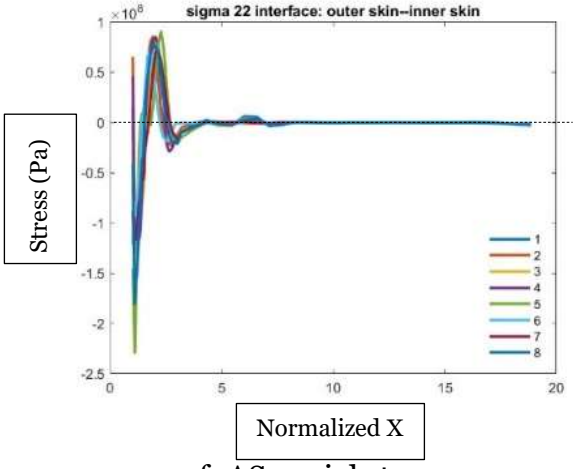

f: AS2 axial stress

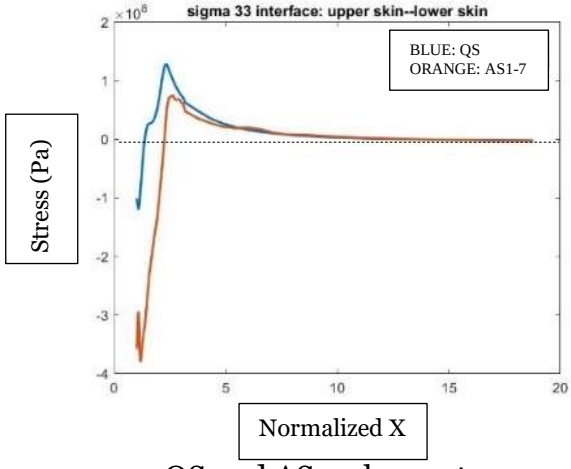

g: QS and AS1-7 hoop stress

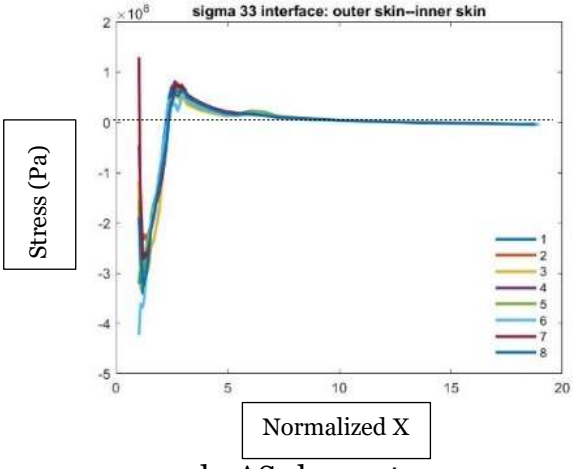

h: AS1 hoop stress

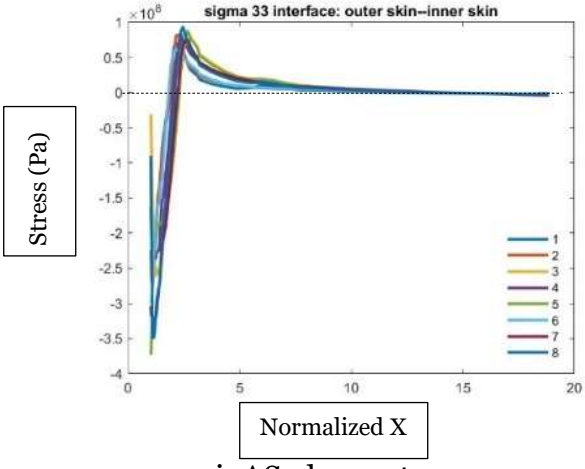

i: AS2 hoop stress

Figure 8.21. Residual stress distributions of QS, AS1 and AS2 simulations at the OI interface.

Referring to figure 8.22a, logarithmic radial strain distribution at interface OI of QS and AS1-7 is shown. There are two inflections in both strain profiles near X=1 and X=2. The strain profiles of QS and AS1-7 are entirely negative. Away from the skin-rivet interface at X=3 strain magnitudes of both distributions become small. Maximum strain magnitude of AS1-7 is 8 times the maximum strain magnitude of QS. From figure 8.22b and 8.22c, the radial strain is found to be negative all percussive simulations near X=1. There are two major inflections in the radial strain trends over the OI domain again near X=1 and X=2. The behavior of all distributions is similar. The magnitude becomes small in all distributions beyond X=3.

Referring to figure 8.22d, logarithmic axial strain distribution at interface OI of QS and AS1-7 is shown. There are inflections in both strain profiles. Inflection of the AS1-7 profile is greater than QS profile. Away from the skin-rivet interface at X=3 strain magnitudes of both distributions become small. From figure 8.22e and 8.22f, the axial strain is found to be positive for some percussive simulations and negative for other percussive simulations near X=1. There are again two major inflections in the axial strain trends over the OI domain near X=1 and X=2. The behavior of all distributions is similar. The magnitude becomes small in all distributions again beyond X=3.

Referring to figure 8.22g, logarithmic hoop strain distribution at interface OI of QS and AS1-7 is shown. Both strain profiles are entirely positive. Away from the skin-rivet interface beyond X=3 strain magnitudes of both distributions become small. Maximum magnitude of AS1-7 strain is 1.6 times maximum magnitude of QS strain. From figure 8.22h and 8.22i, the hoop strain is found to be positive for some and negative for other simulations near X=1. The strain remains positive for some distributions over the entire OI domain. While for other distributions there is an inflection near X=2. The magnitude of the strain becomes small in all distributions beyond X=3.

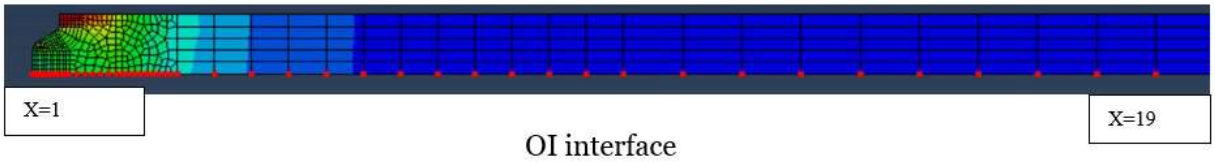

OI interface

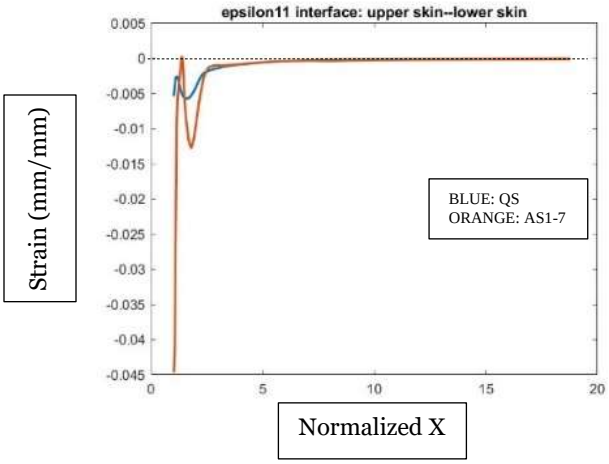

a: QS and AS 1-7 radial strain

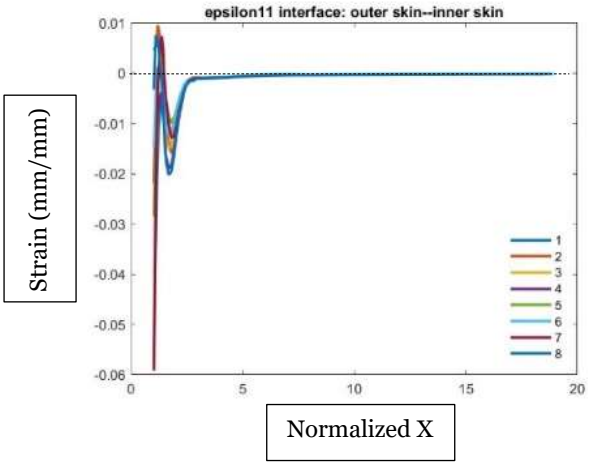

b: AS1 radial strain

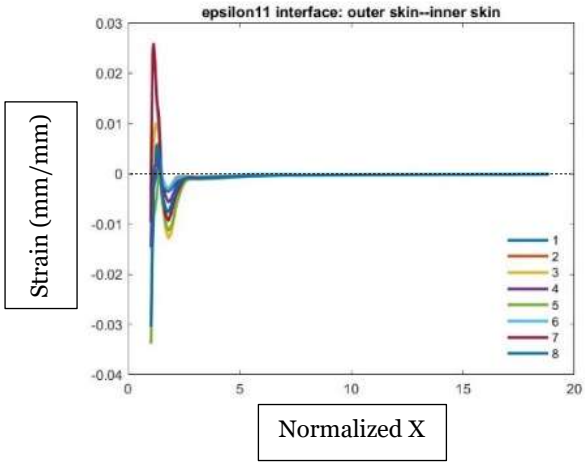

c: AS2 radial strain

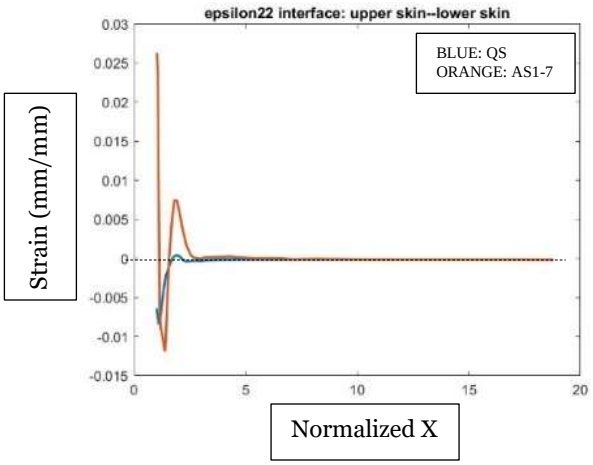

d: QS and AS1-7 axial strain

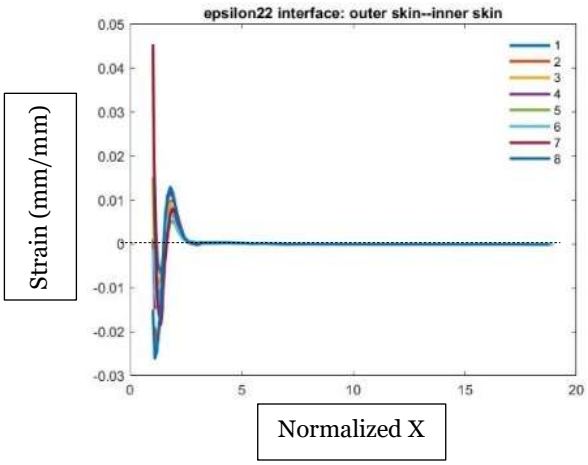

e: AS1 axial strain

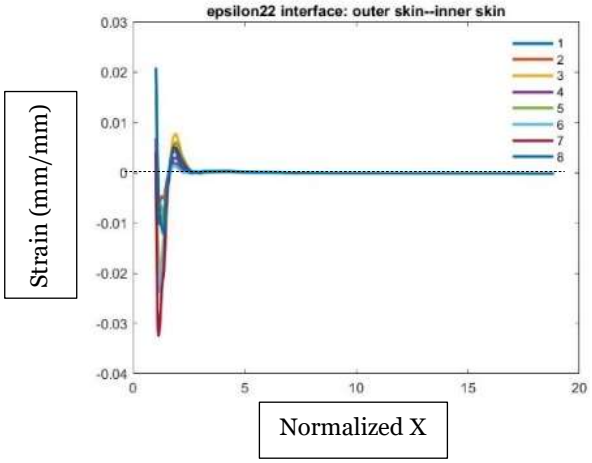

f: AS2 axial strain

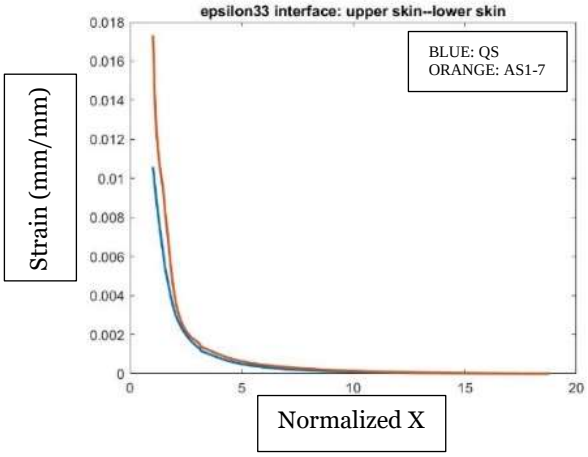

g: QS and AS1-7 hoop strain

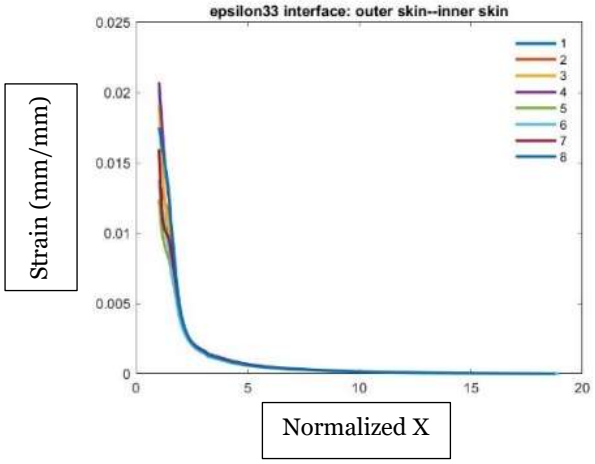

h: AS1 hoop strain

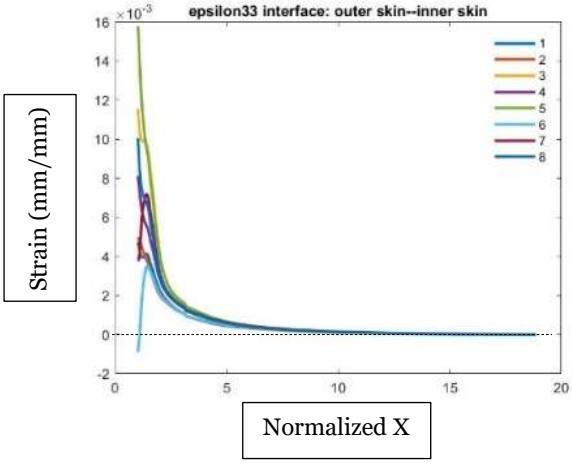

i: AS2 hoop strain

Figure 8.22. Residual strain distributions of QS, AS1 and AS2 simulations at the OI interface.

Referring to figure 8.23a, radial stress distribution at interface RH of QS and AS1-7 is shown. There are profile inflections at Y=0.55 corresponding to the head of the rivet button and Y=0.95 corresponding to the rivet crown. At Y=0.55, both stress profiles become tensile. Both profiles are entirely negative in the regions of RH adjacent to the inner skin and non-countersunk region of the outer skin. In the crown region the QS profile is entirely compressive and the AS1-7 profile is tensile or marginally compressive. From figure 8.23b and 8.23c, the significant inflections in the radial stress trends of the percussive simulations over the RH domain but are at Y= 0.5, Y=0.75, Y=0.87, and Y=0.95.

Referring to figure 8.23d, axial stress distribution at interface RH of QS and AS1-7 is shown. There are profile inflections at Y=0.55 corresponding to the head of the rivet button, at Y=0.87 corresponding to the base of the countersink and at Y=0.95 corresponding to the rivet crown. In the button region between Y=0.3 and Y=0.55, QS profile is tensile and AS1-7 profile is compressive. Between Y=0.55 and Y=0.75, the RH region is adjacent to the inner skin. Here the QS profile is compressive and the AS1-7 profile is both compressive and tensile. Above Y=0.9 in the rivet crown region, the QS profile is both tensile and compressive while the AS1-7 profile is distributions, H: All AS1 distributions, I: All AS2 distributions. X-axis: Pa, Y-axis: dimensionless entirely tensile. From figure 8.23e and 8.23f, the axial stress is found to be compressive for all percussive simulations near Y=0.3. There are many inflections in the axial stress trends over the RH domain but the significant ones are near Y= 0.45, Y=0.5, Y=0.75, and Y=0.87.

Referring to figure 8.23g, hoop stress distribution at interface RH of QS and AS1-7 is shown. There are profile inflections across the entire RH domain. In the button region between Y=0.3 and Y=0.55, QS profile is tensile and AS1-7 profile is mostly tensile. Between Y=0.55 and Y=0.75, the RH region is adjacent to the inner skin. Here both stress profiles are mostly compressive. Above Y=0.75 in the remaining RH region, both stress profiles are both tensile and compressive. From figure 8.23h and 8.23i, the hoop stress is found to be compressive for some percussive

simulations and tensile for others near Y=0.3. There are many inflections in the hoop stress trends over the RH domain and the significant ones are at Y= 0.5, Y=0.75, Y=0.87, and Y=0.95.

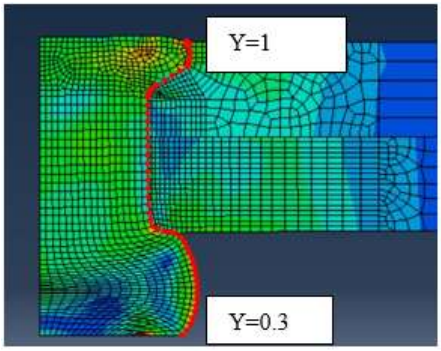

RH interface

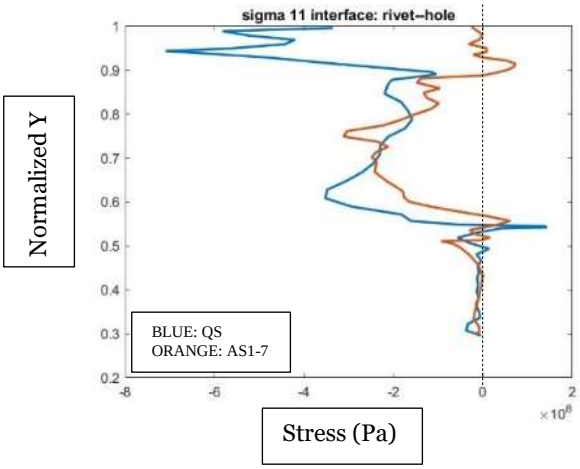

a: QS and AS 1-7 radial stress

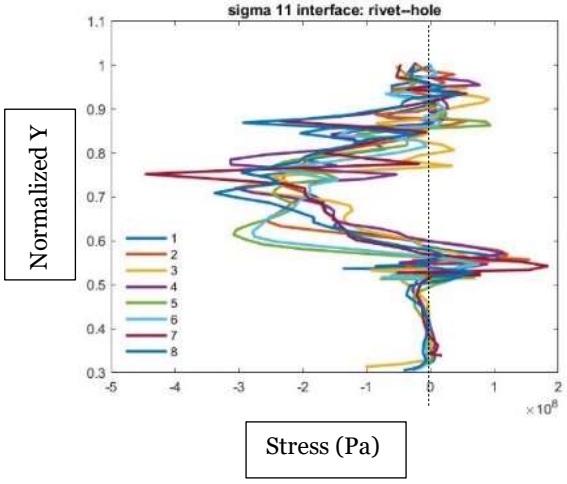

b: AS1 radial stress

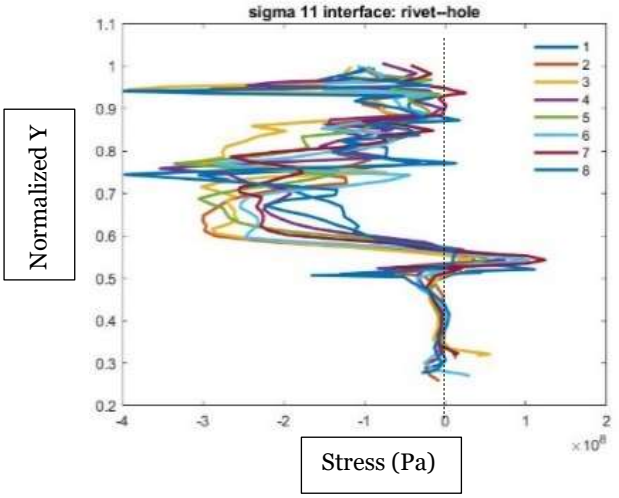

c: AS2 radial stress

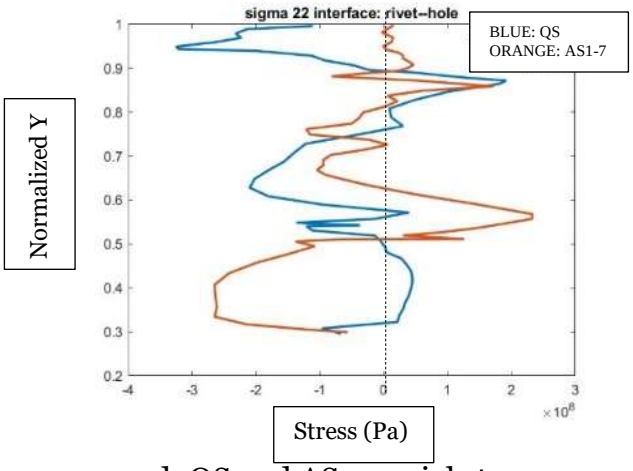

d: QS and AS1-7 axial stress

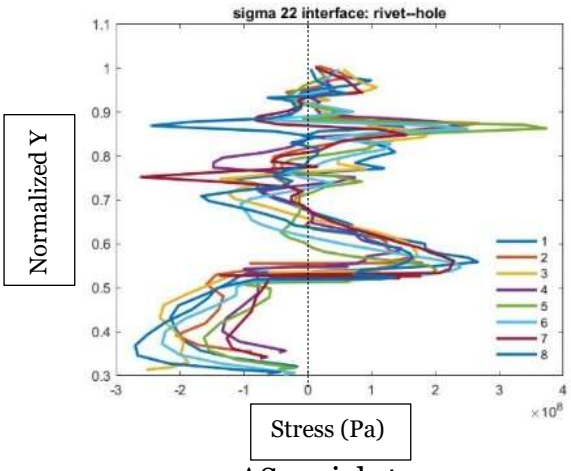

e: AS1 axial stress

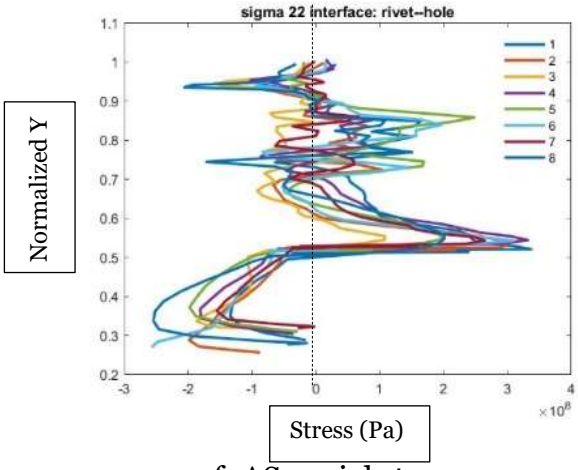

f: AS2 axial stress

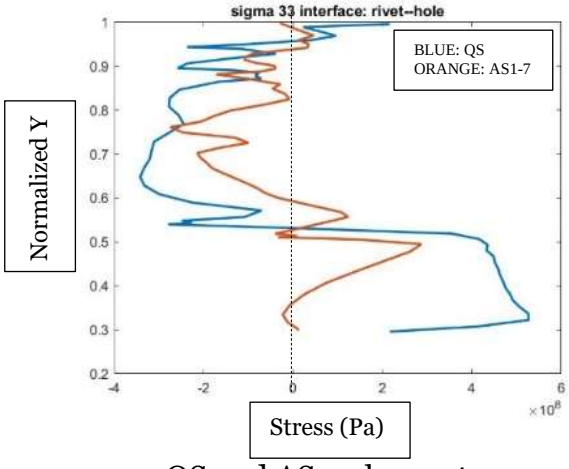

g: QS and AS1-7 hoop stress

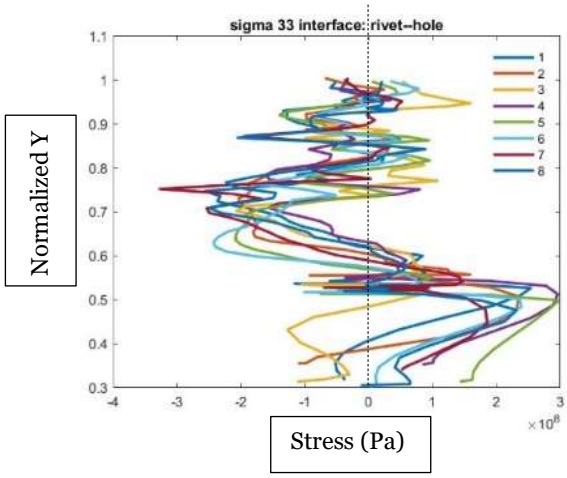

h: AS1 hoop stress

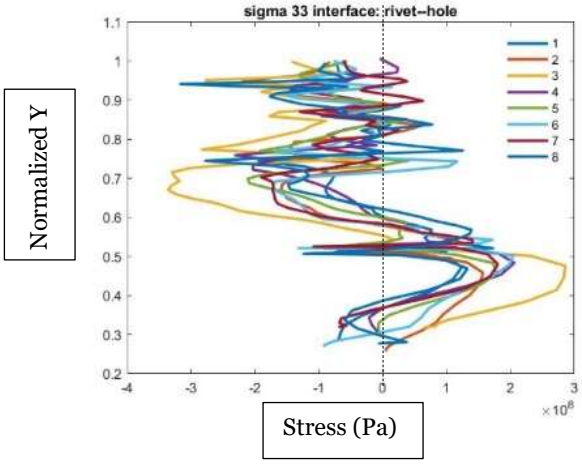

i: AS2 hoop stress

Figure 8.23. Residual stress distributions of QS, AS1 and AS2 simulations at the RH interface.

Referring to figure 8.24a, logarithmic radial strain distribution at interface RH of QS and AS1-7 is shown. There are profile inflections at Y=0.55, Y=0.87, and Y=0.93. In the button region between Y=0.3 and Y=0.55, QS profile is mostly negative and AS1-7 profile is mostly positive. Between Y=0.55 and Y=0.9, both strain profiles are positive. Above Y=0.9 in the remaining RH region, QS strain profile is marginally positive and AS1-7 strain profile is both positive and negative. From figure 8.24b and 8.24c, the radial strain is found to be positive for some percussive simulations and negative for others near Y=0.3. There is one major inflection in the strain distributions near Y= 0.5. Relatively smaller inflections can be found near Y= 0.87 and Y= 0.95. The behavior of all distributions is similar.

Referring to figure 8.24d, logarithmic axial strain distribution at interface RH of QS and AS1-7 is shown. There are profile inflections again near Y=0.55 and Y=0.9. In the RH region between Y=0.3 and Y=0.92, both strain profiles are negative. Above Y=0.92 in the rivet crown region, strain of AS1-7 becomes positive while strain of QS remains negative. From figure 8.24e and 8.24f, the axial strain is found to be negative for all percussive simulations near Y=0.3. There are inflections in the strain distributions near Y=0.5, Y=0.87, and Y=0.95. The behavior of all distributions is similar.

Referring to figure 8.24g, logarithmic hoop strain distribution at interface RH of QS and AS1-7 is shown. Both strain profiles are entirely positive over the RH domain. The AS1-7 profile has a greater magnitude compared to the QS profile in the rivet button region, inner skin region and countersunk outer skin region. The magnitudes of both profiles are approximately the same in the non-countersunk region of the outer skin. From figure 8.24h and 8.2i, the hoop strain is found to be positive for all percussive simulations over the whole RH domain. There is one major inflection in the strain distributions near Y=0.5. The behavior of all strain distributions is similar.

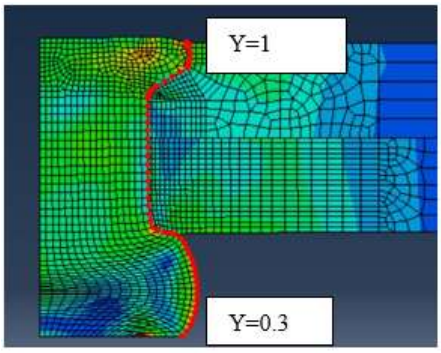

RH interface

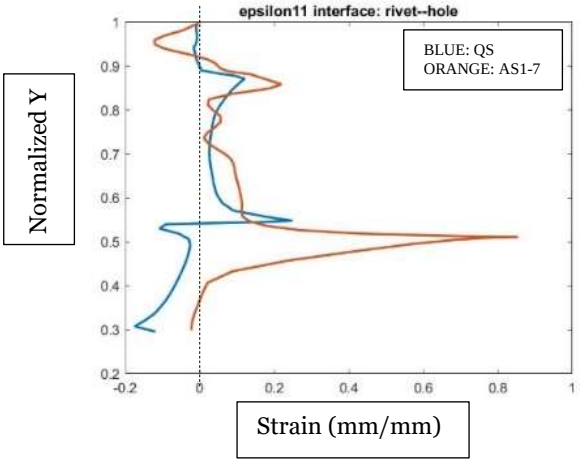

a: QS and AS 1-7 radial strain

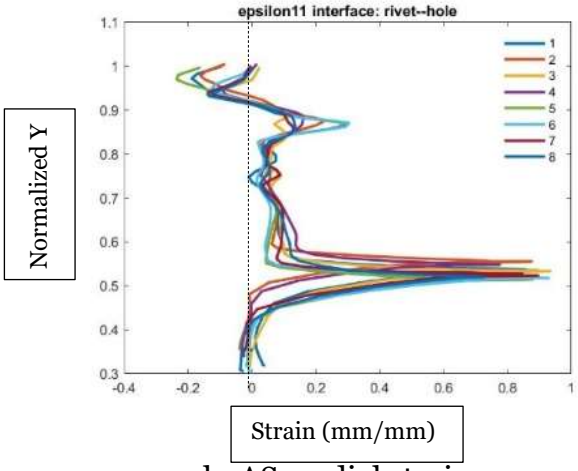

b: AS1 radial strain

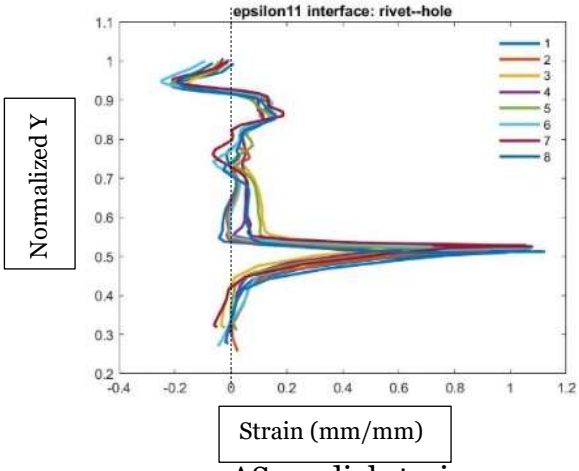

c: AS2 radial strain

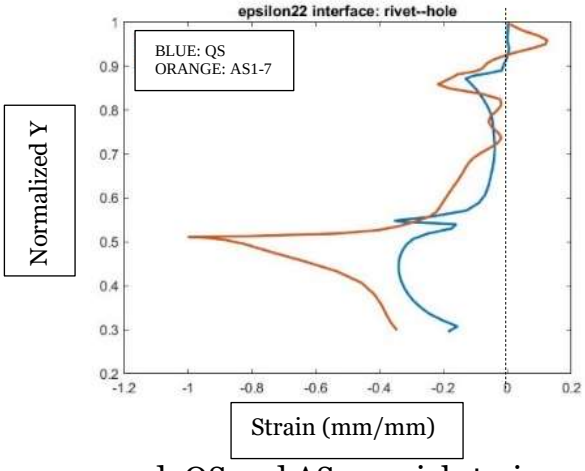

d: QS and AS1-7 axial strain

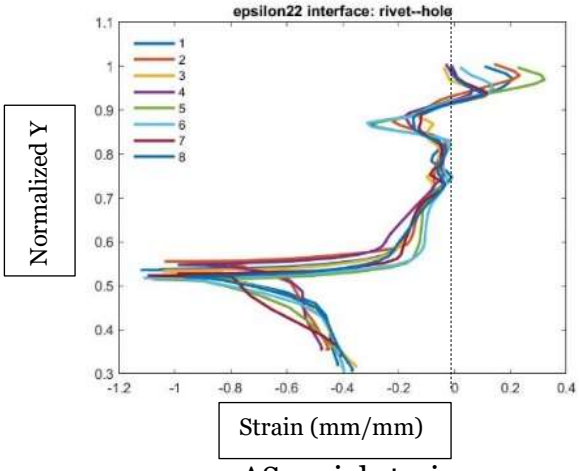

e: AS1 axial strain

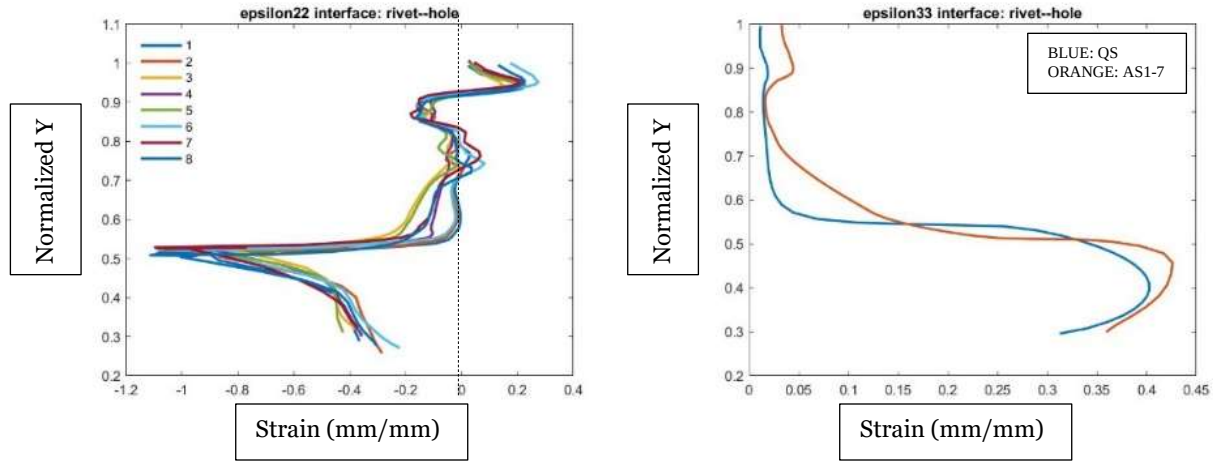

f: AS2 axial strain

g: QS and AS1-7 hoop strain

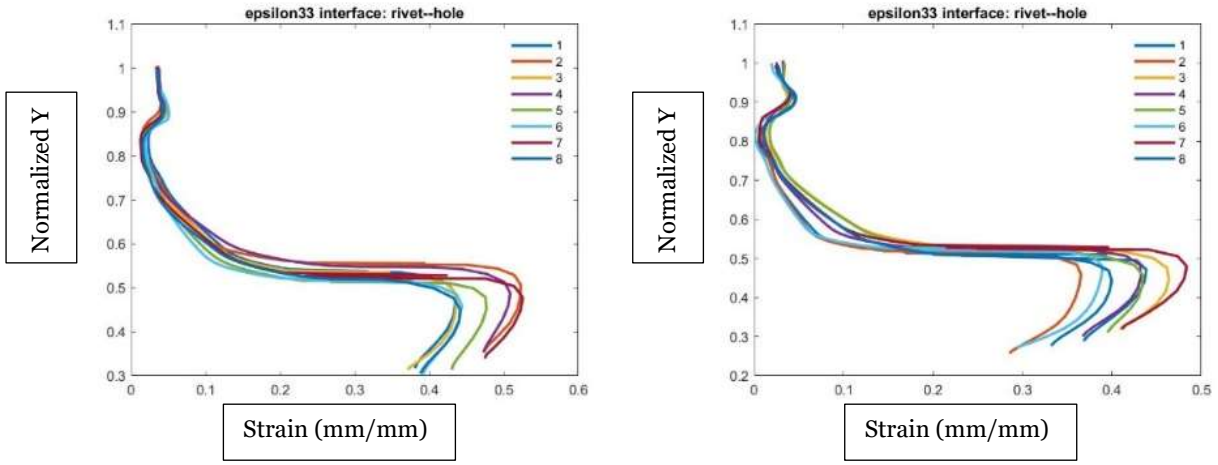

h: AS1 hoop strain

i: AS2 hoop strain

Figure 8.24. Residual strain distributions of QS, AS1 and AS2 simulations at the RH interface.

Figure 8.25 shows stress levels at mesh elements with the highest magnitude of the stress components within the entire FE mesh.

In AS1-8, highest compressive ratio of stress component/V-M stress in the entire FE mesh is exhibited by mesh element 701 of the inner skin and it is -3.53. This element is in the inner skin near the outer skin interface. It is part of region 'F'. The same element of the inner skin has the highest compressive stress component of -415 MPa. Mesh element 703 of the rivet has the highest tensile ratio of stress component/V-M stress (1.27) and highest tensile stress component (439 MPa). This element is in the inner skin near the head of the rivet button and is part of region 'F'.

Component	Stress	V-M Stress	Stress/V-M
radial (11)	(Pa)	(Pa)	
D226 lower pa-1 703	1.51E+08	3.47E+08	0.44
D226 lower pa-1 701	-3.73E+08	1.18E+08	-3.17
axial (22)			
D226 lower pa-1 704	3.19E+08	4.08E+08	0.78
D226 lower pa-1 701	-3.60E+08	1.18E+08	-3.06
hoop (33)			
D226 lower pa-1 703	4.39E+08	3.47E+08	1.27
D226 lower pa-1 701	-4.15E+08	1.18E+08	-3.53
shear (12)			
Riv 225 pa-SI-1 467	1.19E+08	2.77E+08	0.43
D226 lower pa-1 703	-1.39E+08	3.47E+08	-0.40

AS1-8

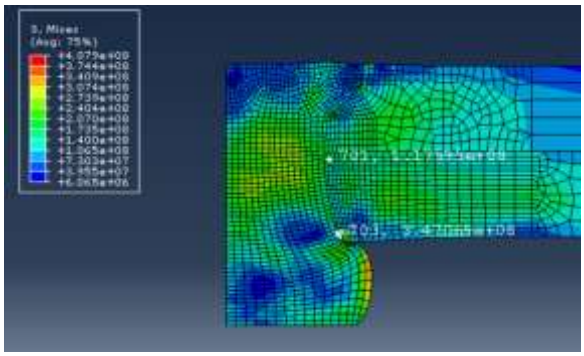

AS1-8

Component	Stress	V-M Stress	Stress/V-M
radial (11)	(Pa)	(Pa)	
D226 lower pa-1 703	1.77E+08	4.17E+08	0.43
Riv 225 pa-SI-1 988	-4.07E+08	2.37E+08	-1.72
axial (22)			
D226 upper pa-1 321	2.52E+08	3.06E+08	0.82
D226 upper pa-1 320	-3.33E+08	1.32E+08	-2.53
hoop (33)			
D226 lower pa-1 703	6.07E+08	4.17E+08	1.46
Riv 225 pa-SI-1 575	-4.35E+08	2.60E+08	-1.67
shear (12)			
Riv 225 pa-SI-1 723	1.77E+08	2.01E+08	0.88
Riv 225 pa-SI-1 699	-1.37E+08	2.51E+08	-0.55

AS2-8

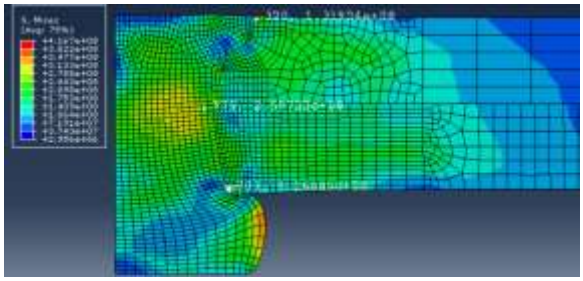

AS2-8

Figure 8.25. Data for Joint Quality Analysis

Mesh element 703 of the inner skin is more critical for crack nucleation than element 701 of inner skin because of high tensile (stress/V-M) ratio and high tensile stress magnitude.

In AS2-8, highest compressive ratio of stress component/V-M stress in the entire FE mesh is exhibited by mesh element 320 of the outer skin and it is -2.53. This element is located adjacent to the rivet crown and is part of region 'D'. Mesh element 575 of the rivet has the highest compressive stress component of -435 MPa. This element is in the rivet in the interior of region 'A'. It can be ignored from crack nucleation perspective. Mesh element 703 of the inner skin has the highest tensile ratio of stress component/V-M stress (1.46) and highest tensile stress

component (607 MPa). This element is in the inner skin just above the rivet button and is a part of region 'F'.

Due to the high tensile (stress/V-M) ratio and high magnitude of tensile hoop stress of element 703 of the inner skin, this location is most critical for crack nucleation.

8.4 SUMMARY

Two-dimensional full dynamic percussive riveting DOE was performed using FEM. An axial gap was observed between the head of the rivet button and the inner surface of the inner skin. It is observed that an increase in μ leads to a reduction in the gap, an increase in KE leads to an increase in R_B and a reduction in H_B, and an increase in TR leads to a reduction in R_B and an increase in H_B. Residual stress and strain results from the simulation were presented and discussed. The dynamic percussive riveting stackup was found to be most critical for crack nucleation inside the inner skin because of presence of high magnitude tensile hoop stress.

Chapter 9. THREE-DIMENSIONAL ASYMMETRIC PERCUSSIVE RIVETING SIMULATION

9.1 INTRODUCTION

In this chapter, discussion and results pertaining to three-dimensional asymmetric full dynamic percussive riveting modeling and analysis. Most of the FE modeling procedure and information for this simulation was discussed in chapter 4, especially section 4.4. Effect of the asymmetric motion of the bucking bar on the distribution of residual stresses and strains is important to study because in reality rivets are not formed axisymmetrically. This impacts the joint fatigue strength.

9.2 THREE-DIMENSIONAL MODEL DEVELOPMENT

Modeling information concerning three-dimensional full dynamic percussive FE model is discussed in section 4.4. One three-dimensional simulation parameters are shown in table 9.1.

Table 9.1. 3D FE model simulation parameters

3D FE model	TR	D_{shank}	CL	Stick-Slip Shear Limit
	1	0.225”	0.9956	269.62 MPa
3D FE model	KE	b_Y	h_Y	μ
	21 J	950 N	1600 N	0.25

9.3 RESULTS AND DISCUSSION

Simulation deformation and residual stress results of the three-dimensional full dynamic percussive model (henceforth referred to as 'PR3') are compared with results of two-dimensional full dynamic percussive model (referred to as 'PR2') and two-dimensional quasistatic squeeze riveting model (referred to as 'QS'). PR2 and QS simulations have the same CL, TR, friction coefficient, D_{shank} and maximum shear stress limit as the PR3 simulation. PR2 simulation has the same KE, b_Y, and h_Y as PR3 simulation. PR3 simulation is carried out for 27 piston strokes.

9.3.1 *Deformation Results*

Final deformation profiles of stackups of QS, PR2 and PR3 simulations are shown in figure 9.1. The deformation profiles for PR3 were extracted from three section cuts as shown in figure 9.2. Section cut corresponding to positive X direction is referred to as 45-degree section. Section cut corresponding to X=0 is referred to as 90-degree section. Section cut corresponding to negative X direction is referred to as 135-degree section. QS and PR2 are axisymmetric simulations, only one deformation profile exists in each case. Normalized measured features (R_1-R_4, H_b and R_b) are shown in table 9.2.

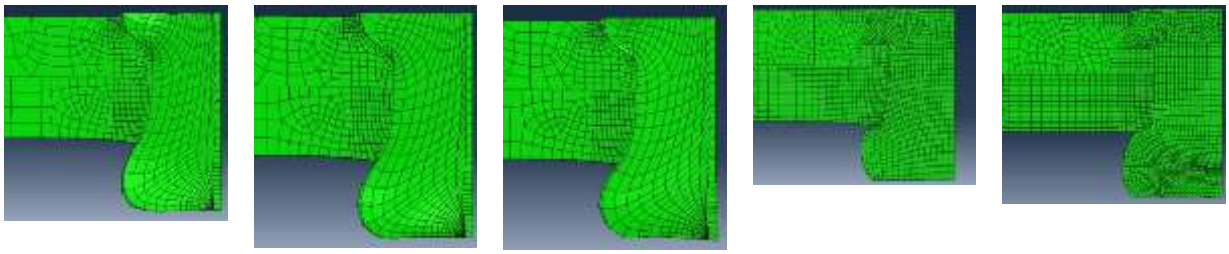

PR3 45-Degree Section | PR3 90-Degree Section | PR3 135-Degree Section | PR2 Section | QS Section

Figure 9.1. Deformed Stackup at End of Simulations.

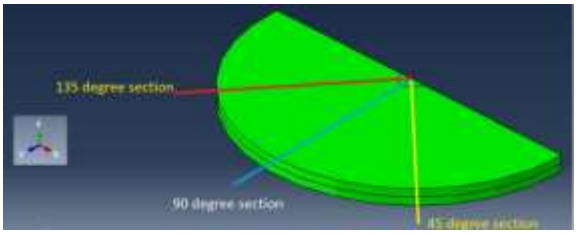

Figure 9.2. PR3 Simulation Section Locations.

Table 9.2. Normalized geometric attribute measurements. R_1 normalized with R_{crown}; R_2, R_3, R_4, R_b normalized with R_{shank}; H_b normalized with L_{shank}

Normalized	R_1	R_2	R_3	R_4	H_b	R_b
QS	1.011	1.015	1.016	1.053	0.286	1.480
PR2	1.033	1.024	1.025	1.164	0.252	1.503
PR3, 45-Degree	1.008	1.019	1.022	1.130	0.319	1.435
PR3, 90-Degree	1.014	1.016	1.022	1.128	0.308	1.442
PR3, 135-Degree	1.013	1.018	1.021	1.134	0.307	1.465

The bucking bar in PR3 is prescribed uniform angular velocity about the Z-axis. Angular velocities about the X-axis and Y-axis are zero. The motion can be roughly described as oscillatory. Compared to bucking bar motion of PR2, this motion is asymmetric because the bucking bar in PR2 has no angular velocity. This asymmetric motion results in different deformation profiles and stress profiles at the 45-degree section, 90-degree section and 135-degree section. Figure 9.3 shows the oscillatory motion of the bucking bar at various points during the PR3 simulation.

It is shown in table 9.2 that R1 of PR2 is the highest. But this is at the end of 40 strokes. R1 of PR3 at 90-degree and 135-degree sections exceed the R1 of QS even though only 27 strokes were completed in the case of PR3. The mesh of PR3 is coarse compared to the mesh of QS and PR2. It is expected that there are going to be some mesh effects. 45-degree section has lesser R1 compared to 90-degree and 135-degree section because the oscillatory motion of the bucking bar dwells for more time in the portion of the stackup that the 135-degree section is part of. A greater dwell time of the bucking bar results in greater amount of plastic deformation.

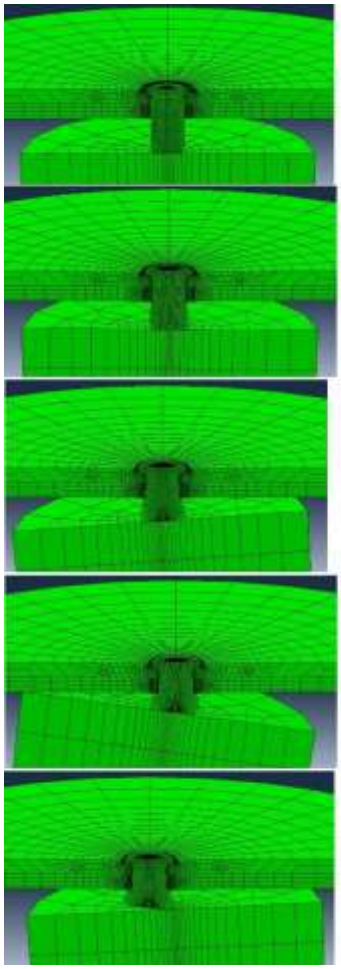

Figure 9.3. PR3 model bucking bar Asymmetric Motion in the X-Y Plane. X-Axis Points to the Left. Y-Axis Points Upward. Z-Axis Angular Velocity Prescribed to the Bucking Bar.

Referring to table 9.2, R2 of QS has the lowest value and the R2 of PR2 has the highest value. Deformation in the rivet crown and rivet shank adjacent to the skins is much lesser than the deformation observed in the portion of the rivet shank that becomes the rivet button. The R2 values of PR3 measured at the three sections lie between R2 of QS and R2 of PR2. R3 of QS has the lowest value and R3 of PR2 has the highest value. This trend is similar to the trend observed in R2 values. The R3 values at the three sections of PR3 are almost the same and lie in between the R3 values of QS and PR2. R4 of QS has the lowest value and the R4 of PR2 has the highest

value. R4 of the 90-degree section of PR3 has the lowest R4 compared to the other sections. Again, because of the extended dwell time of the bucking bar in this section's region of the stackup, R4 of 135-degree section of PR3 is the highest compared to the other two sections. R4 values of PR3 are lower compared to PR2 because of lower number of strokes in the PR3 simulation.

H_b of PR2 is the lowest and H_b of 45-degree section of PR3 is the highest. H_b of QS and PR2 are smaller compared to PR3 because of the reduced of strokes in PR3. Strokes were reduced in PR3 to curtail the simulation time. Again because of greater bucking bar dwell in this section's region of the stackup, H_b of 135-degree section of PR3 is smaller compared to the other two sections. As mentioned earlier, 45-degree section of PR3 has the highest H_b and this corresponds to the lesser dwell time of the bucking bar in this section's region of the stackup.

R_b of PR2 is the greatest and R_b at 45-degree section of PR3 is the lowest. R_b of QS and PR2 are greater compared to PR3 because of the reduced of strokes in PR3. Because of greater bucking bar dwell in its region of the stackup, R_b of 135-degree section of PR3 is higher compared to the other two sections. As mentioned earlier, 45-degree section of PR3 has the lowest R_b and this corresponds to the lesser dwell time of the bucking bar in this section's region of the stackup.

9.3.2 *Residual Stress Results*

Figure 9.4 shows the stress contours of all three sections considered in PR3 simulation *after completion of the PR3 simulation*. Figure 9.5 shows stress levels at mesh elements with the *highest magnitude of the stress components* within the entire FE mesh *after completion of the PR3 simulation*. The mesh elements with the highest stress magnitudes and highest stress/V-M ratios are also shown in figure 9.5.

At the 45-degree section of PR3 simulation, highest compressive ratio of (stress component/V-M stress) in the entire FE mesh is exhibited by mesh element 1003 of the outer skin and it is -1.56. Same element has the highest compressive stress component of -803 MPa. Mesh element 995 of the outer skin has the highest tensile ratio of stress component/V-M stress (1.84).

Mesh element 994 of the outer skin has the highest tensile stress component (1840 MPa). These three elements are in the outer skin adjacent to the rivet crown. Hence, this region is most critical in the 45-degree section for crack nucleation.

Component	Stress	V-M Stress	Stress/V-M
radial (11)	(Pa)	(Pa)	
UPPER-3D-1 995	9.88E+08	5.38E+08	1.84
UPPER-3D-1 1003	-8.03E+08	5.14E+08	-1.56
axial (22)			
UPPER-3D-1 994	1.84E+09	1.80E+09	1.02
UPPER-3D-1 1003	-6.54E+08	5.14E+08	-1.27
hoop (33)			
UPPER-3D-1 994	9.52E+08	1.80E+09	0.53
UPPER-3D-1 988	-6.50E+08	4.81E+08	-1.35
shear (12)			
UPPER-3D-1 1003	2.53E+08	5.14E+08	0.49
UPPER-3D-1 994	-2.87E+08	1.80E+09	-0.16
shear (13)			
RIV-3D-1 1164	1.62E+08	1.29E+08	1.26
UPPER-3D-1 994	-1.39E+08	1.80E+09	-0.08
shear (23)			
RIV-3D-1 1163	1.11E+08	1.57E+08	0.71
UPPER-3D-1 994	-6.04E+08	1.80E+09	-0.34

45-degree section

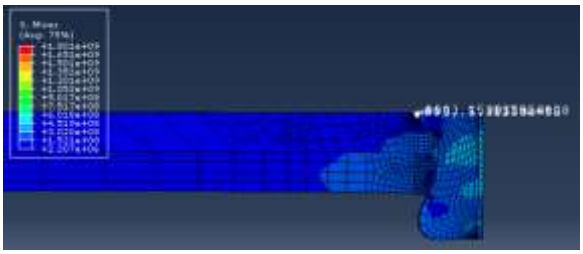

45-degree section

Component	Stress	V-M Stress	Stress/V-M
radial (11)	(Pa)	(Pa)	
UPPER-3D-1 1843	7.25E+08	4.88E+08	1.49
LOWER-3D-1 2187	-1.05E+09	9.99E+08	-1.06
axial (22)			
UPPER-3D-1 1843	1.09E+09	4.88E+08	2.22
UPPER-3D-1 1772	-6.13E+08	3.41E+08	-1.80
hoop (33)			
UPPER-3D-1 1843	7.89E+08	4.88E+08	1.62
UPPER-3D-1 1772	-7.95E+08	3.41E+08	-2.33
shear (12)			
UPPER-3D-1 1841	2.28E+08	4.24E+08	0.54
LOWER-3D-1 2186	-2.76E+08	5.17E+08	-0.53
shear (13)			
RIV-3D-1 1946	8.88E+07	3.55E+08	0.25
LOWER-3D-1 2187	-1.36E+08	9.99E+08	-0.14
shear (23)			
LOWER-3D-1 2187	1.94E+08	9.99E+08	0.19
UPPER-3D-1 1842	-4.45E+08	1.18E+09	-0.38

90-degree section

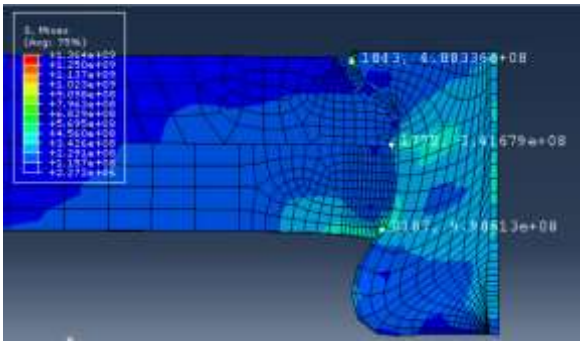

90-degree section

Component	Stress	V-M Stress	Stress/V-M
radial (11)	(Pa)	(Pa)	
UPPER-3D-1 2691	7.95E+08	5.76E+08	1.38
RIV-3D-1 3887	-6.41E+08	3.75E+08	-1.71
axial (22)			
RIV-3D-1 3873	9.10E+08	3.78E+08	2.41
LOWER-3D-1 3159	-6.34E+08	6.22E+08	-1.02
hoop (33)			
RIV-3D-1 3873	7.51E+08	3.78E+08	1.99
RIV-3D-1 3869	-5.61E+08	3.22E+08	-1.74
shear (12)			
UPPER-3D-1 2689	2.89E+08	6.19E+08	0.47
UPPER-3D-1 2711	-2.08E+08	4.93E+08	-0.42
shear (13)			
UPPER-3D-1 2711	8.38E+07	4.93E+08	0.17
UPPER-3D-1 2690	-1.95E+08	1.61E+09	-0.12
shear (23)			
RIV-3D-1 2874	1.33E+08	4.56E+08	0.29
UPPER-3D-1 2690	-8.95E+08	1.61E+09	-0.56

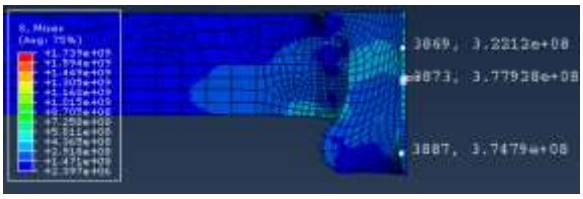

135-degree section 135-degree section

Figure 9.4. Data for Joint Quality Analysis

At the 90-degree section of PR3 simulation, highest compressive ratio of (stress component/V-M stress) in the entire FE mesh is exhibited by mesh element 1772 of the outer skin and it is -2.33. This element is in the outer skin adjacent to the inner skin and the rivet shank. Mesh element 2187 of the inner skin has the highest compressive stress component of -1050 MPa. This element in the inner skin near the head of the rivet button. Mesh element 1843 of the outer skin has the highest tensile ratio of stress component/V-M stress (2.22) and the highest tensile stress component (1090 MPa). This element is in the outer skin adjacent to the rivet crown.

Element 1843 of the outer skin is more susceptible to crack nucleation compared to element 2187 of inner skin and element 1772 of outer skin because of high tensile (stress/V-M) ratio and high tensile stress.

At the 135-degree section of PR3 simulation, highest compressive ratio of (stress component/V-M stress) in the entire FE mesh is exhibited by mesh element 3869 of the rivet and it is -1.74. This element is in the outer skin adjacent to the inner skin and the rivet shank. Mesh element 3887 of the rivet has the highest compressive stress component of -641 MPa. This element in the inner skin near the head of the rivet button. Mesh element 3873 of the rivet has the highest tensile ratio of stress component/V-M stress (2.41) and the highest tensile stress

component (910 MPa). All the three elements are on the rivet axis. This is the region of the mesh where the brick elements transition to wedge elements. Element 3873 is the most critical for crack nucleation.

9.4 SUMMARY

Three-dimensional, 180-degree sector, full dynamic percussive riveting FE model was built and simulated. Residual stress results from three sections within the three-dimensional simulation stackup were presented and discussed. Asymmetric motion of the bucking bar was implemented. A coarse mesh was utilized in the rivet and simulation was only run up to 27 rivet hammer strokes because of computational time overruns. It was observed that the bucking bar dwelled for more time in the 135-degree section compared to the 45-degree section. The outer skin region adjacent to the rivet crown was found to be critical for crack nucleation in the 45-degree and 90-degree sections. The area of the rivet at the rivet axis was found to be critical for crack nucleation in the 135-degree section. A finer rivet mesh and a 360-degree stackup mesh devoid of 6-node wedge (C3D6RT) elements at the rivet axis must be used in future studies.

Chapter 10. CONCLUSION AND RECOMMENDATIONS FOR FUTURE WORK

10.1 CONCLUSION

- Residual stress and strain distributions of joints manufactured using percussive riveting manufacturing process have not been modeled and characterized till date. Numerical modeling and analysis of the percussive riveting manufacturing process was performed and the residual stress/strain trends were studied. In the percussive riveting process, both rivet hammer and bucking bar are free to move. A DOE was also performed to study the effects of some important manufacturing and joint geometry parameters. A three-dimensional percussive riveting simulation was carried out to study the impact of the asymmetric motion of the bucking bar.
- In the two-dimensional squeeze riveting analysis, *inner skin region adjacent to the rivet button* was observed to be *most critical* location for crack nucleation by compression-induced shearing.
- In two-dimensional, partial dynamic riveting analysis, a radial gap was observed between the rivet shank the outer skin below the countersink wedge. The *rivet crown region adjacent to the rivet wedge* was observed to be *most critical* for crack nucleation.
- In two-dimensional, full dynamic percussive riveting analysis, an axial gap was observed between the head of the rivet button and the inner surface of the inner skin. *The inner skin region adjacent to the rivet button* was found to be *most critical* for crack nucleation because of compression-induced shearing. *Inability to include convective heat transfer* in the numerical simulation framework, results in *higher temperature rise* than what is expected. This leads to larger deformation because of *thermally induced softening*. Due to *free relative motion* of the *rivet* inside the rivet hole and due to the *different curvature*

of the skins under the application of the unequal rivet hammer and bucking bar constraint forces, *large gap and large deformation parameters* were observed.

- Two-dimensional, full dynamic percussive riveting DOE was performed using FEM. From the fit statistics of the models, it was observed that an increase in μ led to a reduction in the gap, an increase in KE led to an increase in R_B and a reduction in H_B, and an increase in TR led to a reduction in R_B and an increase in H_B. Hence, *for a good quality joint*, *μ and KE need to be maintained high*, *and TR needs to be comparatively low*.
- Three-dimensional, 180-degree sector, full dynamic percussive riveting FE model with a coarse mesh was analyzed. Asymmetric motion of the bucking bar was implemented. *Bucking bar dwell time* was observed to *impact magnitude of rivet deformation*. The *outer skin region adjacent to the rivet crown* and *area of the rivet at the rivet axis* were found to be *critical* for crack nucleation.

10.2 Recommendations for Future Work

- Comparison of future countersunk rivet simulation results with experimental data from either image correlation or neutron diffraction should be performed.
- Fatigue analysis of joints manufactured using percussive riveting technique should be undertaken and compared with squeeze riveting fatigue data.
- Damage model can be incorporated into future percussive riveting simulations to further address crack nucleation concerns.
- Johnson-Cook is an isotropic material flow model. So, kinematic hardening can be incorporated into future simulations.
- A full 360° rivet stackup with two-axis bucking bar movement can be studied to further gain understanding of asymmetric bucking bar motion on the stackup residual stresses and strains.

BIBLIOGRAPHY

[1] Szolwinski, M. P., and Farris, T. N., *Linking Riveting Process Parameters to the Fatigue Performance of Riveted Aircraft Structures*, J. Aircr., 37(1), pp. 130-137, (2000)

[2] Yuwen Li, Fengfeng Xi and Kamran Behdinan, *Dynamic Modeling and Simulation of Percussive Impact Riveting for Robotic Automation*, Journal of Computational and Nonlinear Dynamics, Vol. 5 / 021011-1, (2010)

[3] Briles, F., US Patent 5,671,521: *Rivet Clamp-up Deformation*. (1997)

[4] Ahn, J.Y., *"Methods for Evaluating the Performance and Human Stress-Factors of Percussive Riveting"*, MS Thesis, Univ. of Washington, Seattle (2017)

[5] Szymczyk, E. Jachimowicz, J. Puchala, K., *Some aspects of dynamic riveting simulations*, J. of KONES Powertrain and Transport, Vol. 19, No. 1, (2012)

[6] J.H. Deng, H.P. Yu, C.F. Li, *Numerical and experimental investigation of electromagnetic riveting*, Materials Science and Engineering A 499, pp. 242–247, (2009)

[7] Peter B. Zieve, Electroimpact, Inc., *Low Voltage Electromagnetic Riveter*, (AD86-680) (White Paper)

[8] Li Huang, John V. Lasecki, Haiding Guo and Xuming Su, *Finite Element Modeling of Dissimilar Metal Self-Piercing Riveting Process*. SAE International Journal of Materials and Manufacturing, Vol. 7, No. 3, pp. 698-705, (2014)

[9] Li Huang et. al., *Finite-Element and Residual Stress Analysis of Self-Pierce Riveting in Dissimilar Metal Sheets*, Journal of Manufacturing Science and Engineering, Vol. 139 / 021007-1, (2017)

[10] J.F.C. Moraes, "*Understanding the Effect of Residual Stresses and Deformation on the Fatigue Behavior of Permanent Fasteners*", Ph.D. dissertation, UA Tuscaloosa, (2016)

[11] Iyer K, Hu S J, Brittman F L, et al., *Fatigue of single and double-rivet self-piercing riveted lap joints*, Fatigue & Fracture of Engineering Materials & Structures, 28(11): 997-1007, (2005)

[12] Hanssen A G, Olovsson L, Porcaro R, et al., *A large-scale finite element point-connector model for self-piercing rivet connections*, European Journal of Mechanics A: Solids, 29(4): 484-495, (2010)

[13] G. Di Bella, C. Borsellino, L. Calabrese, E. Proverbio, *Durability of orbital riveted steel/aluminium joints in salt spray environment*, Journal of Manufacturing Processes, 35, 254–260 (2018)

[14] Rans, C., Straznicky, P. V., and Alderliesten, R., *Riveting Process Induced Residual Stresses Around Solid Rivets in Mechanical Joints*, J. Aircr., 44(1), pp. 323-329, (2007)

[15] R.P.G. Muller, "*An Experimental and Analytical Investigation on the Fatigue Behavior of Fuselage Riveted Lap Joints*", Ph.D. dissertation, Delft Univ. of Technology (1995)

[16] A. Atre, "*A Finite Element and Experimental Investigation on the Fatigue of Riveted Lap Joints in Aircraft Applications*", Ph.D. dissertation, GA Tech (2006)

[17] A Atre, WS Johnson., *3D FEA Simulations to Assess Residual Stresses in Riveting Processes*, Journal of ASTM International 3:3, 13077 (2006)

[18] Langrand, B., *Riveted joint modeling for numerical analysis of airframe crashworthiness*, Finite Elements in Analysis and Design, (2001)

[19] Fung CP, Smart J, *An experimental and numerical analysis of riveted single lap joints*, Proc Inst Mech Eng 208:79-90 (1996)

[20] Li, G., Shi, G., and Bellinger, N. C., *Residual Stress/Strain in Three-Row, Countersunk, Riveted Lap Joints*, J. Aircr., 44 (4), pp. 1275-1285, (2007)

[21] Abdelal, G. F., et al., *Numerical and Experimental Investigation of Aircraft Panel Deformations During Riveting Process,* Journal of Manufacturing Science and Engineering, 137(1) (2015)

[22] Blanchot, V., Daidie, A., *Riveted Assembly Modelling: Study and Numerical Characterisation of a Riveting Process*, Journal of Materials Processing Technology, (2006)

[23] Jerzy Kajtoch, *Strain in the Upsetting Process*. Metallurgy and Foundry Engineering-Vol. 33, No. 1, (2007)

[24] de Rijck J J M, Homan J J, Schijve J, et al., *The driven rivet head dimensions as an indication of the fatigue performance of aircraft lap joints*. International Journal of Fatigue; 29(12): 2208-2218, (2007)

[25] Boni, L., Lanciotti, A., and Polese, C., *Some Contraindications of Hole Expansion in Riveted Joints*, Eng. Failure Anal., 46, pp. 140-156 (2014)

[26] Langrand, B., Deletombe, E., Markiewicz, E., and Drazetic, P., *Riveted Joint Modeling for Numerical Analysis of Airframe Crashworthiness*, Finite Elements in Analysis and Design, 38(1), pp. 21-44 (2001)

[27] Bloxsom, W. A., "*Modeling of the Reciprocating, Pneumatic Impact Hammer*", Ph.D. thesis, University of Nevada, Reno, NV (2003)

[28] JCE Ekvall, *Fatigue of riveted metallic joints*. ASTM STP 927:172-189 (1986)

[29] Deng, X., and Hutchinson, J. W., *The Clamping Stress in a Cold-Driven Rivet*, Int. J.Mech. Sci., 40(7), pp. 683-694, (1998)

[30] Fitzgerald TJ, Cohen JB, *Residual stress in and around rivets in clad aluminum alloy plates*. Mater Sci Eng 188:51-58 (1994)

[31] Johnson, T. J., Manning, R., Adams, D.E., Sterkenburg, R., Jata, K., *Diagnostics of Tool-Part Interactions During Riveting on an Aluminum Aircraft Fuselage*, Journal of Aircraft, Vol. 43, No. 3, 2006.

[32] Abdelal, G. F., Georgiou, G., Cooper, J., Robotham, A., Levers, A., Lunt, P., *Numerical and Experimental Investigation of Aircraft Panel Deformations During Riveting Process*, Journal of Manufacturing Science and Engineering, Vol. 137, 2015.

[33] Yoon, T. H., Kim, S. J., *Refined Numerical Simulation of Three-Dimensional Riveting in Laminated Composites*, Journal of Aircraft, Vol. 48, No. 4, 2011.

[34] Atre, A., Johnson, W. S., *Analysis of the Effects of Interference and Sealant on Riveted Lap Joints*, Journal of Aircraft, Vol. 44, No. 2, 2007.

[35] Figueira, J. A. N., Trabasso, L. G., *Riveting-Induced Deformations on Aircraft Structures*, Journal of Aircraft, Vol. 52, No. 6, 2015.

[36] Zeng, C., Tian, W., Liao, W.H., *Improved Model Concerning Driven Rivet Head Dimensions Based on Material Flow Characteristics*, Journal of Aircraft, Vol. 53, No. 4, 2016.

[37] Zheng, B., Haidong, Y., Lai, X., Lin, Z., *Analysis of Residual Stresses Induced by Riveting Process and Fatigue Life Prediction*, Journal of Aircraft, Vol. 53, No. 5, 2016.

[38] Li, G., Bellinger, N. C., *Studies of Residual Stress in Single-Row Countersunk Riveted Lap Joints*, Journal of Aircraft, Vol. 43, No. 3, 2006.

[39] Li, G., Shi, G., Bellinger, N. C., *Stress in Triple-Row Riveted Lap Joints Under the Influence of Specific Factors*, Journal of Aircraft, Vol. 48, No. 2, 2011.

[40] Huan, H., Liu, M., *Effects of Squeeze Force on Static Behavior of Riveted Lap Joints*, Advances in Mechanical Engineering, Vol 9(5), 2017.

[41] Yi, Y. P., *Investigation of Flow Stress Behavior and Microstructural Evolution of 7050 Al alloy*, Materials Science Forum, (2007)

[42] Don Lesuer, *Experimental Investigations of Material Models for Ti-6AL4V and 2024-T3* (UCRL-ID-134691), (1999)

[43] I. Rohr, H. Nahme, K. Thoma, C.E. Anderson, *Material characterisation and constitutive modelling of a tungsten-sintered alloy for a wide range of strain rates*, International Journal of Impact Engineering, 35 (8), 2008.

[44] Johnson, Gordon R., *Numerical Algorithms and Material Models for High-Velocity Impact Computations*, International Journal of Impact Engineering, (2011)

[45] Dassault Systemes, *Abaqus 6.14 documentation*

[46] Krovvidi, Sai C., Ramulu, M., Reinhall, Per G., *Numerical Study of the Percussive Riveting Process: Initial Results*, https://doi.org/10.1115/IMECE2019-11544, (2019)

[47] J. Gilbert Kaufman, *Chapter 4: Understanding the Aluminum Temper Designation System, [Introduction to Aluminum Alloys and Tempers. p39-76, ASM International]* (2000)

[48] Krovvidi, Sai C., Ramulu, M., Reinhall, Per G., *Numerical Study of the Percussive Riveting Process: Simulation Results*, https://doi.org/10.1115/IMECE2020-24096, (2020)

APPENDIX

The normalized values of geometric deformation parameters measured for AS1 and AS2 simulations are shown in tables AP1 and AP2. MATLAB's fitlm function was used to derive the model estimates of these responses.

Table AP1. Normalized geometric measurements from AS1

AS-1	Normalized geometric measurement						
	R_1	R_2	R_3	R_4	R_B	H_B	G
1	1.0369	1.0353	1.0399	1.1585	1.5300	0.2239	0.0459
2	1.0363	1.0286	1.0339	1.1324	1.6525	0.2021	0.0241
3	1.0336	1.0224	1.0311	1.1470	1.5259	0.2277	0.0516
4	1.0346	1.0280	1.0308	1.1676	1.6298	0.1988	0.0236
5	1.0361	1.0275	1.0311	1.1455	1.5780	0.2054	0.0382
6	1.0363	1.0290	1.0318	1.1282	1.5346	0.2180	0.0378
7	1.0328	1.0199	1.0266	1.1662	1.6382	0.1929	0.0236
8	1.0311	1.0238	1.0252	1.1540	1.5266	0.2172	0.0228

Table AP2. Normalized geometric measurements from AS2

AS2-	Normalized geometric measurement						
	R_1	R_2	R_3	R_4	R_B	H_B	G
1	1.0254	1.0155	1.0179	1.0928	1.5297	0.2359	0.0342
2	1.0204	1.0091	1.0105	1.0703	1.4678	0.2580	0.0406
3	1.0294	1.0193	1.0211	1.1111	1.5223	0.2304	0.0336
4	1.0259	1.0158	1.0183	1.0812	1.4348	0.2689	0.0291
5	1.0279	1.0183	1.0236	1.1399	1.4773	0.2350	0.0433
6	1.0269	1.0144	1.0169	1.1265	1.5916	0.2136	0.0248
7	1.0302	1.0267	1.0281	1.1585	1.5286	0.2179	0.0118
8	1.0294	1.0221	1.0264	1.1554	1.5705	0.2100	0.0064

Shown next are the model statistics obtained for normalized parameters from both analysis sets. In table AP3 it can be observed that the R^2 and adjusted R^2 of R_2 and R_4 are low. R_4's model statistics show the p-value greater than 0.05 which indicates a poor fit. From table 8.7, p-values of all model fits are less than 0.05 except for R_4. *Significant effects are shown in bold*. None of the terms have a significant effect on R_1 and R_4. This means the parameters of analysis set 1 (TR, CL, and μ) *cannot* be used to describe R_1 and R_4. Only CL is found to have a significant effect on

R_2. TR and CL both are found to have significant effect on R_3. TR, μ, and (TR)(μ) are found to influence R_B and H_B. Finally, TR, CL, μ, (TR)(μ) and (TR)(CL) are found to significantly affect G.

Table AP3. AS1 parameter model statistics

Fit Statistics	Term	p-value
Linear regression model: R_{1M}	Intercept	0.74923
Number of observations: 8, Error degrees of freedom:3	TR	0.22868
Root Mean Squared Error: 0.000815	CL	0.31356
R-squared: 0.933, Adjusted R-Squared 0.843	μ	0.66592
F-statistic vs. constant model: 10.4, p-value of fit: 0.0417	(TR)(CL)	0.22633
Linear regression model: R_{2M}	Intercept	0.00070727
Number of observations: 8, Error degrees of freedom:5	TR	0.16458
Root Mean Squared Error: 0.0036	**CL**	**0.028898**
R-squared: 0.703, Adjusted R-Squared 0.585		
F-statistic vs. constant model: 5.93, p-value of fit: 0.0479		
Linear regression model: R_{3M}	Intercept	0.00010468
Number of observations: 8, Error degrees of freedom:5	**TR**	**0.012968**
Root Mean Squared Error: 0.00197	**CL**	**0.0090533**
R-squared: 0.862, Adjusted R-Squared 0.807		
F-statistic vs. constant model: 15.7, p-value of fit: 0.00703		
Linear regression model: R_{4M}	Intercept	0.42587
Number of observations: 8, Error degrees of freedom:6	CL	0.083341
Root Mean Squared Error: 0.012		
R-squared: 0.418, Adjusted R-Squared 0.321		
F-statistic vs. constant model: 4.3, p-value of fit: 0.0833		
Linear regression model: R_{BM}	Intercept	0.016016
Number of observations: 8, Error degrees of freedom:4	**TR**	**0.0048734**
Root Mean Squared Error: 0.023	**μ**	**0.0040763**
R-squared: 0.901, Adjusted R-Squared 0.827	**(TR)(μ)**	**0.0042037**
F-statistic vs. constant model: 12.2, p-value of fit: 0.0176		
Linear regression model: H_{BM}	Intercept	0.0014895
Number of observations: 8, Error degrees of freedom:4	**TR**	**0.0026812**
Root Mean Squared Error: 0.00477	**μ**	**0.0028343**
R-squared: 0.919, Adjusted R-Squared 0.858	**(TR)(μ)**	**0.0029075**
F-statistic vs. constant model: 15, p-value of fit: 0.0121		
Linear regression model: G_M	Intercept	0.035875
Number of observations: 8, Error degrees of freedom:2	**TR**	**0.032948**
Root Mean Squared Error: 0.0022	**CL**	**0.032773**
R-squared: 0.99, Adjusted R-Squared 0.963	**μ**	**0.0144**
F-statistic vs. constant model: 37.8, p-value of fit: 0.026	**(TR)(CL)**	**0.030426**
	(TR)(μ)	**0.015952**

Table AP4. AS2 parameter model statistics

Fit Statistics	Term	p-value
Linear regression model: R_{1M}	(Intercept)	6.34E-05
Number of observations: 8, Error degrees of freedom: 2	KE	0.84814
Root Mean Squared Error: 0.000541	**b_Y**	**0.043766**
R-squared: 0.992, Adjusted R-Squared 0.971	(KE)(b_Y)	0.088999
F-statistic vs. constant model:47.7, p-value of fit: 0.0207	**(KE)(h_Y)**	**0.04722**
	h_Y	**0.031669**
Linear regression model: R_{2M}	(Intercept)	1.68E-09
Number of observations: 8, Error degrees of freedom: 4	**KE**	**0.003508**
Root Mean Squared Error: 0.00125	**b_Y**	**0.001652**
R-squared: 0.968, Adjusted R-Squared 0.944	**h_Y**	**0.006632**
F-statistic vs. constant model:40.6, p-value of fit: 0.00188		
Linear regression model: R_{3M}	(Intercept)	5.96E-07
Number of observations: 8, Error degrees of freedom: 3	**KE**	**0.000952**
Root Mean Squared Error: 0.000729	b_Y	0.11882
R-squared: 0.993, Adjusted R-Squared 0.984	**h_Y**	**0.00782**
F-statistic vs. constant model:105, p-value of fit: 0.00148	**(b_Y)(h_Y)**	**0.019044**
Linear regression model: R_{4M}	(Intercept)	3.09E-06
Number of observations: 8, Error degrees of freedom: 4	**KE**	**0.000515**
Root Mean Squared Error: 0.00778	**b_Y**	**0.025286**
R-squared: 0.969, Adjusted R-Squared 0.946	**h_Y**	**0.035123**
F-statistic vs. constant model:42.2, p-value of fit: 0.00174		
Linear regression model: R_{BM}	(Intercept)	0.000583
Number of observations: 8, Error degrees of freedom: 4	**KE**	**0.016627**
Root Mean Squared Error: 0.023	**h_Y**	**0.0099**
R-squared: 0.891, Adjusted R-Squared 0.81	**(KE)(h_Y)**	**0.00932**
F-statistic vs. constant model:10.9, p-value of fit: 0.0213		
Linear regression model: H_{BM}	(Intercept)	0.68364
Number of observations: 8, Error degrees of freedom: 4	**KE**	**0.037086**
Root Mean Squared Error: 0.00752	**h_Y**	**0.01153**
R-squared: 0.926, Adjusted R-Squared 0.871	**(KE)(h_Y)**	**0.013334**
F-statistic vs. constant model:16.7, p-value of fit: 0.00997		
Linear regression model: G_M	(Intercept)	0.69548
Number of observations: 8, Error degrees of freedom: 4	KE	0.27021
Root Mean Squared Error: 0.00735	b_Y	0.26263
R-squared: 0.82, Adjusted R-Squared 0.685	(KE)(b_Y)	0.14334
F-statistic vs. constant model:6.07, p-value of fit: 0.0571		

In table AP4, it can be observed that the R^2 and adjusted R^2 of G are low. Also, G's model statistics show the p-value of 0.0571 which indicates a poor fit. In table AP4, the p-values of all

model fits are less than 0.05 *except* G. *Significant effects are shown in bold.* None of the terms have a significant effect on G. This means the parameters of analysis set 2 (KE, b_Y, and h_Y) *cannot* be used to describe G. b_Y, h_Y, and (KE)(h_Y) are found to affect R_1. KE, b_Y, and h_Y are all found to significantly affect both R_2 and R_4. KE, h_Y, and (b_Y)(h_Y) are all found to significantly affect R_3. KE, h_Y, and (KE)(h_Y) are found to affect both R_B and H_B.

So, it is observed that R_1 is influenced by three terms from analysis set 2. R_2 is influenced by one term from analysis set 1 and three terms from analysis set 2. R_3 is influenced by two terms from analysis set 1 and three terms from analysis set 2. R_4 is influenced by three terms from analysis set 2. R_B and H_B are both influenced by three terms from analysis set 1 and three terms from analysis set 2. G is influenced by five terms from analysis set 1. A larger study can be performed to investigate the existence of more interaction effects.

Normalized parameter models of AS1 and AS2 simulations are shown in eqns. (1) – (7). In eqns. (1)-(7), 'Δ' is CL and 'μ' is friction coefficient 'MU'. In the parameter models, signs of b_Y and h_Y are neglected. R_1's model (R_{1M}) is given by (1), R_2's model (R_{2M}) can be described using 2a or 2b. R_3's model (R_{3M}) is given by 3a or 3b. R_4's model (R_{4M}) is given by 4. R_B's model (R_{BM}) can be described using 5a or 5b. H_B's model (H_{BM}) can be described using 6a or 6b. G's model (G_M) is given by 7. In the plots accompanying the equations, the relative size of the blue bubbles correspond to the magnitude of normalized parameters that are shown in tables AP1 and AP2.

$$R_{1M} = 1.023 + 9.70(10^{-5})(KE) + 2.15(10^{-5})(b_Y) - 1.6(10^{-5})(h_Y) - 7.97(10^{-7})(KE)(b_Y) + 7.07(10^{-7})(KE)(h_Y) \quad (1)$$

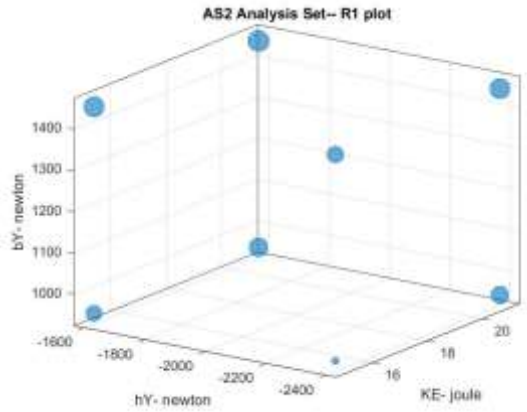

Figure AP1. R1 model plot

$$R_{2M} = 1.7925 - 0.0353(TR) - 0.7388(\Delta) \quad (2a)$$

$$R_{2M} = 0.9967 + 9.09(10^{-4})(KE) + 1.33(10^{-5})(b_Y) - 5.72(10^{-6})(h_Y) \quad (2b)$$

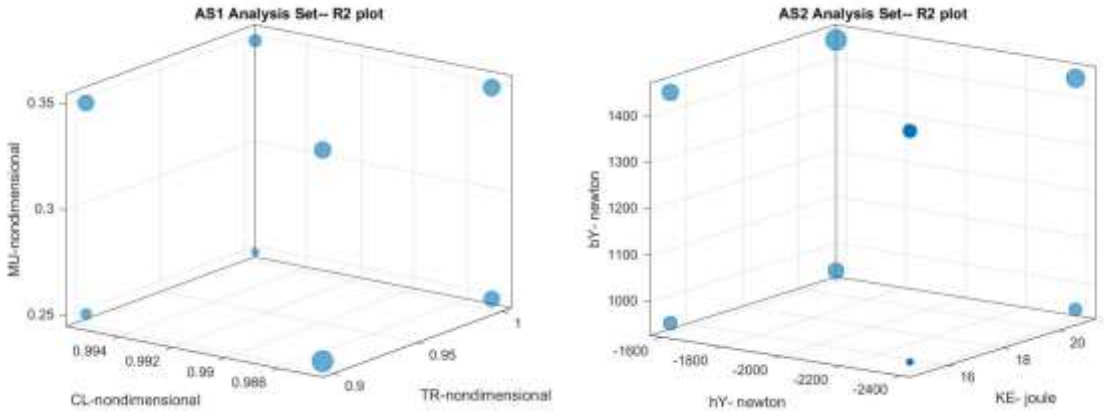

Figure AP2. R2 model plots

$$R_{3M} = 1.7215 - 0.0525(TR) - 0.6461(\Delta) \quad (3a)$$

$$R_{3M} = 1.0254 + 1.1298(10^{-3})(KE) - 1.14(10^{-5})(b_Y) - 2.01(10^{-5})(h_Y) + 1.19(10^{-8})(b_Y)(h_Y) \quad (3b)$$

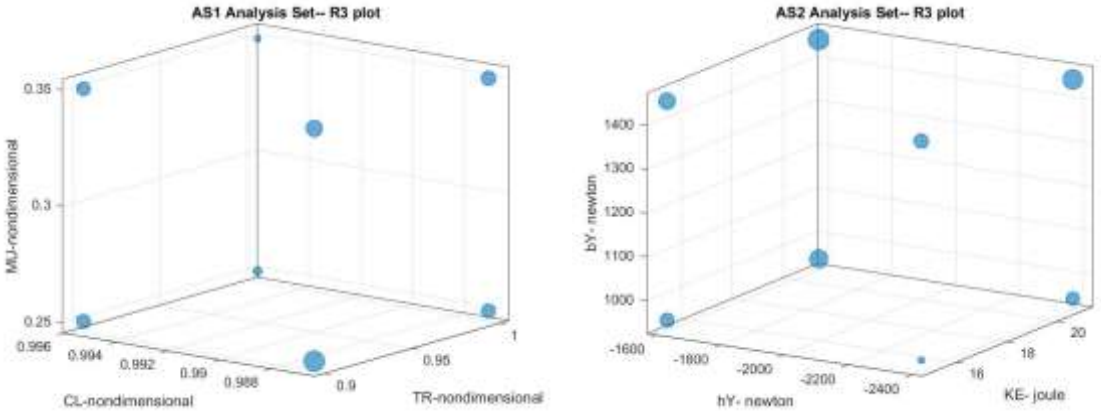

Figure AP3. R3 model plots

$$R_{4M} = 0.9453 + 9.3734(10^{-3})(KE) + 3.83(10^{-5})(b_Y) - 2.15(10^{-5})(h_Y) \quad (4)$$

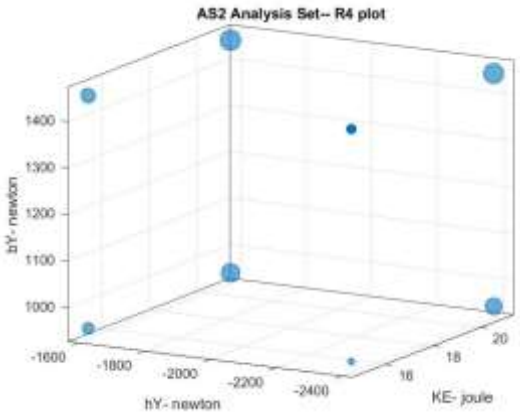

Figure AP4. R4 model plot

$$R_{BM} = -3.7671 + 5.569(TR) + 18.295(\mu) - 19.07(TR)(\mu) \quad (5a)$$

$$R_{BM} = 2.4967 - 0.0548(KE) - 5.7067(10^{-4})(h_Y) + 3.18(10^{-5})(KE)(h_Y) \quad (5b)$$

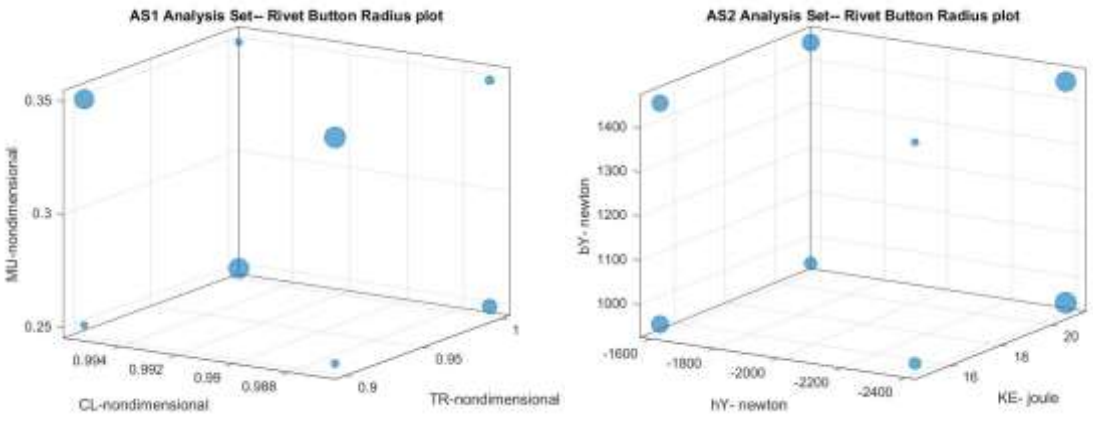

Figure AP5. R_B model plots

$$H_{BM} = 1.5145 - 1.3615(TR) - 4.1955(\mu) + 4.38(TR)(\mu) \quad (6a)$$

$$H_{BM} = -0.0362 + 0.0139(KE) + 1.7871(10^{-4})(h_Y) - 9.38(10^{-6})(KE)(h_Y) \quad (6b)$$

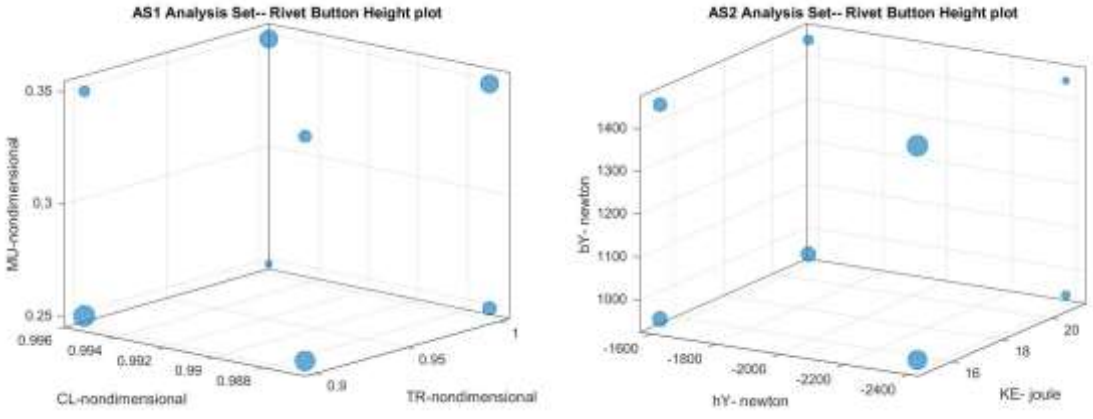

Figure AP6. H_B model plots

$$G_M = -16.911 + 18.592(TR) + 17.888(\Delta) - 2.436(\mu) - 19.551(TR)(\Delta) + 2.43(TR)(\mu) \quad (7)$$

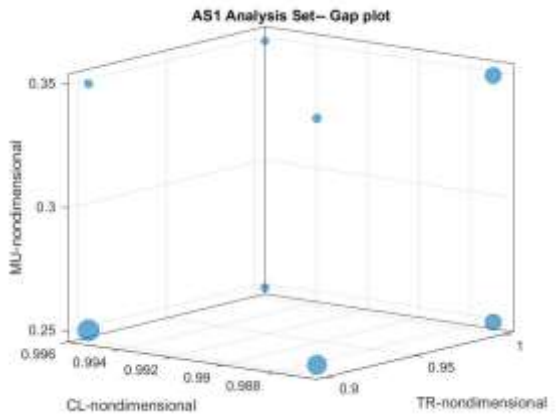

Figure AP7. G model plot

Table AP5 shows the AS1 parameter model estimates and model error percentage ($E_{\%}$). $E_{\%}$ is given by eq. (8). Table AP6 shows the AS2 parameter model estimates and model error percentages.

$$E_{\%} = 100\left(\frac{\text{Model Estimate} - \text{Measured Value}}{\text{Measured Value}}\right) \quad (8)$$

Table AP5. Model estimates and error percentages from AS1

AS1-	Model estimates and Error percentages							
	R_{1M}	$E_{\%}$	R_{2M}	$E_{\%}$	R_{3M}	$E_{\%}$	R_{4M}	$E_{\%}$
1	1.04	-0.02	1.03	-0.33	1.04	-0.30	1.14	-1.50
2	1.04	0.01	1.03	0.32	1.04	0.28	1.14	0.77
3	1.03	0.06	1.03	0.28	1.03	-0.01	1.16	1.02
4	1.03	-0.06	1.03	-0.27	1.03	0.02	1.16	-0.76
5	1.04	0.02	1.03	0.08	1.03	0.04	1.14	-0.38
6	1.04	-0.02	1.03	-0.07	1.03	-0.03	1.14	1.15
7	1.03	-0.07	1.02	0.18	1.03	-0.08	1.16	-0.64
8	1.03	0.07	1.02	-0.20	1.03	0.06	1.16	0.41
AS1-	Model estimates and Error percentages							
	R_{BM}	$E_{\%}$	H_{BM}	$E_{\%}$	G_M	$E_{\%}$		
1	1.53	-0.13	0.23	0.84	0.05	4.06		
2	1.64	-0.68	0.20	-0.83	0.02	-5.12		
3	1.53	0.14	0.23	-0.85	0.05	-2.39		
4	1.64	0.70	0.20	0.82	0.03	7.90		
5	1.61	1.91	0.20	-3.06	0.04	1.09		
6	1.53	-0.26	0.22	-0.19	0.04	0.58		
7	1.61	-1.83	0.20	3.23	0.02	0.92		
8	1.53	0.27	0.22	0.17	0.02	1.83		

Table AP6. Model estimates and error percentages from AS2

AS2-	Model estimates and Error percentages							
	R_{1M}	$E_{\%}$	R_{2M}	$E_{\%}$	R_{3M}	$E_{\%}$	R_{4M}	$E_{\%}$
1	1.02	-0.05	1.01	-0.16	1.02	-0.05	1.09	-0.45
2	1.02	0.02	1.01	0.01	1.01	-0.01	1.07	0.04
3	1.03	0.02	1.02	0.11	1.02	0.02	1.11	-0.36
4	1.03	-0.05	1.02	0.01	1.02	0.07	1.09	0.80
5	1.03	-0.02	1.02	0.10	1.02	0.06	1.14	0.37
6	1.03	-0.01	1.01	0.03	1.02	0.03	1.13	0.04
7	1.03	-0.01	1.03	-0.07	1.03	-0.01	1.16	0.41
8	1.03	-0.02	1.02	-0.08	1.03	-0.06	1.15	-0.80
AS2-	Model estimates and Error percentages							
	R_{BM}	$E_{\%}$	H_{BM}	$E_{\%}$	G_M	$E_{\%}$		
1	1.53	-0.27	0.23	-1.13	0.04	9.30		
2	1.45	-1.17	0.26	2.17	0.04	-7.89		
3	1.53	0.21	0.23	1.24	0.03	-6.80		
4	1.45	1.10	0.26	-1.97	0.03	7.73		
5	1.50	1.69	0.23	-3.57	0.03	-21.4		
6	1.58	-0.73	0.21	-0.74	0.03	37.2		
7	1.50	-1.72	0.23	3.98	0.01	-23.1		
8	1.58	0.61	0.21	0.95	0.01	41.5		

VITA

Sai Krovvidi has worked as an Aerospace Engineer in Washington state on projects dealing with finite element analysis (FEA), Fused Filament Fabrication (FFF) and Structural Substantiation (SS). His interests include finite element analysis, fracture mechanics, fatigue analysis and structural dynamics/aeroelasticity.

Sai got his Bachelor's degree in Mechanical Engineering from Jawaharlal Nehru Technological University in India. He then continued his education to obtain a Master's degree in Aeronautics and Astronautics Engineering from Purdue University in West Lafayette, Indiana. After moving to Washington state to start his Doctoral program in Mechanical Engineering at UW Seattle, he concurrently started working as an Aerospace Engineer at Pacific Rim Aerospace in Kirkland, Washington.

He worked on aircraft and helicopter fuselage modification projects leading the efforts in FEA. His analysis contributions were instrumental in drafting SS reports for the company's clients. He also worked as part of a team comprising of engineers from Pacific Rim and Safran Engineering Services tasked with the objective of designing and testing electrical-grade parts built using the FFF process for use in wide-body commercial airplanes.

He has worked as a research assistant and as a teaching assistant during his time as a doctoral student. His research was focused on developing and characterizing analytical and numerical models to evaluate residual stresses and strains set up inside joints manufactured using the percussive riveting process in the aerospace industry. His teaching experience comprised of assisting students with all academic and industry subject matter pertaining to aerospace elasticity, fatigue and fracture mechanics.